MAGNETIC AND ELECTRICAL TRANSPORT PROPERTIES OF ARTIFICIAL SPIN ICE

by

Katharina Zeissler

A Thesis submitted to Imperial College London

for the Degree of Doctor of Philosophy

Department of Physics

Imperial College London

London SW7 2AZ

August 2013

ABSTRACT

This thesis explores the mechanisms of the magnetic reversal of permalloy artificial spin ice arrays. The main research foci include the influence of domain wall propagation on the magnetic reversal of honeycomb artificial spin ice, the low temperature behaviour of honeycomb artificial spin ice and the classification of inverse permalloy opals as three dimensional artificial spin ice.

Room temperature imaging of the magnetisation configuration of the nanobars through the magnetic reversal, via scanning transmission X-ray microscopy, photoemission electron microscopy and Lorentz transmission electron microscopy, showed non random domain wall propagation through the frustrated vertices of the honeycomb artificial spin ice arrays. OOMMF simulations suggest that the origin of such non-randomness lies in the domain wall chirality. Boundary conditions necessary for domain wall injection into artificial spin ice arrays were investigated. A reduction of the edge nanobars width of 2/3 was needed to prevent random domain wall nucleation from the array edges.

Electrical transport measurements showed evidence of a change in the magnetic reversal, driven by domain wall propagation, of honeycomb permalloy artificial spin ice below 15 K. The transition temperature was found to be proportional to the square of the saturation magnetisation of the ferromagnetic material used. The change in the magnetic reversal was associated with the non-random vertex domain wall positioning below the transition temperature due to the influence of vertex dipole interactions.

Room temperature Lorentz transmission electron microscopy images and temperature dependent electrical transport measurements of three dimensional permalloy inverse opals showed the potential of magnetic inverse opals to act as three dimensional artificial spin ice systems.

Contents

List of Figures

List of Tables

DECLARATION OF ORIGINALITY

The material presented in this thesis "Magnetic and electrical transport properties of artificial spin ice" originated entirely as a result of my own independent research under the supervision of Dr. W.R. Branford and Prof. L.F. Cohen. Where I have incorporated the work of others I have made this clear and provided appropriate references.

Katharina Zeissler

27^{th} August 2013

PUBLICATIONS

K. Zeissler, S.K. Walton, S. Ladak, D.E. Read, T. Tyliszczak, L.F.Cohen and W.R. Branford. The non random walk of chiral magnetic charge carriers in artificial spin ice. *Scientific Reports*, 3:1252, 2013

S.K. Walton, **K. Zeissler**, W.R. Branford and S. Felton. Malts: A tool to simulate Lorentz Transmission Electron Microscopy from micromagnetic simulations. *IEEE Transactions on Magnetics*, 2013 (accepted for publication)

S. Ladak, S. Walton, **K. Zeissler**, D.E. Read, T. Tyliszczak, W.R. Branford and L.F. Cohen. Disorder-independent control of magnetic monopole defect population in artificial spin-ice honeycombs. *New Journal of Physics*, 14:045010, 2012

W.R. Branford, S. Ladak, D.E. Read, **K. Zeissler** and L.F. Cohen. Emerging chirality in artificial spin ice. *Science*, 335:6076, 2012

K. Kumar, A.M. Nightingale, S.H. Krishnadasan, N. Kamaly, M. Wylenzinska-Arridge, **K. Zeissler**, W.R. Branford, E. Ware, A.J. deMello and J.C. deMello. Direct Synthesis of dextran-coated superparamagnetic iron oxide nanoparticles in a capillary-based droplet reactor. *Journal of Materials Chemistry*, 22:11, 2012

D.S. Bhachu, M.R. Waugh, **K. Zeissler**, W.R. Branford and I.P. Parkin. Textured Fluorine-Doped Tin Dioxide Films formed by Chemical Vapour Deposition. *Chemistry*, 17:41, 2011

ACKNOWLEDGMENTS

I would like to thank my supervisors, Dr. Will R. Branford and Prof. Lesley F. Cohen, who enabled me to do this work and without whom this thesis would have never reached its completion. I owe them a great debt for their generous support and guidance.

My thanks goes to Dr. Dan Read, Dr. Sam Ladak and Dr. Adam Gilbertson for introducing me to the art of lithographic techniques. I am especially grateful to Dr Karen Yates, Dr Kelly Morrison, Dr Ulli Hannemann, Dr Gary Perkins, Dr Peter Spencer, Dr Julia Lyubina and Dr Ana-Vanessa Jausovec for their indispensable support in all matters of laboratory work and equipment handling. I am thankful for the valuable simulations provided by Stephanie Walton included in chapter 4 and chapter 6.

None of the Beam line experiments would have been possible without the extensive involvement of Dr. Sam Ladak, Dr. Dan Read and Stephanie Walton, as well as, Dr. Tolek Tyliszczak (ALS) and Prof. Sarnjeet Dhesi, Dr. Jorge Miguel and Dr. Francesco Maccherozzi (Diamond).

I am especially grateful for the collaboration with Prof. Mary Ryan, Dr. Solveig Felton, Chahat Kansal, Dr. Benoit Illy and Dr. Amy Cruickshank from the Materials Science Department at Imperial College, which enabled the work on magnetic inverse opals and for contributing their valuable expertise on the fabrication of inverse opals and Lorentz transmission microscopy.

Thank you to Dr. Tyler Roschuk and Dr. Karen Yates for valuable discussions and proof-reading this thesis. I also would like to thank Prof. David Caplin and Dr. Andre Trindade Pereira for their helpful insight into various aspects of magnetism and electrical transport.

I will not forget all the members of the Functional Magnetism group and the Plasmonics group, past and present, for making my time at Imperial College such a pleasurable

and enjoyable experience both at the office and away during evenings spent playing board games (Despite the traitorous Eclipse playing attitudes of some).

Finally I would like to thank my parents, friends, siblings and the whole Martin clan for their love and support and for being like beams of light in my life.

The studentship was jointly funded under grant EPSRC (EP/G004765/1) (WRB) and an EPSRC Doctoral Training Award. This work was carried out with the support of the Diamond Light Source and the Advanced Light Source. The ALS is supported by US DoE under contract DE-AC03-76SF00098.

Chapter 1

Introduction

In recent years extensive research has been conducted on complex configurations of single domain ferromagnetic bars exhibiting frustration despite being geometrically ordered. Geometrical frustration refers to materials where not all pairwise interactions can be minimised simultaneously. The realization that an assembly of ferromagnetic nanowires, if arranged on specific lattices, can exhibit geometrical frustration has opened up a whole new branch of frustrated materials. The first realization of frustrated correlations, a signature of spin ice, of single domain bars arranged on a square lattice was realised by Wang *et al.* in 2006 [1]. Two years later, Qi *et al.* published the first experimental evidence of geometrical frustration of ferromagnetic nanowires arranged on a honeycomb lattice [2]. Since then, the study of two dimensional artificial spin ice has evolved into a fast moving research area. Extensive efforts have been made into developing demagnetization protocols and studying bar correlations.

Artificial spin ice research became even more exciting with the realisation that the magnetic state of the vertices can be approximated as a quasi-particle possessing a magnetic charge. The interactions of such quasi-particles can be studied and visualised using common magnetic imaging techniques. Thus far, the dynamics of these quasi particles have not been investigated. The large energy barrier between the two Ising-like magnetization states of single domain ferromagnetic bars, of the order of 10^5 K [2], results in the require-

ment of an applied magnetic field to achieve quasi-particle dynamics. The intricacies of the field driven magnetic reversal is a complex interplay of constraints introduced by the frustration and ferromagnetic domain wall behaviour.

Due to the high Curie temperature of the ferromagnetic bars and the large interaction energies, artificial spin ice was considered to be athermal at and below room temperature. However, recent electrical transport measurements showed an unusual feature below 50 K which is not compatible with the assumption that thermal energy does not play a role in the magnetic switching of the frustrated arrays [3]. Thus far the exact origin of this effect has not been established, although the influence of the vertex dipole arising due to deviations from perfect Ising-like behaviour has been proposed.

Investigations exploring the behaviour of artificial spin ice thus far has been limited to two dimensional systems. A logical next step is the elevation of artificial spin ice into the third dimension, closing the structural gap between crystalline bulk spin ice and the artificial analogues. However, the creation of three dimensional spin ice is a challeging problem which exceeds the capabilities of conventional lithographic techniques.

The aim of this thesis is to develop the understanding of the field driven magnetic reversal of artificial spin ice, focusing primarily on two dimensional permalloy honeycomb artificial spin ice arrays. The addition of a magnetic field introduces dynamics into the otherwise static system allowing artifical spin ice to access unique, ordered and disordered, states otherwise inaccessible due to high energy barriers between the macroscopic Ising spin states.

Chapter 2 provides a brief introduction of the key concepts necessary for the understanding of the results discussed in the later chapters. Preceding work and advances in spin ice are reviewed establishing the framework for this research.

Chapter 3 discusses the details of artificial spin ice fabrication, measurement equipment, and data analysis used in the quest for understanding the magnetic reversal of artificial spin ice.

Chapter 4 presents the particularities of the magnetic reversal of two dimensional

permalloy honeycomb artificial spin ice via domain wall nucleation and propagation. The magnetic reversal was driven by a magnetic field applied parallel to the horizontal bars. A focal point of this chapter is to establish the controlling influence of the micromagnetic configuration of the domain walls mediating the reversal process. It was found that the magnetic charge model, while powerful, does not capture the controlling effect of the domain wall chirality (the unique micromagnetic arrangement of the domain wall) on the propagation through the vertices. This deterministic feature of the reversal could be utilised in conjunction with the controlled injection of domain walls into artificial spin ice arrays to contolled reversal cascades. The possibility of such controlled domain wall injection was explored and successful domain wall injection was achieved through a modulation of the edge bar thickness with respect to the central bars.

Chapter 5 explores the temperature dependance of the magnetic reversal by monitoring the field dependent resistance change caused by the reversal of the honeycomb artificial spin ice. A change in the resistance behaviour, mirroring a change in the magnetisation reversal mechanism, was detected below 15 K. This confirms that the unusual electrical transport behaviour first observed by Branford *et al.* [3] is indeed a charateristic of the frustrated bar arrangement. The critical temperature associated with this phenomenon was found to be proportional to the square of the magnetisation. The origin of the low temeprature Hall signature was proposed to lie in an asymmetric arrangement of the vertex domain walls and is at its heart an anisotropic magnetoresistance phenomen.

This is in agreement with the original proposal of the vertex dipole influence. The origin the resistance signature was proposed to lie in the position of the vertex domain wall, which is influenced by the vertex dipole interaction.

Chapter 6 considers whether permalloy cubic close packed inverse opals are a class of three dimensional artificial spin ice. Lorentz transmission electron microscopy and electrical transport measurements show characteristic features associated with artificial spin ice, suggesting that the inverse opals do indeed behave like their two dimensional analogue. However, the addition of the out of plane bar adds additional complexity. Three dimen-

sional artificial spin ice brings artificial spin ice one step closer to its crystalline counterpart, bulk spin ice.

Chapter 7 concludes the thesis, providing an overview of the key results and discussing further research avenues.

Chapter 2

Key Concepts

This chapter briefly introduces the key concepts necessary for the understanding of the results discussed in the later chapters.

2.1 Artificial Spin Ice

2.1.1 Geometrical Frustration

Geometrical frustration refers to the inability of a system to reach a unique energy minimum due to its geometrical layout, its lattice [4]. Not all the interactions of such a system can be satisfied, leading to a compromise being struck. Antiferromagnetic coupled Ising spins can exhibit frustration depending on their lattice constraint. If the spins are arranged as shown in figure 2.1(a) on a square lattice; an anti-parallel arrangement of all nearest neighbours can be found leading to a unique ground state [4]. However if said spins are arranged on a triangular lattice satisfying the constraint that all nearest neighbouring spins shall be anti-parallel is not so straight forward. Figure 2.1(b) shows the difficulty of satisfying the microscopic constraint of the problem [4]. No long range order can form spontaneously and the system possesses degenerate ground states [4]. Geometrically ordered systems possessing frustrated interactions include water ice [5], Spin Ices [6] and artificial spin ices [1].

2.1.2 Water Ice

Water ice is a geometrically ordered frustrated system (see figure 2.1(c)). Each oxygen ion sits on the site of a diamond lattice surrounded by four hydrogen ions [5]. Each hydrogen ion is shared between two oxygen ions and hence sits on a connective line between the two; Connected to one oxygen via a close covalent bond and connected to the other via a long hydrogen bond [5]. Hence each oxygen is surrounded by four hydrogen atoms of which two are situated close by the oxide ion and two are situated further away (see figure 2.1(c)). This two-close/two-far away arrangement was dubbed the ice rule and leads to a degenerate ground state as there are $2^4 = 16$ possible configurations complying with this ice rule. This degeneracy of the water ice ground state was calculated by Pauling to be $(3/2)^{N/2}$ where N is the number of water molecules in the system, leading to a ground state entropy of $(R/2)\ln 3/2 = 1.68$ Jmol^{-1}K^{-1} per hydrogen atom [5] (R is the ideal gas constant). There is no long range order and hence the system is disordered and remains as such down to 0 K.

2.1.3 Spin ice

Spin ice materials are systems exhibiting geometrical frustration analogous to water ice at low temperatures, however, the strong geometrical frustration is magnetic in origin and hence the absence of long range order results in magnetic disorder down to 0.2 K [6]. The class of spin ices consists of rare earth oxide materials. Rare earth materials are a family of oxides following the structure $A_2B_2O_7$ where A is the rare earth magnetic material and B is a non magnetic transition metal. Spin ice materials experimentally explored so far include $Ho_2Ti_2O_7$ [7,8], $Dy_2Ti_2O_7$ [6] and $Ho_2Sn_2O_7$ [9,10].

The rare earth ion position in the crystalline lattice can be described by a pyrochlore sublattice which results in a system of corner sharing tetrahedra where the magnetic ions sit on said corners. The crystalline anisotropy [11] leads to a confinement of the magnetic spins to the local $< 111 >$-type axes, essentially forcing Ising like behaviour of the spins

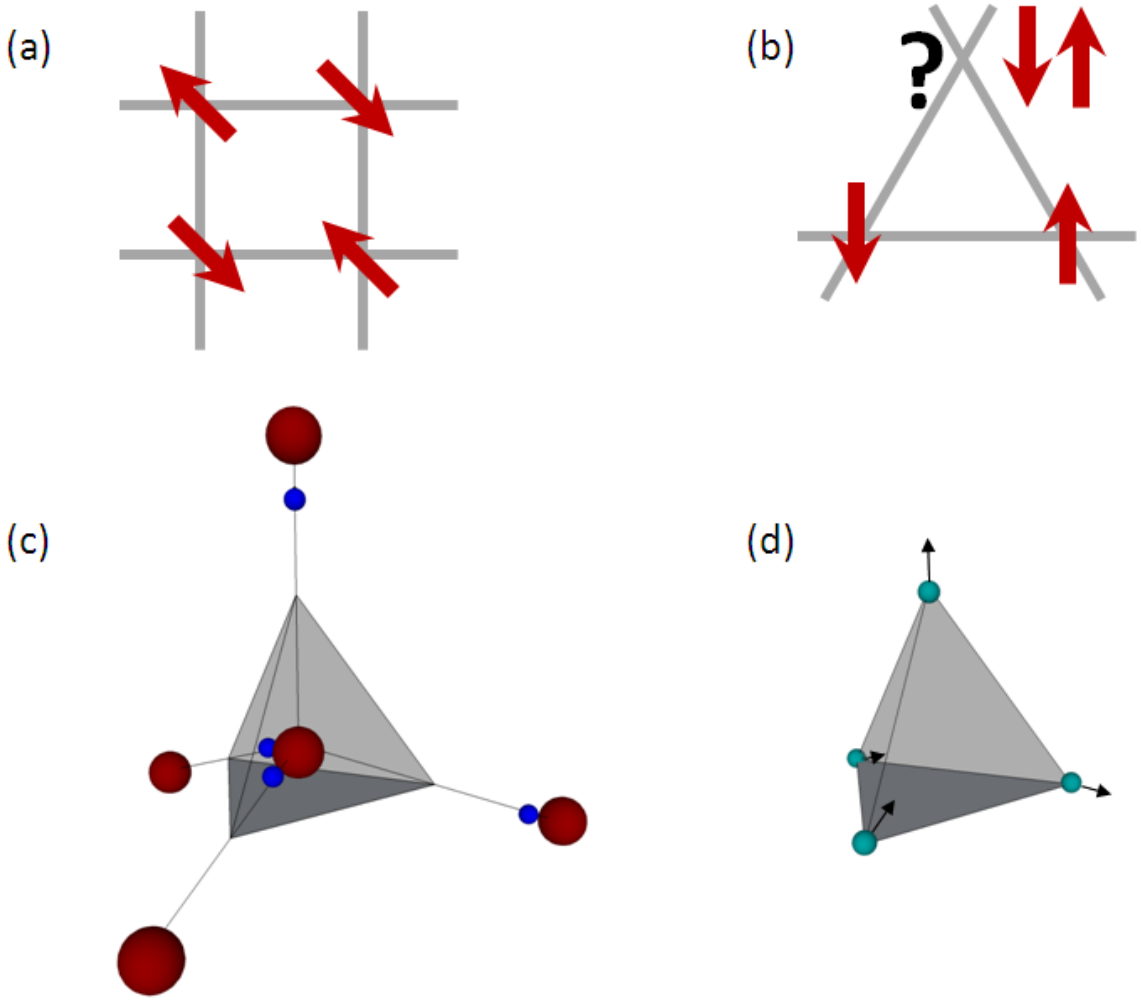

Figure 2.1 Principal of geometrical frustration and its realisation in water and spin ice. (a) shows the unfrustrated square lattice with anti-ferromagnetic coupled spins. (b) Frustration on a trangular lattice with anti-ferromagnetic coupling. (a) and (c) adapted from [4]. (c) Schematic of the water ice structure; oxygen ions in red and hydrogen atoms in blue. The gray tetrahedron indicates the mapping of the pyrochlore structure. (d) One tetrahedron/vertex of the pyrochlore structure in an ice rule state. Green spheres are the locations of the rare earth atoms.

along the axes joining the center of two interlinked neighbouring tetrahedra. At each tetrahedron center four Ising axes meet. Figure 2.1(c) shows the mapping of the pyrochlore spins onto the water ice structure. Each of the four spins sitting on each of the four Ising axes can be in one of two states: pointing towards or away from the tetrahedron center (see figure 2.1(d)). Hence each vertex/ tetrahedron will be in one out of $2^4 = 16$ possible configurations, however, none of the 16 spin arrangements will simultaneously satisfy all of the six pairwise interactions. If the interaction of the spins is ferromagnetic in nature the resulting spin ice is static in nature and the spins are frozen into its spin ice state at temperatures $\sim$1 K [7, 9].

The ground state of spin ice is governed by an analogy of the water ice rule: Each individual tetrahedron is in a configuration where two spins point towards the tetrahedron center and two point out. This lowest energy configuration, the ground state configuration, is six fold degenerate. Therefore any projection of such a ice rule state on a single tetrahedron onto a full scale spin ice crystal leads to a macroscopic degeneracy of ground states without long range order. The expected ground state entropy of spin ice materials was experimentally measured, in the case of $Dy_2Ti_2O_7$, to be very close to the water ice ground state entropy (down to 0.2 K) [6] (see figure 2.2(a)).

Original models describing spin ice systems involved nearest neighbour ferromagnetic exchange interactions between Ising spins [7]. More recently it was discovered that even though the near neighbour spin ice model captures the key characteristics of the spin ice behaviour, a dipolar spin ice model including long range dipole interactions on top of weaker antiferromagnetic nearest neighbour exchange interactions leads to a better agreement with experimental neutron diffraction data [12–14] (see figure 2.2(b)-(d)).

2.1.4 Artificial Spin Ice

Artificial spin ice refers to artificially fabricated arrays of nanoscale ferromagnetic materials which exhibit geometrical frustration. They form the two dimensional analogue to the three dimensional bulk spin ices. Recent advances in nanotechnology have enabled

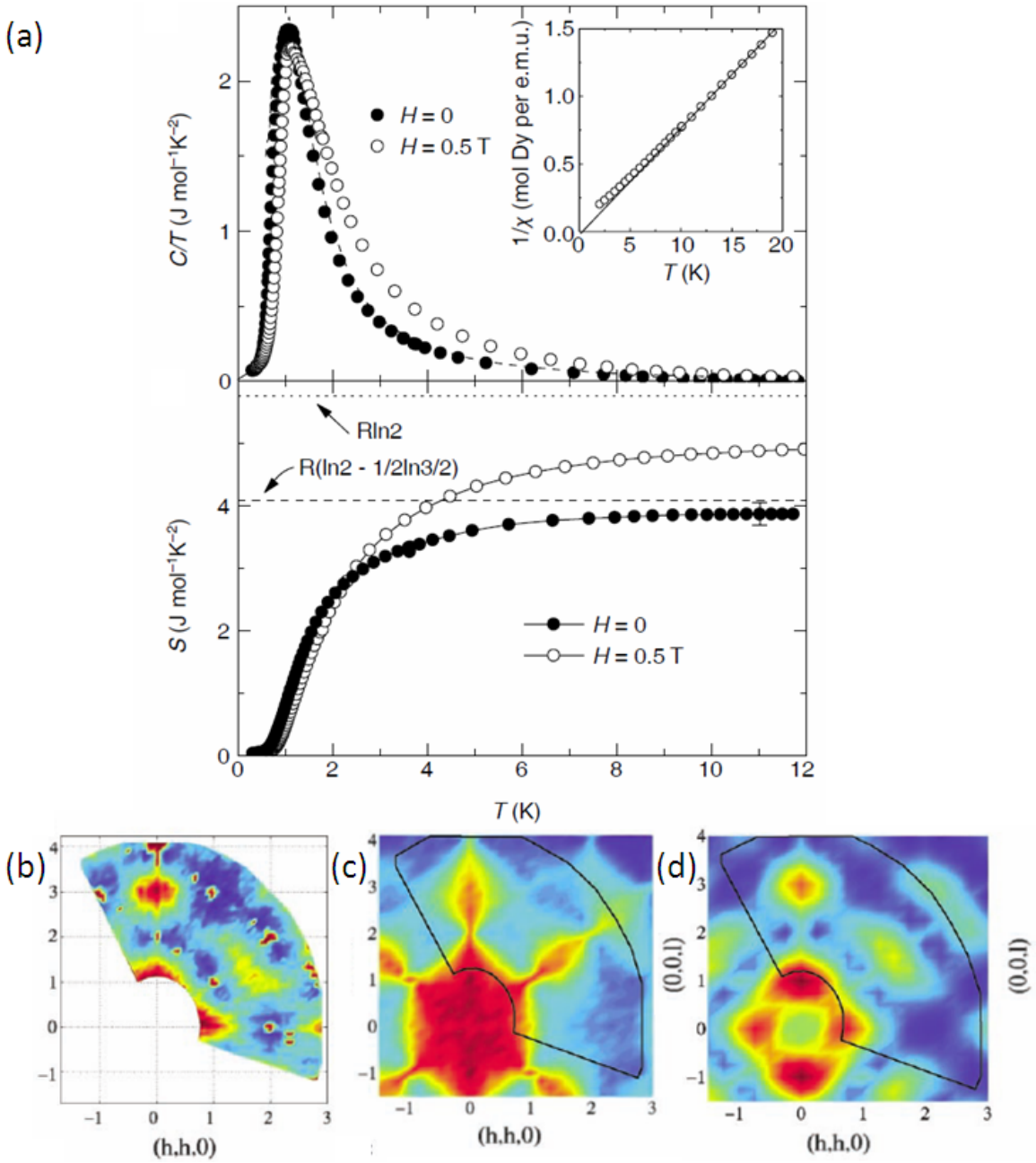

Figure 2.2 Spin ice entropy (a) specific heat measurement and the extracted entropy between paramagnetic phase and spin ice phase [6]. (b) Neutron scattering data of $Ho_2Ti_2O_7$ in the (hhl) reciprocal space at 50 mK [12], (c) simulated neutron scattering using nearest neighbour model [12], (d) simulated neutron scattering using the dipolar spin ice model [12].

this custom tailoring of standard ferromagnetic materials in order to study and visualize geometrical frustration. Artificial spin ice arrays consists of single domain ferromagnetic bars or islands whose magnetic behaviour is dominated by their shape anisotropy [1, 15]. Hence the microscopic magnetic moments are aligned pointing parallel to the long axis essentially forming a macroscopic 'Ising'-like spin state. The macroscopic spin has two allowed states: pointing parallel or anti-parallel along the Ising axis. It is assumed that deviations from the Ising axis of the microscopic moments only occur close to the vertex [16].

Two lattices, square [1, 17–19] and honeycomb [2, 3, 20, 21], have been extensively studied so far. Artificial spin ice addresses some of the difficulties and limitations of bulk spin ice: Spin ice only exhibits geometrical frustration at very low temperatures (<2 K), Spin ice behaviour is limited to a few chemical compounds with set lattice dimensions and finally the spin configuration of individual tetrahedra in spin ice cannot be imaged directly. All the limitations listed above can be remedied in artificial spin ice; the lattice and bar geometry can be varied and distorted [22], the geometrical frustration is present up to the Curie temperature of the individual bars [23, 24] and as the dimensions of the bars range from 10-1000 nm their magnetic configuration can be probed directly using Lorentz transmission electron microscopy [2], scanning transmission X-ray microscopy [21], photoemission electron microscopy [20, 25] and magnetic force microscopy [1].

Furthermore, due to its fabrication flexibilities it is possible to study the onset of frustration by breaking the artificial spin ice array down into its building blocks [20].

Square Artificial Spin Ice

Geometrical frustration of artificial spin ice consisting of ferromagnetic elongated nanobars arises as a consequence of 4 bars meeting at each vertex at 90° to each other. Hence each vertex can be in one of 16 possible configurations (see figure 2.3(a)). Out of these 16 possibilities six configurations comply with the ice rule (2 in - 2 out/ 2out - 2 in), eight configurations express a magnetically excited state of 1 in - 3 out / 3 in - 1 out and the two remaining possibilities which are energetically very unfavourable, exhibit the 4 in or 4

out configuration. Artificial spin ice on a square lattice was first studied by Wang *et al.* [1]. However, the analogy with spin ice falls short as not all six ice rule states are energetically equivalent [23, 26], the six configurations can be divided into type I and type II (see figure 2.3(a)). Furthermore it was observed that a significant fraction of the square spin ice vertices failed to follow the ice rule [1, 23]. Depending on whether the ferromagnetic nanobars are disconnected or connected at the vertex type I or type II vertices are the minimum energy configuration in the demagnetised state [27]. The unconnected square spin ice possesses the predicted two fold degenerate ground state consisting of antiferromagnetically tiled type I vertices [18, 28] creating a pattern in which the magnetisation of each square follows a closed loop of alternating chirality (see figure 2.3(b)). However as the artificial square spin ice cannot reach thermal equilibrium below the Curie temperature, great efforts have been invested into demagnetisation protocols [17, 18, 28, 29]. Morgan *et al.* argued in a recent publication that controlling the metal growth temperature during the fabrication process can result in large domains exhibiting the predicted ground state ordering [19, 30]. Despite this, artificial square spin ice only shows a statistical preference favouring the ice rule configuration and short range vertex interactions are enough to model its behaviour [18] which are both shortcomings in the analogy with pyrochlore spin ice materials where long-range dipolar interactions play a significant role.

Honeycomb Artificial Spin Ice

Wills *et al.* proposed a highly frustrated ferromagnetic spin ice on the two dimensional Kagomé lattice [31]. Under the addition of long range dipolar interactions between the Ising spins novel low temperature ordering states can be predicted [32]. The two dimensional honeycomb artificial spin ice captures the geometry and the basic physical interactions of the Kagomé spin ice, replacing the atomic spin with macroscopic spins in form of single domain ferromagnetic bars [33]. Therefore honeycomb artificial spin ice represents a new avenue to study frustration by direct observation.

Artificial spin ice on a honeycomb lattice exhibits frustration due to the same principle

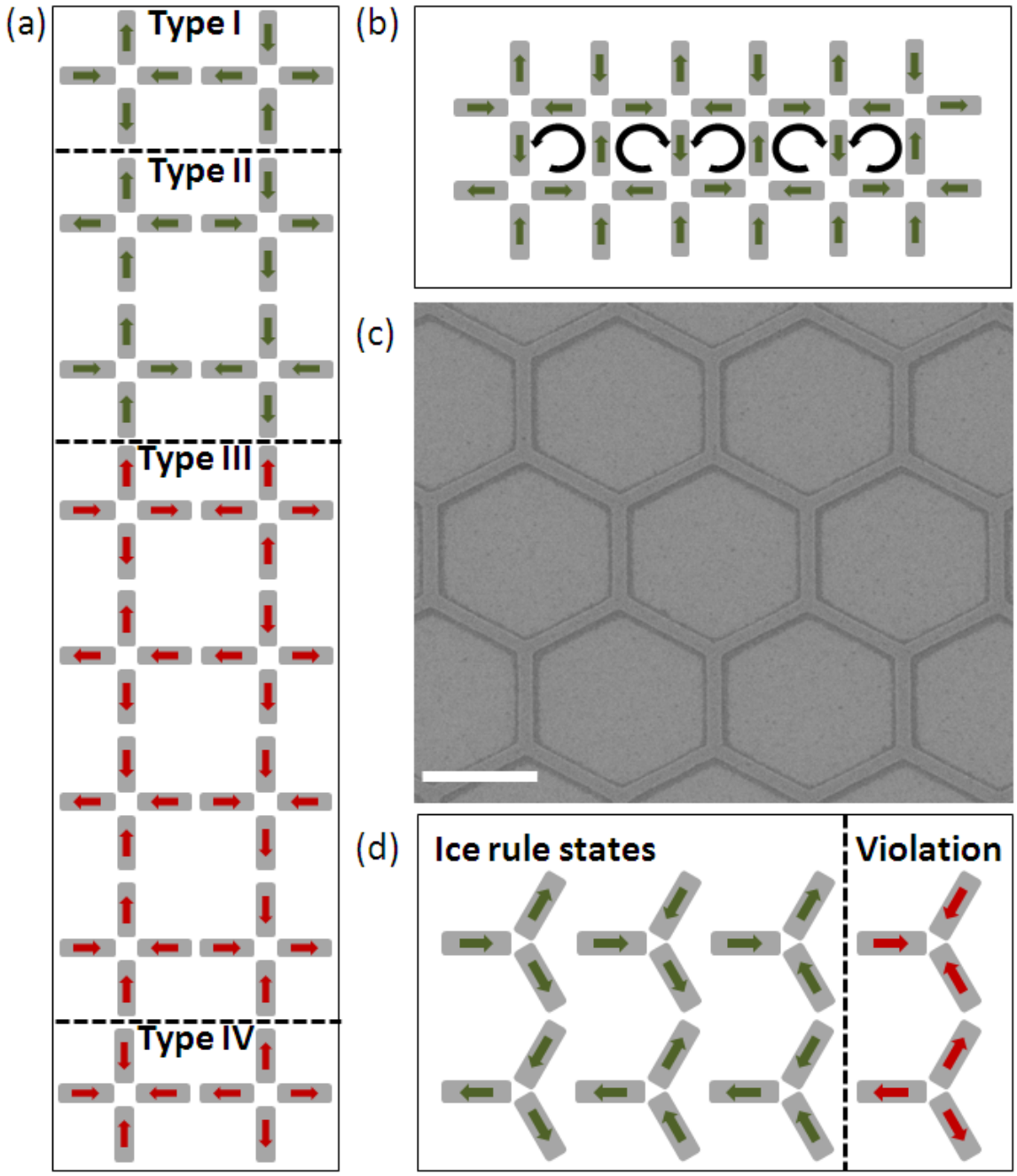

Figure 2.3 Artificial spin ice states. (a) All 16 possible states for single domain bars on a square lattice. Type I and II are ice rule states, type III and IV are ice rule violations. Adapted from [1]. (b) Type I two fold degenerate ground state for single domain bars on a honeycomb lattice. (c) SEM image of a permally honeycomb artificial spin ice. (d) List of all 8 possible states. Adapted from [2]

as square artificial spin ice. A SEM image of a honeycomb artificial spin ice array is shown in figure 2.3(c). Three bars 120° to each other intersect at each vertex. The ice rule now refers to the 2 in - 1 out/ 2 out - 1 in states, as postulated by Wills *et al.* [31] and first observed by Saitoh *et al.* [16]. There are $2^3 = 8$ possible configurations, six ice rule states and two ice rule violation states [2] (see figure 2.3(d)). In comparison to square artificial spin ice, the ice rules are energetically equivalent and the bar interactions are dominated by dipolar interactions [2]. Due to the large energy difference of the ice rule in comparison to the ice rule violation states, 72 % in case of connected vertices and 38 % in case of islands (for 500 nm long 110 nm wide and 23 thick permalloy bars). Despite demagnetisation protocols the ice rule was found to be always enforced [2].

Ice rule violations can occur under the application of an in-plane external magnetic field [34]. The defect density is dependent on the field direction [35]. In connected structures, external magnetic field application leads to nucleation of domain walls which propagate through the array resulting in the formation of ice rule violating vertices depending on the alternating magnetic charge background enforced by the odd number of bars joined at each connection point [36]. The stabilization of the violations can arise due to quench disorder (e.g. fabrication imperfections, material properties) [36], or due to domain wall interactions [21]. In disconnected structures magnetic excitation states at vertices occur due to quench disorder [37]. Ice rule violation creation and mobility through the spin ice were investigated experimentally by Mengotti *et al.* [25] and theoretically by Hügli *et al.* [38]. However these violations of the ice rule are only allowed in systems switching via transverse domain walls [39].

2.2 Magnetic Charges in Spin Ice

The magnetic behaviour of pyrochlore and artificial spin ice materials, especially the creation and movement of ice rule violations, has been described by treating the complex structure at the vertices as magnetic quasiparticles. This is a result of treating the dipolar

spin as a dumbbell (see figure 2.4(a) and (b)), consisting of two opposite charges separated by a distance equal to the vertex separation. The quasiparticle is then the sum of 'magnetic dumbell charges' sitting at the individual vertices. The switching behaviour is captured by the attractive and repulsive force between these quasiparticles and can be described by the magnetic version of Coulomb's law given by [40]

$$V(r_{\alpha\beta}) = \begin{cases} \frac{\mu_0}{4\pi}\frac{Q_\alpha Q_\beta}{r_{\alpha\beta}} & \text{if } \alpha \neq \beta \\ \nu_0 Q_\alpha Q_\beta & \text{if if } \alpha = \beta \end{cases} \tag{2.1}$$

where Q_α and Q_β refers to the 'magnetic charge' at vertex sites α and β respectively, $\neq_0$ is the onsite contribution, μ_0 is the vacuum permeability and $r_{\alpha\beta}$ is the distance between the two sites.

2.2.1 Bulk Spin Ice

In the case of pyrochlore spin ice, the dumbbell consists of two charges $\pm q$ separated by the diamond lattice bond length, $a_d = \sqrt{3/2}a$ (where $a \approx 3.54$ Å is the pyrochlore nearest-neighbour distance) [40]. The dipole/dumbbell has a moment of $\mu = qr_{\alpha\beta} = qa_d \approx 10\ \mu_B$ (μ_B refers to the Bohr magneton) [40]. The charge Q_α of the 'quasiparticle' sitting at vertex α then becomes the sum of the charges $\pm q$, effectively treating the two charges forming the dumbbell as separate entities. An ice rule is then associated with a charge $Q = \pm q \pm q \mp q \mp q = 0$. Therefore a 'quasiparticle' is only formed by an ice rule violating vertex $Q = \pm q \mp q \mp q \mp q = \mp 2q = \mp q_m = \mp 2\mu/a_d$ [40].

If one starts with a spin ice where all vertices obey the ice rules, then one dipole/dumbbell flip will result in ice rule violations on the vertices sharing the flipped dumbbell of opposite charge. Switching another dipole on one of the two involved vertices will result in the quasiparticle of that vertex appearing on the third vertex while the former becomes charge neutral again. This effective separation of the magnetic quasiparticles results in a

Coulombic interaction with pair wise interaction energy [40]:

$$E = -\frac{\mu_0 q_m^2}{4\pi r} \tag{2.2}$$

The energy cost of creating these magnetic quasiparticle pairs is extracted at the first switching event. Any further switching which separates the oppositely charged pair does not require any additional energy inviting analogies with magnetic monopoles whose 'Dirac strings' are a trail of flipped dipoles/dumbbells [40]. Bramwell *et al.* published experimental evidence of the movement of these quasiparticles and extracted the elemtary unit of magnetic charge to be equal to 5 μ_BÅ^{-1} [41].

2.2.2 Artificial Spin ice

The magnetic switching of artificial honeycomb spin ice has quite successfully been described using a purely Coulombic magnetic charge model analogous to the spin ice dumbbell model [37,42,43]. However, instead of treating the atomic spin as a dumbbell the entire single domain bar is treated as such (see figure 2.4(c)). Each bar has a magnetic moment, m of [42]

$$m = Matw \tag{2.3}$$

where a is the length, t is the thickness and w is the width of the bar. M refers to the saturation magnetisation of the ferromagnetic material forming the nanobar. The dipole moment, μ is given by

$$\mu = q_m a \tag{2.4}$$

where q_m is the dumbbell charge sitting at each of its end. Equating the magnetic moment to the dipole moment then results in the charges forming the dumbell to be equal to [42]

$$q_m = \pm Mtw \tag{2.5}$$

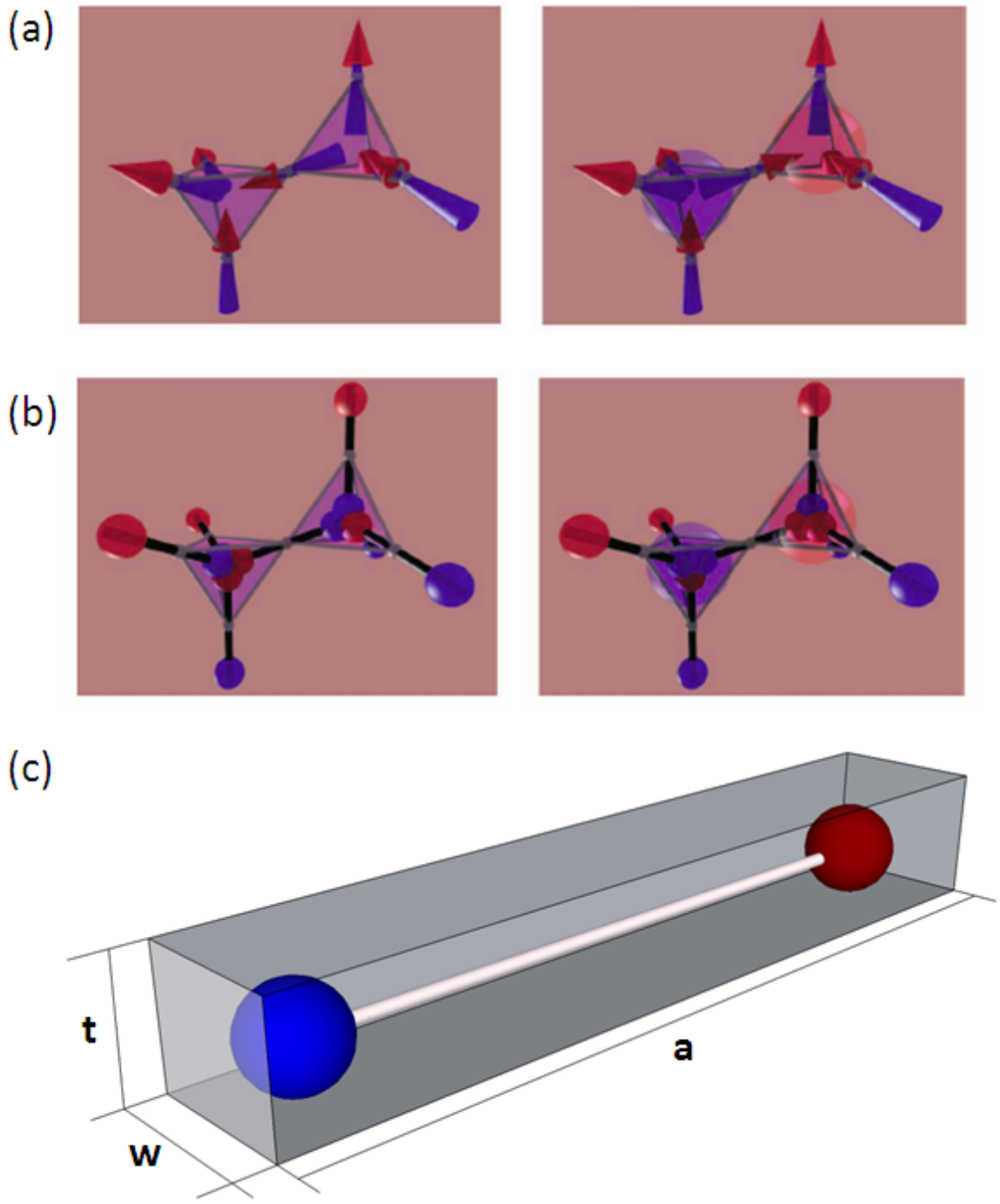

Figure 2.4 Schematics illustrating the dumbbell model in artificial and bulk spin ice. (a) Bulk spin ice rule and ice rule violation state in the spin dipole model [40]. (b) Dumbbell representation of states shown in (a) [40]. (c) Ferromagnetic nanobar in the dumbbell representation.

Hence the vertex charge is the sum of the individual charges sitting at the ends of the three involved dumbbells. Henceforth q_m is going to be refered to as q. The charge of the quasiparticle describing an ice rule expressing vertex is then $Q = \pm Mtw = \pm q$. The charge describing the ice rule violating vertex on the other hand is equal to $Q = \pm 3Mtw = \pm 3q$ [42].

In comparison to the bulk spin ice where thermal energy and the magnetic interaction energy is of the same order and hence spin flips are accessible without an external magnetic field, in the connected artificial spin ice changes in the bar magnetisation can only occur under the application of an external magnetic field via the creation of magnetic domain walls. The domain walls originate and terminate at vertices leaving behind a trail of switched nanobars. The domain walls in turn can be expressed as a quasiparticle of magnetic charge $Q_{DW} = \pm 2q$ with a diameter, d, equal to the width of the wire w [42]. During the magnetic reversal the domain walls are nucleated and pushed through the array via the external magnetic field. As the point charge travels through the array it encounters vertices of charge $Q_V = \pm q$ (starting point is a saturated state).

It is postulated that the overall switching is governed by the charge of the domain wall, the strength of the external field and the charge of the vertex [42]. As in spin ice the switching is dominated by the Coulombic interaction of these quasi-particles, however in the special case of a connected artificial spin ice the interaction is between the domain wall charge and the vertex charge [42]. Assuming one starts with a vertex of charge $+q$ as depicted in figure 2.5 (a) then in order to create a domain wall and still conserve charge, the creation of a domain wall of charge $+2q$ will require the vertex to change to a charge $-q$. As the vertex and the domain wall are of opposite charge they mutually attract each other and the Zeeman force, exerted by the applied magnetic field ($H_{applied}$), will have to exceed this attractive force (see figure 2.5(b)). The Coulombic attraction of the $-q$ vertex and the $+2q$ domain wall reaches its maximum when the two charges are separated by a length equal to their diameter a (roughly equal to the wire width) and is equal to [42]

$$F_{max} = \frac{\mu_0 |Q_V Q_{DW}|}{4\pi a^2} \tag{2.6}$$

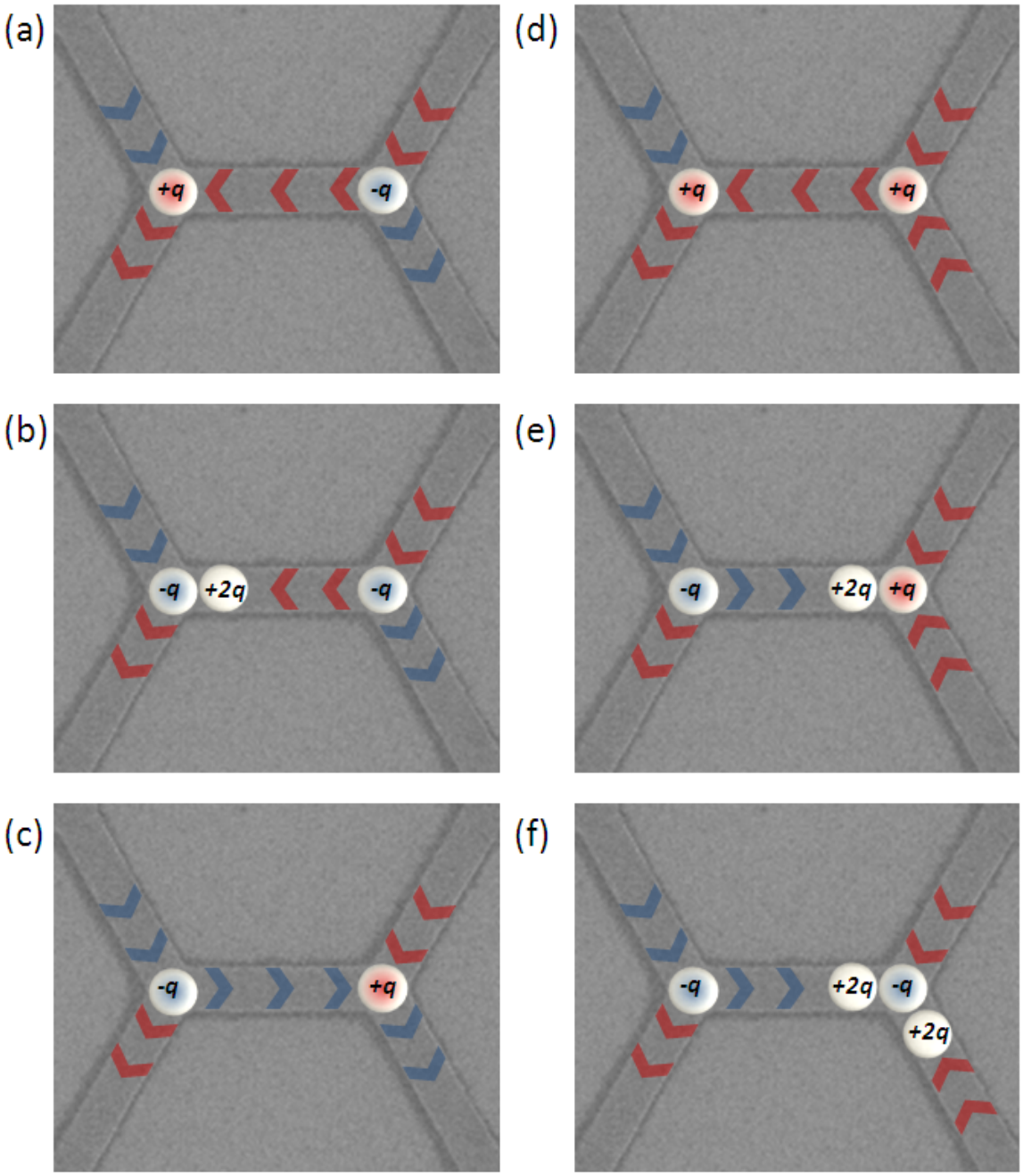

Figure 2.5 Schematic of artificial honeycomb spin ice switching in the Coulombic magnetic charge model. (a)-(c) Magnetic reversal vie nucleation of a $\pm 2q$ charged domain wall. (d)-(f)A typical 180° reversal.The reversal would result in an ice rule violation, however it is energetically favourable for a second domain wall to be nucleated in order to avoid a $\pm 3q$ vertex. The arrows indicate the magnetisation direction of the bars. Adapted from [43]

The Zeeman force perceived by the domain wall is equal to [42]

$$F_{Zeeman} = \mu_0 |Q_{DW}| H_{applied} \tag{2.7}$$

hence the critical external field needed to nucleate a domain wall from a vertex can be calculated by setting equation 2.6 and equation 2.7 equal, and is [42]

$$H_{critical} = H_{applied} = \frac{|Q_V|}{4\pi a^2} = \frac{Mtw}{4\pi a^2} \tag{2.8}$$

where t refers to the thickness of the bars. Assuming $a \approx w$ leads to [42]

$$H_{critical} = \frac{Mt}{4\pi w}. \tag{2.9}$$

Therefore if a strong enough external field is applied, a domain wall is nucleated and dragged away from the vertex of origin. This domain wall will travel down the bar and encounter the next vertex. Applying the same Coulombic argument leads to the conclusion that if the $+2q$ charge encounters a $-q$ charge then the Coulombic attraction will lead to the absorption of the domain wall into the vertex causing its charge to change from $-q$ to $+q$. However if the vertex approached possesses a charge of $+q$ then they repel each other and this magnetostatic repulsion forces the domain wall to stop a distance a away from the vertex. Mellado *et al.* argue that whilst this could be a new equilibrium position, simple field strength arguments favour the occurrence of another event [43]. The domain wall creates a magnetic field of strength $2H_{critical}$ which superimposes onto the external field creating a net field strength of $3H_{critical}$ in the vicinity of the vertex, hence the diagonal bars experiencing a field of strength $3H_{critical}\cos 60^\circ = 1.5H_{critical}$, enough force to nucleate another $+2q$ domain wall switching one of the diagonal bars leading to a vertex which is now charged $-q$ (see figure 2.5(d)-(f)). Therefore the $\pm 3q$ vertices are rare.

2.3 Micromagnetism

Magnetism is, at its heart, a result of the orbital and spin motion and interaction of electrons. Hence materials which exhibit ferromagnetic magnetic properties are mainly restricted to compounds of transition metals and lanthanides as they have a tendency to possess unpaired d or f electrons.

Materials possessing a net magnetic moment due to unpaired electrons in the partially filled orbitals can be classed mainly into two categories: paramagnetic or magnetically ordered (ferromagnetic or antiferromagnetic). In a paramagnet the net magnetic moment on the atoms is orientated randomly hence without an external magnetic field there is no net moment throughout the material as the atomic moments cancel (see figure 2.6(a)). However if an external field is applied the moments align with this field resulting in a non zero net magnetic moment. A ferromagnet is a material which possesses a non-zero magnetic moment even without the application of an external magnetic field, the so called saturation magnetisation or spontaneous magnetisation, M_S (see figure 2.6(b)). This spontaneous magnetisation is temperature dependent and goes to zero at the Curie temperature, T_C above which the ferromagnet behaves like a paramagnet (see figure 2.6(c)). As the temperature increase the thermal fluctuations destroy the alignment of the magnetic moments.

2.3.1 Micromagnetic Energy Terms

In the micromagnetic theoretical framework, the individual atomic magnetic moments are replaced by a position dependent continuous entity of magnetisation. The micromagnetic framework incorporates quantum mechanical effects like the exchange interactions and the magneto-crystalline anisotropy as well as classical phenomena such as the magnetostatic energy. The ferromagnetic configuration is found assuming that the spontaneous magnetisation is constant and that the system relaxes into a energetic minimum. The total energy of the system is given by the sum of all the relevant energy terms [44]:

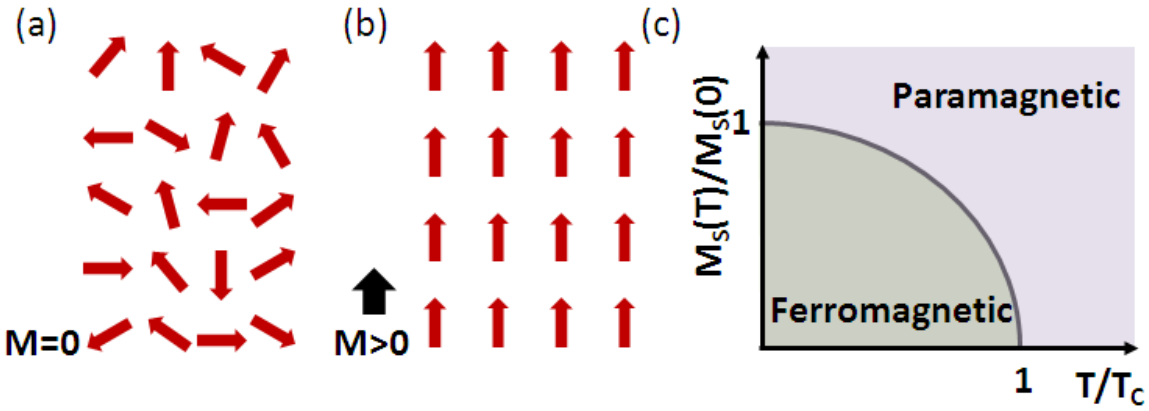

Figure 2.6 Illustration showing the key facts of a ferromagnet: (a) Paramagnetic material, the net magnetisation is zero without the application of an external magnetic field. (b) Ferromagnetic materials possess a net magnetisation even at zero field, the spontaneous magnetisation M_S (c) Temperature dependence of the spontaneous magnetisation; Above the Curie temperature the material behaves like a paramagnet. Adapted from [44]

$$E_{total} = E_{ex} + E_m + E_A + E_Z \tag{2.10}$$

where E_{ex}, E_m, E_A and E_Z refer to the exchange energy, the dipolar or magnetostatic energy, the magneto-crystalline anisotropy and the Zeeman energy respectively.

Exchange Energy

The exchange energy arises from the interaction of the electron spin. In the case of two adjacent atoms the exchange energy is given by [44]

$$e_{ex} = -2J_{i,j}\mathbf{s}_i \cdot \mathbf{s}_j \tag{2.11}$$

where $J_{i,j}$ is the exchange integral and $\mathbf{s}_i$ and $\mathbf{s}_j$ are the spins of the i^{th} and j^{th} atom respectively. From this it appears naturally that the minimum energy state is when both spins are parallel or anti-parallel. In a ferromagnetic material the exchange integral is positive and hence the minimum energy configuration dictates parallel spins. Any deviation from a parallel spin set up is associated with an energy penalty, however, as the interaction is isotropic the direction of displacement is irrelevant. If exchange were the only term in

equation 2.10 then all the moments in the material would point along the same direction. In general the exchange energy is given by [45], [44]

$$E_{ex} = -\frac{A}{M_S^2}\int_V [\nabla \mathbf{M}]^2 \, \mathrm{d}V, \tag{2.12}$$

where A is the exchange stiffness.

Magnetostatic Energy

The magnetic induction **B** inside a magnetic material given as

$$\mathbf{B} = \mu_0(\mathbf{H} + \mathbf{M}) \tag{2.13}$$

where μ_0 is the permeability of free space, **H** is the magnetic field strength and **M** is the magnetisation. The divergence of **M** can be written as [44]

$$\nabla \cdot \mathbf{M} = \frac{\nabla \cdot \mathbf{B}}{\mu_0} - \nabla \cdot \mathbf{H} \tag{2.14}$$

however, from Maxwell's equations $\nabla \mathbf{B} = 0$ and hence [44]

$$\nabla \cdot \mathbf{H} = -\nabla \cdot \mathbf{M}. \tag{2.15}$$

Maxwell's equations dictate the continuity of the flux lines of **B** across the sample surface, however, zero divergence of **M** is not enforced. This results in a demagnetisation field **H** ($\nabla \cdot \mathbf{H}_d = -\nabla \cdot \mathbf{M}$). A discontinuity of the magnetisation at the surface of the material gives rise to the stray field. As flux lines of this stray field, emerging from the magnetic material, form closed loops they will have, at some point, passed through the magnetised material itself. The magnetostatic contribution inside the material is referred to as the demagnetisation field, $\mathbf{H}_d$.The magnetostatic energy associated with the stray field is given by [44]

$$E_m = -\frac{\mu_0}{2}\int_V \mathbf{M} \cdot \mathbf{H}_\mathrm{d} \, \mathrm{d}V \tag{2.16}$$

When the stray fields are absent the magnetostatic energy is minimised.

Magneto-crystalline Anisotropy Energy

So far neither the exchange energy nor the magnetostatic energy put restrictions on the direction of the magnetisation of a single crystal. Hence in a demagnetised state the moments could point along all directions. Therefore the field strength needed to saturate the magnetic moments along a particular direction should be isotropic. However experimental magnetisation curves showed that there are directions which require a stronger field to achieve saturation (hard axis) [44]. The opposite can be the case for other directions (easy axis). Magnetisation deviations away from the easy axis result in an increase of the anisotropy energy. The hard axis points along the direction of maximum anisotropy energy. Polycrystalline permalloy ($Ni_{80}Fe_{20}$) has no overall magnetocrystalline anisotropy [44] making it the ideal material for artificial spin ice arrays.

Zeeman Energy

The Zeeman energy is the energy needed to align the magnetisation with the external field direction. In an external field $\mathbf{H}_{applied}$ the magnetic moments tend to align parallel to the field however the energy need to do so depend on the respective orientation of the field and the magnetisation [44]

$$E_Z = -\mu_0 \int_V \mathbf{H}_{\text{applied}} \cdot \mathbf{M} \, \mathrm{d}V \tag{2.17}$$

2.3.2 Ferromagnetic Domains

The domain theory in ferromagnetic materials postulates that in a ferromagnetic material there exist large regions of uniform magnetisation, magnetic domains. The individual regions of uniform magnetisation are separated by regions, the domain wall, in which the magnetisation rotates from one easy direction to the other [44]. The possibility of parts of

a magnetic material being magnetised in opposite directions was first proposed by Weiss in 1907 [46]. This concept of magnetic domains was first confirmed by Barkhausen in 1919 by observing discontinuous variations in the magnetisation of a ferromagnet during the magnetic reversal in an applied field [46]. The creation, existence and the orientation of the domains in ferromagnetic material is governed by energy considerations mainly between the cost associated with the existence of stray fields radiating out from the sample and the exchange energy penalty acquired by the creation of a domain wall (see figure 2.7(a)). An applied magnetic field changes the net magnetisation by either rotating the magnetisation within a domain or by moving existing domain walls.

2.3.3 Domain Walls

Domain walls are regions of finite thickness over which the magnetisation rotates gradually from one domain to the next. The exact nature of the domain wall is controlled by the dimensions of the ferromagnet determining the competing interactions. For bulk materials the magnetisation distribution is controlled by the exchange and the magneto-crystalline anisotropy energy resulting in the magnetisation rotation out of plane, a 180° Bloch domain wall (see figure 2.7(d)) [44]. The magnetic moments between domains in ferromagnetic thin films, rotate within the plane of the domain magnetisation due to the competing interaction of the exchange, magnetostatic and magneto-crystalline anisotropy energy forming a Néel domain wall (see figure 2.7(e)) [44]. Néel domain walls are only stable in films thinner than the wall width. In a permalloy film the Bloch-Néel crossover is at 60 nm [44].

Magnetic domains in permalloy are of the order of 10 μm [47] separated by domain walls of width 2 μm [44]. Reducing the later dimensions of a ferromagnet reduces the number of domains supported throughout the material, until no domain walls are energetically sustainable, typically below lateral dimensions of $\sim$1μm [47].

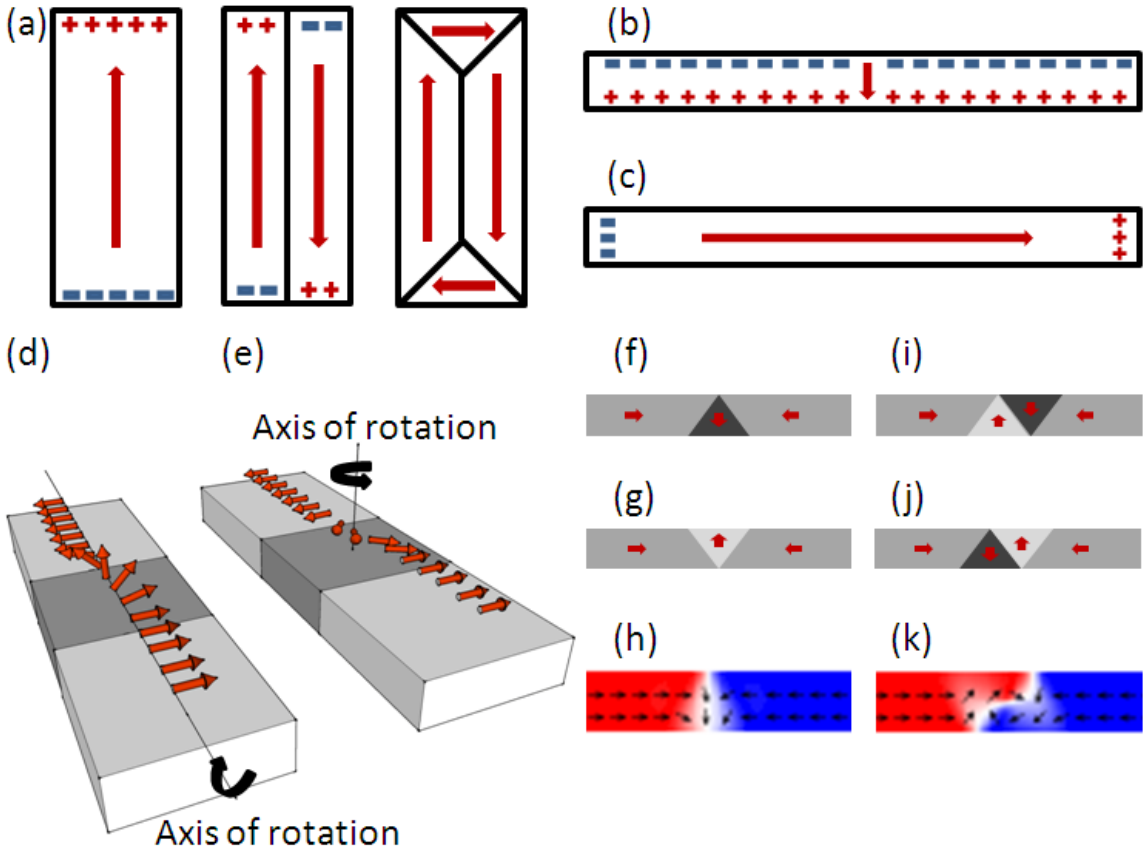

Figure 2.7 Ferromagnetic domains and domain walls. (a) Evolution from single domain state to multidomain flux closure state. (b) Long thin single domain state with large surface charge build up (c) shape anisotropy results in magnetisation along the long axis of wire to minimise the magnetostatic energy, avoiding state (b). Illustration showing (d) a Bloch domain wall and (e) a Néel domain wall (dark gray shaded region). The magnetisation rotates out of the plane for the former and in the plane in case of the latter. Illustrations adapted from [44]. Micromagnetic configuration of transverse and vortex domain walls in ferromagnetic wires. (f) Transverse domain wall with down chirality, (g) up chiral transverse domain wall, (h) OOMMF simulations of a down transverse domain wall. (i) Schematics of clockwise chiral vortex domain wall, (j) anticlockwise vortex domain wall and (k) Object Orientated MicroMagnetic Framework (OOMMF) simulation of magnetisation of a clockwise domain wall.

2.3.4 Ferromagnetic Nanowires

The exact magnetic configuration is in general dependent on the shape and size of the structure. If the dimensions are reduced sufficiently then single domain behaviour can be observed as the exchange energy becomes dominant [44]. The energy penalty due to the stray fields at the extremes of the wire is smaller than the domain wall creation cost. However magnetostatic considerations result in the magnetisation of such a single domain ferromagnetic nanowires to lie along the long axis minimizing the magnetic charge built up at the edges (see figure 2.7(b)-(c)) [44]. Shape and magnetic moment configuration of domain walls in these long thin nanowires is greatly influenced by the geometrical constraints of the wire [44]. The shape anisotropy forces the magnetisation of any domains formed in the wire to lie along the long axis of the wire resulting in a head-to-head (see figure 2.7(f)-(k)) or tail-to-tail arrangement where the magnetisation of the domains point towards the domain wall or points away from the domain wall respectively. Typically there are two main types of domain walls separating such domains: transverse domain walls (a type of Néel domain wall) (see figure2.7(f)-(h)) and a vortex domain wall (see figure 2.7(i)-(k)). The width and thickness of the wire determines which wall type manifests; The dimensionless ratio $= wt/l_{ex}^2$ gives an indication which type of wall is favoured. A ratio of r less than ~ 100 indicates that transverse domain walls are favoured by the wire geometry [44]. According to this guideline permalloy wires of thickness 18 nm will favour transverse domain walls up to a width of around 200 nm (assuming $l_{ex} = 6$ nm [48]). McMichael *et al.* proposed a phase diagram mapping the transition from transverse domain walls to vortex domain walls [49]. Using their published phase boundary critical condition of $tw = C\delta^2$, where $C = 128$, a permalloy wire of thickness 18 nm will support transverse domain walls below a wire width of $\sim$260 nm. The magnetisation in a transverse domain wall lies transverse to the long axis of the nanowire. The sense of rotation, left handed or right handed, determines the chirality of the domain wall: down (see figure 2.7(f)) or up (see figure 2.7(g)). In a vortex domain wall the magnetisation curls around an

out of plane center either in a clockwise sense (see figure 2.7(i)) or anti-clockwise sense (see figure 2.7(j)). The energy predominately associated with a transverse and vortex domain wall stems from magnetostatics however the vortex domain wall has a more significant exchange energy contribution [49]; In a transverse domain wall 93 % of the wall energy is attributed to magnetostatic and 7 % to exchange energy for a vortex domain wall the ratio is 78 % to 22 % [49].

2.3.5 Magnetisation Reversal

The typical magnetic reversal of a ferromagnetic thin film exhibits domain wall nucleation, domain wall motion and coherent rotation [44]. The characteristic change of magnetisation with applied field is referred to as a hysteresis loop and can be seen in figure 2.8(a). The magnetic moment of any ferromagnetic sample in its virgin state is zero. The net sum of the magnetisation of the individual magnetic domains adds up to zero. However an external magnetic field will result in the movement of the domain walls causing the elimination of all domains apart from one, the domain whose magnetisation is most favourably orientated (Segment 1 to 2) [44]. This process is irreversible due to the randomness of the domain wall motion through the material caused by pinning. Segment 2 to 3 represents the coherent rotation of said domain towards the applied field until complete saturation is achieved [44]. This coherent rotation is a reversible process.

In order to reverse the magnetisation after magnetic saturation domain walls will have to be nucleated and begin to propagate. This typically happens in segment 4 to 5. Eventually there will be a multidomain state with no net magnetisation. The field at which this occurs is called the coercive field H_C.

In single domain permalloy nanowire with suitably large aspect ratios (l/w) the magnetic reversal is mediated by the creation of a single domain wall which is nucleated at the edge of the wire at a random pinning site and then propagates through the wire.

2.3.6 Domain Wall Dynamics

Domain walls are entities which propagate under the influence of magnetic fields or electrical currents. If they are treated as quasi-particles then their motion can be described in terms of velocity and mobility [50]. Three domain wall motion regimes have been identified. According to the one dimensional model, developed in 1974, in which the domain wall is described such that the magnetisation varies only in the direction perpendicular to the domain wall [51], the velocity in the weak field limit is linearly proportional to the field H (as illustrated by region (1) in figure 2.8(b(1))) [50],

$$v(H) = \frac{\gamma\Delta}{\alpha}H \tag{2.18}$$

where γ is the gyromagnetic factor, α is the Gilbert damping constant and Δ is the domain wall width. When the magnetic field exceeds a threshold, the Walker breakdown field, H_W, the average velocity drops sharply, the second regime (see figure 2.8(b(2))). Increasing the field further results in the restoration of linear field dependence of the domain wall velocity (see figure 2.8(b(3))), however, the mobility is strongly reduced. The velocity at high fields is given by [50]

$$v(H) = \frac{\gamma\Delta}{(\alpha+\alpha^{-1})}H. \tag{2.19}$$

Domain wall mobilities up to $\sim$31 $\mathrm{ms^{-1}Oe^{-1}}$ for a 5 nm thick 200 nm wide permalloy nanowire have been experimentally observed [52]. The one dimensional model ignores domain wall pinning. Above the walker breakdown field the domain wall velocity evolves from a simple translational propagation to more complex precessional modes. Resistive measurements by Hayashi *et al.* showed that the drop in domain wall mobility is associated with a periodic change of the domain wall shape; The originally transverse domain wall oscillates between up and down chirality via intermediate vortex or anti-vortex domain walls [53]. Figure 2.8(c) shows simulations of the domain wall position (top) correlated to the change in magnetoresistance due to the wall type (bottom). The associated magnetisation configurations are depicted in the right hand panel [53].

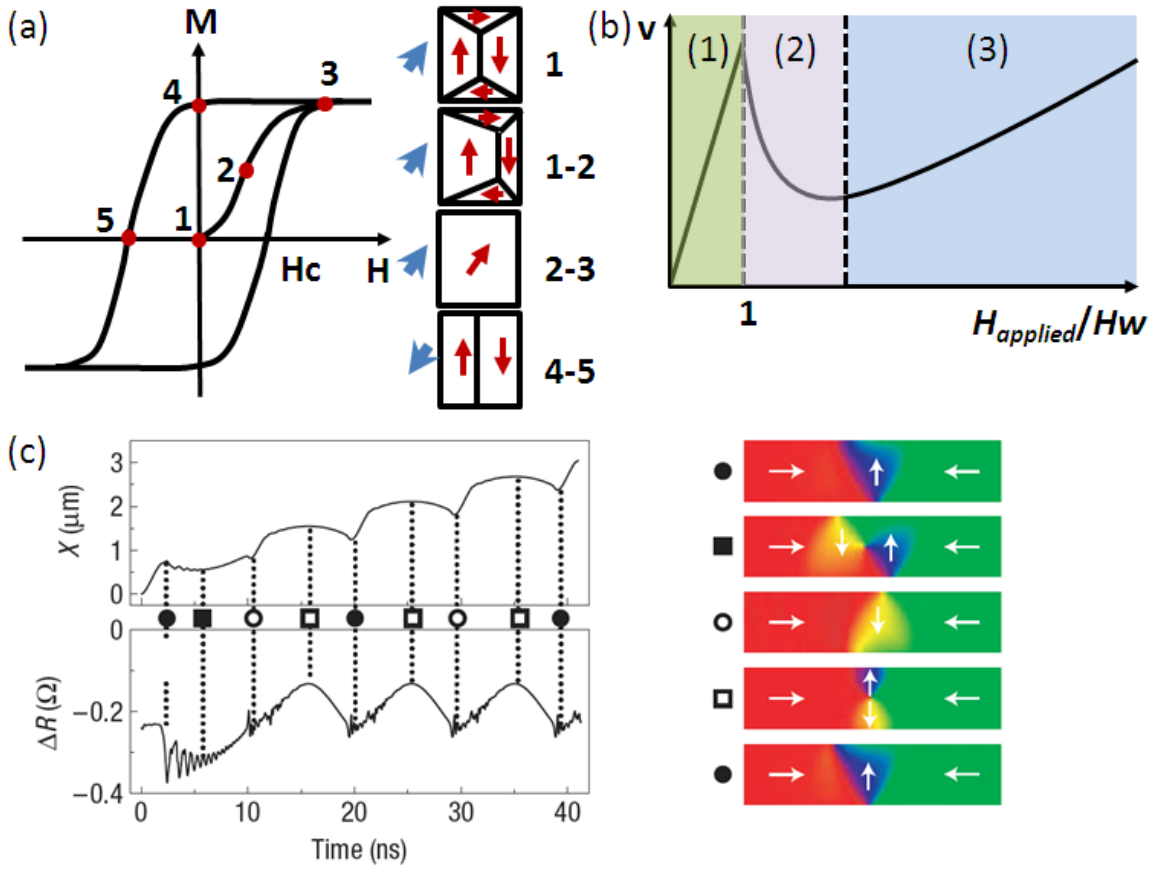

Figure 2.8 Magnetic reversal and domain wall movement. (a) Schematics of a hysteresis loop, showing the typical evolution of magnetisation versus applied field: (1)-(2) transition between the virgin state, net $M = 0$, and a state where only one domain prevails, (2)-(3) coherent rotation of that domain until the materials magnetisation is aligned with the external magnetic field,; the sample is saturated, (5)-(6) new domain walls are nucleated and start to propagate through the material reversing the magnetisation. Adapted from [44]. (b) Schematics of the three domain wall velocity regimes in a ferromagnetic wire: (1) Weak field regime $H < H_W$, the domain wall propagates with uniform velocity, $v \propto H$, (2) $H > H_W$, the domain wall velocity drops sharply and (3) $H \gg H_W$, velocity increases linearly with field, however the domain wall type is not conserved. (c) Simulations performed by Hayashi *et al.* (shown on the right) correlating the drop in average velocity with an oscillation of the domain wall chirality via intermediate states (figure taken from [53].

2.4 Magnetotransport

Magnetotransport refers to all galvanomagnetic effects, by which we mean the physical effects of a magnetic field on matter carrying an electric current [54]. For the purposes of this thesis the two most important galvanomagnetic effects are the Hall effect, ordinary and anomalous, and the magnetoresistance effect.

2.4.1 The Ordinary Hall Effect

The Hall effect was discovered by E.H. Hall in 1879 [55] and refers to the deflection of quasi-free charge carriers due to the Lorentz force under the influence of a magnetic field. The Lorentz force is given by [54]

$$\mathbf{F} = e\mathbf{E} + e[\mathbf{v} \times \mathbf{B}] \tag{2.20}$$

where e stands for the carrier charge ($e = -q$ for electrons and $e = +q$ for holes where q is the magnitude of the electron charge), $\mathbf{E}$ is the electrical field, $\mathbf{v}$ is the velocity of the charge carriers and $\mathbf{B}$ is the magnetic induction. The first term in equation 2.20 refers to the electrical part of the Lorentz force, also called the electrostatic force, and the second part refers to the magnetic part of the Lorentz force.

Lets consider a long thin conductor, with length l and width w (see figure 2.9) [54]. The coordinate system is chosen such that the x direction is parallel to the long axis of the strip and the xz plane leans on one of the large faces of the strip. Under the application of $\mathbf{E}_e = (E_x, 0, 0)$ the charge carriers drift along the strip. In the case of zero magnetic field the drift velocity is given by [54]

$$\mathbf{v}_d = \mu \mathbf{E}_e \tag{2.21}$$

where μ is the charge carrier mobility. The current density is then given by [54]

$$\mathbf{J} = q\mu n \mathbf{E}_e \tag{2.22}$$

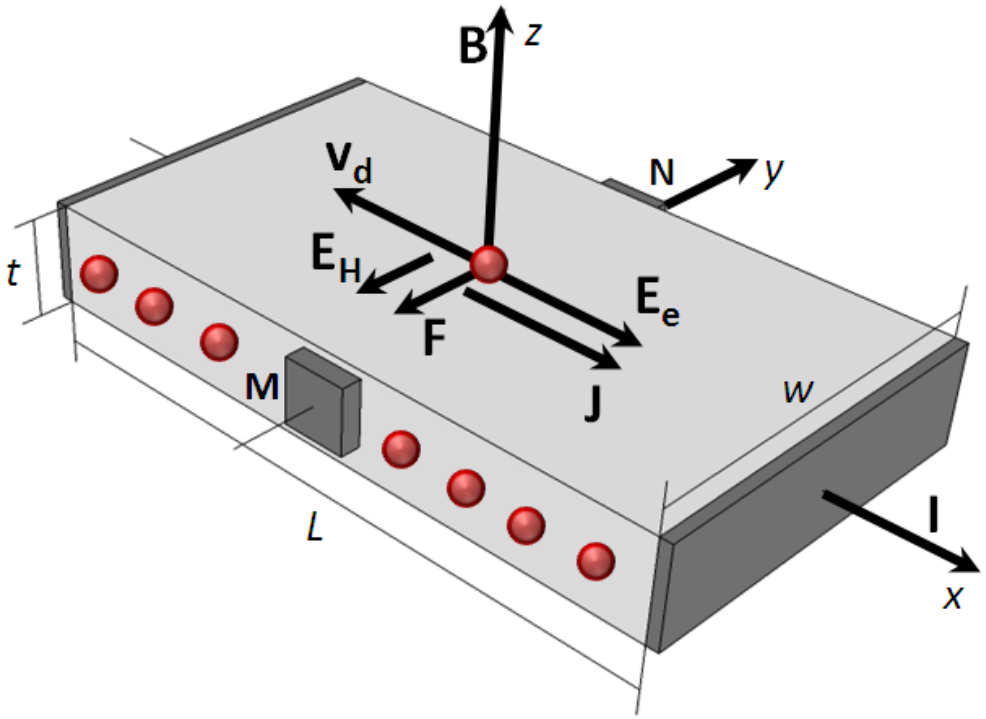

Figure 2.9 The Hall effect in a long strip with electrons as the charge carrier. $\mathbf{E}_e$ is the external electric field, **B** is the magnetic induction, v_d is the drift velocity of the electron, **F** is the magnetic part of the Lorentz force, **J** is the current density and $\mathbf{E}_H$ is the Hall electric field. The magnetic force pushes the electrons to one side.The dark shaded areas are the current and voltage leads.

where n denotes the charge carrier density. If a magnetic field is now applied along the z direction then the magnetic part of the force in equation 2.20 comes into effect and is given by [54]

$$\mathbf{F} = e[\mathbf{v}_d \times \mathbf{B}]. \tag{2.23}$$

Inserting equation 2.21 into equation 2.23 leads to [54]

$$\mathbf{F} = e\mu[\mathbf{E}_e \times \mathbf{B}] \tag{2.24}$$

For the given geometry the force acts along the y axis and is given by [54]

$$\mathbf{F} = (0, -e\mu E_x B_z, 0). \tag{2.25}$$

In other words the magnetic field results in an accumulation of charge carriers towards one side of the carrier. This leads to the appearance of an electric field, $\mathbf{E}_H$ between the strip edges [54]. $\mathbf{E}_H$, acts on the carriers such that it opposes the carrier deflection to the edges, eventually canceling the transverse magnetic force. The carriers again move parallel to the x axis [54]

$$\mathbf{F} = e\mathbf{E}_H \tag{2.26}$$

which leads to [54]

$$\mathbf{E}_H = [\mathbf{v}_d \times \mathbf{B}] \tag{2.27}$$

$\mathbf{E}_H$ is called the Hall electric field. As there is a Hall electric field, there is also a Hall voltage associated with the electrical field, given by [54]

$$V_H = \int_M^N \mathbf{E}_\mathrm{H}\,\mathrm{d}y \tag{2.28}$$

where M and N are two points at the opposite edges which lie on the same equipotential plane when $\mathbf{B} = 0$. Hence in the current problem the Hall voltage is given by [54]

$$V_H = -eE_x B_z w. \tag{2.29}$$

The Lorentz force for both electrons and holes acts in the same direction, however the drift velocity and the Hall electrical field are in opposite directions.

Two fundamental features of the Hall effect are the Hall angle, Θ_H, and the Hall coefficient, R_H. The Hall angle arises as the total electric field in the conductor $\mathbf{E} = \mathbf{E}_e + \mathbf{E}_H$ is not collinear to the external electric field $\mathbf{E}_e$ and is given by [54]

$$\tan\Theta_H = |\mathbf{E}_H|/|\mathbf{E}_e|. \tag{2.30}$$

Inserting equations 2.21 and 2.22 into equation 2.27 shows the relationship between the current density $\mathbf{J}$ and the Hall field $\mathbf{E}_H$ and is given by [54]

$$\mathbf{E}_H = \frac{1}{en}[\mathbf{J} \times \mathbf{B}] \tag{2.31}$$

which can be written as [54]

$$\mathbf{E}_H = R_H[\mathbf{J} \times \mathbf{B}] \tag{2.32}$$

where the Hall coefficient, R_H, is a material parameter which characterizes the intensity and sign of the Hall effect. R_H is defined as [54]

$$R_H = \frac{1}{en}. \tag{2.33}$$

The sign of the Hall coefficient is determined by the type of majority carrier; it is positive if the conductor consists of a p-type semiconductor and negative if the material is

n-type. For the case of a long Hall device with a current in the x direction and the magnetic field in the z direction (see figure 2.9), the Hall voltage is given by [54]

$$V_H = -\frac{R_H}{t} I_x B_z \tag{2.34}$$

where t is the thickness of the strip and $I_x = J_x wt$ is the current.

In this treatment of the Hall effect, the charge carrier velocity was approximated as an average drift velocity assuming all carriers move uniformly as a result of an electric field and that the velocity of the movement is the same for all carriers [54]. Thermal motion is not taken into account and scattering effects are incorporated as smooth friction. The smooth-drift approximation holds for carrier motion in a very weak magnetic field [54].

2.4.2 The Anomalous Hall Effect

In metals exhibiting appreciable magnetisation effects, the Hall voltage shows some unusual features in comparison with the expected behaviour from simple Lorentz force arguments. The unusual resistance response of ferromagnetic materials is called the anomalous Hall effect. The characteristic field dependent response of a ferromagnet involves a steep linear rise of the Hall resistivity with increasing external field followed by a linearly dependent high field region with considerately smaller gradient (see figure 2.10(a)). Phenomenologically this behaviour has been described by an additive contribution of the normal Hall effect due to Lorentz force considerations and a second, strongly temperature dependent, component proportional to the materials magnetisation, M, [56]

$$\rho_{xy} = R_0[H_z + 4\pi M(1-N)] + 4\pi R_S M \tag{2.35}$$

where R_0 is the Lorentz Hall coefficient associated with the ordinary Hall effect, R_S is the anomalous Hall coefficient, N is the demagnetisation factor and M is the magnetisation. H_z is the external field applied along the z-axis. When considering a thin film with the field

applied out of the plane, $N = 1$ [44] and equation 2.35 reduces to [56]

$$\rho_{xy} = R_0 H_z + 4\pi R_S M \tag{2.36}$$

The second term is entirely dependent on the domain configuration encountered; For a large amount of randomly orientated domains the macroscopic value of the transverse electric field will be zero. As the external field aligns more and more domains along the z-axis a net transverse electrical field is established.

A complete understanding of the origin of the anomalous Hall effect involves comparatively novel concepts of topology and geometry. There are two mechanisms dominating the anomalous Hall effect, an extrinsic one and an intrinsic contribution [57].

The extrinsic contribution is generally referred to as the skew scattering. Skew scattering describes the scattering of spin-up and spin-down conduction electrons from magnetic impurities due to spin-orbit interactions [44, 56] (see figure 2.10(b)). Spin up and spin down electrons get scattered towards opposite ends of the sample [44, 56]. A Hall voltage builds up due to the fundamental imbalance in the population of the spin up and spin down bands in ferromagnet materials. In the skew scattering regime the anomalous Hall conductivity is found to be proportional to the longitudinal conductivity, $\sigma_{xy} \propto \sigma_{xx}$. However, scattering events not involving magnetic impurities will randomize this asymmetric scattering, hence skew scattering is only dominant in superclean metals $\sigma_{xx} > 10^6$ $(\Omega\text{cm})^{-1}$ [57].

In dirty metals the intrinsic mechanism dominates. The intrinsic mechanism is a consequence of the Berry-phase effect and is dissipationless, hence independent of the scattering rate of the current carriers and $\sigma_{xy} \propto constant$, when $10^4 < \sigma_{xx} < 10^6$ $(\Omega\text{cm})^{-1}$ [57]. At lower longitudinal conductivities,$\sigma_{xx} < 10^4$ $(\Omega\text{cm})^{-1}$, this dissipationless scattering is suppressed $\sigma_{xy} \propto \sigma_{xx}^{1.6}$ [57]. The three conduction regimes are shown in figure 2.10(d).

The Berry phase is a geometrical concept which affects the electron movement through a periodic potential [59]. A unit vector moving along a closed path on a curved surface

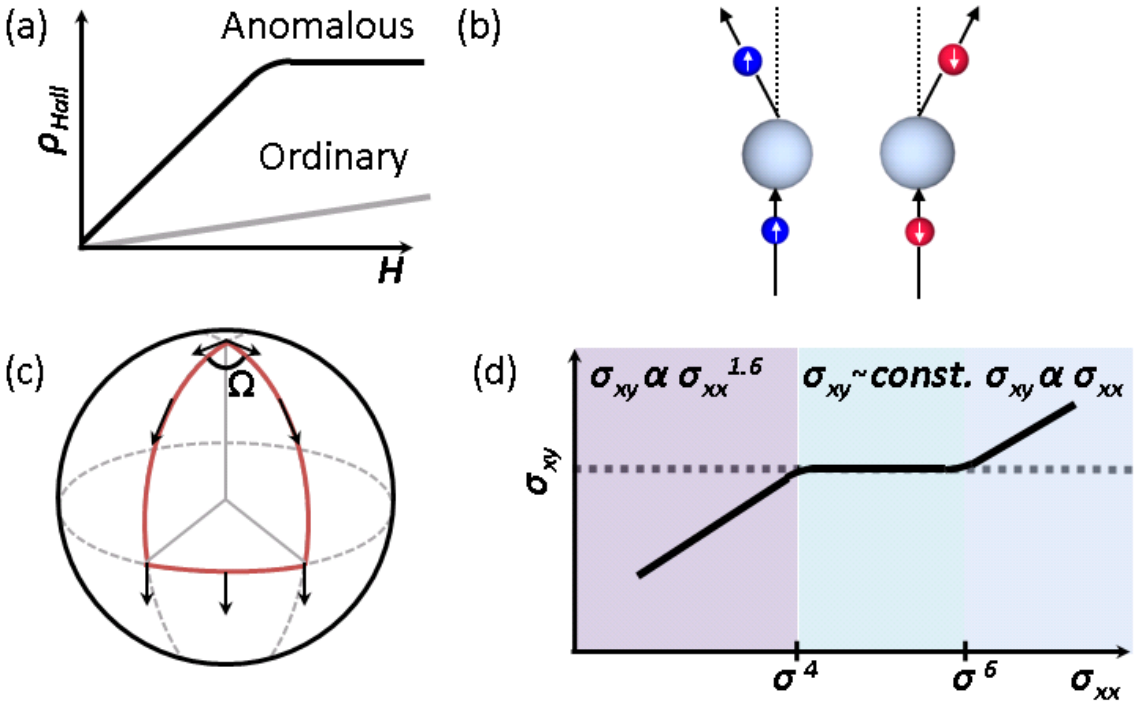

Figure 2.10 Anomalous Hall effect schematics. (a) Typical resistivity change under field application for non magnetic metals (gray curve) and magnetic metals (black curve) (adapted from [44]). (b) skew scattering; Side deflection of conduction electrons (red) from magnetic impurity (blue) (adapted from [44]). (c) Berry phase, Ω, arising by moving a vector along a closed path on a spherical surface (adapted from [58]). (d) Illustration of the three conduction regimes (adapted from [57]).

will have rotated with respect to its initial configuration by the time it has returned to the starting point [58] (see figure 2.10(c)). Using the complex vector notation this angle appears as a phase shift [58]. Applying this problem to a nucleus with one bound electron slowly tracing a path on a closed curve, then when the nucleus returns to its initial position the electron wave function will have acquired a phase shift [58]. This concept can be transferred to a metal by considering electrons in a periodic potential created by a regular arrangement of atoms [58]. Electrons in such a confinement can be described by Bloch waves and their velocity is given by the group velocity

$$\hbar \mathbf{v} = \nabla \varepsilon_n \tag{2.37}$$

where ε_n is the wave-vector dependence of the energy of the band which the electron originated in. However, with the application of a constant electrical potential, an additional term appears in the group velocity. Incorporating the notion that electrons moving on a closed path acquire a phase shift, equation 2.37 becomes [58]

$$\hbar \mathbf{v} = \nabla \varepsilon_n - e\mathbf{E} \times \Omega \tag{2.38}$$

where Ω, the Berry curvature, acts like a 'magnetic field' in reciprocal space. The additional term yields a sizable current, $\mathbf{J}_{xy}$ perpendicular to the applied electric field $\mathbf{E}$ [58]

$$\mathbf{J}_{xy} = \frac{e^2}{\hbar}\mathbf{E} \times \sum_k \Omega(\mathbf{k}) f^0_{\mathbf{k}} \tag{2.39}$$

where $f^0_{\mathbf{k}}$ is the equilibrium distribution function. In a ferromagnet, the sum in 2.39 is none zero provided there is a net magnetisation.

In band ferromagnets the intrinsic term is the major contribution to the anomalous Hall effect [60]. In the case of permalloy: R_S was measured to be positive for alloy compositions Ni_5Fe_{95}, $Ni_{10}Fe_{90}$, $Ni_{15}Fe_{85}$ and $Ni_{20}Fe_{80}$. The authors commented that R_S changes sign for compositions of Ni % above 80 % [61].

2.4.3 Magnetoresistance

Magnetoresistance refers to the change of conduction in a metal under the influence of an external magnetic field. In a non magnetic metal the magnetoresistance is given by [45]

$$\frac{\Delta\rho}{\rho} = \frac{\rho(B) - \rho(0)}{\rho(0)}. \tag{2.40}$$

Under the influence of a magnetic field, charge carriers undergo cyclotron motion caused by the Lorentz force. As the resistance of a metal is inversely proportional to the mean free path, λ, any change in the charge carrier path will lead to a change in ρ. Figure 2.11(a) illustrates the change in the charge carrier path, leading to an effective reduction in the mean free path, and hence an increase in the resistance. This effect is independent of the field polarity; the change in resistance must be a function of B^n where n is an even number. Evaluating the change of the mean free path and using its relation to the resistivity, $\rho = mv/(ne^2\lambda)$, one finds that the magnetoresistance is proportional to [45]

$$\frac{\Delta\rho}{\rho} \propto \left(\frac{B}{\rho}\right)^2, \tag{2.41}$$

This is known as Kohler's rule. The effect on the resistance under the application of a magnetic field is proportional to B^2 at low fields.

In the case of non magnetic metals $\mathbf{B} = \mu_0\mathbf{H}$ where $\mathbf{H}$ is the externally applied magnetic field. However in ferromagnetic materials $\mathbf{B} = \mu_0(\mathbf{H} + \mathbf{M})$ and hence the matter is slightly more complicated. Now the resistance change is not only dependent on the external field but also on the microscopic magnetic configuration of the material in response to the external magnetic field. The coupling between the current density $\mathbf{j}$ and internal field $\mathbf{M}$ is non trivial and is quantum mechanical in origin. A simple classical picture is not enough anymore. This magnetisation orientation dependent contribution to the magnetoresistance is referred to the anisotropic magnetoresistance. Kohler's rule then becomes [45]

$$\frac{\Delta\rho}{\rho(0)} \propto a\left(\frac{H}{\rho(0)}\right)^2 + b\left(\frac{M}{\rho(0)}\right)^2 \tag{2.42}$$

where the first term refers to the ordinary magnetoresistance as seen for non magnetic materials and the second term is the anisotropic magnetoresistance. a and b are constants. The additional term is dependent on the angle between the current and the magnetisation.

The origin of the anisotropic magnetoresistance is found in the spin dependent scattering of the current carriers. In general, conduction electrons of $3d$ ferromagnetic metals (e.g. permalloy) are either s-like electrons or d-like electrons. The two types coexist at the Fermi level. s electrons resemble free electrons whereas d electrons have higher effective mass and hence a lower mobility. Most of the current will be carried by s electrons. The d-band, however, is spin-split and there is an inequality of the density of states between the spin $\uparrow$ and spin $\downarrow$ subband at the Fermi level [44]. Ignoring the possibility of spin flip scattering events, $\uparrow$ s-electrons scatter into $\uparrow$ d-electrons and $\downarrow$ s-electrons scatter into $\downarrow$ d-electrons. Hence, the density of states imbalance at the Fermi level of the d-band will result in an inequality of the effective scattering cross-section of the $\uparrow$ and $\downarrow$ electrons. The magnetisation dependence of the resistance comes into play for finite spin flip probability allowing s-electrons to scatter into unoccupied d-electron states. The spin flip scattering probability is dependent on the angle between the current and the magnetisation. The likelihood of such spin mixing is higher in the case of **J** being parallel to **M** [45]; effectively increasing the resistivity (see figure 2.11(b)).

Anisotropic magnetoresistance can be measured, without the influence of Hall effects, by applying an in-plane magnetic field. Considering the case of a sample magnetised in the xy-plane, **M**, at an angle, φ, to the current flow j_x, caused by an in-plane magnetic field H_y, then the electrical field along **M** can be separated into a parallel component $E_\parallel$ and into a perpendicular component $E_\perp$ to the magnetisation **M** (see figure 2.11(c)). This results in [44]

$$E_\parallel = \rho_\parallel j_x \cos\varphi \tag{2.43}$$

and

$$E_{\perp} = \rho_{\perp} j_x \sin\varphi \tag{2.44}$$

where $\rho_{\parallel}$ and $\rho_{\perp}$ are the resistivity parallel and perpendicular to **M** respectively. Hence the electrical field component in x, E_x, and the component along y, E_y, (see figure 2.11(d)) are given by [44]

$$E_x = E_{\parallel} \cos\varphi + E_{\perp} \sin\varphi \tag{2.45}$$

and

$$E_y = E_{\parallel} \sin\varphi - E_{\perp} \cos\varphi. \tag{2.46}$$

Inserting equations 2.43 and 2.44 into equations 2.45 and 2.46 leads to [44]

$$E_x = \rho_{\parallel} j_x \cos^2\varphi + \rho_{\perp} j_x \sin^2\varphi \tag{2.47}$$

and

$$E_y = \rho_{\parallel} j_x \cos\varphi \sin\varphi - \rho_{\perp} j_x \sin\varphi \cos\varphi \tag{2.48}$$

which can be simplified to [44]

$$E_x = j_x \left(\rho_{\perp} + \left(\rho_{\parallel} - \rho_{\perp}\right) \cos^2\varphi\right) \tag{2.49}$$

and

$$E_y = j_x(\rho_{\parallel} - \rho_{\perp}) \cos\varphi \sin\varphi = j_x \frac{1}{2}(\rho_{\parallel} - \rho_{\perp}) \sin 2\varphi. \tag{2.50}$$

The anisotropic magnetoresistance is then given by

$$\rho_x = E_x / j_x = \rho_{\perp} + \left(\rho_{\parallel} - \rho_{\perp}\right) \cos^2\varphi. \tag{2.51}$$

The $\cos\theta$ dependence of the anisotropic magnetoresistance results in a minimum resistance when the current and the magnetisation are perpendicular to each other and in a maximum when the current and the magnetisation are parallel to each other.

The y-component is generally referred to as the planar Hall resistance and is given by

$$\rho_y = E_y/j_y = \frac{1}{2}(\rho_\parallel - \rho_\perp)\sin 2\varphi, \tag{2.52}$$

with an associated planar Hall voltage is given by [44]

$$V_{pH} = \int_0^w \mathbf{E}_\mathrm{y}\,\mathrm{d}y = w j_x \frac{1}{2}(\rho_\parallel - \rho_\perp)\sin 2\varphi \tag{2.53}$$

where w is the width of the film. The planar Hall voltage is zero if the angle between the magnetisation and the current is 0 or an even integer multiples of $\pi/4$.

For $Ni_{0.8}Fe_{0.2}$, $\Delta\rho/\rho \sim 4$ % [45]. This is close to the peak value of the anisotropic magnetoresistance which occurs at 90 % Ni, however permalloy has the advantage that the magnetostriction and crystalline anisotropy are very close to zero [45]. According to Bogart *et al.* a thin film of permalloy of thickness 20 nm has a resistivity of between $\rho \sim 0.2 - 0.4$ $\mu\Omega$m [62]. Overall resistivity decreases as the film thickness increases, however, this trend tends to be weak until the film thickness is comparable to the mean free path, around 6 nm [62]. This is due to the increase influence of diffuse scattering at the film surface [62]. The bulk resistivity value of permalloy is $\rho \sim 0.16$ $\mu\Omega$m [44].

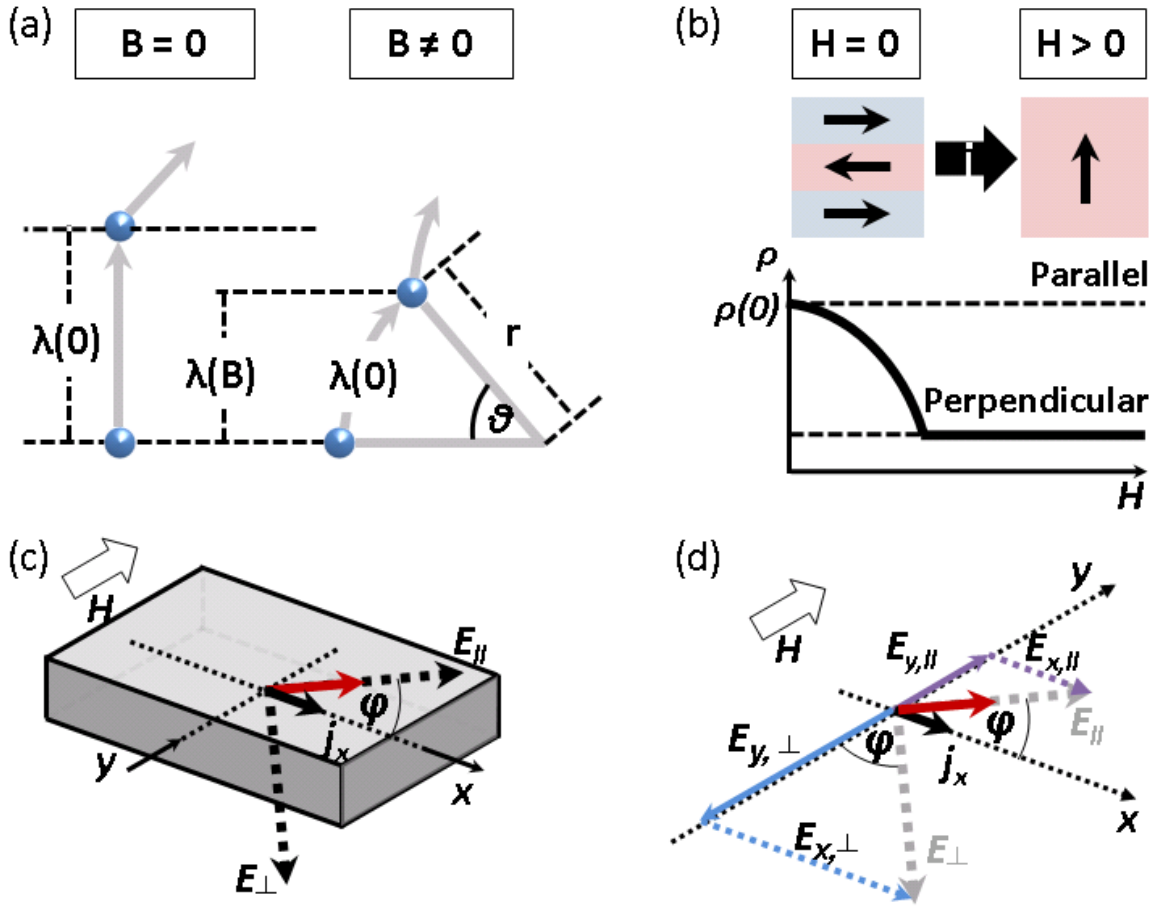

Figure 2.11 Magnetoresistance mechanisms. (a) Mean free path change under the influence of a magnetic field in a non magnetic metal between scattering events (blue circle). (b) Schematic of anisotropic magnetoresistance dependence on the relative magnetisation and current orientation in a ferromagnet. (a)-(b) adapted from [45]. (c) A schematic of the planar Hall transport set up. The red arrow indicates the direction of magnetisation **M**. (d) Breakdown of the electrical field components parallel ($E_{\parallel}$) and perpendicular ($E_{\perp}$) to the magnetisation. (c)-(d) adapted from [44].

2.4.4 Magnetoresistance in Permalloy Wires

A nanowire fabricated from a ferromagnetic material which exhibits anisotropic magnetoresistance will undergo a change in resistance if a domain wall travels down the wire [50]. In a nanowire the magnetisation lies parallel to its long axis unless a domain wall is presence. Within the domain wall the magnetisation deviates from the parallel case and thus there is a non trivial angle between the current and the magnetisation leading to a drop in the anisotropic magnetoresistance [50]. When no domain wall is present and the magnetisation and the current flow are parallel, a constraint enforced by the geometry of the wire, the resistance is given by [50]

$$R_{Sat} = \frac{\rho_{\parallel} L}{wt} \tag{2.54}$$

where L is the length of the wire and t is the thickness. An estimate of the change in resistance between a single domain state, R_{Sat} and a state where two head-to-head domains are separated by a single domain wall, R_{DW} with width Δ can be found if one assumes uniform magnetisation in plane at 90° to the domains.

The difference in resistance then can be expressed as [50]

$$R_{DW} - R_{Sat} = \left(\frac{\rho_{\perp} \Delta}{wt} + \frac{\rho_{\parallel}(L-\Delta)}{wt} \right) - \frac{\rho_{\parallel} L}{wt} = \frac{(\rho_{\perp} - \rho_{\parallel})\Delta}{wt} \tag{2.55}$$

To a first approximation the domain wall width in permalloy scales with the nanowire width $\Delta \propto w$ and the change in resistance is only dependent on the wire thickness [50]. The position of the domain wall in the wire is of no importance for the anisotropic magnetoresistance, only its presence or absence matters. It was found that the magnetoresistance of a 4 μm long, 10 nm thick and 300 nm wide permalloy wire changed by $\sim$0.2 Ω when a domain wall was introduced into the wire [62,63]. R_{Sat} was measured to be $\sim 473.7\ \Omega$ [50].

2.4.5 Temperature Dependence

The temperature dependence of the zero field resistivity of metals is described by Matthiesen's rule. Matthiesen's rule states that the total zero field resistivity can be separated into a temperature independent term, ρ_i, and a temperature dependent term due to scattering from lattice vibrations (phonons), ρ_{ph}, [44]

$$\rho = \rho_i + \rho_{ph}. \tag{2.56}$$

ρ_i results in a finite resistance at 0 K, the residual resistivity, caused by scattering from impurities, dislocations and strain [64]. The resistivity caused by scattering from phonons is split into two regimes: above the Debye temperature, θ_D, where $\rho_{ph} \propto T$ and below θ_D where $\rho_{ph} \propto T^5$. As the temperature drops below θ_D ρ_{ph} is described by

$$\rho_{ph} = \alpha_{ph} \left(\frac{T}{\theta_D}\right)^5 \int_0^{\theta_D/T} \frac{x^5}{(e^x - 1)(1 - e^{-x})} \, dx, \tag{2.57}$$

where α_{ph} is a constant proportional to the square of the electron-lattice interaction constant. However White *et al.* showed that the resistivity of nickel, iron and cobalt, which are ferromagnetic transition metals, varies with a T^3 dependence following the functional form [65]

$$\rho_{ph} = d \left(\frac{T}{\theta_D}\right)^3 \int_0^{\theta_D/T} \frac{x^3}{(e^x - 1)(1 - e^{-x})} \, dx, \tag{2.58}$$

where d is a constant (different to α_{ph}). It was suggested that the change is due to an increased scattering caused by electrons transitioning from the *s*-to the *d*-band [65].

In a ferromagnetic material the scattering from disordered spins results in the addition of another term to equation 2.56. The spin disorder increases as the ferromagnet approaches the Curie temperature (T_C) as the local exchange potential encountered by the current carriers increases. The spin disorder reaches a maximum in the paramagnetic phase of the metal. Below T_C the resistivity due to the spin disorder scattering is given

by [44],

$$\rho_{ferro} = \rho_{para}\left(1 - [M(T)/M(0)]^2\right), \tag{2.59}$$

where $M(0)$ is the maximum saturation magnetisation at 0 K and ρ_{para} is the maximum contribution to the resistivity due to spin disorder reached when the magnetic material crosses over into the paramagnetic phase

$$\rho_{para} \sim \frac{k_F m_e^2 J_{sd}^2}{e^2\hbar^2} S(S+1), \tag{2.60}$$

where J_{sd} is the exchange between localized and conduction electrons, m_e is the electron mass, e is the elementary charge, k_F is the Fermi wave vector and S is the spin quantum number. The resistivity in a transition metal scales, to a first approximation, as [4]

$$\rho = \rho_i + \rho_{ph} + \rho_{ferro}. \tag{2.61}$$

The temperature dependence of ρ_{ferro} is determined by the change of M with temperature. Using the molecular field theory which postulates that there is a 'molecular field' proportional to the magnetisation which aligns the magnetic moment of the individual atoms within the magnetic domains, then the temperature evolution of the magnetisation is given by [4]

$$\frac{M}{M(0)} = B_J(x) \tag{2.62}$$

where B_J is the Brillouin function and x is given by [4]

$$x = \frac{\mu_B g J(\lambda M + B)}{k_B T}, \tag{2.63}$$

where g is the Landé g-factor, $J = L + S$ where L is the orbital quantum number, k_B is the Boltzmann constant and λ is the Weiss coefficient and is given by $\lambda = 3k_B T_C/(g\mu_B J(J+1))$. The 'molecular field' thus adds to the internal contribution of any external field and the resulting field is then given by $\mathbf{B}^i = \lambda\mathbf{M} + \mathbf{B}$ [4].

Chapter 3

Experimental Methods

In this chapter details are provided of the measurement equipment and the data analysis used. In the second half of the chapter the fabrication process using thermal evaporation and electron beam lithography is described.

3.1 Equipment

3.1.1 Scanning Probe Microscopy

Scanning probe microscopy measures physical phenomenons which occur close to the sample surface via their interaction of an atomically sharp tip. Scanning probe microscopy techniques are those where such tip-sample interactions are utilised to recreate an image of the sample topology or an image of the force gradient associated with the physical phenomenon, for example stray fields perpendicular to the sample surface. A Digital Instruments nanoScope IIIa with a positioning stage resolution of 2μm was used for all scanning probe microscopy.

Atomic force microscopy is a scanning probe technique where the tip is influence by the forces associated with the sample surface is called atomic force microscopy (AFM). AFM recreates an image of the sample topology. The tip can either be brought in contact with the sample surface or can be used in tapping mode [66]. In contact mode, also called

contact height mode, the topographic variations are directly translated into a deflection of the cantilever [66]. This technique will result in a fast but slightly noisier topology image compared to non contact atomic force microscopy modes as no feedback loop is used [66]. In tapping mode, a non-contact mode, the cantilever is excited to its resonance frequency and then brought close to the sample surface. The oscillation of the cantilever diminishes with the decreasing tip-surface distance due to long-range forces like the van der Waals- or electrostatic forces. A change in the oscillation amplitude indicates a change in the sample-tip interaction [66]. When the tip is close to the sample an amplitude set point is defined and the tip-sample distance is changed via a feedback loop in order to maintain this set-point amplitude.This change in the tip-sample distance is a representation of the topology. The change in the amplitude is monitored via the deflection of a laser pointed at the cantilever. The resolution is to some extend sample and tip dependent however the lateral resolution of AFM is typically around $\sim$30 nm whereas the vertical resolution can be up to 0.1 nm [66].

3.1.2 Vibrating Sample Magnetometry

An Oxford Instruments vibrating sample magnetometer (VSM) was used to measure the bulk magnetisation as a function of field (see figure 3.1(a)). The measurement instrument was originally designed by S. Foner [67]. The VSM working principle is based on Faraday's law of electromagnetic induction; a change in the magnetic flux will induce a voltage in a wire encircling the flux lines which is proportional to the change. A magnetic sample placed between 'pick-up' coils, vibrating vertically up and down will induce an ac voltage in said coils. The stray field of the vibrating sample was detected using two orthogonal Mallinson 4 pick-up coil arrangements [68, 69] (see figure 3.1(b)). An external magnetic field generated by a split coil magnet was used to magnetise the sample. The sample experiences an uniform magnetic field perpendicular to the vibrational motion. The Mallison 4 pick-up coil arrangement is illustrated in figure 3.1(b); Such an arrangement leads to the cancelation of the magnetic induction induced by the changing applied field. Hence only

the induction due to the magnetised sample is measured. A lock-in amplifier, sensitive only to the vibrational frequency of the sample, is used to amplify the induced alternating emf.

The samples in this work where vibrating at a frequency of 45Hz with an amplitude of 1.4mm. Angular dependent magnetisation measurements with respect to the direction of the applied field at a precision of 0.1° weres possible. Samples could be placed in a uniform magnetic field parallel or perpendicular to the film surface. Before each measurement the VSM was calibrated using a 1.9 mm x 1.9 mm nickel foil (Goodfellow, 99.99%)with an in-plane moment of 0.188 emu in a field of strength 1 T at 294 K. The noise floor of the vibrating sample magnetometer used is 1×10^{-4} emu.

3.1.3 X-ray Microscopy

X-ray microscopy encompasses high resolution microscopy techniques such as photoemssion electron microscopy and scanning transmission microscopy. Magnetic contrast is achieved using the principles of X-ray magnetic circular dichroism (XMCD) allowing element specific imaging of magnetic domains.

XMCD is a magneto-optical phenomenon. It utilizes the concept of the magnetic properties having an influence on the spectroscopic spectra in either transmission or absorption geometries. In a ferromagnet the absorption of circular polarised X-rays depends on the projection of the magnetisation onto the helicity of the photons. Hence a sign change is observed if either the magnetisation or the circular polarization of the X-rays is reversed [70].

A two-step model can be used to explain the physical origin of XMCD [71]. The first step encompasses the excitation of a core electron by circular polarised X-ray photon carrying an angular momentum with a value of $+\hbar$ or $-\hbar$ for a right handed photon or a left handed photon respectively [71]. In terms of the corresponding helicity vector this means that the vector is parallel to the direction of propagation in case of a right circular polarised x-ray photons and anti-parallel in case of a left handed photon [71]. Due to the law of angular momentum conservation during the absorption process the angular

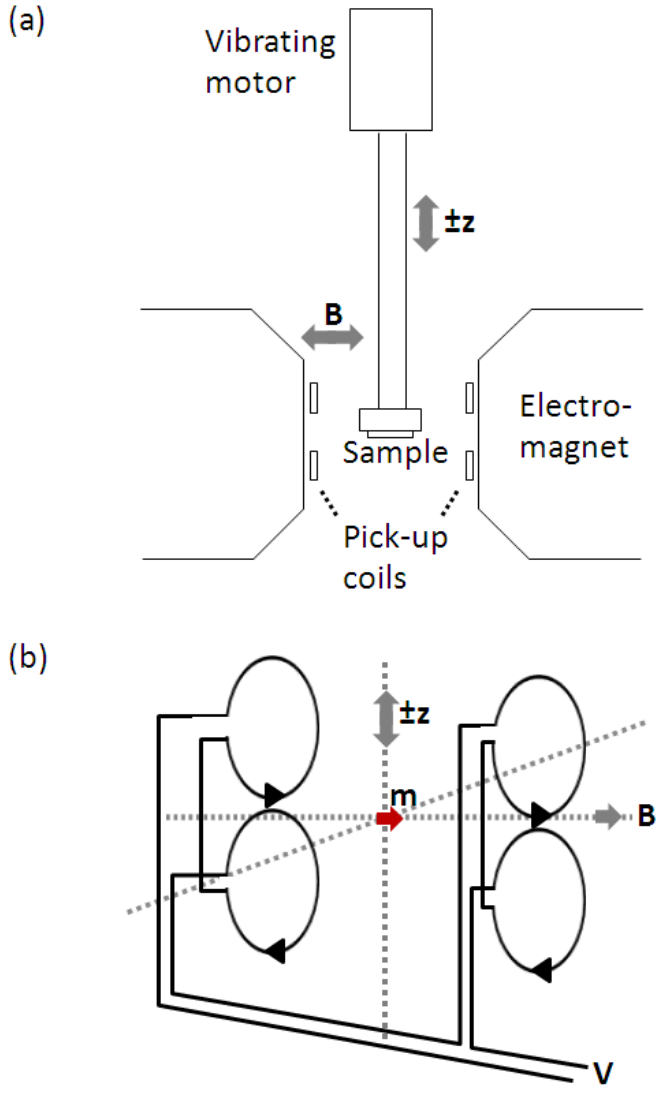

Figure 3.1 Principal of vibrating sample magnetometer. (a) Illustration of vibrating sample magnetometer. (b) Set up of the Mallinson 4 pick-up coil arrangement. Illustration adapted from [69].

momentum of the photon is completely transfered to the photoelectron [71]. However, not only the orbital momentum of the excited photoelectron, but also its spin can be affected by the momentum transfer [71]. If we consider a photoelectron which was excited from the L_2 and L_3 absorption edges, in other words, if we consider a photoelectron excited from spin-orbit-split core levels $2p_{1/2}$ and $2p_{3/2}$ into an unoccupied $3d$ state, then the spin-orbit coupling will lead to a conversion of part of the angular momentum carried by the photon into spin [71]. The importance of this is reflected in the fact that even though the photoelcetron's spin moment is always parallel to the direction of the incident photon propagation its sign depends on the helicity of the incident X-rays and on the spin-orbit coupling [71]. The spin moment of the photoelectron excited at the L_3 edge is of opposite sign to the spin moment of the photoelctron excited at the L_2 edge [71]. In the absence of spin-orbit coupling the angular momentum of the photon is converted completely into orbital momentum and no spin polarization of the photoelectron occurs [71].

The second step of the model is driven by the magnetic properties of the sample and involve sum rules which have been proposed to deduce quantitative magnetic information from XMCD spectra [71]. In general X-ray absorption spectra are mainly governed by the density of empty states which the photoelectron is allowed to be excited into by a photon with angular momentum l given by the symmetry of the initial core state and the selection rules of the transition [71]. In the special case of XMCD the absorption spectra reflect the difference in the allowed density of final states with different spin or orbital moments [71]. If one considers the above case of spin-orbit split initial states then the excited photoelectron carries an orbital momentum and a spin [71]. Any imbalance of the final states in either spin or orbital momentum will lead to a dichroic effect [71]. In a ferromagnet the density of unoccupied states is dependent on whether the electron's spin is parallel or anti-parallel to the magnetisation (see figure 3.2(a)) [70]. In other words, for a certain helicity more electrons of one spin direction, with respect to the direction of incoming light, are excited into the unoccupied 3d states than of the other spin direction [70]. Additionally, from step one we know that the helicity of the incoming photon will

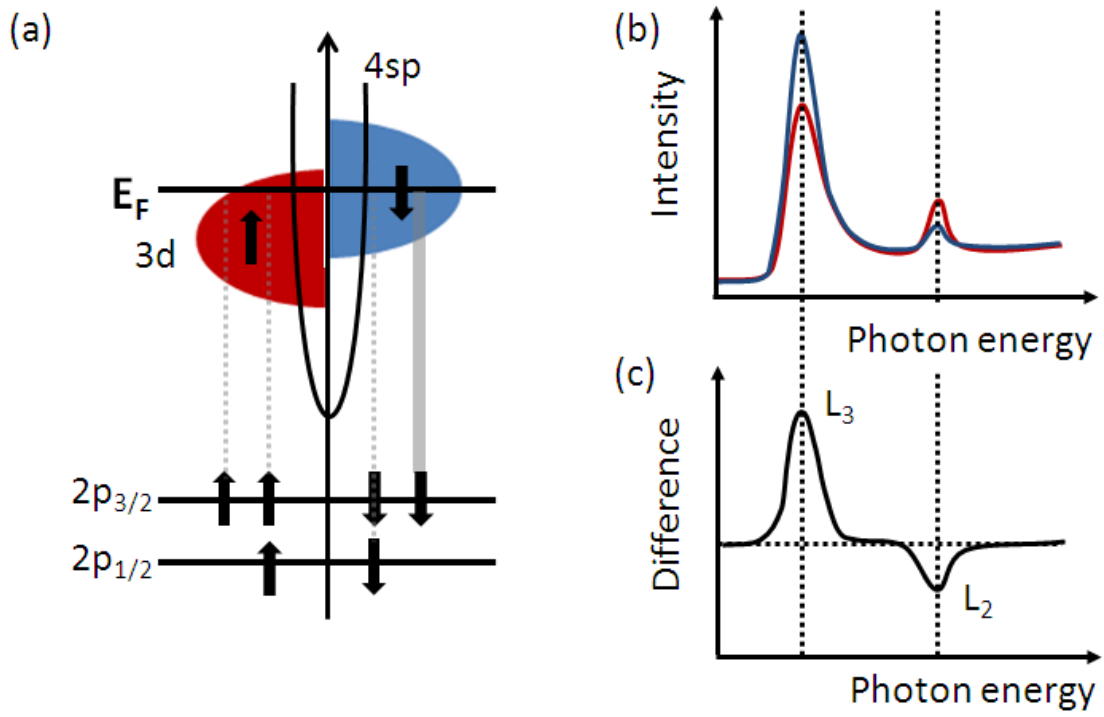

Figure 3.2 Schematics illustrating the principal of XMCD (a) shows the available density of final states. The thickness of the gray arrow indicates the likelihood for a core electron from the L_3 edge to be excited into the 3d spin up or spin down band for right handed circular polarised X-rays (The thicker the more probable). (b) Schematic of the intensity versus X-ray energy for left (red line) and right (blue line) handed polarised X-rays. (c) Schematic of the difference between the two spectra in (b). Illustration adapted from [72].

affect the spin of the excited electron due to spin-orbit interactions. For a certain X-ray helicity there is a preferential excitation into the 3d band of electrons of one spin direction with respect to the direction of the incoming light [70]. Hence the absorption intensity is affected by the magnetisation of the sample and the helicity of the X-rays [70,71].

In conclusion circular polarised X-rays can be used to probe the direction of the magnetic moment in a ferromagnet. The total intensity of the absorption signal is dependent on the angle, α, between the X-ray helicity vector σ which is always parallel to the X-ray

propagation direction (σ^+ and σ^+ for right and left circular polarization), and the magnetisation **M** [70]:

$$I_{XMCD} \propto |\mathbf{M}| \cos\alpha(\sigma, \mathbf{M}) \tag{3.1}$$

The magnetisation of the sample will dictate the amount of absorption of the incoming X-rays from the core level to the unoccupied states with respect to the circular polarization of the photons (see Figure 3.2(b) for schematics showing the helicity dependent spectra of a uniformly magnetised sample). The difference between the absorption levels of left and right circular polarised X-rays allows one to identify if the magnetisation is parallel or anti-parallel to the incident direction of the photons and can be used to image the micromagnetism of artificial spin ice. More precisely the XMCD contrast is obtained from the pixel-by-pixel intensity asymmetry ratio [73]

$$\frac{(I^{\sigma^+} - I^{\sigma^-})}{(I^{\sigma^+} + I^{\sigma^-})} \tag{3.2}$$

Photoemission electron microscopy

Photoemission electron microscopy (PEEM) measures the difference in absorption indirectly via the secondary electrons which are excited by the decay of the core hole [74]. The hole is caused by the excitation of a core electron by the incident photon [74]. The decay of the hole results in a cascade of low energy electrons of which some penetrate the sample surface and escape into vacuum. The incident photon absorption coefficient averaged over the probe thickness is directly proportional to the electron emission of the sample [74]. These escaped electrons are then accelerated towards the PEEM optics via a large potential difference between the sample and said optics [74]. Transition metal ferromagnets like Fe, Co and Ni possess a strong XMCD effect at the L_2 and L_3 edge [70]. For Fe, Co or Ni the energy of the incident X-rays are tuned to the energy of the L_2 or L_3 transition [70]. PEEM is a surface sensitive microscopy technique due to the limited secondary electron escape

depth of about 2-3 nm [73].

The room temperature PEEM measurements were conducted in collaboration with Sarnjeet Dhesi, Francesco Maccherozzi and Jorge Miguel at the I06 experimental hutch of the Diamond synchrotron facility, UK. PEEM operates in ultra high vacuum. The secondary electrons emitted from the sample surface were accelerated towards the imaging optics via an electric field of strength -20 kV. The spacial resolution of this PEEM facility is around 50-100 nm with an imaging spectral resolution of 300 meV. All images are the average of three repeats. Each measurement consisted of 40 images with an acquisition of 1 s, 20 with left circular polarised X-rays and 20 with right circular polarised X-rays. Out of the 20 images at each X-ray polarization, 10 images were acquired using X-rays with energy equivalent to the Fe L_3 edge transition (708 eV) and 10 images at off peak energy (705 eV). A magnetic field was applied via a coil magnet situated on the sample holder allowing an *in situ* field application of around $\pm$25 mT.

Scanning Transmission X-ray Microscopy

As in PEEM the magnetic contrast obtained via scanning transmission X-ray microscopy (STXM) is achieved via XMCD. However instead of measuring the secondary electrons created by the absorption process, STXM measures the intensity loss of the focused X-ray beam after it has traveled through the ferromagnetic sample.

Room temperature STXM was carried out on beamline 11.02 at the Advanced Light Source (Berkeley, CA, USA) in collaboration with T. Tyliszczak. The sample was mounted between pole pieces of an electromagnet allowing the *in situ* application of an in-plane field of $\pm$25 mT. The chamber was pumped down to a pressure of approximately 100 mTorr before filling with He gas in order to avoid heating the piezo stages of the sample holder and detector. Circularly polarised X-rays were provided by an undulator beamline after which they were focused to a spot size of approximately 30 nm using a Fresnel zone plate. The lateral resolution of the STXM is 20-30 nm. The in-plane component of the magnetisation was probed using the XMCD effect by mounting the sample and an electromagnet at ap-

proximately 30° with respect to the X-ray propagation vector. A black and white contrast indicates the magnetic moment being parallel and anti-parallel to the X-ray propagation.

3.1.4 Lorentz Transmission Electron Microscopy

Transmission electron microscopy in general is a high resolution technique which can give a multitude of information about the sample composition, electronic and structural properties and the in plane magnetic domains. Lorentz transmission electron microscopy (LTEM) is a transmission electron microscopy technique which images magnetic contrast via the electron deflection due to the Lorentz force experienced by the incident electrons when propagating through a magnetic sample [75]. This Lorentz force is only experienced if the magnetic moments of the domains are perpendicular to the motion of the propagating electrons and only then if the forces on the electrons due to the magnetic interaction does not cancel to zero over the beam path [75] (see figure 3.3 (a)-(c)).

The Lorentz force is given by [76]:

$$\mathbf{F} = |e|\nu \times \mathbf{B} \tag{3.3}$$

where e and ν are the charge and velocity of the electrons respectively, $\mathbf{B}$ is the magnetic induction averaged along the trajectory of the electron. Consider a sample consisting of a thin ferromagnetic foil with two domains separated by a single domain wall. If the magnetic moments of the domains point in the $\pm$y direction and the electrons move along the z-axis then the Lorentz force acting upon the electrons will lead to a deflection in the x direction (see figure 3.3(a)). The angle of deflection, β, is given by [75]

$$\beta = e\mathbf{B}_0\lambda t/h \tag{3.4}$$

where h is the Planck's constant, λ is the wavelength of the electron and t is the sample thickness.

All LTEM images shown in this work were taken by Solveig Felton (Material Science

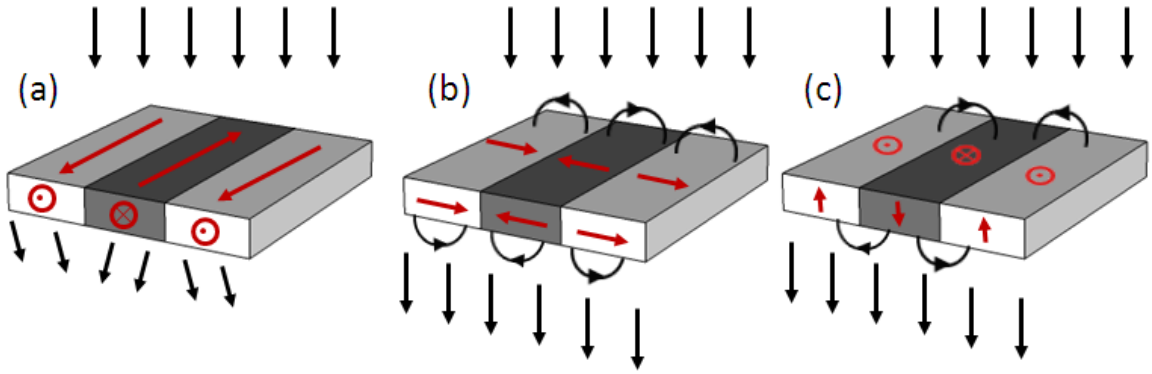

Figure 3.3 Schematics showing the effect of magnetic domains of an electron beam propagating through the sample. (a) Domains will result in a net deflection of the electron beam by an angle β. (b) Even though the domains are perpendicular to the incident beam the stray fields above and below the sample cancel the beam deflection caused by the magnetic domain, no net deflection. (c) No net deflection as the magnetic domains are parallel to the incident beam. Illustration adapted from [46]

Department, Imperial College London, UK) in the Fresnel imaging mode using a JEOL 2010 TEM. In the Fresnel imaging mode the image is taken out of focus and the magnetic domains are imaged as alternating bright and dark lines running parallel to the magnetisation of the domain. Typical achievable spacial resolution is around 0.2 nm for structural imaging and 2-20 nm for magnetic imaging, LTEM. Due to the transmission geometry the sample thickness is limited to $\sim$100 nm. The images were taken in zero field. An *in situ* magnetic field was applied via the electromagnetic field created by the objective lens. However, the magnetic field created by the lens is perpendicular to the sample; An in-plane field component along the sample is achieved by rotating the sample with respect to the field; A rotation of up to 30° is possible, hence as well as a in-plane field component a large out of plane field component is experienced by the sample.

3.1.5 Magnetotransport Measurements

All magnetotransport measurements were measured in a cryogen free superconducting magnet system (CFM) with an integrated Cryogenic Ltd 7.5 Tesla vertical field. The temperature was controlled via an integrated variable temperature insert (VTI) which allows measurements in a range of 2 K $\leq$ T $\leq$ 290 K. The temperature in the CFM is regulated via the circulation of cold He gas. When the He flow is optimised, cryogenic temperatures, down to 2K, can be maintained for a long period of time. The transport probe, provided by Cryogenic Ltd, attached to the end of the sample stick which is inserted into the CFM, consists of an anodised Al block.The sample temperature is monitored via a calibrated Cernox^{TM} sensor in thermal contact with the Al block (In close proximity to the sample). The temperature control unit (LakeShore 340) and the magnet power supply are controlled via the computer software. The sample can be mounted either parallel or perpendicular to the vertical magnetic field. The sample can be connected to 8 pins situated on the Al block. The sample is electrically connected to the 8 pins via copper wires contacted to the sample by silver paint. The longitudinal voltage V_{xx} and the Hall voltage V_{xy} were measured using a low frequency AC lock-in technique at a measurement current I.

A schematic of the measurement set up is shown in figure 3.4. The measurement was controlled by a Delphi computer software written by Dr. Gerry Perkins; The software controls the generation of a AC signal, performs the software lock-in procedure and the data collection. The circuit incorporates a variable resistor in series with the sample which allowed the current through the system to be monitored, $I = V_{Resistor}/R_{Series}$. For all measurements in this thesis a series resistor of 1.5kΩ was used. The voltage drop across the sample and series resistor R_S is acquired by the computer via a National Instruments Data Acquisition Card (NI-DAQ). The signal V_{A-B} passed through a Stanford Research Systems SR560 Low Noise Preamplifier (input noise level of 4 $nV/\sqrt{Hz}$) before passing through the NI-DAQ card. Shielded coaxial cables connected the sample stick with the current source (output from the NI-DAQ card) and the pre-amp.

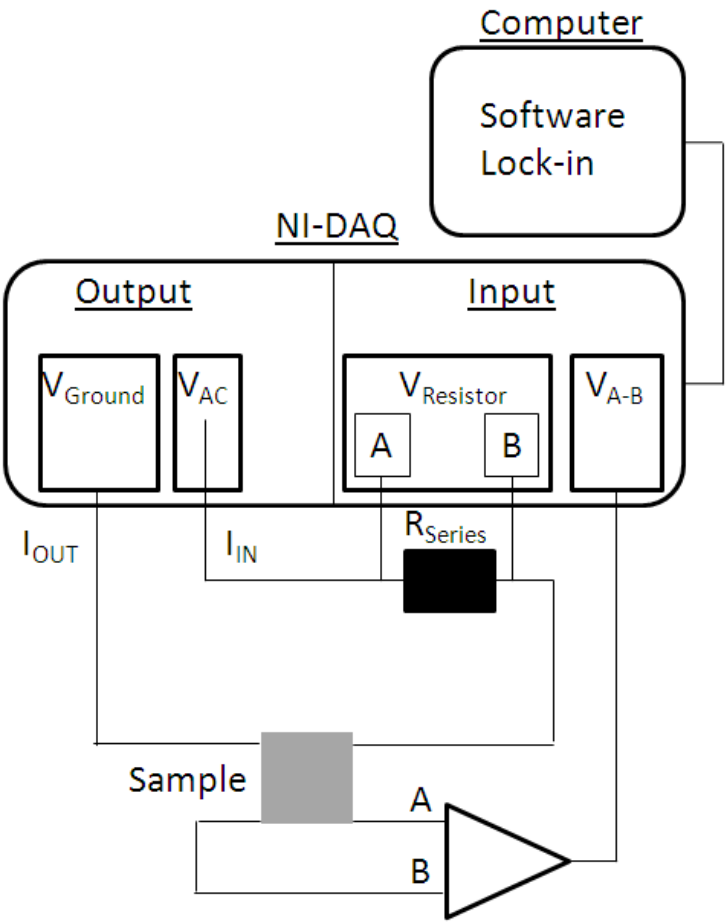

Figure 3.4 Magnetotransport measurement set up. Schematics showing the magnetotransport set up.

The Hall voltage, V_{xy}, was measured by measuring the voltage across the sample perpendicular to the current path along x. The longitudinal voltage V_{xx} was measured across the sample parallel to the current flow. The field dependence of the voltages was investigated at fixed temperatures keeping the respective sample geometry constant. Mixing between the Hall and magnetoresistance contributions can occur due to deviation from uniform and unidirectional current flow.

3.2 Analysis

3.2.1 Micromagnetic Simulations

When simulating the magnetic reversal for a particular field cycle, static models where only stable states at the local energy minima are considered, will not give an accurate description. The exact reversal path will influence the end state. Hence a dynamic model needs to be taken into consideration where the system stays in a particular stable state until it is no longer an energy minimum. A new stable state is found by solving the dynamic equations associated with magnetic moments in an external field. In such a dynamic model the total energy contribution is substituted by an effective field $\mathbf{H}_{eff}$. This effective field is a derivative of the ferromagnetic system's total energy density ε_{total} [77]

$$\mathbf{H}_{eff}(t) = -\frac{1}{\mu_0}\frac{\partial \varepsilon_{total}}{\partial \mathbf{M}(t)} \tag{3.5}$$

$\mathbf{H}_{eff}$ exerts a torque on the magnetisation vector $\mathbf{M}$ causing the magnetisation to precess around the effective field. The time dependence of $\mathbf{M}(t)$ can be expressed as [77]

$$\frac{d\mathbf{M}}{dt} = -\gamma_0[\mathbf{M} \times \mathbf{H}_{eff}] \tag{3.6}$$

where γ_0 is the Landau-Liftshitz gyromagnetic ratio and can be expressed as $\gamma_0 = \mu_0(gq_e/2m_e)$ (g is the Lande factor, q_e and m_e are the charge and mass of an electron respectively). The magnetisation precesses at a frequency known as the Larmor frequency,f_{Larmor}, around the effective field ($f_{Lamor} = (\gamma/2\pi)\mathbf{H}_{eff}$). The local energy minimum is reached when [77]

$$\mathbf{M}(t) \times \mathbf{H}_{eff}(t) = 0 \tag{3.7}$$

Equation 3.7 is known as Brown's equation.

Precession alone cannot result in a saturation limit. It is known that beyond some value of the applied field any ferromagnetic sample can be considered saturated, the magnetic

moments are as aligned as they can possibly get, hence a damping term has to be included in equation 3.6. This will allow the magnetisation to become aligned with the applied field after some finite time. Equation 3.6 takes the form of the Landau-Lifshitz equation [77]

$$\frac{d\mathbf{M}}{dt} = -\bar{\gamma}[\mathbf{M}(t) \times \mathbf{H}_{eff}(t)] - \frac{\bar{\gamma}\alpha}{M_S}[\mathbf{M}(t) \times (\mathbf{M}(t) \times \mathbf{H}_{\mathbf{eff}}(t))] \tag{3.8}$$

where α is the damping constant. For permalloy $\alpha = 0.02$ gives good agreement with experiments [78].The Landau-Lifshitz equation was later rewritten in terms of the Landau-Lifshitz gyromagnetic ratio by Gilbert [77]

$$\frac{d\mathbf{M}}{dt} = -\gamma_0[\mathbf{M}(t) \times \mathbf{H}_{eff}(t)] - \frac{\alpha}{M_S}\left[\mathbf{M}(t) \times \frac{d\mathbf{M}}{dt}\right] \tag{3.9}$$

and is known as the Landau-Lifshitz-Gilbert equation. The Landau-Lifshitz gyromagnetic ratio is related to $\bar{\gamma}$ via $\bar{\gamma} = \gamma_0/(1+\alpha^2)$. Without damping, i.e. $\alpha = 0$, equation 3.9 reduces to equation 3.6.

Object Orientated Micromagnetic Framework

The Object Orientated Micromagnetic Framework (OOMMF) project is a simulation package published by the Information Technology Laboratory at the National Institute of Standards and Technology [79]. The main developers of the package are M. Donahue and D. Porter. Throughout this work version 1.2a3 was utilised.

OOMMF solves the Landau-Lifshitz equation (equation 3.8). OOMMF takes into account the applied field, the exchange, the demagnetisation and the anisotropy. The simulation package solves the magnetic state of a magnetic material with arbitrary shape during a particular field cycle. The Landau-Lifshitz ordinary differential equation solver relaxes 3D magnetisation spins, positioned at the center of the individual square cells making up a 2D mesh. The simulation is terminated when $d\mathbf{M}/dt$ drops below a specified value. The local minima in the energy surface is found using OOMMF.

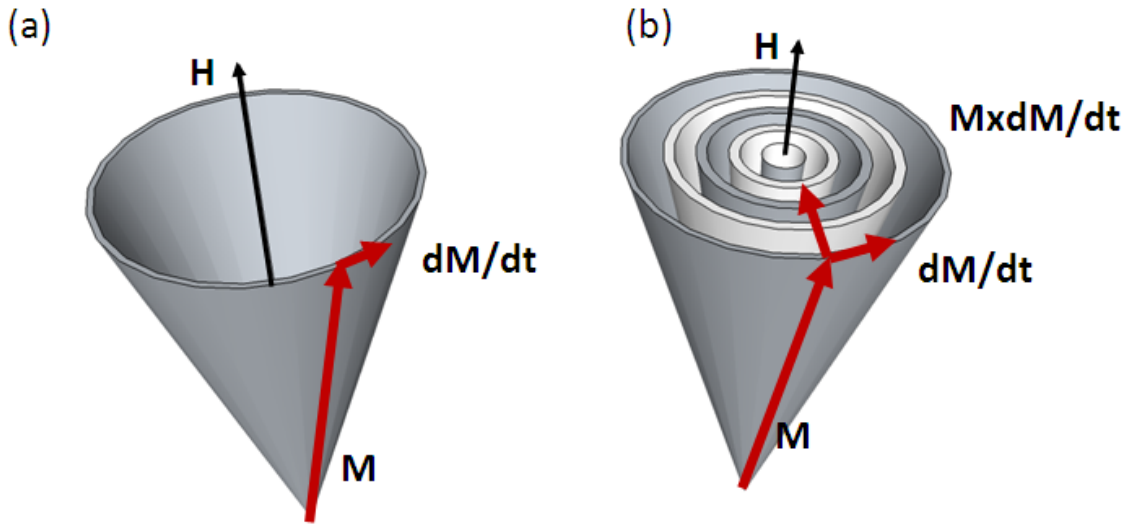

Figure 3.5 Magnetic precession (a) Without damping the magnetic moment precesses around the external field H (b) with damping the precession radius of the magnetic moment slowly decreases until the magnetic moment aligns with H. Illustration adapted from [80].

MuMax

MuMax is a general purpose micromagnetic simulation tool which runs on Graphical Processing Units developed by A. Vansteenkiste and B. Van de Wiele [81]. It solves the same equation as OOMMF, the Landau-Lifshitz equation, however, MuMax is more suitable for large simulations as it runs on Graphical Processing Units and has the additional benefit of allowing for periodic boundary conditions.

3.2.2 Magnetotransport

The field asymmetry introduced by Hall contributions were investigated by virtue of their different symmetries with respect to field inversion: the Hall signal is antisymmetric while the magnetoresistive contribution is symmetric with field inversion. In the simplest case (no hysteresis) the separation into V_{xy} and V_{xx} is described as follows

$$V_{xx} = \frac{V_{down} + V_{up}}{2}, \tag{3.10}$$

and

$$V_{xy} = \frac{V_{down} - V_{up}}{2}, \tag{3.11}$$

where V_{down} and V_{up} are the voltages measured while the magnetic field is swept from positive to negative value and vice versa. In case of a ferromagnet the resistance is hysteretic under the application of an external magnetic field. The reversible component is extracted using

$$V_{xy,Sat} = \frac{V_{down}(+B) - V_{up}(-B)}{2} + \frac{V_{up}(+B) - V_{down}(-B)}{2} \tag{3.12}$$

Where (+B) indicates that only the values corresponding to the measurement at positive field are taken into account while the negative field values are ignored and vice versa for the (-B) notation.

The Hall resistance is obtained using the relation $R_{xy,Sat} = V_{xy,Sat}/I$. The extrapolated $\mu_0 H = 0$ value of the linear high field part, i.e. the intercept of the line fitted through the high field data, is proportional to the anomalous Hall coefficient R_S.

The irreversible components of the resistance measured in the magnetoresistance geometry ($R_{xx,Avg}$, $R_{xx,Diff}$) and Hall geometry ($R_{xy,Avg}$, $R_{xy,Diff}$) are extracted using

$$V_{xx,Avg} = \frac{V_{up}(+B) - V_{down}(+B)}{2} + \frac{V_{down}(-B) - V_{up}(-B)}{2} \tag{3.13}$$

$$V_{xx,Diff} = \frac{V_{down}(-B) - V_{up}(-B)}{2} - \frac{V_{up}(+B) - V_{down}(+B)}{2} \tag{3.14}$$

and

$$V_{xy,Avg} = \frac{V_{up}(+B) - V_{down}(+B)}{2} + \frac{V_{down}(-B) - V_{up}(-B)}{2} \tag{3.15}$$

$$V_{xy,Diff} = \frac{V_{down}(-B) - V_{up}(-B)}{2} - \frac{V_{up}(+B) - V_{down}(+B)}{2} \tag{3.16}$$

Figure 3.6(b) shows a schematic of the physical meaning of $R_{Avg} = V_{Avg}/I$ and $R_{Diff} = V_{Diff}/I$. R_{Avg} is the average between the peak at positive field and negative field and $2R_{Diff}$ is the difference between the two.

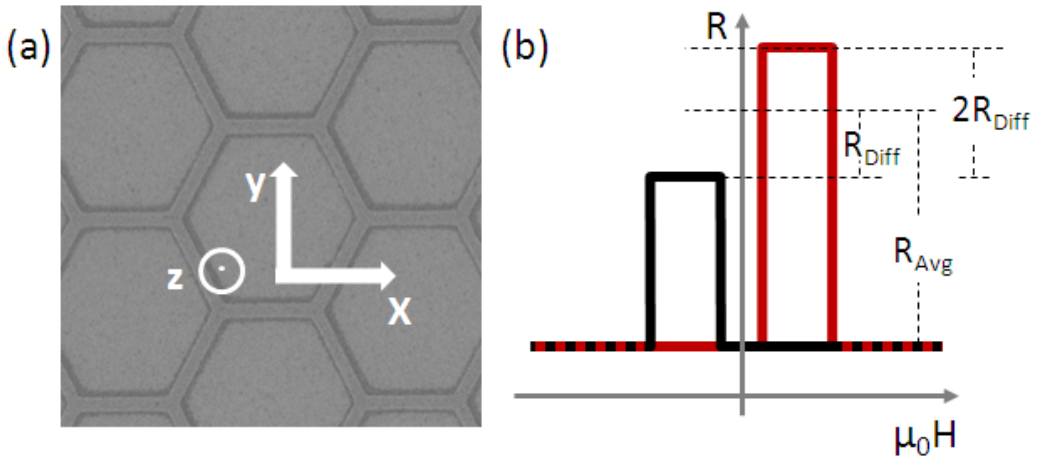

Figure 3.6 Transport measurement set up. (a) Schematics showing the coordinate system of the measurement. (b) Schematics of a magnetotransport curve (black (red) curve represent the down (up) sweep) illustrating the meaning of R_{Diff} and R_{Avg}, the components extracted from the irreversible part of the resistance curves. R_{Diff} is a measure of the asymmetry of the resistance measured at positive and negative fields and R_{Avg} is the average of the two peaks.

3.3 Sample Fabrication

The permalloy ($Ni_{80}Fe_{20}$) honeycomb artificial spin ice arrays were fabricated using electron beam lithography and thermal evaporation. The electrical contacts attached to the honeycomb artificial spin ice array were fabricated using an additional electron beam lithography step, photo lithography and thermal evaporation. The devices were fabricated in a class 1000 environment cleanroom (less than 1000 0.5 μm particles per ft^3).

The magnetostransport samples were grown on a silicon (100) wafer with a 300 nm oxide layer providing an insulating substrate. The artificial spin ice arrays investigated by STXM were fabricated on 50 nm thick silicon nitride membranes (Si_3N_4 membranes). The PEEM samples were grown on conductive silicon (100). The silicon substrates were cleaned by sonication while submerged in acetone for 30 s followed by 30 s in isopropanol after which they were blow dried using pressurised nitrogen gas. Due to their fragility the membranes were cleaned using a light breeze of pressurised nitrogen gas applied at a shallow angle.

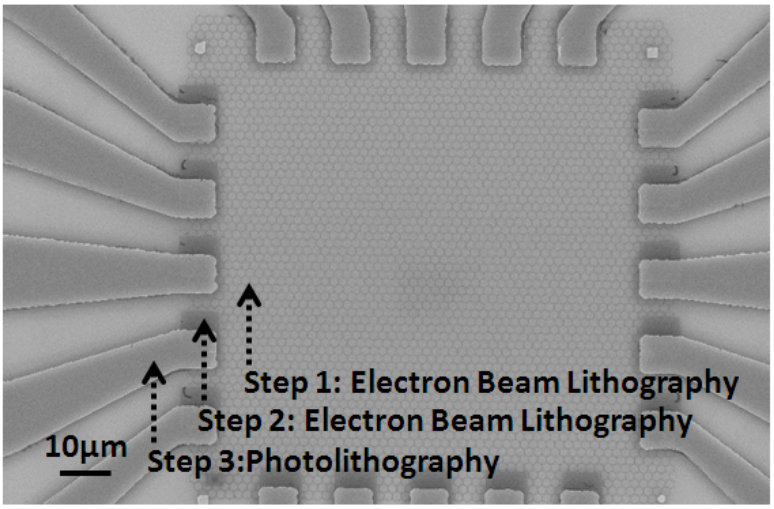

Figure 3.7 SEM images of the magnetotransport samples. Permalloy artificial spin ice arrays with permalloy electrodes. The labels indicate the first and second electron beam fabrication steps (permalloy evaporation) and the subsequent photo lithography (gold evaporation) step.

3.3.1 Electron Beam Lithography

Electron beam lithography allows the creation of patterns into electron sensitive resist with feature sizes well below 1 μm. A focused beam of high energy electrons is moved across the resist, breaking or strengthening the polymer bonds depending on weather positive resist or negative resist is used. A Raith e-line system with a Carl Zeiss electron beam column was used to control the electron beam movement and exposure. The Raith system allows an easy design of exposure patterns to nanometer precision through its software. A positive resist was used in the creation of the artificial spin ice arrays: polymethyl methacrylate (PMMA) 950 A4. A uniform layer of resist, 300 nm thick, was spun onto the substrates using a mechanical spinner. A spin speed of 1800 rpm for 2 min was used for all substrate types. Both spun substrates were baked at 155°C for 5 min. After the electron beam exposure the resist was developed for 1min in 3:1 isopropanol:methyl isobutyl ketone and then washed for 30 s in isopropanol.

The electron beam was focused to a spot size of 20 nm using an acceleration voltage of 20 keV and a 20 μm aperture. The artificial spin ice array buildingblocks, the nanowires, were created by writing 2 lines spaced 20 nm apart. The exposure parameters are summarised in table 3.1 for the two substrates.

PMMA 950 A4		
Substrate	Step size (nm)	Line Dose (pC/cm^2)
Oxidised silicon	2	3500
Silicon	2	1400
Membranes	2	2000

Table 3.1 Table summarizing the electron beam exposure parameters.

Before the thermal evaporation step, the patterned resist layer on the substrate was plasma ashed with an oxygen plasma (Emitech K1050X Plasma Asher). The chamber was

pumped out with a rotary pump and then backfilled with oxygen to a pressure of 6×10^{-1} mBar. The sample was then ashed for 2 min at 10 W.

3.3.2 Photo Lithography

Photo lithography refers to the process of transferring a pattern from a 'mask' onto a polymer photoresist film. The 'mask' consists of a metal layer (chrome) where the desired pattern has been cut out, attached to a clear glass plate. Due to the wavelength of the light used to expose the photoresist, ultraviolet (UV) light, this technique only yields structures larger than $\sim$1 μm. The photoresist reacts chemically when exposed to UV light, either hardening it (negative resist) or making it more soluble (positive resist). When the ex-

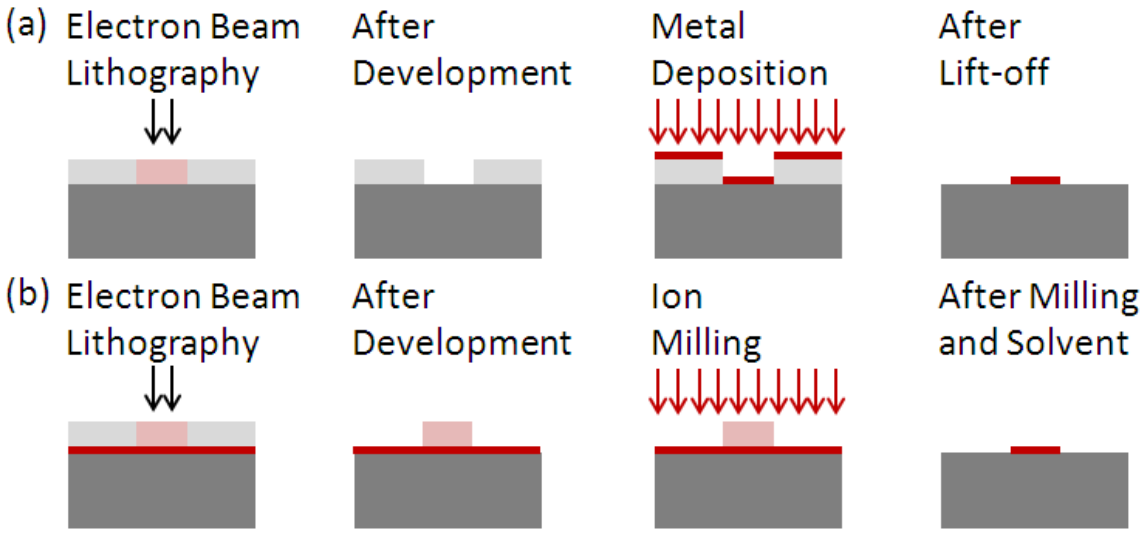

Figure 3.8 Schematics showing the principles of electron beam lithography (a) Lift off approach starting with electron beam lithography, development and metal deposition into the trenches followed by a dissolving of the remaining resist through which the unwanted metal floats off the sample. (b) Top down approach in which the electron beam step is carried out on top of a metal thin film followed by ion beam milling removing the unwanted metal. The remaining resist is dissolved leaving only the desired structure behind.

posed resist film is then submerged in a developer the exposed areas are either resist free (positive resist) or the only ones still standing (negative resist). The pattern of the mask is transfered to the resist layer by bringing the former into contact with the latter and exposing the resist-mask assemble to UV light from above; the areas not covered by the metal are exposed to the UV light. A Karl Suss Contact Mask Aligner was used to align the mask containing the current contacts with the artificial spin ice array and to control the subsequent UV exposure.

A uniform photo resist layer was achieved by evenly distributing photoresist over the sample surface using a mechanical spin coater. The uniform layer was then baked on a hot plate in order to form a solid film as the solvents are evaporated. The resist film thickness is dependent on the time and speed of the spinning.

A bi-layer process was used for a good lift-off of the gold/permalloy electrodes. Two types of photoresist are layered upon each other. Due to their different exposure parameters an exposure by the same intensity of UV results in the creation of an undercut which improves the metal lift-off. Initially photoresist PMGI SF6 was spun at a speed of 3500 rpm for 10 s and was baked for 10 min at 95°C. After the substrate and first resist layer cooled down to room temperature ($\sim$ 5 min) a second photoresist was spun onto the first layer. S1805 resist was spun at 3500 rpm for 10 s and then baked at 80°C for 5 min. Typical thicknesses of this recipe are 300nm for the PMGI SF6 resist and 500nm for the S1805 resist. The bi layer resist was exposed for 5.7 s to UV light.

After development (8 s in developer MF319 followed by washing in dionised water for 30 s) gold was evaporated onto the resist and into the resist trenches using thermal evaporation. All the metal not in contact with the substrate was lifted-off by dissolving the remaining resist.

3.3.3 Thermal Evaporation

Thermal evaporation is a physical vapor deposition technique. A material is vaporised by placing it in a heated crucible. This is done in a low pressure environment to prevent inter-

action between the vapor and the atmosphere. At pressures between 10^{-7} and 10^{-6}mbar the atoms of the vapor travel in a straight line outwards from the evaporation source.

A bell jar Edwards 306 evaporator, pumped down to 2×10^{-6} mbar, was used. The permalloy evaporation source was placed in an integral tungsten wire basket (wire diameter 0.02 ") coated with alumina (Length: 4 ", height: 0.5 ") (Megatech Limited, Cannock, UK). The $Ni_{81}Fe_{19}$ permalloy source came in shape of a cylinder with diameter 1/4 " and length 1/4 " with material purity of 99.95% (Kurt J Lesker, Hastings, UK). The crucible was heated to temperatures above the permalloy melting point by passing 32 A through it. The sample was placed directly above the source separated by a vertical distance of around 30 cm. A typical deposition rate of 0.3nm/s was used. A quartz crystal thickness monitor was used to monitor the deposition rate and thickness. The evaporation onto the sample was started and stopped by opening and closing a shutter.

Energy dispersive x-ray spectrometry measured the composition of the typical evaporated thin film to be consistent with the evaporation material within 2%.

Chapter 4

Magnetic Charge Carrier Control in Artificial Spin Ice

In this chapter the influence of the magnetic domain wall shape on artificial spin ice was investigated. Permalloy artificial spin ice arrays were fabricated via electron beam lithography. The room temperature magnetic reversal of honeycomb artificial spin ice was studied via various magnetic imaging techniques (STXM, PEEM and LTEM). Magnetic reversal in connected artificial spin ice occurs via edge nucleation and propagation of domain walls. The influence of domain wall propagation through the artificial spin ice array was studied as a function of the magnetic moment distribution of the domain wall, the so called domain wall chirality. The domain wall chirality was seen to have a deterministic influence on the switching and could potentially be used as a means of controlled switching. It could enable the creation of ice rule violation states during the early stages of the reversal. Controlled injection of domain walls into artificial spin was attempted. Introducing soft injection pads allowed the reduction of randomness introduced by domain wall nucleation needed to initiate the array switching. An alteration of the array edge geometry was used to achieve controlled domain wall injection by suppression of edge nucleation of domain walls.

4.1 Sample Characterization

The magnetic reversal of a selection of artificial honeycomb spin ice arrays was studied with a variety of techniques. The domain wall propagation through the arrays and the effect of magnetically soft pads situated on the left hand side of the array was investigated.

A summary of the dimensions associated with the twelve arrays studied can be found in table 4.1. The width was evaluated from line scans profiles acquired from AFM scans taken over an area of 1.28 μm x 1.28 μm at a scan speed of 0.86 s/line and was taken to be the width at the point of half the bar thickness (FWHM). The stated width is an average of 3 bars situated at the edge and 3 bars situated in the centre of the array where 3 line scan profiles were taken per bar. AFM scans for PHC1 and the line scan profile of a bar at the edge and at the centre of the honeycomb array can be seen in figure 4.1. Figure 4.2 shows large area images of selected arrays studied.The maximum areas imaged were as follows for the different arrays: 16μm x 16μm for PHC1 and PHC2, 32 μm x 32 μm for SHC1,15 μm x 15 μm for LHC1, 11 μm x 11 μm for SHC0, 28 μm x 28 μm for SHC15 and 48 μm x 48 μm for SHC15T. A detailed description of the fabrication method can be found in chapter 3.3. From figure 4.3 it can be seen that in LHC1 and SHC0 not all hexagons have 'lifted off' due to fabrication difficulties associated with the SiN membrane substrate.

A schematic and corresponding image of the types of injection pads, whose influence on the magnetic reversal of artificial spin ice was studied, can be seen in figure 4.3: (a)-(b) show the polygonal and (c)-(d) show the triangular pads dimensions. PHC1 possesses three triangular pads spaced apart by 6 hexagons (in the y-direction) on the left hand side of the array. They are connected to the artificial spin ice by 1.00$\pm$0.05 μm wires in the case of the top and bottom triangles and by a 1.48$\pm$0.05 μm wire in the case of the middle triangle (figure 4.2 (a)). Sample PHC2 on the other hand has two mirrored triangles on the left hand side, spaced one hexagon apart (in the y-direction) and connected via 0.50$\pm$0.05 μm long wires. SHC0, SHC1, SHC15 and SHC15T have a single polygonal injection pad on the left hand side connected to the honeycomb array via a 0.370$\pm$0.005 μm long, 147$\pm$5 nm

Artificial Honeycomb Spin Ice Arrays						
Array	Pad	Length	Thickness	Edge width	Centre width	Technique
PHC0	None	533±5 nm	18±1 nm	146±5 nm	149±5 nm	PEEM
PHC1	Triangle	528±5 nm	18±1 nm	144±5 nm	147±5 nm	PEEM
PHC2	Triangle	539±5 nm	18±1 nm	147±5 nm	151±5 nm	PEEM
PHC3	None	530±5 nm	18±1 nm	152±2 nm	220±3 nm	PEEM
LHC1	Polygon	1000±10 nm	18±1 nm	150±10 nm	150±10 nm	LTEM
LHC2	Polygon	1000±10 nm	18±1 nm	150±10 nm	150±10 nm	LTEM
SHC0	Polygon	1120±5 nm	18±1 nm	210±7 nm	283±7 nm	STXM
SHC1	Polygon	1070±5 nm	18±1 nm	129±5 nm	114±5 nm	STXM
SHC15	Polygon	1551±5 nm	18±1 nm	187±10 nm	186±10 nm	STXM
SHC15T	Polygon	1551±5 nm	36±1 nm	183±10 nm	173±10 nm	STXM
SHC2	Polygon	2098±5 nm	18±1 nm	99±17 nm	124±15 nm	STXM
SHC2T	Polygon	2100±5 nm	36±1 nm	207±14 nm	181±5 nm	STXM

Table 4.1 Physical dimensions of the honeycomb artificial spin ice bars in the arrays investigated.

wide, wire. Sample LHC1 was fabricated with the addition of 17 polygonal pads attached to the left hand side via a 0.370±0.005 μm long wire.

The large surface area of the pads, in comparison to the available nucleation area of the un-padded artificial honeycomb spin ice, shifts the balance between the energy associated with the existence of magnetic stray field lines and the energy loss associated with the creation of domain walls due to magnetic exchange penalties in favour of the domain wall creation. Hence lower fields are necessary to nucleate a new domain wall within the pads [82]. Without pads the domain walls nucleate at the point where the two diagonal bars meet at the array edges. The effect of the shape of the pads is beyond the scope of the thesis; both pad shapes were designed to be sufficiently larger than the nanobars leading to them being magnetically softer than the wires of the array.

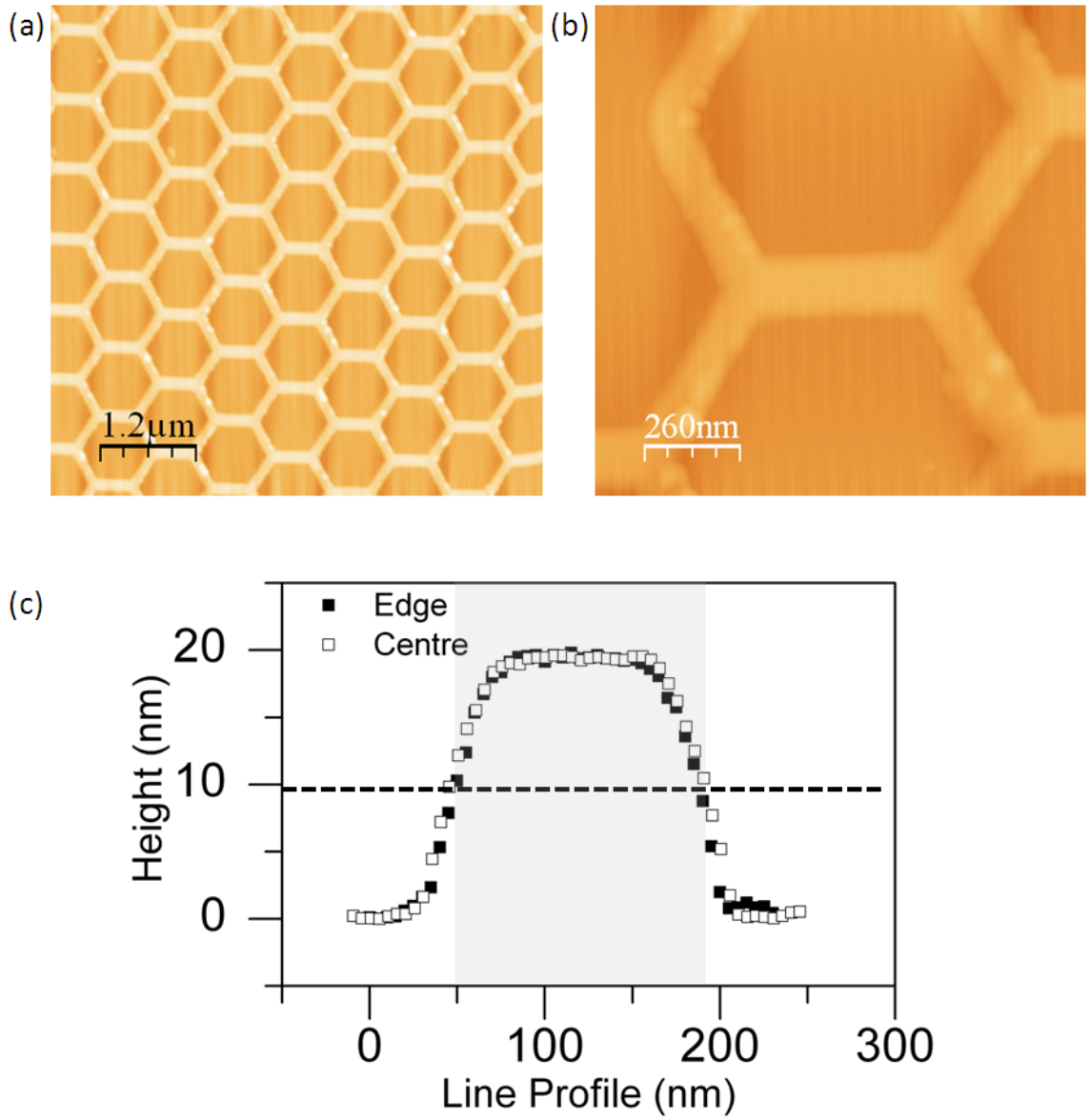

Figure 4.1 Typical bar profile of artificial spin ice arrays. (a) 6 μm x 6 μm AFM scan of PHC1 (b) 1.28 μm x 1.28 μm AFM scan of PHC1 (c) Typical line scan through PHC1 bars situated at the edge and at the centre of the array. The black dotted line is situated at 1/2 the height of the bar and the gray shaded area indicates the FWHM of the edge bars. The FWHM was taken to be the bar width.

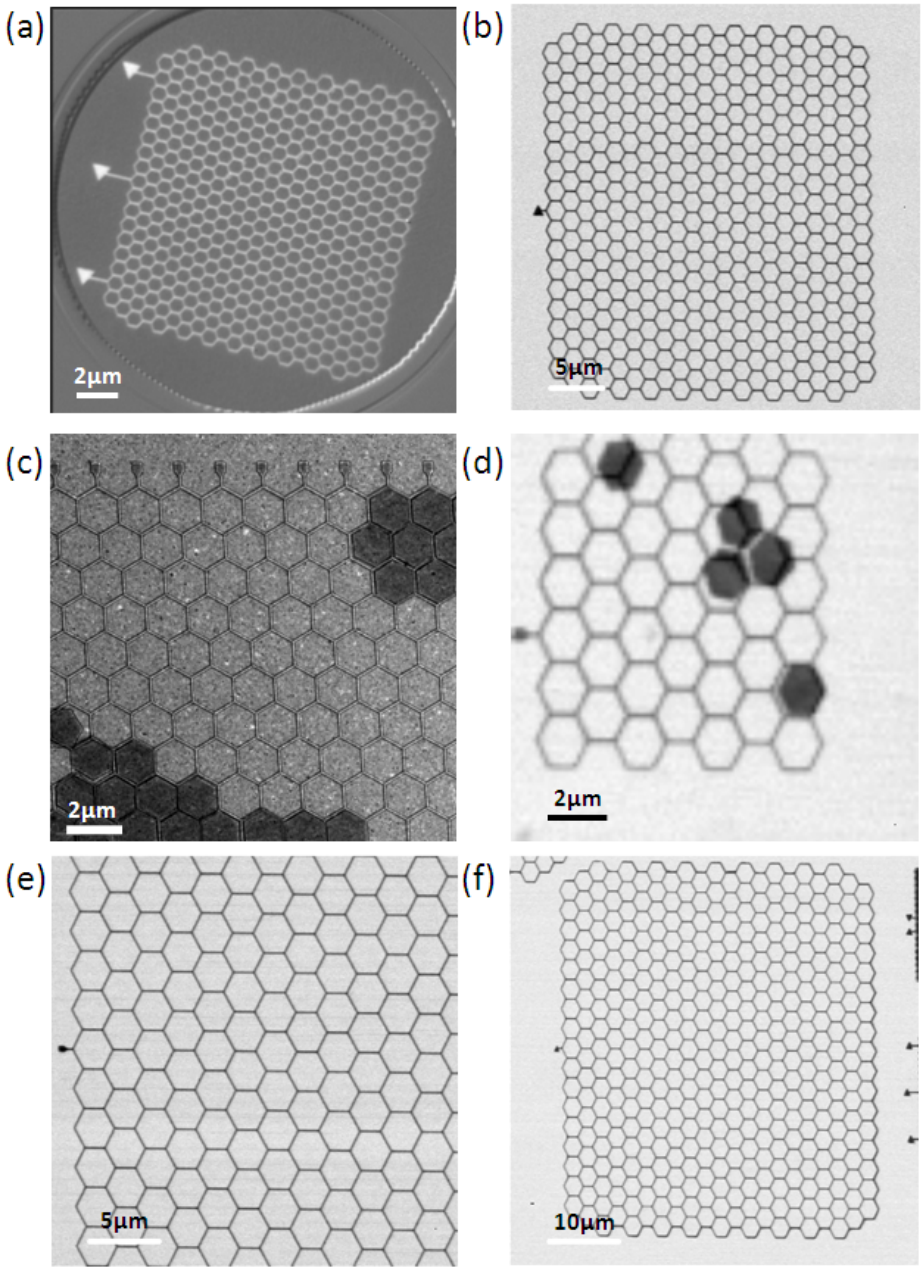

Figure 4.2 Images of artificial spin ice arrays at remanence. (a) Intensity PEEM image of PHC1. (b) Single circular polarised scan of SHC1. (c) Lorentz TEM image at a defocus of 1 mm LHC1. (d) Single circular polarised scan of SHC0. (e) Single circular polarised scan of SHC15. (f) Single circular polarised scan of SHC15T. The bar dimensions are tabulated in table 4.1.

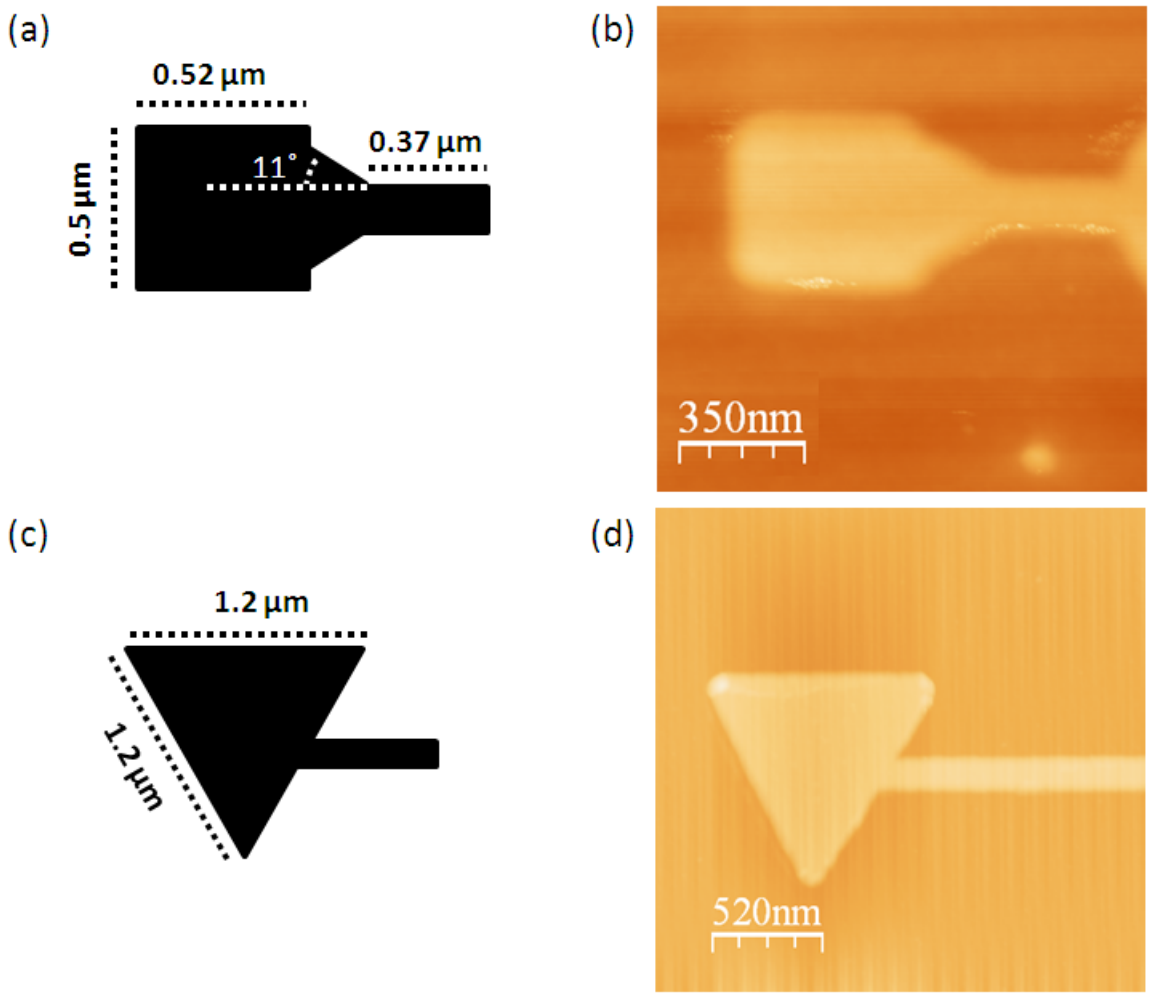

Figure 4.3 Injection pad overview. (a) Schematic of a polygon injection pad. (b) AFM image of a polygon injection pad. (c) Schematic of a Triangular injection pad. (d) AFM image of a triangular injection pad.

4.2 Chirality Controlled Propagation of Magnetic Charge Carriers

Thus far the switching of artificial spin ice has been described via nucleation and propagation of domain walls, in particular, using the description of the domain walls as point charges of magnetic charge $\pm 2q$ [21, 36, 42, 43]. The interaction of such charges with each other and with the vertex charge background, $\pm q$ and $\pm 3q$, via a magnetic Coulomb force manages to explain most trends of the magnetic reversal in artificial honeycomb spin ice; It certainly captures the occurrence of avalanche cascades of reversed bars in the 180° reversal [43], [25], [38]. However recent work has shown that ice rule violations do occur even at very low quench disorder [39]; very unlikely in a pure Coulombic picture. A crucial aspect is neglected in such a charge argument; The magnetic moment distribution and hence the magnetic charge distribution of the domain wall shows distinct deviation from the point charge model especially when considering a transverse domain wall. This section explores the subtleties introduced by the unique shape of magnetic domain walls.

Domain walls moving through nanowires have been studied extensively for spintronic applications [83–85]. It is widely accepted that domain walls in thin wires have defined micromagnetic configurations [49]. Within the ranges of artificial spin ice fabricated so far they can either be transverse domain walls or vortex domain walls [39]. In the spin ice arrays studied, the 18 nm thick 100-200 nm wide bars ensure the nucleation of transverse domain walls [86]. In a 36 nm thick spin ice array with bar width of 180 nm the magnetic reversal is mediated via vortex domain walls [86]. In both cases the micromagnetic moment distribution diverges from the assumption of a disc of magnetic charge. The magnetic moment at the centre of the transverse domain wall points at 90° to the nanowire axis. Furthermore, the direction of magnetic moment rotation, i.e. the chirality of the domain wall, adds a degree of freedom. For transverse domain walls there exist two possible ways for the magnetic moments to rotate the required 180°, referred to as up chiral transverse domain walls and down chiral transverse domain walls depending on whether the

in-plane rotation is anticlockwise or clockwise [87]. In the case of vortex domain walls the magnetic moment can swirl clockwise or anticlockwise around its out of plane centre [88]. Hence, an important question is raised: Does the micromagnetic structure of the domain walls, mediating the reversal of artificial spin ice, have an impact on the magnetic reversal of the arrays?

If we assume the Coulombic treatment of the magnetic charges is correct, then as the charge is pushed through a horizontal bar, by an external magnetic field parallel to that bar, it will encounter a vertex with two propagation paths open for consideration. As the junction in such an arrangement is symmetric there should be a 50/50 chance of the disc domain wall ending up in the upper diagonal bar, the +60° bar, or in the lower diagonal bar, the -60° bar. Hence after two consecutive decisions there is a 25 % chance of the domain wall to be at the extremities and a 50 % chance of the domain wall to be in the horizontal bar in the middle (see figure 4.4 (b)). The domain wall movement, in the purely Coulombic view, is expected to follow a random walk, where the probability, $P_{n,m}$, of the domain wall being at a certain point, (n,m), in the array after n decisions is determined by the total number of path leading to point m divided by the total number of possible paths, 2^n [89].

$$P_{n,m} = \frac{n!}{q!(n-q)!}\frac{1}{2^n} \tag{4.1}$$

where $q = (n+m)/2$ and m is the displacement away from the origin (see figure 4.4(a)). A comparison between the artificial spin ice reversal and the random walk model assumes domain wall back propagation is negligible. However, when looking at images taken at remanence in mid transition of the magnetic reversal it is striking that long unidirectional chains can be observed (see figure 4.4(c)). Following a random walk model, it is very unlikely to observe a domain wall which has chosen the +60° bar nine consecutive times (<0.2 %).

The path distribution of the domain walls reversing the artificial spin ice was quantified for a series of artificial spin ices with different bar lengths (PHC0, PHC1, PHC2,

PHC3, SHC1, SHC2 and SHC2T). Table 4.1 summarizes the bar dimensions of the artificial spin ice arrays measured. The path was mapped by identifying the origin of an isolated chain, assigned (Number of decisions, Y-Displacement) = (0,0) and then consequently following the change in Y-Displacement assigning a unique coordinate (Number of decisions, Y-Displacement). The mapping methodology is illustrated in figure 4.4 (d). The domain wall originating at (0,0), propagated through the -60° bar leading to an observation of a switched bar at position (1,-1) and finally the chain was seen to terminate at (7,3).

The recorded isolated charge carrier path displacement in the y direction, the direction perpendicular to the applied field, through PHC0, PHC1 and PHC2 is shown in figure 4.5(a). N_y, the number of observed chains at each coordinate (x,y) normalised by N is represented via the colour of each point (see legend at the right hand site). The total number of chains observed (N) at a certain chain length is plotted as a black histogram in figure 4.5(a). Figure 4.5(b) shows N_y normalised by $N_{P,y} = NP_{n,m}$, the number of observations expected at (x,y) assuming random walk. Normalising to the random walk probability which assumes $\Delta y = +1$ and $\Delta y = -1$ are equally likely, highlights the unusual unidirectional chains. $N = 1$ observations were discarded. The data acquired from PHC0, PHC1 and PHC2 were summarised in the same plot as the arrays are nominally the same, written and evaporated on the same substrate in the same fabrication process and measured one after each other without changing the measurement setup. Figure 4.6(a) and 4.6(b) show the recorded data acquired during magnetic reversals of SHC1 and SHC2 respectively. Figure 4.6(c) and (d) shows N_y normalised by $N_{P,y}$ for SHC1 and SHC2 respectively (see legend for the colour code). For a complete numerical break down of the experimental data see appendix C.

The long unidirectional chains observed through the various samples are striking (see figure 4.5(a) and figure 4.6(a) and (b)). However as the number of observations decreases rapidly with increasing chain length (see histograms in figure 4.5(a) and figure 4.6(a) and (b)) acquiring data on a statistically significant number of chains is difficult. In order to allow a statistical treatment of our data the chains were deconstructed into observations of two consecutive decisions (see table 4.2).

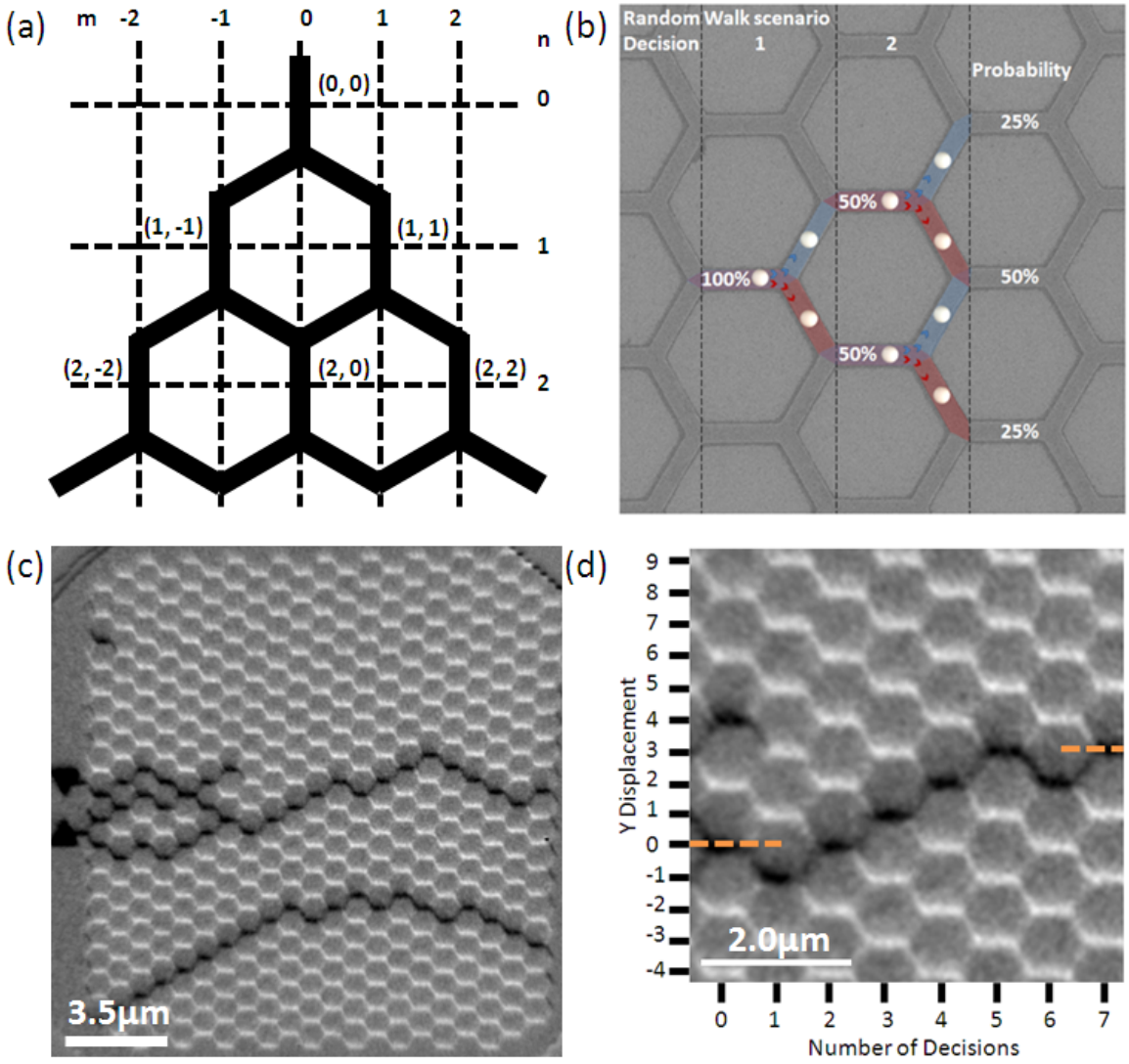

Figure 4.4 Schematic of chirality determined domain wall movement through artificial honeycomb spin ice. (a) Principle of random walk, at each junction there is a 50/50 chance of going right or left. The probability of ending up at point (m,n) is given by equation 4.1. (b) Random walk scenario expected for a point charge domain wall propagating through an artificial spin ice array (Published in [90]). Illustration of individual charge mapping methodology. (c) Magnetic contrast of a PEEM image of PHC1 at -8.5 mT applied in the -x-direction. (d) Magnified cut of (c) illustrating the classification of individual long chains of magnetic reversed bars into number of decisions versus y-displacement form its origin (0,0). The orange lines are guides to the eye indicating the y-displacement of the chain at the start and end of the chain.

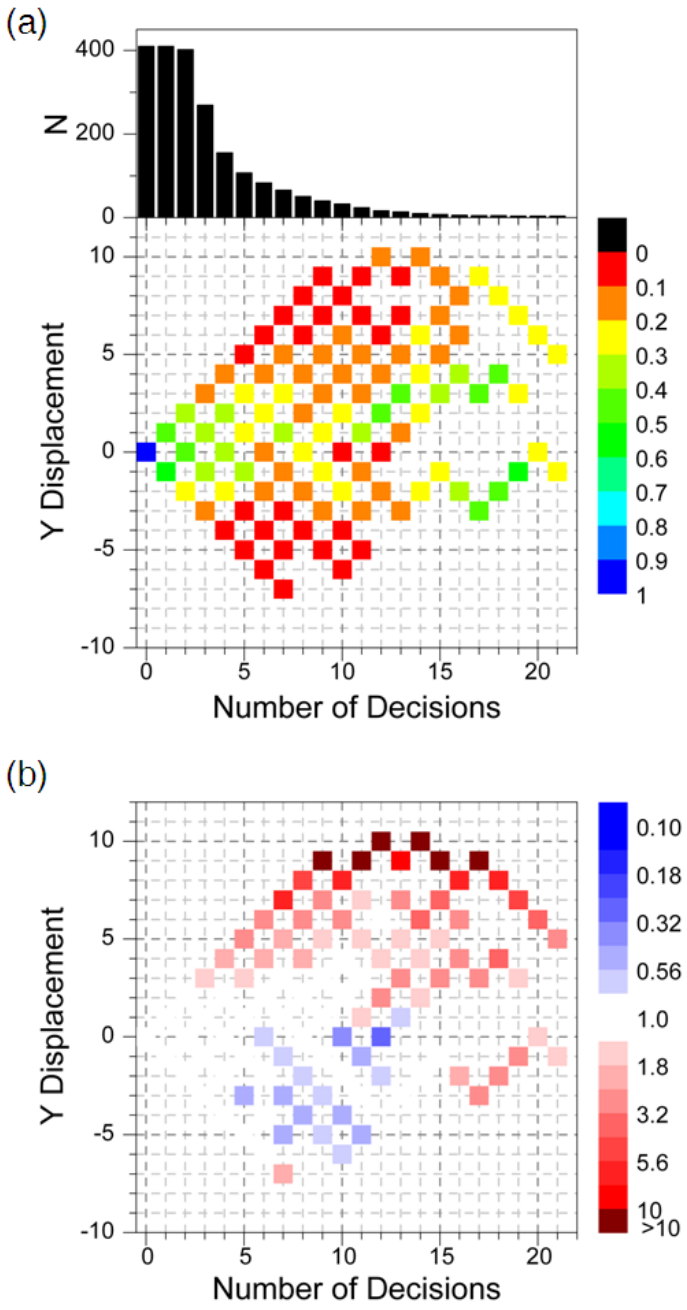

Figure 4.5 Magnetic charge paths distribution during 180° magnetic reversals of PHC0, PHC1 and PHC2. Magnetic charge path displacement in the direction perpendicular to the applied field (y-coordinate) as a function of the number of decisions (x-coordinate). (a) N_y, the number of observed chains at point (x,y), normalised by N, the sum of all N_y's at that chain length (see histogram). (Colour keys on right hand side) (b) shows the N_y of (a) normalised by the number of occurrences expected assuming a random walk, $N_{P,y}$ where the two possible outcomes of each decision point $\Delta y = \pm 1$ are equally likely. (Colour keys on right hand side; $N_y/(NP_{n,m}) = N_y/N_{P,y} > 1$ ($N_y/(NP_{n,m}) = N_y/N_{P,y} < 1$), highlights more, red, (less, blue) observations than expected for a random walk.)

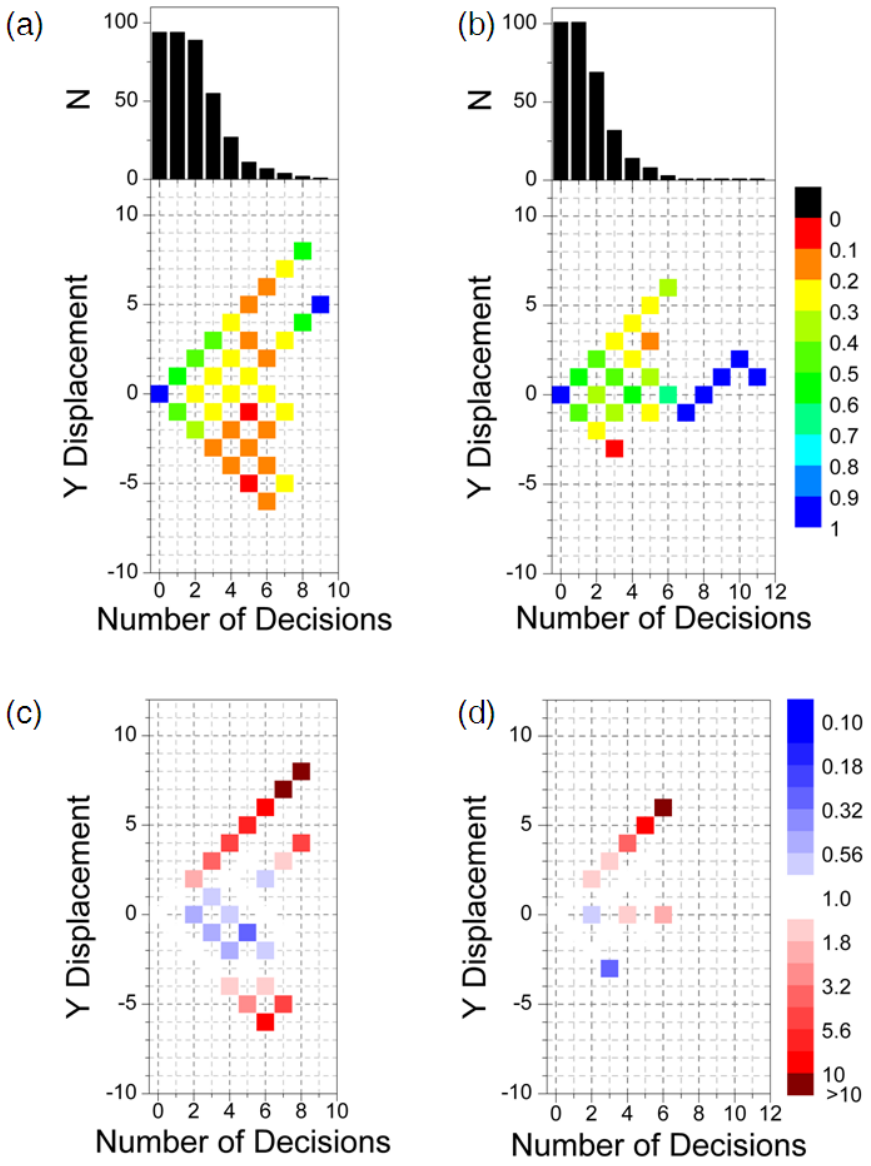

Figure 4.6 Distribution of observed magnetic charge paths during 180° magnetic reversals in permalloy artificial honeycomb spin ice. The total number of chains (N) observed at any given number of decisions is shown in the black histogram for (a) SHC1 and (b) SHC2 (Colour key on the right hand side). The isolated charge carrier path displacement in the direction perpendicular to the applied field is recorded as a function of chain length or number of decisions. The displacement changes by $\Delta y = \pm 1$ at each decision point. N_y, the number of observed chains at each coordinate, normalised by N is encoded via the colour (see legend at the right hand site). (c) and (d) show N_y of (a) and (b) respectively normalised by the number of observations expected assuming a random walk, $N_{P,y}$. (see the colour key on the right hand side; $N_y/N_{P,y} > 1$ ($N_y/N_{P,y} < 1$), highlights more, red, (less, blue) observations than expected for a random walk.) (Published in [90]).

A 1-tailed binomial test was performed, inquiring about the likelihood of observing the given number of chains terminating at (2,±2) or more assuming a random walk probability, p, of success of 0.5. The null hypothesis of observing a random walk is rejected if [91]

$$\sum_{x}^{n} \binom{n}{x} p^x (1-p)^{n-x} \leq \alpha \tag{4.2}$$

where x is the number of successes, n is the number of total trials and α denotes the significance level. Within a significance level of 1 % in the case of PHC0-2 and SHC1 and 5 % in the case of SHC2 the null hypothesis of observing a random walk scenario is rejected. The results clearly indicate that the propagation direction of a domain wall at each vertex is not entirely random.

Simulations of 1000 random walks undergoing nine consecutive decisions were performed for both an unbiased walk and for a biased random walk (figure 4.7(a) and (b)

Artificial Honeycomb Spin Ice Arrays				
End Coordinates	PHC0-2	SHC1	SHC2	SHC2T
(2,2)	418	68	56	27
(2,0)	501	47	55	35
(2,-2)	254	56	20	23
(2,±2)	672	124	76	50
(2,0)	501	47	55	35
Total	1173	171	131	85
1-Tailed Binomial Test	$3.3\text{x}10^{-7}$	$1.7\text{x}10^{-9}$	0.04	0.06

Table 4.2 Propagation choices made by the domain walls mediating the magnetic reverse. Each chain was truncated into chains of length 2. A 1-tailed binomial test was used to investigate if the observed quantity of chains ending in (2,±2) is likely assuming a random walk model.

respectively) (Simulated by S.K. Walton). The biased random walk model assumes that there is no overall preference for $\Delta y = \pm 1$, but that a subsequent decision is correlated with the immediately preceding decision. We used the apparent bias factor for the SHC1 experimental two decision correlation data (see table 4.2) of 72.5:27.5. The difference in the expected number of observations at the outer most possible path in both positive y displacement and negative y displacement ($N_{|Ymax|}$) is shown in figure 4.7(c). Witnessing a unidirectional chain after nine consecutive path decisions is nearly 20 times more likely for a biased walk.

OOMMF simulations show that the deviation from a random walk scenario can be attributed to the magnetic moment distribution of the domain walls. The simulation outcome for 100 nm wide and 18 nm thick wires can be seen in figure 4.8 (a)-(h) (Simulated by S.K. Walton). An up chiral transverse domain wall arriving at a vertex via the horizontal bar will lead to the switching of the +60° bar (see figure 4.8(a)-(b)), a down chiral transverse domain wall will result in the switching of the -60° bar (see figure 4.8(c)-(d)). Furthermore a domain wall arriving from the lower (upper) diagonal bar will result in an up (down) chiral domain wall subsequently propagating through the next horizontal bar (see figure 4.8(e)-(f) and (g)-(h)).

The transverse domain wall, as region of magnetic moment change, has an influence on the magnetic moment distribution of the vertex when it is in close proximity. This is not an entirely new concept; W. R Lewis *et al.* showed that the potential energy landscape experienced by a transverse domain wall when being pushed through a curved permalloy wire, depends on its chirality with respect to the direction of curvature [92]. Furthermore, D. Petit *et al.* showed that the pinning of a domain wall traveling through a T-junction is also chirality dependent [93]; The V-shaped structure of the domain wall not only influences the type of energy potential the wall is experiencing but also the strength of the pinning (see figure 4.9(a) and (b)).

A down transverse domain wall propagating through an inverse T-junction, where the magnetisation of the domain wall is parallel to the vertical arm of the junction, experiences

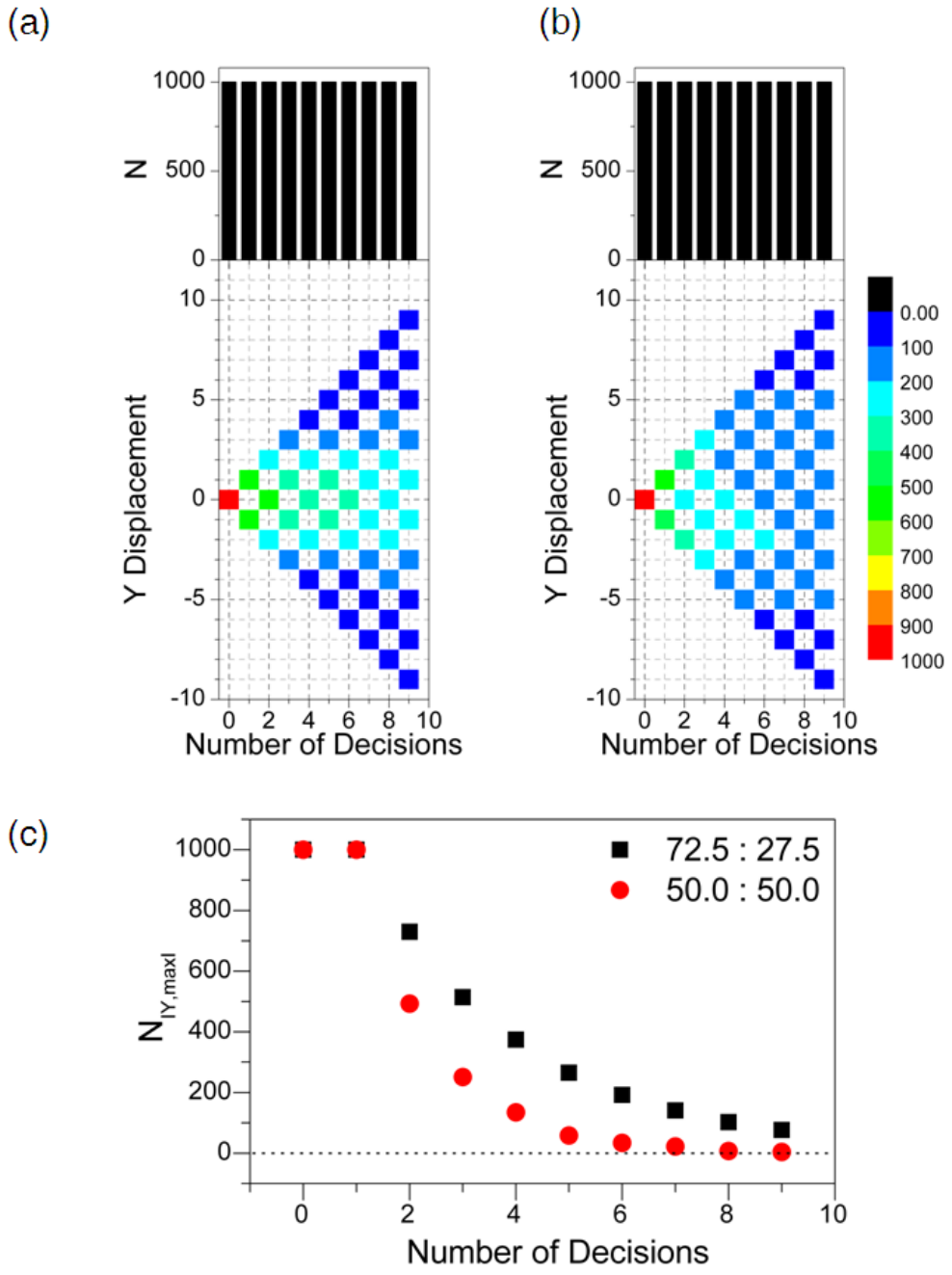

Figure 4.7 Pseudorandom walk scenario model. The colour-coded (see legend) full path distribution is shown in (a) for random walks and (b) biased random walks. The biased random walk model assumes that there is no overall preference for $\Delta y = \pm 1$, but that a subsequent decision is correlated with the immediately preceding decision. We used the apparent bias factor from the SHC1 experimental two decision correlation data (see table 4.2) of 72.5:27.5. (c) Expected number of observations at the outer most possible path ($N_{|(N_{max}|}$) after 1000 random walks and biased random walks. Simulation by S.K. Walton. (Published in [90])

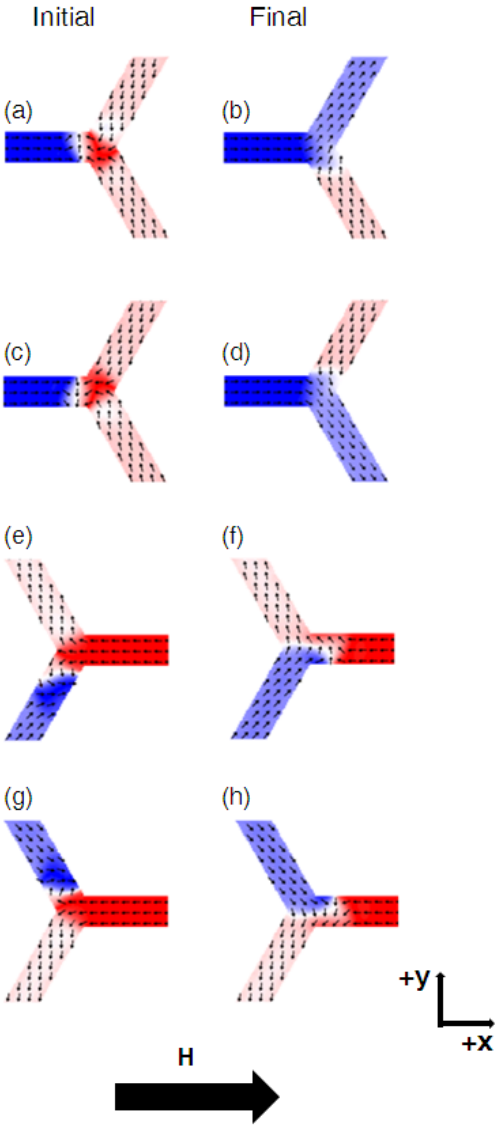

Figure 4.8 Simulation of a single transverse domain wall moving through a vertex. OOMMF simulation of (a)-(b) up chiral wall (c)-(d) an down chiral wall moving thorough a vertex when approaching the vertex from the horizontal bar. An up domain wall results in the subsequent switching of the upper diagonal bar and a down chiral domain wall switches the lower diagonal bar. (e)-(f) and (g)-(h) are simulations of a transverse domain wall approaching from the lower and upper diagonal bar respectively. The initial and final states show the magnetic structure before and after the artificially transverse domain wall has traveled through the vertex.The domain wall movement is driven by an applied field in the +x direction after a saturation in the -x direction. Simulation by S.K. Walton. (Published in [90])

a double potential barrier (see figure 4.9(a)). Experimentally, a field of 35±5 Oe was needed in order to push the domain wall through the barrier. At the centre of the a potential barrier a local minimum was observed caused by a local minimum in the exchange energy, a consequence of the parallel moment alignment of the domain wall and the vertical bar [93].

Despite obvious geometrical differences between the Y-shaped junctions of artificial honeycomb spin ice arrays and T-junctions quantitative comparisons between the two can be drawn. Both an up transverse domain wall leading to a switching of the +60° bar and a down transverse domain wall switching the -60° bar, are similar to the parallel inverse T-junction switching shown in figure 4.9(a). Assuming the domain wall does not deform while it moves through the vertex then as the wall is pushed into the vertex the magnetic moments, at the centre of the up (down) domain wall, are in near alignment with the lower (upper) diagonal bar.

A down transverse domain wall propagating through a T-junction, the magnetisation of the vertical arm is anti-parallel to the magnetic moment configuration of the domain wall, experiences a single potential barrier (see figure 4.9(b)). A transition field of 45±5 Oe was observed experimentally. The potential barrier is higher than the double potential barrier and hence is energetically unfavourable. The anti-parallel T-junction configuration is similar to the honeycomb artificial spin ice configuration where a domain wall with up (down) chirality switches the - (+) 60° bar. It is reasonable to assume that such a case has a higher transition field in comparison to a down (up) transverse domain wall switching the + (-)60° bar and hence it would typically not be observed experimentally.

The above assumption of non-deformation is quite unlikely, however the local exchange minimum argument does have some validity as the simulations in figure 4.8 (a) and (c) show a 'C'-like state (a low exchange energy intermediate state as seen in the reversal of nanodisks with a diameter of 340-370 nm [94]) which stabilizes when the domain wall is in vicinity of the vertex (see figure 4.9(c)).

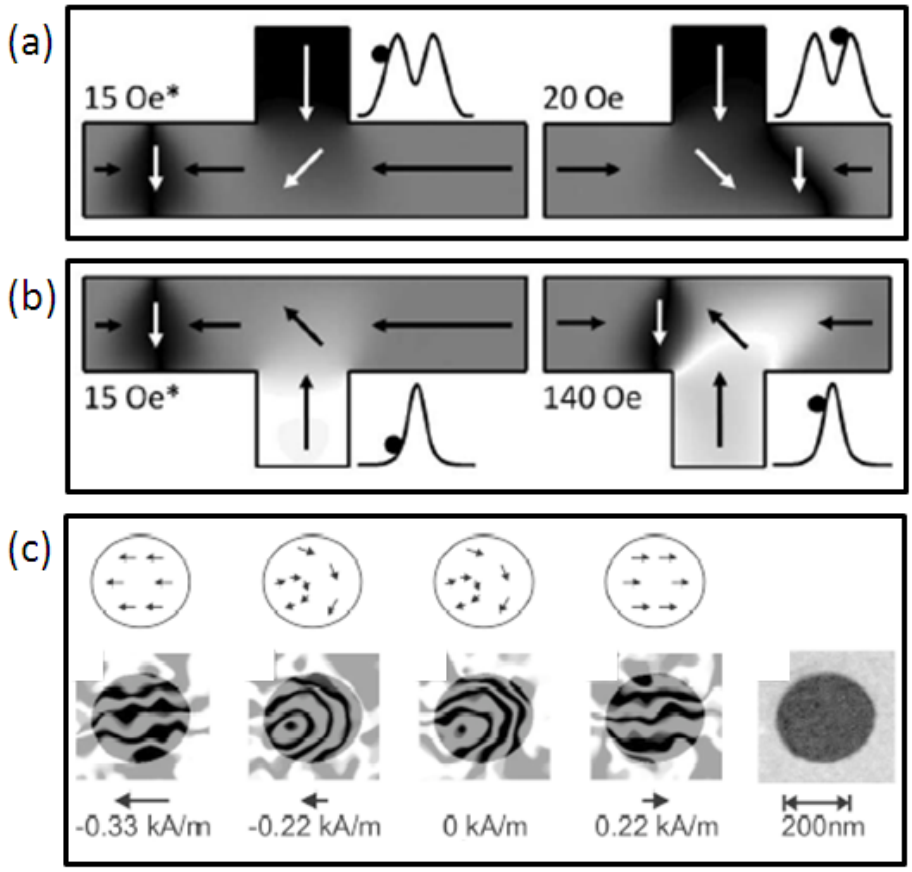

Figure 4.9 Chirality dependent switching of T-junctions (a) OOMMF simulation of a down transverse domain wall propagating through an inverse T-junction. The vertical bar magnetisation is parallel to the magnetic moment of the domain wall. Published by D. Petit *et al.* [93]. (b) OOMMF simulation of a down transverse domain wall propagating through a T-junction. The vertical bar magnetisation is anti-parallel to the magnetic moment of the domain wall. Published by D. Petit *et al.* [93]. (c) Switching via 'C-like state of permalloy nanodisks. Published by Heumann *et al.* [94]

Furthermore as a consequence of the domain wall shape the magnetostatic charge density $\rho = -\mu_0 \nabla \cdot \mathbf{M}$ is uniquely distributed across the triangular shape with a negatively charged hot spot at the narrow end and a spread out positively charged wide edge [95]. It has been shown that this nonuniform charge density has a large influence on the switching of cross-shaped permalloy junctions when two domain walls are injected into two adjacent bars [96]. The domain walls were seen to attract and repel each other depending on their charge distribution leading to completely different switching fields. In the case when a $+Q_{DW}$ domain wall encounters another $+Q_{DW}$, already pinned in the cross-shaped junction the repulsive magnetostatic interactions lead to a depinning of the originally pinned domain wall. This pinning occurs at a lower field than expected. In the case of a $\pm Q_{DW}$ encountering a $\mp Q_{DW}$ the attractive magnetostatic interaction leads to a stabilization of the two domain walls at the junction vertex. In this position there are two oppositely charged charge density hot spots close to the corner shared between the two adjacent bars. Hence there is also a high exchange energy around this corner. Any further movement of the two domain walls into the junction would lead to a compression of the magnetisation and hence an increase in the exchange energy and so neither domain wall can move through the junction. This blockage is only lifted when a new domain wall nucleates at high fields switching a third bar.

In the case of a honeycomb vertex the bar configuration naturally leads to a domain wall being trapped at the vertex. After the application of an external field applied along the direction of the horizontal bars this trapped domain wall sits between the two diagonal bars. If we consider the configuration in figure 4.8(c) there is a negative charge hot spot situated at the junction of the two diagonal bars which will interact repulsively with the narrow, negatively charged, end of the transverse down domain wall propagating along the horizontal bar. As discussed above it is favourable, in terms of the exchange energy, for the domain wall moments to align with one of the diagonal bars, in this case the upper diagonal bar, however this would push the negatively charged end of the domain wall closer to the negatively charged hot spot of the trapped domain wall. Adopting a similar

argument as made in the publication of O'Brian *et al.* [96] in the repulsive case leads to the conclusion that it is likely that the trapped domain wall gets pushed out of the vertex switching the -60° bar.

Despite the ambiguity in exactly what mechanism leads to the chiral dependent switching rules it is clear that the results observed here can be understood by combining the extensive artificial spin ice research with that related to domain wall propagation in ferromagnetic nanowires.

Similar OOMMF simulations on 36 nm thick and 100 nm wide bars show that vortex domain walls follow equivalent rules (Simulated by S.K. Walton). An anticlockwise (clockwise) vortex switches the upper (lower) diagonal bar (see 4.10 (a)-(d)). The result of the mapping of the reversed chains of a 36 nm artificial spin ice, SHC2T, can be seen in figure 4.10 (e)-(f). However the 1-Tailed binomial test does not reject the null hypothesis of a random walk within a significance level of 5 %.

Despite the statistical evidence suggesting that the magnetic reversal of PHC0-2, SHC1 and SHC2 might be governed by simple chirality based rules, there are three aspects of the measurement and samples which can have a major contribution on the domain wall movement through the artificial spin ice vertices:

- Field misalignment
- Systematic fabrication imperfections
- Walker breakdown

Field Misalignment

Field misalignment in the y direction will lead to an asymmetric path distribution. The Zeeman force would result in the domain walls preferentially being pushed into the diagonal bar most aligned with the field offset, leading to a 100 % selectivity. The experimental set up in both cases , the STXM and the PEEM leave room for misalignment. In the STXM the sample is mounted between the two poles of an electromagnet. The alignment of the

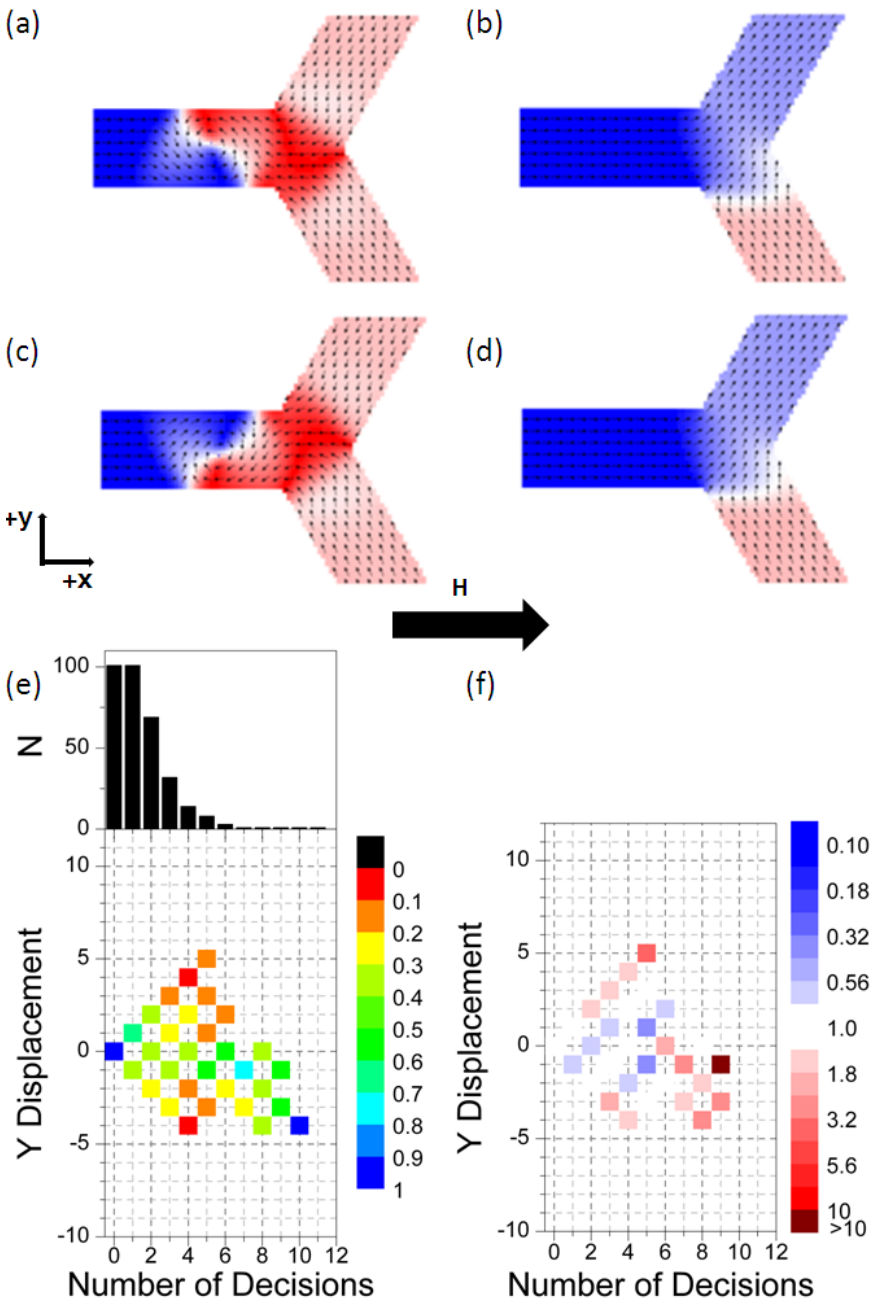

Figure 4.10 Simulation and Experimental data of 36 nm thick artificial honeycomb spin ice. OOMMF simulation of (a)-(b) an anticlockwise vortex domain wall (c)-(d) a clockwise vortex domain wall moving through a vertex, approaching the vertex from the horizontal bar. An anticlockwise wall results in the subsequent switching of the upper diagonal bar and a clockwise domain wall switches the lower diagonal bar. Simulation by S.K. Walton. (e) Distribution of observed magnetic charge paths during 180 degree magnetic reversals in SHC2T (see legend at the right hand site for values of N_y/N). (f) Data normalised by the number of observations expected assuming random walk, $N_{P,y}$. (see legend for colour code)

two is done by eye, hence an offset from a perfect alignment of up to five degrees is a reasonable assumption. However simulations showed that a change in the switching behaviour in the above described manner only takes place at angles above $\pm 10^{\circ}$ (see figure 4.20). In the PEEM set up the sample sits on a sample holder and a field is applied via a coil wrapped around a 'C' shaped iron core piece situated underneath the sample. This leads to a position dependent magnetic field strength and direction ambiguity. The strength of the magnetic field was calibrated by comparing the current that needed to be applied to the coil to switch an equilateral triangle of length 1 μm to the observed magnetic field needed to switch a triangle of the same dimensions measured via STXM. The error in the current to field conversion of the novel sample holder was estimated to be around 1 mT. The field misalignment is dependent on the exact mounting of the sample on the sample holder and the position of the array on the substrate. The artificial spin ice arrays PHC0, PHC1 and PHC2 are seen to reverse their magnetisation in a sharp manner, within 5 mT. Only a slight step around the coercive field, as expected for a 180° reversal in agreement with previous publications by Daunheimer *et al.* [37], was observed. This is a good indication that the field is not significantly misaligned. Furthermore, long cascades of reversed chains which transversed in both directions are readily seen in the same image; Significant field misalignment would result in the domain wall being restricted to propagate along the direction of the misalignment.

In comparison, the reversal of PHC3 shows a large asymmetry between the occurrence of (2,+2) and (2, -2) chains (50:3) (a mapping of the reversal can be seen in figure 4.11 (b) together with a numerical breakdown of the data 4.11 (c)). The PHC3 data shows a clear field misalignment. PHC3 is situated on the same substrate as PHC0-2 and was measured in the same run as the latter arrays. However whereas PHC0, PHC1 and PHC2 are situated within the same writefield, positioned between the gap of the 'C' shaped core pieces, PHC3 was displaced by 600 μm in the positive y-direction from the other three arrays. PHC3 was situated far enough away from the gap of the iron core to experience field lines at an angle to its horizontal bars; The angle is estimated to be bigger than 10°.

A misalignment of this order was observed to diminish any subtle domain wall chirality effects. The magnetisation versus field plot (see figure 4.11(a)) in conjunction with the fact that long chains are observed in both the +y-direction and the -y-direction lead to the conclusion that in PHC0, PHC1, PHC2, SHC1, SHC2 and SHC2T the field is not misaligned to such a degree that the chirality rules are negated.

Systematic Fabrication Imperfections

A systematic fault in the bars of the artificial spin ice arrays, for example one set of bars being thinner or wider than the other two, could also lead to the lifting of the symmetry of the vertex. Figure 4.12 (a)-(d) show AFM images of PHC2, SHC1, SHC2 and SHC2T. Small fabrication defects are observed, mainly small lumps of permalloy on the surface of bars and in the case of SHC2T imperfect lift off on some vertices, however the defects are not systematic and appear randomly. The influence of the imperfections will affect the travel of the domain wall through the bars but cannot account for long unidirectional chains.

Walker Breakdown

Walker breakdown refers to the stochastic change of chirality of a domain wall propagating along a nanowire above a critical field, the Walker field, H_W [53], [51]. There are three regimes associated with Walker breakdown which are dependent on the external field strength. In a field below H_W the domain wall propagates without deformation at a constant speed. As the external field increases the propagation speed increases linearly until H_W. Above H_W a transverse domain wall undergoes a periodic chirality change from up to down and back to up via the formation of intermediate antivortex states ($1 < H_{external}/H_W < 5.5$). In the field region $H_{external}/H_W > 5.5$ the chirality changes irregularly via multivortex and multiantivortex states [97], [98]. Theoretical calculations predict the critical field above which Walker breakdown occurs in 18 nm thick and 150 nm wide permalloy wires to be $\sim$0.5 mT and $\sim$0.4 mT in the case of 200 nm wide wires [99]. This would place our structures well in the third Walker breakdown regime. According

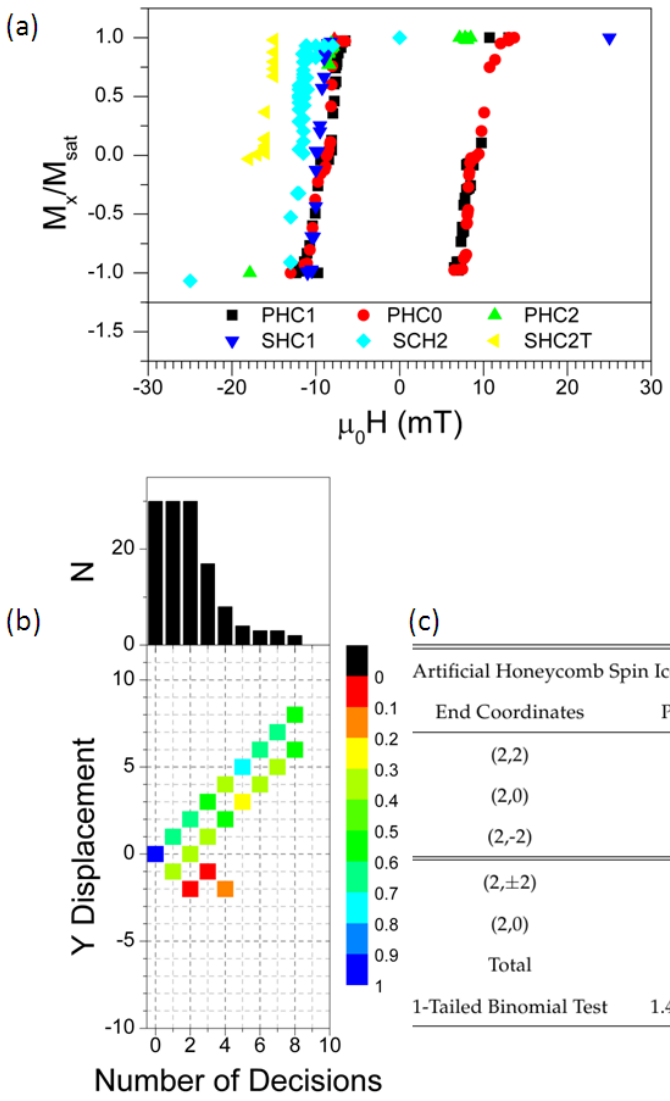

Figure 4.11 External field strength and direction dependence on magnetic reversal of artificial spin ice. (a) Plot showing the magnetisation versus μ_0H. The normalised magnetisation was calculated by summing the number of bars with a particular STXM magnetic contrast. (b) Distribution of observed magnetic charge paths during a 180° magnetic reversals in permalloy artificial honeycomb spin ice with large field misalignment $> 10°$ (PHC3). The isolated charge carrier path displacement in the y direction, in the direction perpendicular to the applied field, is recorded as a function of chain length or number of decisions (x-coordinate). The displacement changes by $\Delta y = \pm 1$ at each decision point. The histogram (top) shows the total number of chains (N) observed at any given number of decisions. (c) The numerical breakdown into chains of length x=2. Large asymmetry in the y displacement is attributed to field misalignment.

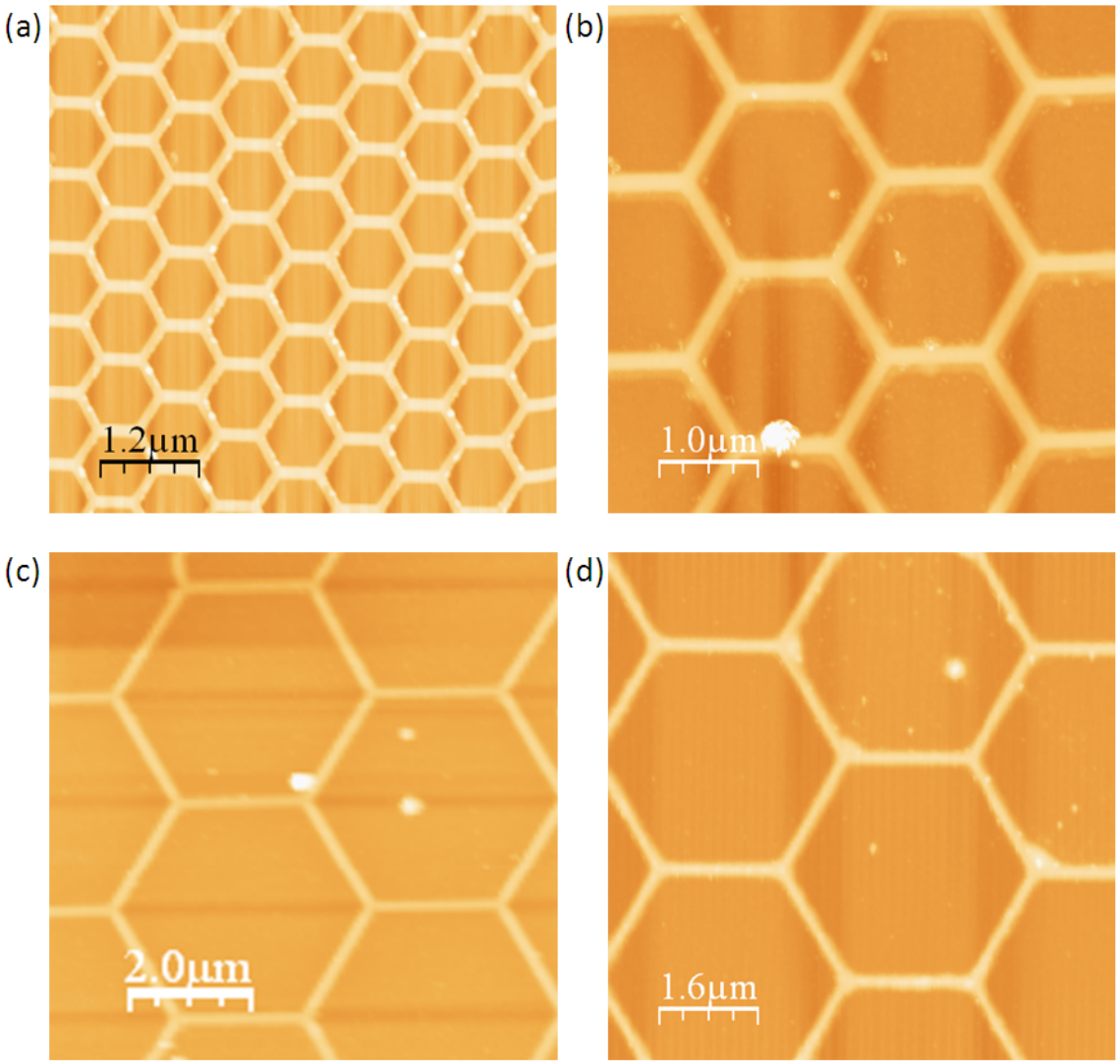

Figure 4.12 AFM images of the artificial spin ice arrays investigated. (a) PHC2, (b) SHC1, (c) SHC2 and (d) SHC2T.

to experiments there is a initial length of travel, the fidelity length, before the breakdown starts occurring. The fidelity length is field dependent [100]. For 90 nm wide 12 nm thick wires in a field of strength 10 mT the fidelity length was measured to be $\sim 0.4 \mu$m. Therefore, in the honeycomb artificial spin ice arrays measured the distance traveled between vertices is longer than the fidelity length leading to a suppression of a 100 % selectivity due to simulated chirality rules. It is quite remarkable that a selectivity of 72 % in case of the 1 μm bars and 58 % for the 2 μm arrays is observed.

4.3 Injection of Domain Walls into Artificial Spin Ice

The magnetic switching of artificial spin ice at present is dominated by random domain wall nucleation at the array edges. The chirality of the domain walls is unknown and the switching fields are stochastic in nature. The controlled injection of domain walls could enable a harnessing of the deterministic nature of the domain wall chirality. It would allow the study of individual cascades and possibly lead to the creation of ice rule violations in the early stages of the reversal. The first step on the way to such a control is to achieve controlled domain wall nucleation and injection and the second step would be to nucleate domain walls of a certain chirality. This section will address the former.

The effect of soft pads connected to an artificial spin ice array was investigated for permalloy artificial spin ice arrays PHC0, PHC1, PHC2, LHC1, LHC2, SHC0, SHC1, SHC15 and SHC15T. See table 4.1 in section 4.1 for a summary of the bar dimensions. Typical low field magnetic reversal of artificial spin ice arrays with uniform bar thickness, length and width throughout the array can be seen in figure 4.13 (a)-(c). Figure 4.13 (a) and (b) show STXM images of SHC1. The images were taken at remanence after initial magnetic saturation in the x-direction (at +25 mT) and subsequent application of -11.5 mT. White colour contrast represents a magnetisation in the +x-direction and black colouring of the bars indicates a magnetisation in the -x-direction. In figure 4.13 (a) it can be seen that the injection pad has switched and a domain wall nucleated from the edge, not connected to the pad, passed through five bars of the array reversing the magnetisation of the connected bars in its wake. In a subsequent reversal, after saturation, the soft pad has switched and injected a domain wall into the array (see figure 4.13(b)). However due to the large field steps chosen the following scenarios cannot be distinguished:

- The injected tail to tail transverse domain wall propagated into the upper diagonal bar and then caused the reversal of the next horizontal bar and the reversal of the edge diagonal bar via a head to head transverse domain wall.
- The pad injected a tail to tail transverse domain wall at the same field as a tail to tail

domain wall nucleated from the edge meeting the horizontal bar.

The soft pads were measured to switch at a field of 4.5±0.5 mT. The depinning of the domain wall nucleated from the pad into the array and the nucleation of the edges occurred at 8±1 mT. However the large field steps in the STXM measurements made it impossible to unambiguously determine if edge nucleation occurred before, at the same field or after the domain wall nucleated from the pad depinned into the array.

Figure 4.13 (c) shows a LTEM image of LHC1 taken at remanence after initial saturation in the +x-direction and a subsequent application of -24 mT. The order of the black and white contrast of each bar holds the magnetisation information and is depicted in figure 4.13 (d) as a colour code (blue and red indicate a magnetisation in the -x-direction and +x-direction respectively). The low field reversal of LHC1 shows the occurrence of edge nucleation and the depinning of the injection pad domain wall at -23 mT.

Typical XMCD contrast obtained by the PEEM at the DIAMOND light source on artificial honeycomb spin ice arrays consisting of 500 nm long bars can be seen in figure 4.14 for sample PHC1 and PHC2. A large saturation field along the horizontal bars was applied followed by subsequent application of a field at 180° in 0.15 mT steps. Figure 4.14 (a) shows that at -6.50 mT the injection pads have injected a domain wall into the connective horizontal bar and depinned into the first diagonal bar of the array. However 14/ 62 edge diagonal bars have reversed as well. After the application of -7.15 mT a long chain of bars has reversed which has not depinned from the injection pad (see figure 4.14(b)). The magnetic reversal of PHC2, however, shows that magnetic reversal of a longer chain spanning nearly the entire length of the array, originating at the depinning sites of the injection pads, occurred before any equivalently long chains originating at the edges are observed (see figure 4.14(f)). This indicates that the field range in which the magnetic reversal occurs via chains originating at the injection pad depinning sites and the field range at which the reversal is initiated via domain walls nucleated at the edge, is of the same order.

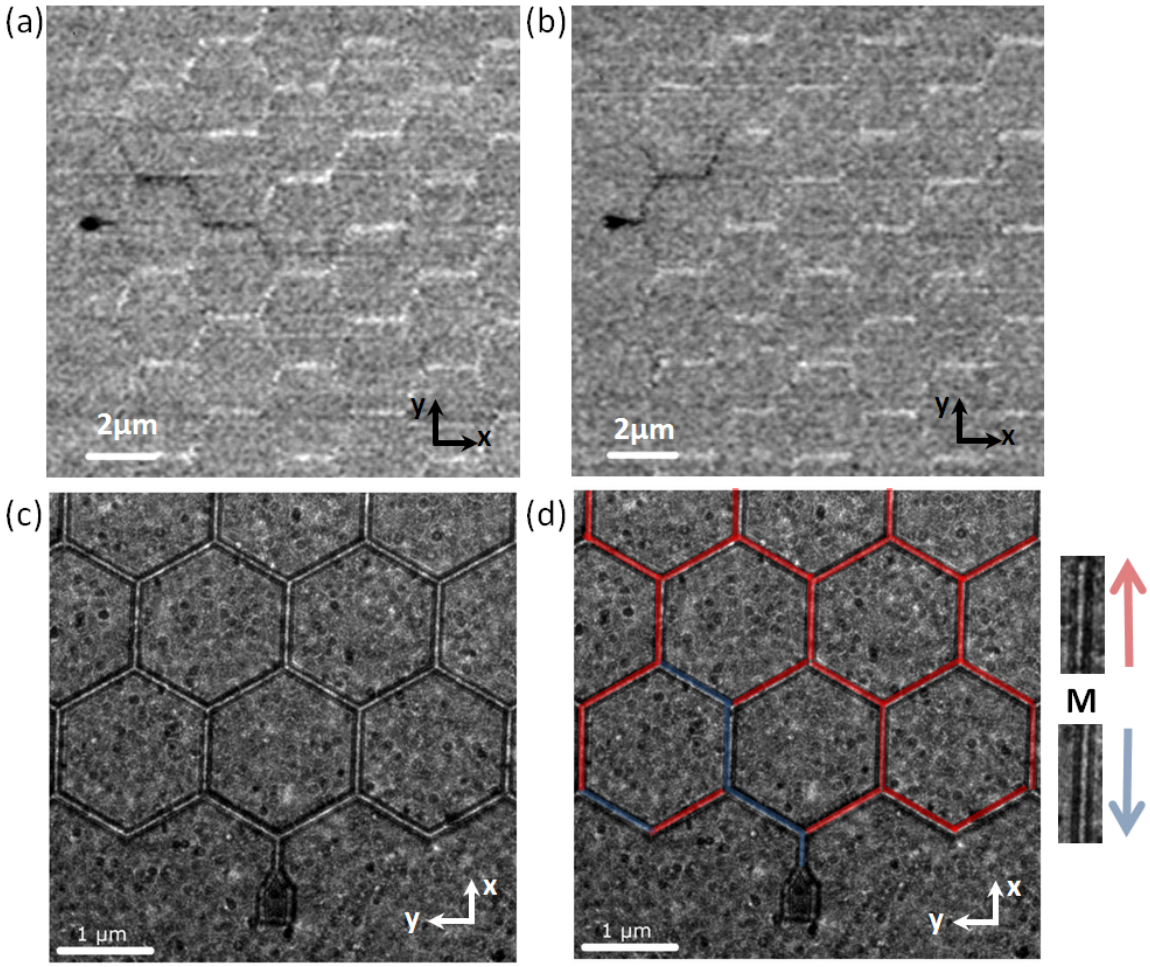

Figure 4.13 STXM and TEM images of artificial spin ice arrays. (a) shows a scan of SHC1 taken at -11.5 mT after initial saturation (25 mT) in the x-direction (b) image taken of the same area as in (a) after saturation at +25 mT and subsequent reapplication of -11.5 mT. Domain wall nucleation occurred at the same fields as the domain wall injection of the polygonal pad. Bars magnetised along +(-)x-direction appear white (black). (c) Lorentz TEM image of THC1 taken at a defocus of +1 mm after magnetic saturation in the +x-direction and the subsequent application of -24 mT (tilt -15°). (d) schematic depicting the magnetic information of (c); the blue areas indicate the reversed bars. A domain wall has been injected from the pad into the array however nucleation of a domain wall from the edge occurred in the same field step.

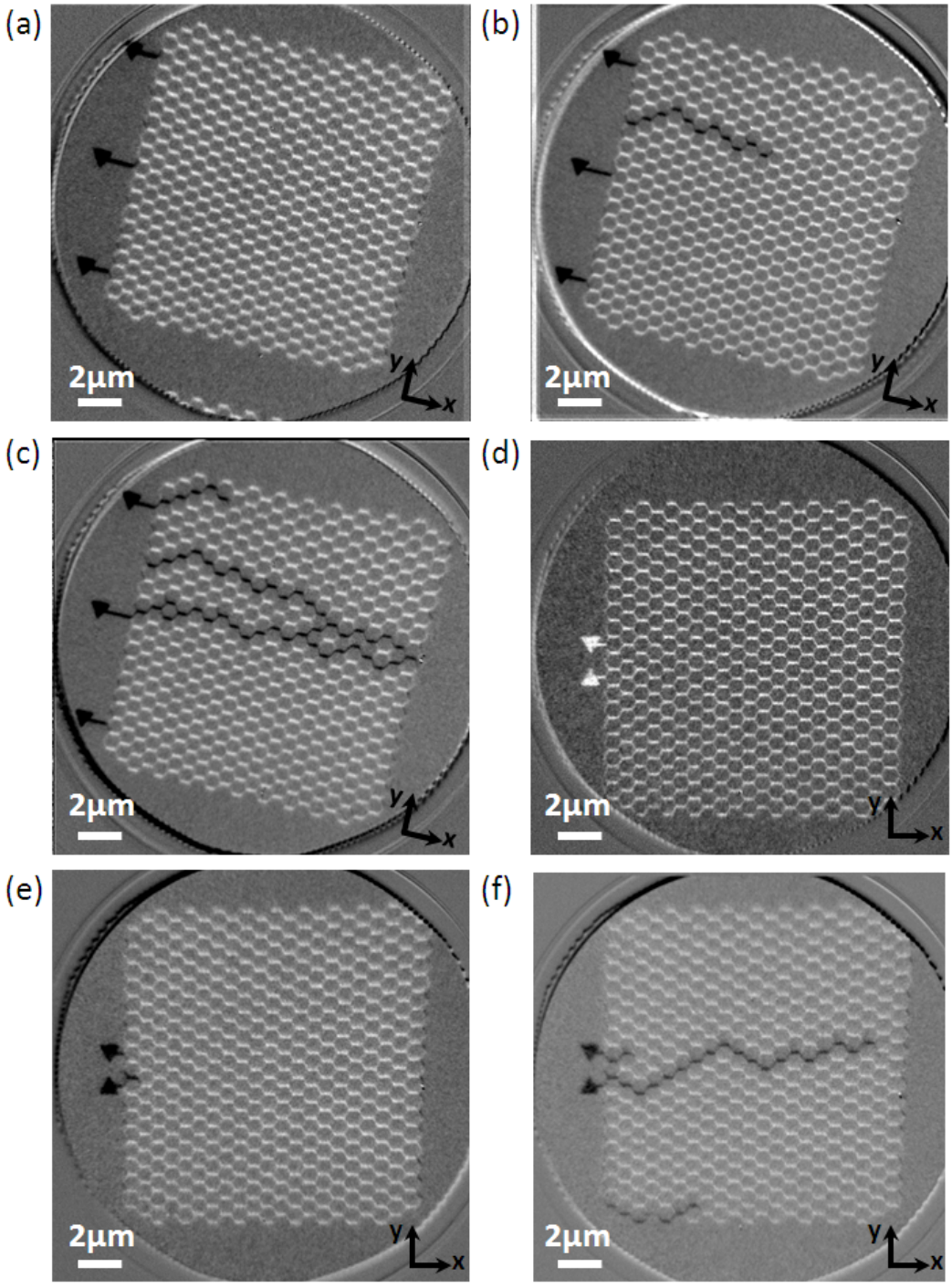

Figure 4.14 XMCD images of artificial honeycomb spin ice arrays. The magnetic reversal was studied after initial saturation at 13.25 mT. All images were taken at remanence. PHC1 after application of (a) -6.5 mT (b) -7.15 mT (c) -7.50 mT. PHC2 after application of (d) +16.25 mT. (e) -8.13 mT (f) -8.50 mT (f). Edge nucleation was always seen to occur in the same field range as the injection of a domain wall from the nucleation pad. The lowest field applied after saturation was 6.50 mT.

The normalised magnetisation versus the external magnetic field extracted from the reversal of PHC1 can be seen in figure 4.15(a). For comparison, the reversal of an identical array without any injection pads (PHC0) is plotted as well. The triangular pads have completely switched at -5.50 mT and a domain wall depinned into the horizontal bar between -6.50 mT and -7.00 mT. A close up of the early magnetisation reversal (see figure 4.15(b)) shows that presence of the injection pads leads to a switching at lower fields; the magnetic reversal starts roughly 0.9 mT earlier. Injection pads lead to an increased likelihood of observing the reversal of long chains at low fields originating in the vicinity of the pads. Despite the similar fields between injection of the domain wall nucleated in the soft pad into the artificial spin ice array and the domain wall nucleation at the edge, the injection pad has a controlling effect on the reversal.

Figure 4.15(c) shows the normalised magnetisation versus external field curves extracted from the image series taken during the magnetic reversal of PHC1, SHC1, SHC15 and SHC15T. The light gray shaded area indicates the field range in which the soft pads switch. The coercive fields of all arrays are listed in table 4.3. A comparison between the coercive fields between LTEM, STXM amd PEEM was not qualitatively possible as the magnetic field strength in the vicinity of the sample of the three measurement techniques was not cross-calibrated. Furthermore, different substrates, optimised for each technique, were used leading to possible differences in the wire roughness. The roughness of magnetic features on the nanometer scale has an influence on the magnetic switching [78], [101]. Surprisingly, SHC15 is roughly 3.5 mT harder than SHC1, this is most likely due to imperfect lift off of the hexagons leading to domain wall pinning sites (see figure 4.16(a)-(b)). AFM images of SHC15T show the inhomogeneous thickness of edge bars which makes the data acquired on this array unsuitable for the purpose of this investigation (see figure 4.16(c) and (d)).

Figure 4.17 shows LTEM images of an artificial spin ice array (LHC2) where all edge hexagons along the y-axis are connected to polygonal injection pads. The LTEM images were taken at remanence after initial saturation at -24 mT in the x-direction and subsequent

application of a field in the +x-direction in 1 mT steps. At a field of 16 mT all the pads have injected a domain wall which depinned into the -60° (with respect to the x-axis) bar (4.17(a) and the corresponding image with a colour contrast overlay (b)). A long chain of reversed bars can be seen at 22 mT (4.17(c) and the corresponding image with a colour contrast overlay (d)). From this it can be seen that even though the depinning of the domain wall nucleated from the pads happens at 4.5±1 mT, long chains of reversed bars only occurs at 14±1 mT; a field nearly a factor of 3 larger.

The normalised magnetisation versus the external magnetic field is shown in figure 4.15(d). The light gray shaded area indicates the field range in which the magnetically soft pads switch (9 mT<μ_0H<10 mT), the dark gray shaded area indicates the field range in which the nucleated domain wall switches the first diagonal bar of the array (11.5 mT<μ_0H<14.5 mT) and the rose shaded area indicates the field range in which the domain wall was seen to be pushed through the first artificial spin ice vertex resulting in the switching of the array via long cascades (17.5 mT<μ_0H<19.5 mT).

In a simplistic view, ignoring the particular artificial spin ice geometry, the nucleation field will depend on the thickness to width ratio of the wire t/w [82]. However, if one magnetically saturates the honeycomb spin ice along the long axis of the horizontal bars and then applies an external field, equivalent to the average coercive field of the individual bars, in the opposite direction, one would find that the likelihood of not observing a switching event is quite high.

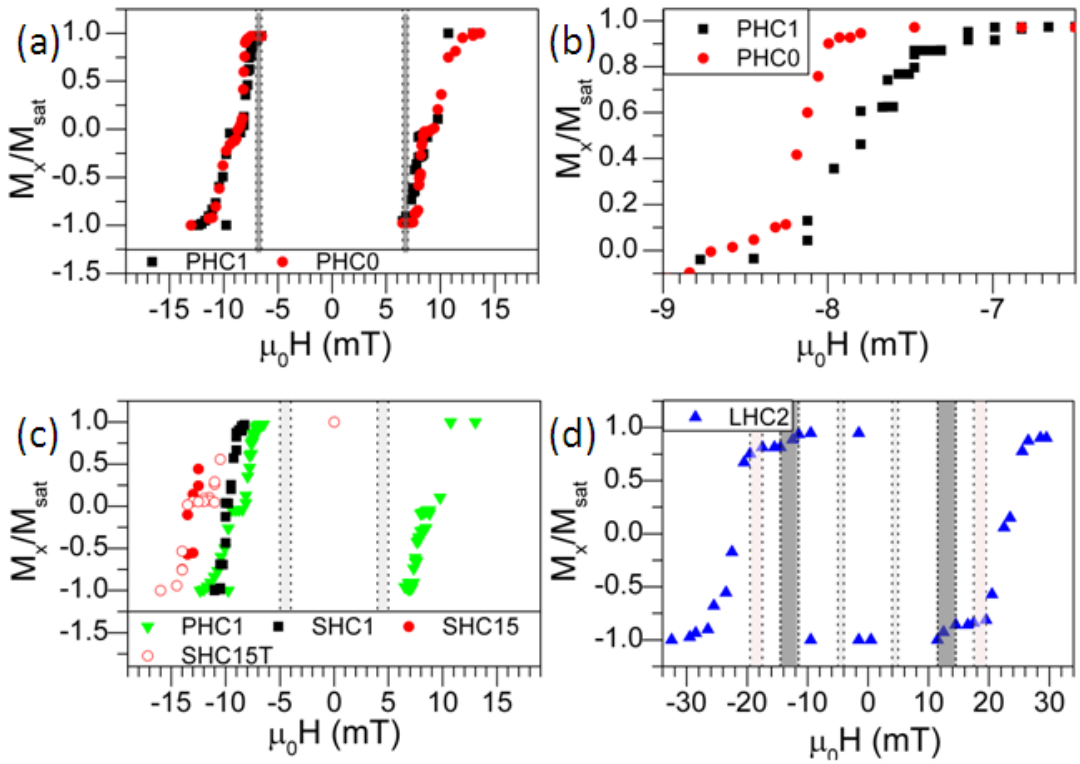

Figure 4.15 Magnetisation versus external field curves extracted from STXM, PEEM and LTEM (a) Magnetisation versus external field extracted from the reversal of PHC1 (three injection pads) and of PHC0 (no injection pads). The dark gray shaded area marks the pad reversal and subsequent depinning of the domain wall into the array. (b) Difference in the early stage reversal of the array with injection pads (PHC1) and without pads (PHC0). Injection pads lead to switching at lower fields. (c) Magnetisation versus external field extracted from PHC1, SHC1, SHC15 and SHC15T. Light shaded areas mark the field range in which the soft pads reverse. (d) Magnetisation versus external field extracted from LTEM images of the magnetic reversal of LHC2 (polygonal pads at all edges). The light gray areas mark the field region in which the pads switch, the dark gray areas mark the switching of the first diagonal bars and the rosa area marks the propagation of the injected domain walls into the first horizontal bar of the array leading to the formation of reversal chains.

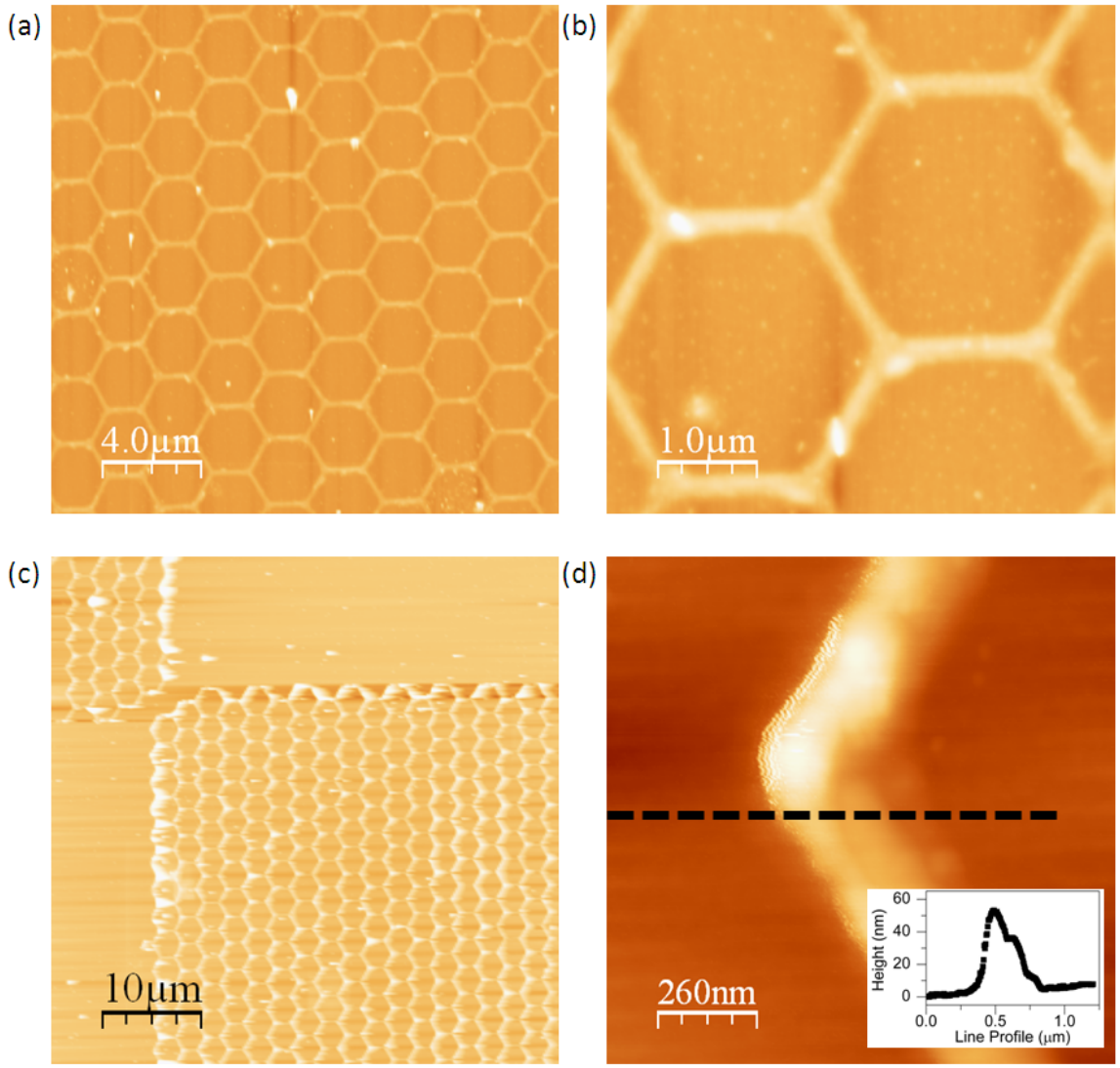

Figure 4.16 AFM images of SHC15 and SHC15T. Area scans of SHC15 (a) 20 μm x 20 μm and (b) 5 μm x 5 μm. Imperfect lift off of the individual hexagons lead to magnetic pinning sites reflected in the large coercive field of SHC15. Area scans of SHC15T (c) a 50 μm x 50 μm scan and (d) a 1.28 μm x 1.28 μm scan taken at the edge. The insert shows the height profile taken across the bar at the black dotted line. Imperfect lift off at the array edges lead to an inhomogeneous height distribution of the edge bars.

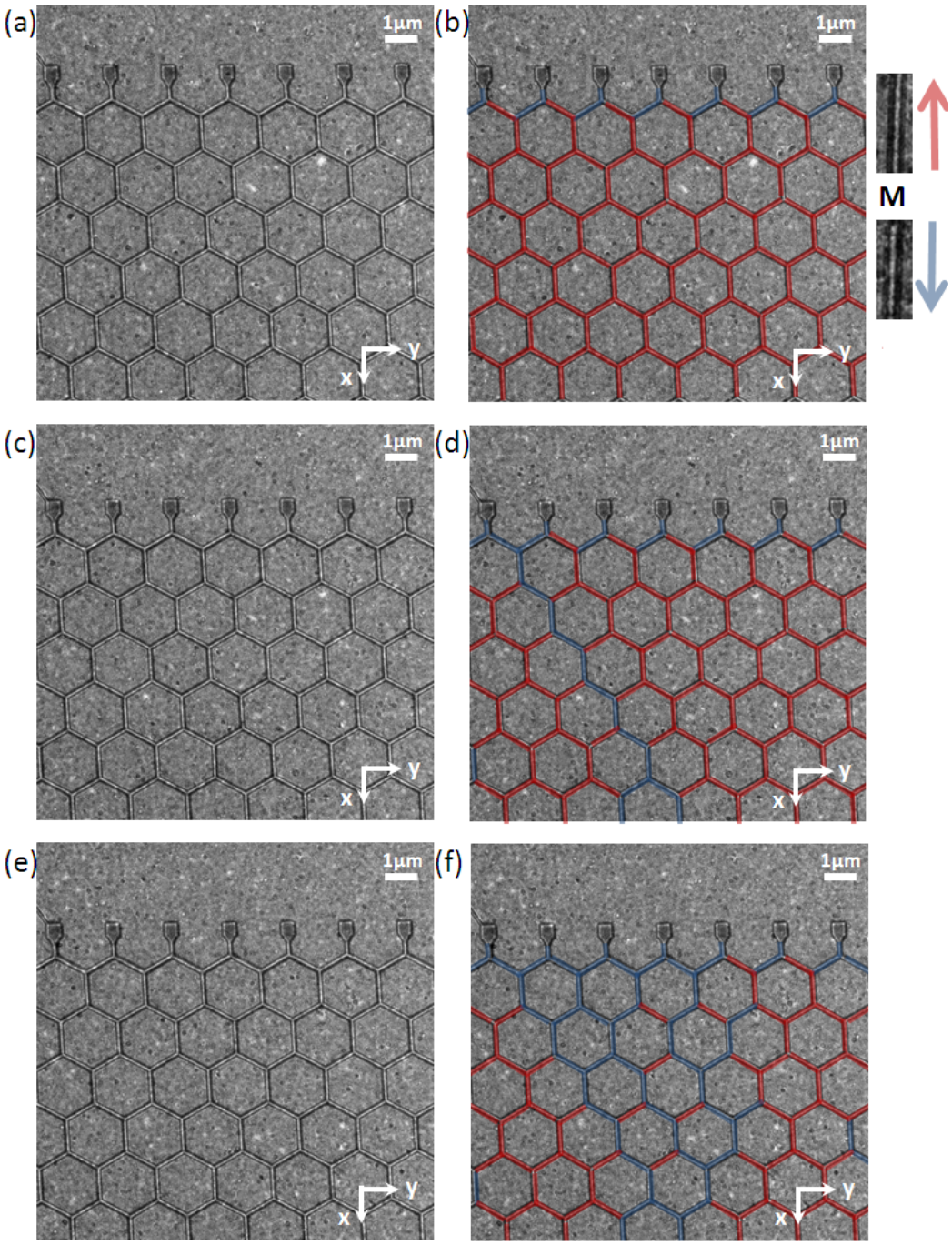

Figure 4.17 Lorenz TEM image of artificial spin ice arrays with polygonal injection pads at the edge (LHC2). (a) Image was taken at a defocus of +1 mm after magnetic saturation in the x-direction at -24 mT and the subsequent application of 16 mT (tilt 10°). (b) Magnetisation of (a) colour-coded. All injection pads injected a domain wall which switched the left bar. (c) after application of 11 mT (tilt 22°). (d) Magnetisation of (c) colour-coded. A tail to tail domain wall switched a long chain of bars into the array. (e) Image taken after the application of 24 mT (tilt 15°). (f) Magnetisation of (e) colour-coded.

The Coulombic charge model predicts a critical field H_C limiting the magnetic reversal. H_C is the field required to separate a $\pm 2q$ from a $\mp q$ vertex. Consequently, it is also the field at which a domain wall is pushed towards a like charged vertex $\pm q$ which could lead to a ice rule violation state of charge ± 3. However, as the domain wall is pushed closer and closer to the like charged vertex, the two charges experience a repulsive force of strength $2H_C$ [43]. The total magnetic force acting on the diagonal bar of the vertex is then $3H_C \cos 60^\circ = 1.5H_C$ [43]. Therefore, the diagonal bar switches and an ice rule violation state cannot be stabilised. In the pure magnetic charge model, ice rule violations are only allowed to occur if there is a large fluctuation (>$1.5H_C$) in the switching field of the individual bars due to fabrication imperfections. The separation of a domain wall $\pm 2q$ from a vertex, if said separation results in the creation of a vertex with charge $\mp 3q$, is not observed, as this would require a separation field field of $3H_C$. Hence in the 180° reversal diagonal bars switch before the horizontal ones.

Room temperature 180 ° magnetic reversal studies show that the artificial spin ice arrays switch via nucleation of domain walls at the edge which then propagate through the array. The nucleation of a domain wall at the edge was observed to occur at a field lower than H_C. Domain wall nucleation is a statistical process greatly influenced by local imperfection, composition changes and pinning sites. Adding injection pads to every edge eradicates a large percentage of the randomness from the switching process. The rose shaded area, highlighted in figure 4.15(d), can be identified as the critical field needed to separate a domain wall of charge $+2q$ from a $-q$ vertex with a mean value of $\mu_0 H_C = 18 \pm 1$ mT; A vertex of charge $-q$ is left behind while the domain wall propagates down the horizontal bar. Using this the switching field of the first diagonal bar is expected to be at $\mu_0 H_C / 1.5 = 12.0 \pm 0.7$ mT which agrees very well with the observed mean value of 13 ± 1.5 mT.

Frustration in artificial spin ice has a crucial effect on the magnetic switching. Hence, the increased likelihood in observing long chains in the early stages of the reversal due to the addition of injection pads observed in arrays PHC1and PHC0 is surprising. The

occurrence of reversal cascades is limited by the field needed to separate a $\pm 2q$ from a $\mp q$ vertex which is irrespective of the field needed to nucleate a domain wall. A possible reason for observing the early onset of cascades could be the stray field of the pads slightly lowering H_C in its vicinity.

However, an exclusive switching induced by the injection pads was not observed; Domain wall nucleation at the edges randomly occurred at the same fields. The functional window for injection from the injection pads of the arrays studied thus far is currently very narrow $\sim$2 mT. Modern nanofabrication techniques allow the widening of this window for example by suppressing edge nucleation by decreasing the width of the edge bars.

Artificial Honeycomb Spin Ice Arrays			
Sample	Substrate	H_C	One Carrier Injection
PHC1	Silicon	8.1$\pm$1.0 mT	0/20
LHC2	30 nm Si_3N_4 membrane	21.4$\pm$0.2 mT	Not conclusive
SHC1	50 nm Si_3N_4 membrane	9.8$\pm$0.3 mT	0/6
SHC15	50 nm Si_3N_4 membrane	13.4$\pm$0.3 mT	0/15
SHC15T	50 nm Si_3N_4 membrane	12.0$\pm$0.4mT	0/5
SHC0	50 nm Si_3N_4 membrane	10.6$\pm$0.3 mT	7/7

Table 4.3 Table summarizing the switching fields and the successful injection of a domain wall before edge nucleation of the artificial spin ice arrays PHC1, LHC2, SHC1, SHC15 and SHC15T.

An advantage of modern nano-fabrication techniques is the manipulation of the switching fields of ferromagnetic nanowires by changing their width to thickness ratio. This can be utilised to achieve 100 % domain wall injection suppressing domain wall nucleation from the edges without pads. If one makes the outer edge wires thinner and hence increases their switching field sufficiently, long single chains of reversed bars originating from the injection pad can be observed (see figure 4.18(a) and (b)). The magnetisation

versus applied field curve clearly shows that the pad causes a domain wall to depin into the array (light grey shaded region) before edge nucleation occurs (red shaded region) in the case when the edge bars width is 2/3 of the bulk width, roughly the ratio achieved in SHC0 (210/283). In this case the success rate of single magnetic carrier injection was 7/7. The nucleation from the diagonal bars is at a sufficiently high field in order to allow sole injection from the pad and the subsequent reversal through the first ice rule violation state. The thinner bars created a 3 mT window of opportunity.

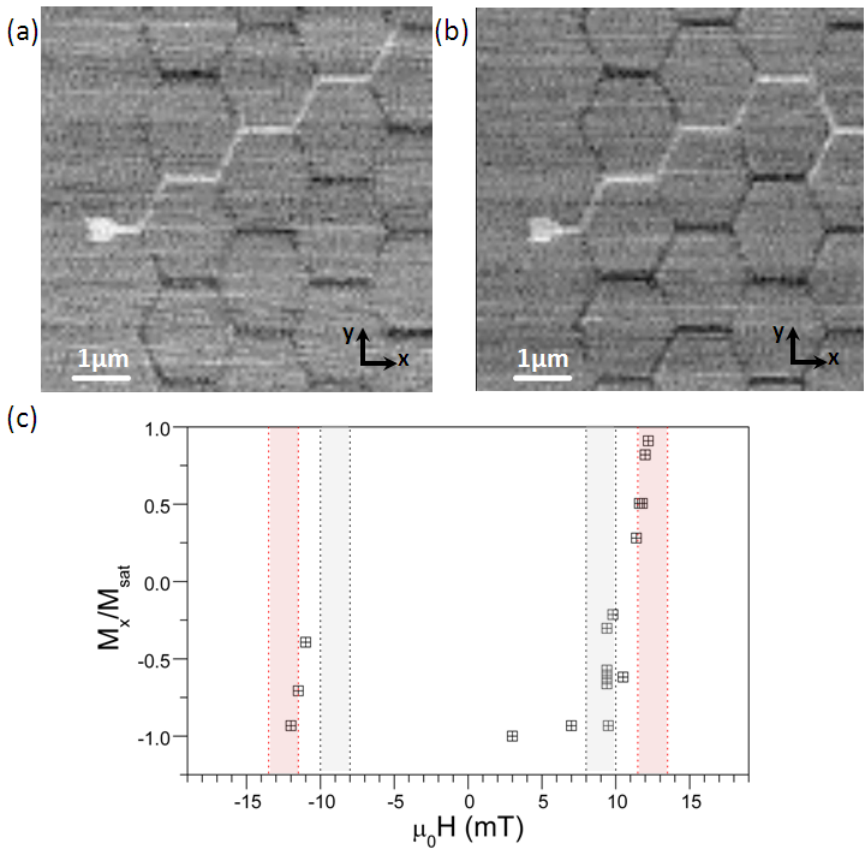

Figure 4.18 STXM images of the artificial spin with thinner edge bars, array SHC0. (a) Image taken at remanence after the application of 9.4 mT (b) Image taken at remanence after the application of 9.4 mT after saturation at -25 mT. (c) Extracted magnetisation plotted versus the external magnetic field. The gray shaded areas indicate the field at which the domain wall is successfully injected into the array. The red shaded area indicates the fields at which the edges nucleate a domain wall. As the edges switch at higher fields a 100 % success rate of injection can be achieved leading to long isolated chains.

4.4 OOMMF Simulations

The magnetic reversal of artificial spin ice arrays consisting of 100 nm wide, 18 nm thick and 1000 nm long wires was simulated using OOMMF for applied fields applied at angles between 0° (figure 4.19) and 10° (figure 4.20) to the +x axis. The following parameters were used: exchange stiffness $A = 1.4 \times 10^{-11}$ Jm^{-1}, $\alpha = 0.5$, $M_S = 800 \times 10^3$ Am^{-1} . The magnetic reversal was calculated using cell mesh of [x, y, z]=[5 nm, 5 nm, 18 nm]. The simulation evaluates the minimum energy configuration of the magnetic moments at each field step (every 5 mT) assuming 0 K.

Figure 4.19 shows selected steps through the 180° magnetic reversal of a permalloy artificial spin ice. The 0 K simulation showed that the random edge nucleation happens at fields between 55 mT<μ_0H<60 mT. As observed in the experimental injection data, the pad was seen to be considerately softer than the artificial spin ice array. A field between 30 mT<μ_0H<35 mT was needed to push the domain wall through the first ice rule, resulting in the switching of the first diagonal bar (see figure 4.19(d)). The domain wall is absorbed into the next vertex changing the vertex charge from $-q$ to $+q$. Despite the different field strength, this is in compliance with the room temperature reversal data. However, simulations show that the fields at which the half switched vertex undergoes complete reversal by nucleating a second domain wall switching the remaining diagonal bar, are lower than both the mean field required to push a domain wall from the $+q$ vertex into the first horizontal bar and the fields needed to nucleate a domain wall from the edges (see figure 4.19(e)). This results in the branching observed in the simulations. Experimentally, this branching was predominantly observed in the second half of the reversal at much higher fields and was less likely to be seen at low fields. Instead long cascades of reversed bars were observed until fields higher than the coercive field were applied and the cascades were seen to change propagation direction. Simulating individual vertices indicates a controlling effect of the domain wall shape, chirality, on the propagation direction. This subtlety seems to be suppressed in simulations of large arrays.

According to Mellado *et al.*'s charge model the field at which a $+2q$ charged domain wall is expected to be pulled away from a $-q$ charged vertex, is expected to be around 49 mT. The simulation showed that between 50 mT<μ_0H<60 mT domain wall nucleation at the edges occurred as well as the first horizontal bar switching (see figure 4.19(f)). The window of opportunity for injected cascades originating from the injection pad is narrow for both simulation and experiment but was shown to be tunable by modifying the edge bars.

A field misalignment of 10° is needed to observe avalanche chain like reversal returns (figure 4.20). However, the field misalignment restricts the domain wall propagation along the misalignment axis. Despite the suppression of branching the domain wall propagation was not observed to change direction (see figure 4.20(c)). Hence the long chains observed experimentally cannot be explained by misalignment as a direction change was readily observed. The misaligned field reduced the domain wall nucleation field by roughly 15 mT, narrowing the injection window even further. Field misalignment cannot, therefore, cause 100 % injection.

OOMMF simulations performed at 0 K are able to explain some of the trends of the magnetic reversal however there are crucial differences between the simulation and room temperature experiments. Restricting the simulation to a single vertex captures some of the discrepancies. A likely explanation between the simulation and experiment is the temperature difference of the two.

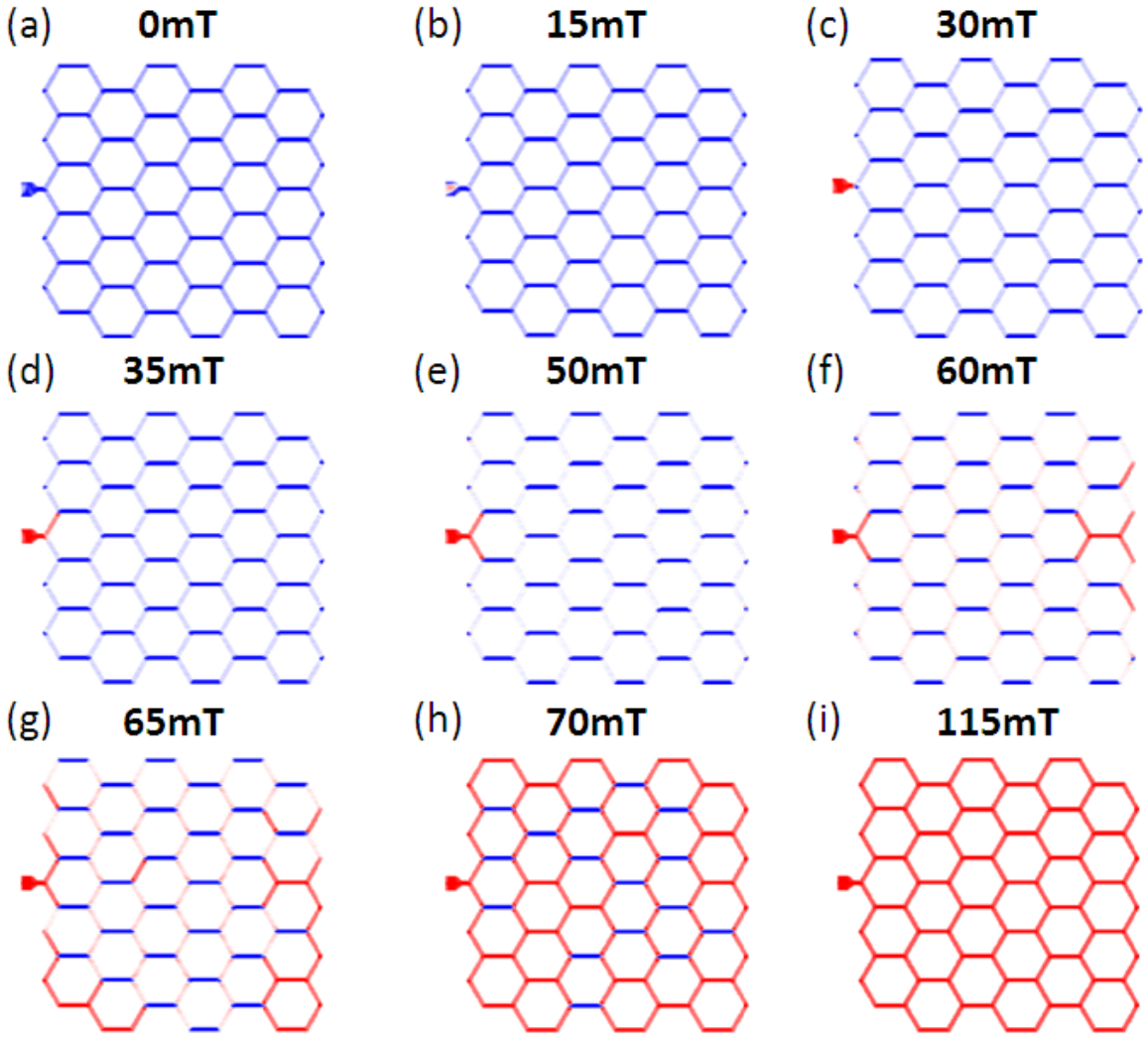

Figure 4.19 OOMMF simulation of the magnetic switching of a polygonal injection pad connected to an artificial spin ice array. (a) Magnetic state at 0mT after initial saturation in the -x-direction. (b) magnetisation of pad rotated such that the magnetic moments align with the external magnetic field, at 15mT. (c) At 30 mT the pad has switched and the depinned domain wall has switched the horizontal bar connecting the pad to the array, creating an ice rule violation state. (d) At 35 mT the injected domain wall switched the upper diagonal bar. (e) A new domain wall depinned from the injection vertex at 50 mT and switched the lower diagonal bar. (f) Domain walls are nucleated at the edges and propagate through the array (60 mT). (g) Nucleation of domain walls occurred in the array switching diagonal bars in their wake. (h) 86 % of the array has reversed leaving 16 ice rule violations (70 mT). (i) At 115 mT the whole array has reversed.

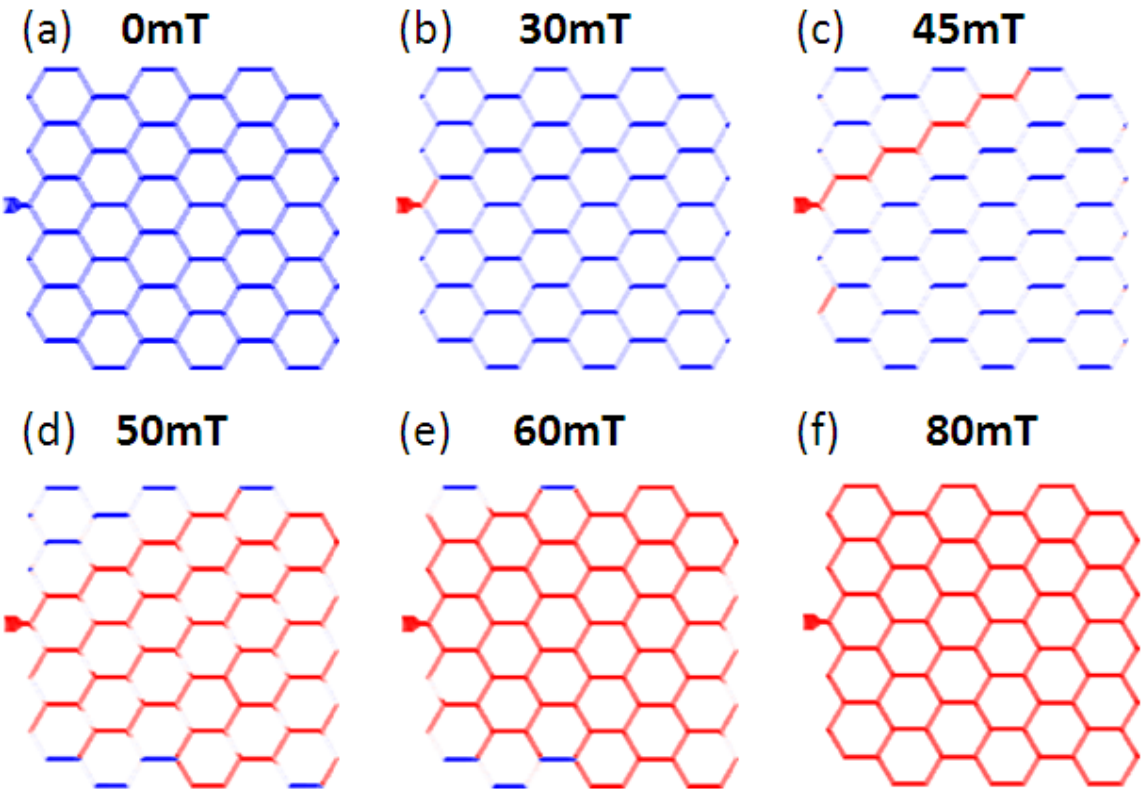

Figure 4.20 OOMMF simulation of the magnetic switching of a polygonal injection pad connected to an artificial spin ice array with a field applied at 10° to the x-direction. (a) Magnetic state at 0mT after initial saturation in the -x-direction. (b) At 30 mT the pad has switched and the depinned domain wall has switched the horizontal bar connecting the pad to the array and caused the switching of the upper diagonal bar. (c) At 45 mT a long diagonal chain of switched bars can be seen originating from the injection pad and nucleation of a domain wall with subsequent switching of a bar occurred. (d) By 50 mT long diagonal chains of switched bars are observed, a majority of the bars at +60° have switched in contrast to only three reversals in the -60°. (e) 88 % of the array has reversed apart from one ice rule violation and the edge bars, 60mT. (f) At 80 mT the whole array has reversed.

4.5 Conclusion

The room temperature 180° magnetic reversal of connected permalloy artificial spin ice was investigated using STXM, PEEM and LTEM. The propagation of domain walls through artificial spin ice arrays was observed to be not entirely random. OOMMF simulation suggest that the domain wall chirality has a deterministic effect on the propagation direction in the 180° reversal. At each vertex a transverse domain wall approaching the vertex from the horizontal bar was observed to be more likely to propagate into the up (down) diagonal bar if it is an up (down) chiral wall. Similarly, OOMMF simulations suggested that equivalent rules exist for vortex domain walls. This revelation is beyond the Coulombic charge model which assumes propagation of point magnetic charges.

Adding injection pads reduces the initial randomness of the magnetic reversal due to domain wall nucleation which is heavily influenced by fabrication defects and pinning sites. Furthermore, soft domain wall injection pads resulted in an increased likelihood of seeing long cascades early on in the switching. The cause for this observation is unclear but could be due to the stray field of the pads influencing the vertices in their vicinity. By thinning the edge bars, by a factor of 2/3, it was possible to overcome the bottleneck created by the first complete vertex before edge nucleation, due to the higher switching fields of the thinner bars, occurred. The domain wall injection pads combined with thinner edge bars widened the window of opportunity presented for injection before nucleation. The absence of the edge nucleation field randomness allowed the experimental measurement of the two critical switching fields predicted by the charge model [43].

The work in this chapter shows that the simple magnetic charge model is a powerful tool to describe artificial spin ice reversal under the application of an external magnetic field, however, it also reveals the limitations of the model by showing that the micromagnetic structure of the domain wall, as well as its charge, plays a role in determining the propagation. Considering the domain wall repulsion and attraction from the charged vertices determines the critical switching field, however any further switching is influenced

by the microscopic distribution of the magnetic moments.

Chapter 5

Magnetotransport of Two Dimensional Artificial Spin Ice

In this chapter the magnetotransport of honeycomb artificial spin ice is explored. In experiments, that predate this work, unusual low temperature transport was observed in cobalt honeycomb artificial spin ice arrays. The aim of this chapter is to investigate if this transport effect is generic to artificial spin ice systems and to further the understanding of its nature. In the cobalt data, a clear change in the magnetotransport symmetry was observed at 50 K. However, two open questions remained: (1) What are the deterministic factors of the temperature scale (2) What is the underlying transport mechanism causing the effect. Theoretical work from literature [32, 102] predicted that artificial spin ice structures will undergo a transition from a nearest neighbour ice structure to a second ice phase when further neighbour interactions become significant. The theory predicts a dependence of the transition temperature on the bar dimensions and on the square of the saturation magnetisation, leading to a predicted onset of this symmetry change of 17 K in the case of permalloy artificial spin ice structures. The onset of the field inversion asymmetry of the electrical transport was measured to be 15$\pm$2 K. The underlying cause of the asymmetry was proposed to be non random domain wall positioning across the entire array, causing the formation of low resistance current path towards the array edges.

Recent temperature dependent transport measurements in two dimensional cobalt honeycomb spin ice showed an unique temperature dependent feature below 50 K [3] (see figure 5.1). At temperatures below 50 K a Hall like asymmetry between the irreversible resistance change at positive fields and negative fields was observed (see figure 5.2(a) and (b)). This is an extremely unexpected development as artificial spin ice is comprised of nanoscale ferromagnets and as such the only critical temperature should be the Curie temperature. The Curie temperature of cobalt (1360 K [44]) is above room temperature and hence orders of magnitude higher than 50 K. However recent advances in the theory of two dimensional dipoles on a kagome lattice predict low temperature magnetisation order due to vertex dipoles which could help explain these unusual features [32, 102].

Möller and Moessner calculated a detailed phase diagram of two dimensional dipole system on a kagome lattice, taking into account deviation of the Ising approximation close to the vertex [102]. They identified a series of ordering regimes [102]:

1. The paramagnetic regime. Random distribution of Ising spins leading to a statistical distribution of vertices of charge $\pm q$ and $\pm 3q$ (see figure 5.3(a)).

2. The kagome ice I, $K1$, regime. The nearest neighbour interaction leads to a suppression of $\pm 3q$ configurations only $\pm q$ vertices remain (see figure 5.3(b)).

3. The kagome ice II, $K2$, regime. Interactions between vertices leads to magnetic charge order (see figure 5.3(c)).

4. Long range order. Completely charge and spin ordered state where six clockwise/ anticlockwise magnetised hexagons surround one none loop state (see figure 5.3(d)).

The above list is in order of increasing interaction strength, hence in order of decreasing energy and temperature. Möller *et al.* modeled the artificial spin ice by treating the macrospins as a Ising spin of length l, hence the magnetic moment density μ/l was assumed to be uniform along the length l [102]. Any deviation away from a perfect Ising spin was taken into account by the introduction of the dimensionless quantity $\varepsilon = 1 - l/a$,

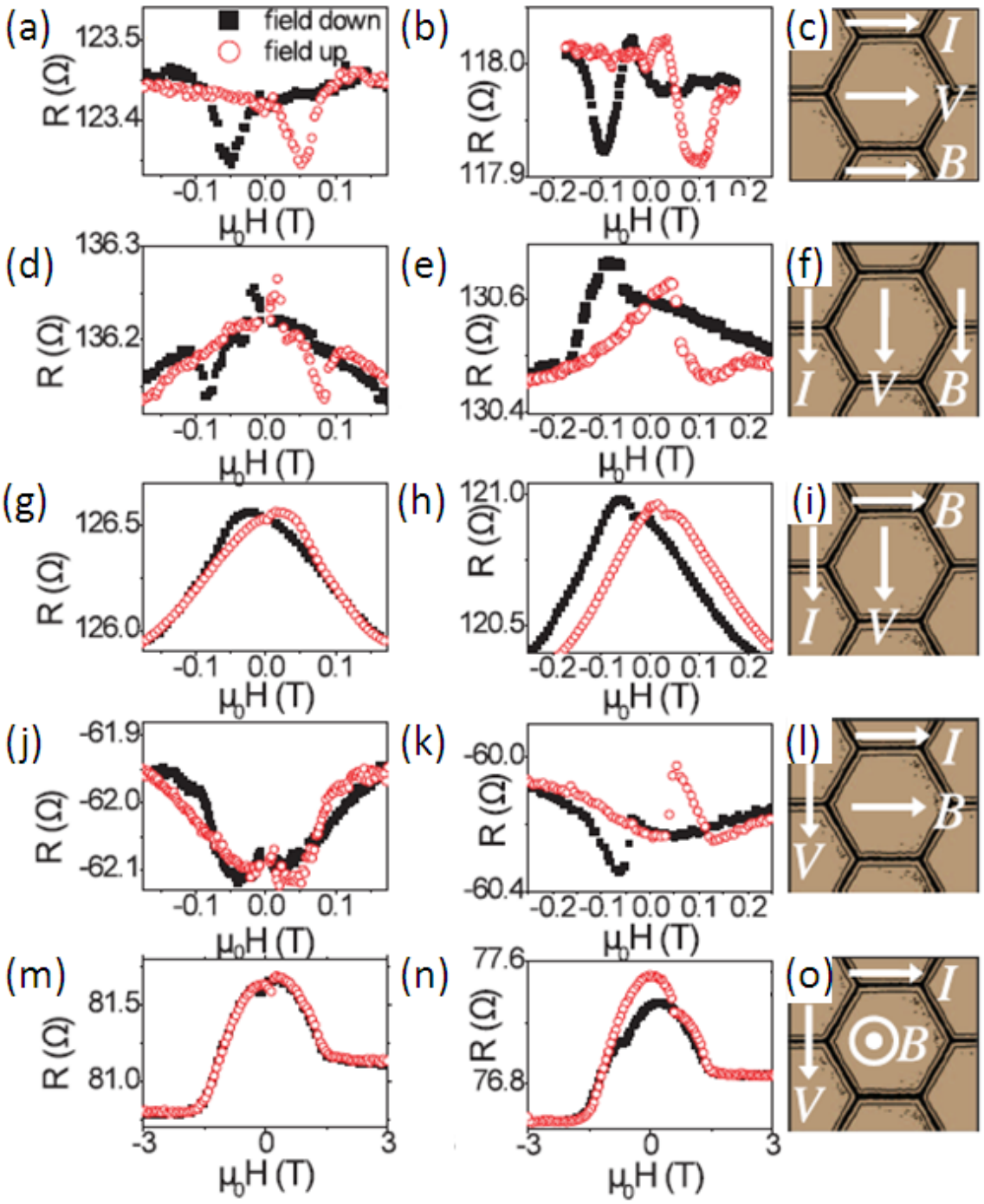

Figure 5.1 Raw magnetotransport data of cobalt honeycomb artificial spin ice. $R_{xx}(B_x)$ (a) at 100 K, (b) at 2 K (c) measurement configuration. $R_{yy}(B_y)$ (d) at 100 K, (e) at 2 K, (f) measurement configuration. $R_{yy}(B_x)$ (g) at 100 K, (h) at 2 K, (i) measurement configuration. $R_{xy}(B_x)$ (j) at 100 K, (k) at 2 K, (l) measurement configuration. $R_{xy}(B_z)$ (m) at 100 K, (n) at 25 K, (o) measurement configuration. Published in [3].

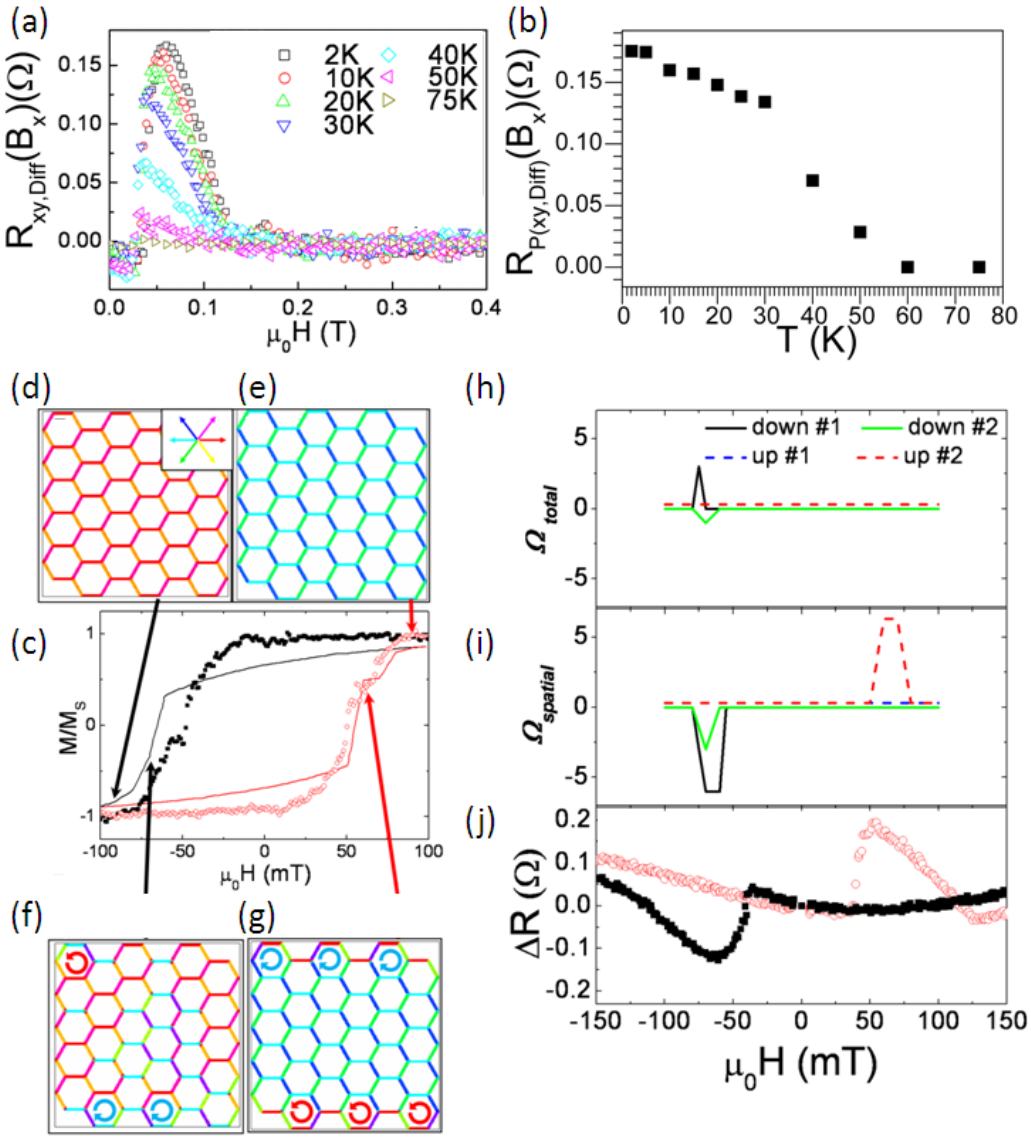

Figure 5.2 Temperature dependence of the resistivity of cobalt artificial spin ice. (a) Field dependent asymmetry of $R_{xy}(B_x)$, $R_{xy,Diff}(B_x)$. (b) Peak height dependence with temperature $R_{P(xy,Diff)}(B_x)$. (c) Normalised magnetisation versus applied field simulated by OOMMF (down sweep black line, up sweep red line) and extracted from $R_{xx}(B_x)$ (down sweep black solid squares, up sweep red open circles). (d)-(f) OOMMF simulation at selected fields (indicated by arrows). (h) Total loop chirality, Ω_{total}, the difference of the number of anticlockwise and clockwise magnetisation loops occurring at each field step. (i) Spatial loop chirality, $\Omega_{spatial} = (A_{bottom} - A_{top}) - (C_{bottom} - C_{top})$, the difference of anticlockwise and clockwise loops appearing at the top and bottom of the array. (j) Change in $R_{xy,Diff}(B_x)$ with field $\Delta R = R_{\mu_0 H} - R_0$ at 2K. Published in [3].

where a is the vertex to vertex distance [102]. A dumbbell representation of this model is shown in figure 5.4(a), where the dumbbell of length l is shorter than the vertex to vertex distance a. The nonuniform magnetisation is then confined to an area enclosed by an equilateral triangle (see figure 5.4(b)). This leads to the three dumbbell charges at each vertex being separated by a distance $r = (a-l)\sqrt{3}/2 = \varepsilon\sqrt{3}/2$. Hence, Möller *et al.* proposed a vertex energy of [102]

$$E_{\pm q} = \frac{-2}{\sqrt{3}\varepsilon a} \tag{5.1}$$

and

$$E_{\pm 3q} = \frac{-2\sqrt{3}}{\varepsilon a} \tag{5.2}$$

in case of a vertex in an ice rule violating state. The transition from a paramagnetic regime to the $K1$ regime occurs below a temperature $T_{ice}^{I} \sim E_{\pm 3q} - E_{\pm q} \sim 2J$ where J is the nearest neighbor Ising coupling strength of the islands [102].

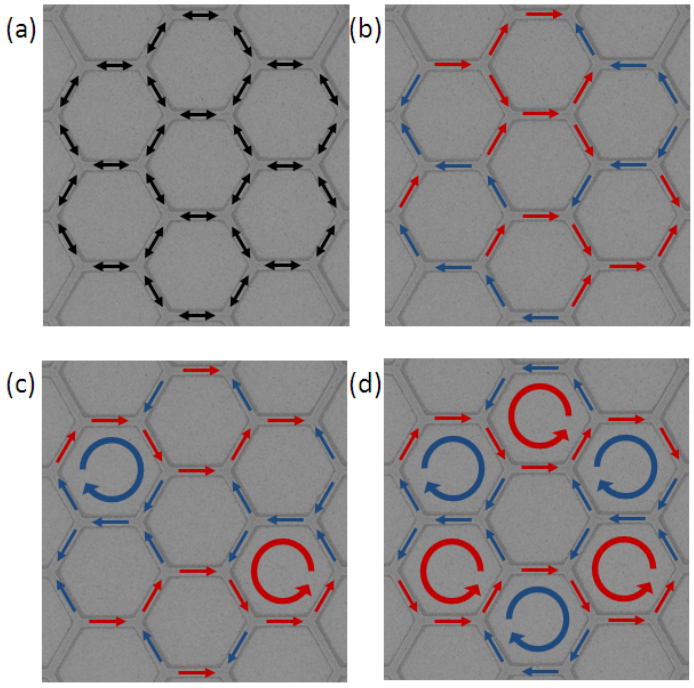

Figure 5.3 Phases of two dimensional dipole kagome spin ice. (a) paramagnetic regime. (b) Kagome ice I, K1, regime. (c) Kagome ice II, K2 regime. (d) Long range order.

The non uniform charge distribution at the vertex leads to a vertex dipole (see figure 5.4(c)). The inclusion of this vertex interaction results in the occurrence of the $K2$ regime where the magnetisation around individual hexagons follow a closed loop pattern, clockwise or anticlockwise (see figure 5.3(c)), due to the interaction between the vertex dipole moments of neighbouring vertices (see figure 5.4(d)). The transition from $K1$ to $K2$ occurs at a temperature [102]

$$T_{ice}^{II} = \frac{\mu_0(\varepsilon q)^2}{4\pi a k_B} \tag{5.3}$$

where $q = M_S t w$ is the charge of the dumbbell and k_B is the Boltzmann's constant. Figure 5.4(e) and (f) show the predicted deviation of the true Ising behaviour for a cobalt and permalloy artificial spin ice vertex (as simulated by OOMMF). The T_{ice}^{II} dependence on the thickness and ε for a cobalt honeycomb artificial spin ice consisting of nanobars of width $w = 100$ nm and a vertex vertex separation of $a = 1000$ nm, is shown in 5.4(g). The transition is very sensitive to the ε. The lower bound of the Ising deviation parameter ε_{lower} is given by the radius of the inscribed circle enclosed by the equivalent triangle encasing the vertex

$$\varepsilon_{lower} = \frac{w}{2a\sqrt{3}} \sim 0.029, \tag{5.4}$$

while the upper bound ε_{upper} is given by the inscribed circle enclosed by the equivalent triangle encasing the area of magnetic moments deviating from the Ising axis as simulated by OOMMF (see figure 5.4(e) and (f))

$$\varepsilon_{upper} = \frac{2.3w}{2a\sqrt{3}} \sim 0.07. \tag{5.5}$$

Hence, a cobalt honeycomb artificial spin ice, consisting of 20 nm thick, 100 nm wide bars and a vertex vertex separation of 1000 nm, a transition from a K1 regime to a K2 regime is predicted to occur between 48 K$< T_{ice,Co}^{II} <$278 K. Therefore, a transition temperature of 50 K, as measured by Branford *et al.* [3], would lead to an ε of 0.0296 (see figure 5.4(i)).

OOMMF simulations on cobalt artificial honeycomb spin ice showed that during the

0 K magnetic reversal, magnetisation loops form at the edges of the array (see figure 5.2(d)-(g)). Branford *et al.* argued that if during the down sweep the carriers get pushed towards the center by the clockwise magnetisation loops at the bottom (C_{bottom}) and the anticlockwise loops at the top (A_{top}) and if the carriers get pushed towards the edges by the anticlockwise magnetisation loops at the bottom (A_{bottom}) and the clockwise loops at the top (C_{top}) then the spacial chirality [3]

$$\Omega_{spatial} = (A_{bottom} - A_{top}) - (C_{bottom} - C_{top}) \tag{5.6}$$

could explain the occurrence of the asymmetry in $R_{xy}(B_x)$ provided there is an inequality in the first and second term in equation 5.6 [3]. The carriers are assumed to get redirected in the opposite sense during the up sweep.

Equation 5.3 shows an expectation for the ordering temperature to scale with the square of the saturation magnetisation (M_S^2). Therefore, the ratio of the ordering temperature of cobalt, $T^{II}_{ice,Co}$, and permalloy, $T^{II}_{ice,Py}$, is given by

$$\frac{T^{II}_{ice,Co}}{T^{II}_{ice,Py}} = \left(\frac{M_{Co}}{M_{Py}}\right)^2 \sim 3 \tag{5.7}$$

assuming identical array dimensions and epsilon, hence a transition temperature of $\sim$17 K is expected for permalloy artificial spin ice.

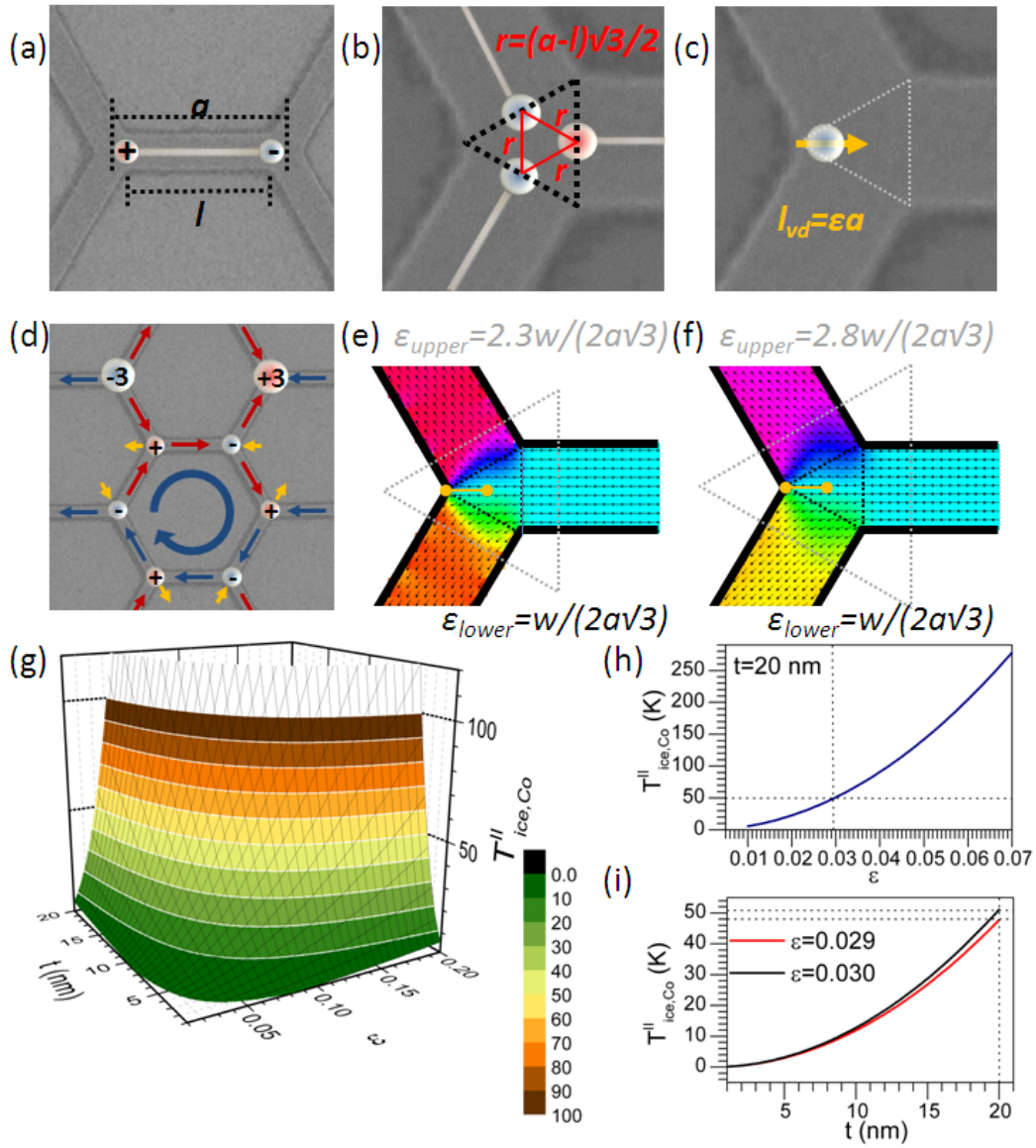

Figure 5.4 Vertex dipole origin. (a) dumbbell of length l connecting two vertices separated by a. (b) vertex charge distribution, separated by $r = (a-l)\sqrt{3}/2$. (c) Vertex dipole moment, of length l_{vd}, due to deviation from the Ising axis. (d) Clockwise magnetisation loop forming due to interaction of vertex dipole moments. (e) OOMMF simulation of a cobalt artificial spin ice vertex showing a deviation from the Ising axis enclosed by an equilateral triangle of length $2.3w$. (f) OOMMF simulation of a permalloy artificial spin ice vertex showing a deviation from the Ising axis enclosed by an equilateral triangle of length $2.8w$. (g) Cobalt artificial spin ice transition temperature dependence on thickness t and ε calculated using $T^{II}_{ice} = \frac{\mu_0(\varepsilon q)^2}{4\pi a k_B}$ (width and vertex separation was taken to be 100 nm and 1000 nm, respectively). (h) $T^{II}_{ice,Co}$ dependence of a 20 nm thick cobalt honeycomb artificial spin ice with respect to changes in ε. (i) $T^{II}_{ice,Co}$ dependence on the thickness for $\varepsilon = 0.029$ (red line) and $\varepsilon = 0.030$ (black line).

Electrical transport is a magnetisation sensitive measurement technique which allows for measurements down to very low temperatures. The electrical transport through a permalloy honeycomb artificial spin ice array was measured using six permalloy electrodes. The array consisted of bars of width 118±2 nm, length 1000±10 nm and thickness 18±2 nm. Current was applied across the array while the magnetoresistance and the Hall resistance were measured simultaneously via two electrode pairs situated perpendicular to one another. See chapter 3.1.5 for a detailed description of the experimental set up. A schematic of the coordinate system, used to identify the different relative orientations of current, voltage, magnetic field with respect to the honeycomb array, is shown in figure 5.5(a). The field dependent asymmetry of resistance was quantified by extracting the difference between the peaks at positive and negative fields, R_{Diff} (see figure 5.5(b)). The average height of the peak occurring in the irreversible part of the resistance curve was defined as R_{Avg}.

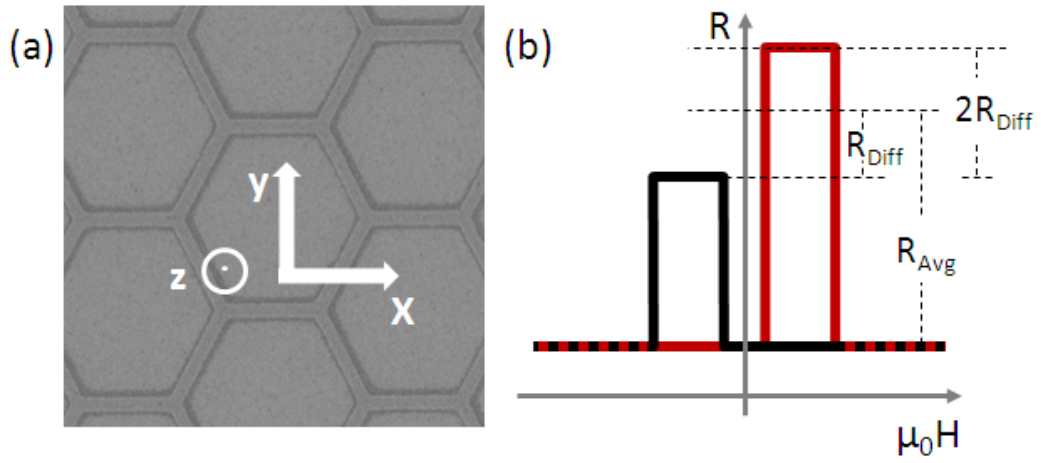

Figure 5.5 Transport measurement set up. (a) Schematics showing the coordinate system of the measurement. (b) Schematics of a magnetotransport curve (black (red) curve represent the down (up) sweep) illustrating the meaning of R_{Diff} and $RAvg$, the components extracted from the irreversible part of the resistance curves. R_{Diff} is a measure of the asymmetry of the resistance measured at positive and negative fields and R_{Avg} is the average of the two peaks.

5.1 Magnetotransport

The magnetoresistance of artificial spin ice arrays is dominated by two anisotropic magnetoresistance effects: the presence and location of domain walls and deviation of the magnetisation away from the Ising axis. The former occurs at low field where shape anisotropy dominates the magnetic configuration, whereas the contribution of the latter increases with increasing field. A vertex in one of the six ice rule states contains a domain wall; the position changes depending on magnetisation direction of the individual bars. Schematics of all six possibilities and the resulting domain wall position are shown in figure 5.6. The magnetic state of the array at zero field is dependent on the initial saturation (refered to as state (1) throughout this chapter). The individual vertices at zero field will be either in state (2) (see figure 5.6(a)-(b)), state (3) (see figure 5.6(c)-(d)) or state (4) (see figure 5.6(e)-(f)) depending on whether the initial saturation field was applied along the x-, the -y- or the y-direction respectively. During the magnetic reversal the state of the vertices changes as domain walls are nucleated and propagate through the artificial spin ice, reaching a saturation state (state (5)) at high fields. The average current path is always parallel to the long axis of the bars. The low and high resistance states depend on the current direction with respect to the domain wall position. The low and high resistance current paths are shown as blue and red arrows respectively. Two current directions were investigated: along the x-direction and along the y-direction. The dotted arrows indicate the current flow in the y-direction and the solid arrows indicate the current flow in the x direction. The current flow marked blue passes through a domain wall at a right angle and hence illustrates a low resistance path. On the other hand, the red arrows indicate a current flowing parallel to the magnetic moments which is a high resistance state.

The resistance of a single magnetically saturated permalloy wire is given by [50]

$$R_{Sat} = \frac{\rho_{\parallel} L}{wt} \tag{5.8}$$

where $\rho_{\parallel}$ =35.5 $\mu\Omega$cm (at room temperature) is the resistivity of permalloy when the cur-

rent and the magnetisation are parallel [50], w is the width of the wire, l is the length and t is the thickness. Using equation 5.8 one estimates the resistance of a wire of width 100 nm, thickness 18 nm and length 1000 nm, to be ∼197 Ω.

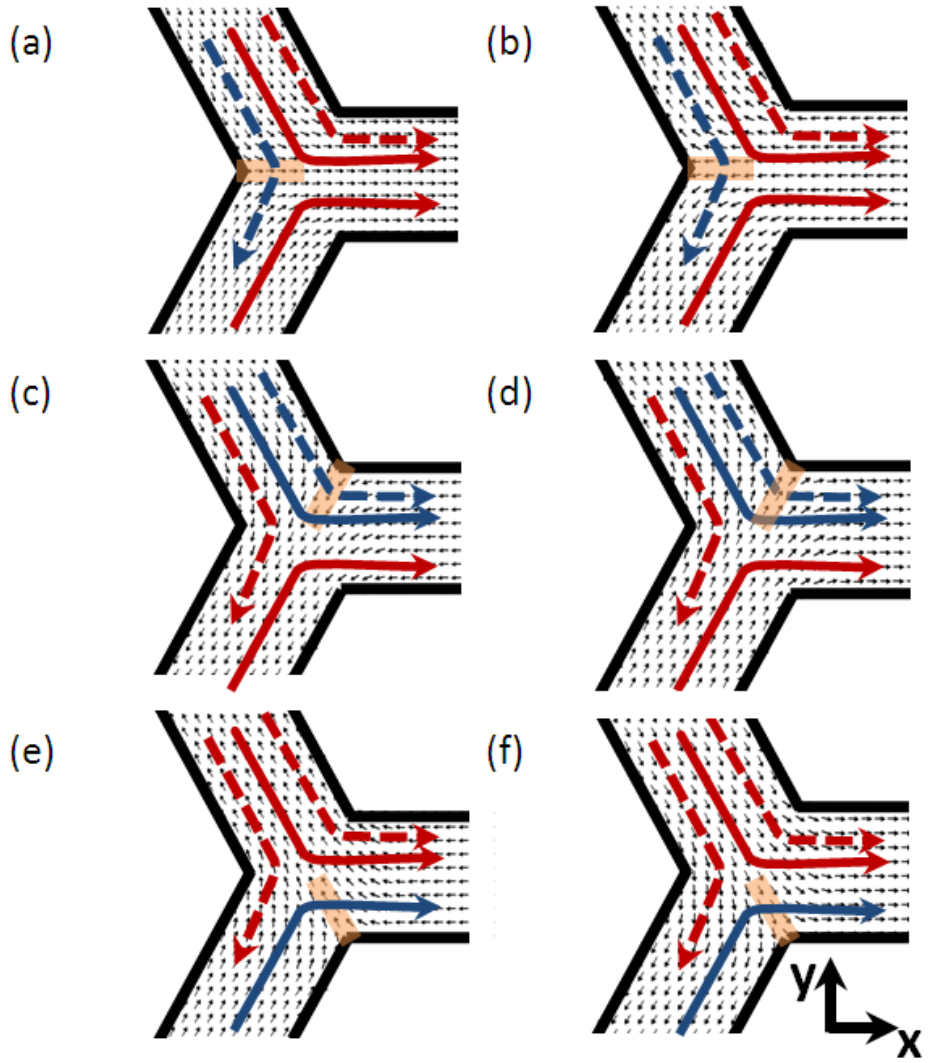

Figure 5.6 Vertex domain wall configuration of the ice rule states at remanence after magnetic saturation along (a) and (b) along the x-direction, (c) and (d) the -y-direction, (e) and (f) the y-direction. The domain wall situated within the vertex is marked by an orange rectangle. The current flow is indicated by dotted arrows in the case of the ARM configuration and solid arrows in the case of the current being applied from left to right. Blue and red coloured arrows highlight low resistance and high resistant current paths.

5.1.1 Out of plane 180° Magnetic Reversal

Figure 5.7 shows low and high temperature magnetoresistance measurements measured during the out of plane magnetic reversal induced by an external field in the z-direction. At saturation the magnetic moments of the permalloy bars are aligned in the z-direction forcing the current, applied in the x- or y-direction, to be perpendicular to the magnetisation at all points (state (1) and (5) in figure 5.8). Hence the magnetoresistance reaches a minimum at fields above magnetic saturation. Figure 5.8(a) and (b) shows that this happens at

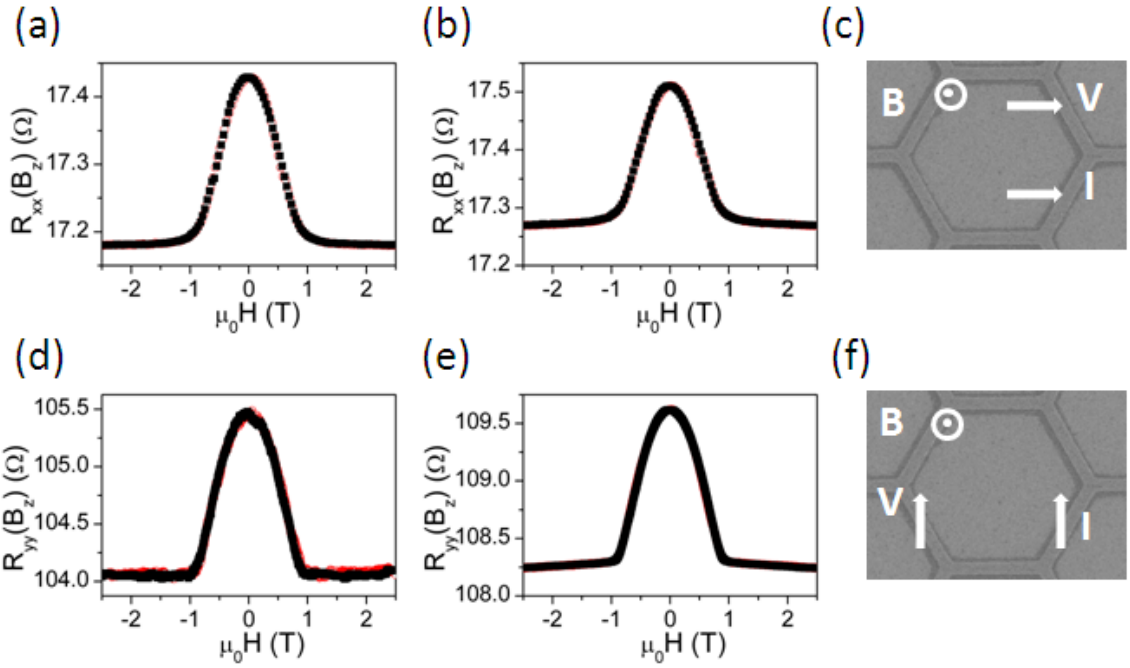

Figure 5.7 Out of plane magnetoresistance data. $R_{xx}(B_z)$ at (a) 5 K, (b) 75 K, for the relative field, current and voltage orientation shown in (c). $R_{yy}(B_z)$ at (d) 5 K, (e) 100 K, for the relative field, current and voltage orientation shown in (f).

fields above ∼1 T. In both configurations, $R_{xx}(B_z)$ and $R_{yy}(B_z)$, the current samples equivalent magnetisation states as the field is applied in the same direction. However, whereas the current can be assumed to flow through all three bars of each vertex in the $R_{xx}(B_z)$ configuration, the diagonal bars are most likely to carry the majority of the current in the $R_{yy}(B_z)$ configuration as they form the shortest path.

Due to the large demagnetisation factor the magnetic moments of the individual bars will snap back into the plane when the external field strength is insufficient to overcome the shape anisotropy. Hence at zero field all vertices are expected to be in one of the six possible ice rule states. The three possible vertex domain wall positions due to the ice rule states are illustrated schematically in figure 5.8 states (2)-(4). The field, H_P, above which the external field is strong enough to destroy the ice rule state, is marked by the gray dotted line. The temperature evolution of H_P extracted from the $R_{yy}(B_z)$ and the $R_{xx}(B_z)$ data is plotted in figure 5.8(c). H_P acquired from the data in the $R_{yy}(B_z)$ configuration is around 120 mT higher than the critical field of the $R_{xx}(B_z)$ data.

The raw magnetoresistance data, at all measured temperatures, is shown in appendix B.1.4. $R_{xx}(B_z)$ was measured at 5 K, 8 K, 10 K, 12K, 15 K, 20 K, 25 K, 30 K, 75 K, 125 K and 290 K. (magnetic field sweep rate of 0.7 A/s). $R_{yy}(B_z)$ was measured at sweep rate of 0.7 A/s at 5 K, 9 K, 12 K, 15 K, 75 K, 100 K and 125 K, resulting in a data point roughly every 4.6 mT.

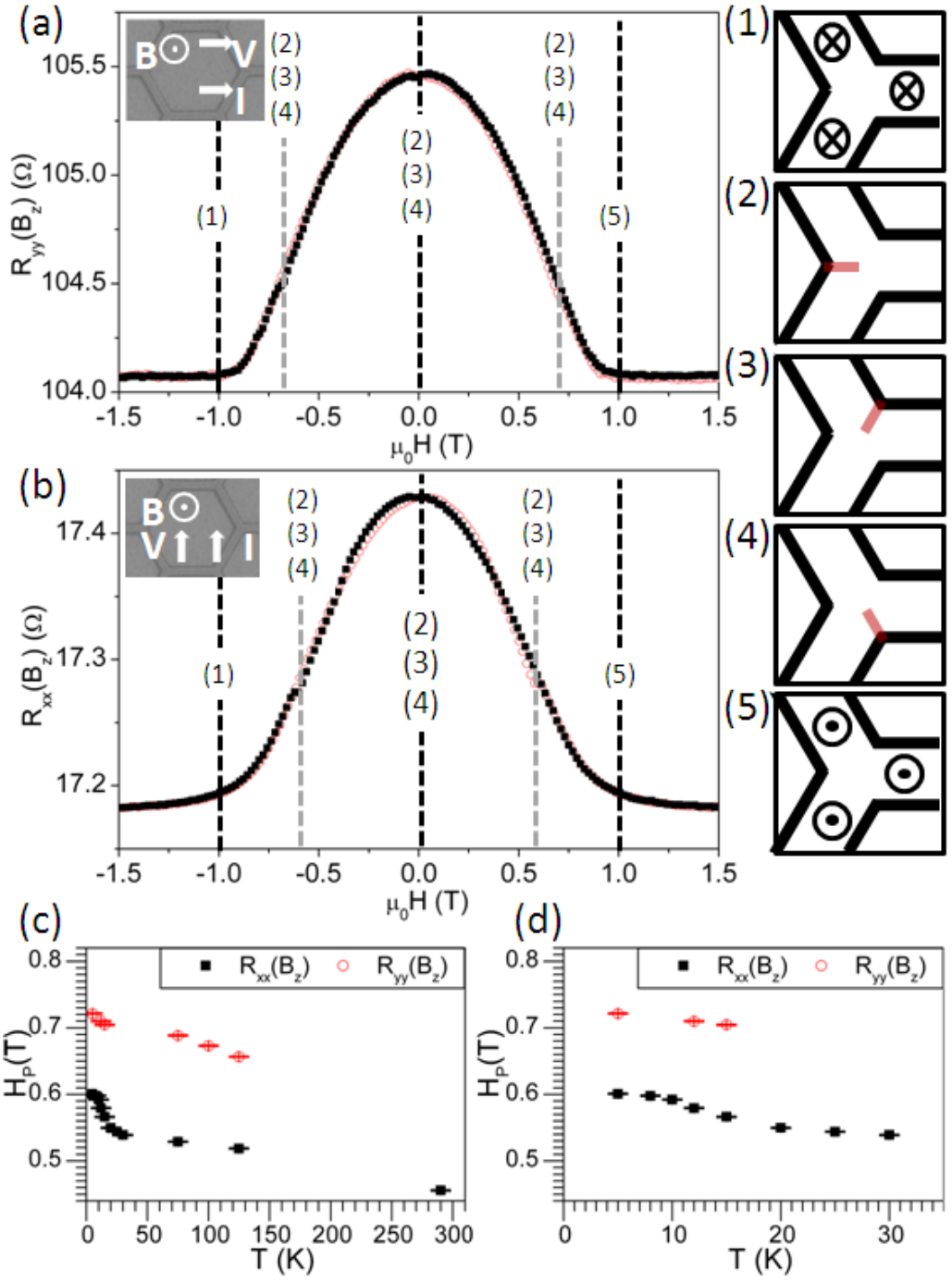

Figure 5.8 Vertex configuration during B_z 180° magnetic reversal. Mapping of the five vertex configurations to the distinct features observed in the magnetoresistance for (a) $R_{yy}(B_z)$ at 12 K and (b) $R_{xx}(B_z)$ at 5 K. The gray line highlights the field H_P at which the irreversible resistance peak reaches its maximum. (c) H_P versus temperature for $R_{yy}(B_z)$ and $R_{xx}(B_z)$. (d) Enlarged low temperature region of (c).

The asymmetry of the irreversible resistance change due to the magnetic reversal at low applied fields was evaluated by comparing the change of the resistance at positive field and negative field after the removal of the background introduced by the curling of the magnetisation away from the long axis. The two components of the irreversible resistance, $R_{yy,Diff}(B_z)$ and $R_{yy,Avg}(B_z)$ are shown in figure 5.9(a) and (b) respectively. Figure 5.9 (d) and (e) show the temperature evolution of height of the peak observed in $R_{yy,Diff}(B_z)$ and $R_{yy,Avg}(B_z)$, $R_{P(yy,Diff)}(B_z)$ and $R_{P(yy,Avg)}(B_z)$. The amplitude of $R_{P(yy,Avg)}(B_z)$ was seen to increase with increasing temperature reaching a maximum of -102.3±6.8 mΩ at around 12 K after which the amplitude of $R_{P(yy,Avg)}(B_z)$ was observed to decrease with increasing temperature. $R_{P(yy,Diff)}(B_z)$ was observed to increase from 19±23 mΩ at 5 K to a maximum at 15 K of 46±23 mΩ and then was seen to decrease as the temperature was further increased; by 75 K $R_{P(yy,Diff)}(B_z)$ was observed to have fallen back to 13±23mΩ. At low temperatures the saturation magnetoresistance was measured to be around -1.28 % (see figure 5.9(c)). The zero field resistance $R_{0,yy}(B_z)$ was observed to decrease with decreasing temperature reaching a base temperature value of 105.461±0.008Ω.

The irreversible components extracted from $R_{xx}(B_z)$ are plotted in figure 5.10(a) and (b). The temperature evolution of $R_{P(xx,Diff)}(B_z)$ and $R_{P(xx,Avg)}(B_z)$ are shown in figure 5.10(d) and (f) respectively. The amplitude of $R_{P(xx,Avg)}(B_z)$, was seen to increase with increasing temperature until a maximum was reached of -11.0±0.2 mΩ at 10±2K. $R_{P(xx,Avg)}(B_z)$ dropped by 3.4±0.2 mΩ between 10 K and 30 K. At 290K $R_{P(xx,Avg)}(B_z)$ was measured to be -4.6±0.2 mΩ; A reduction of 3±0.2 mΩ over a temperature range of 260 K. $R_{P(xx,Diff)}(B_z)$ was measured to be 2.5±0.9 mΩ at 5 K. A maximum was reached at 30 K of 6.7±0.9 mΩ after which $R_{P(xx,Diff)}(B_z)$ was seen to decrease with increasing temperature. At low temperatures the saturation magnetoresistance was measured to be around -1.25 % (see figure 5.10(c)). The residual zero field resistance was measured to be 17.185±0.008Ω (see figure 5.10(f)).

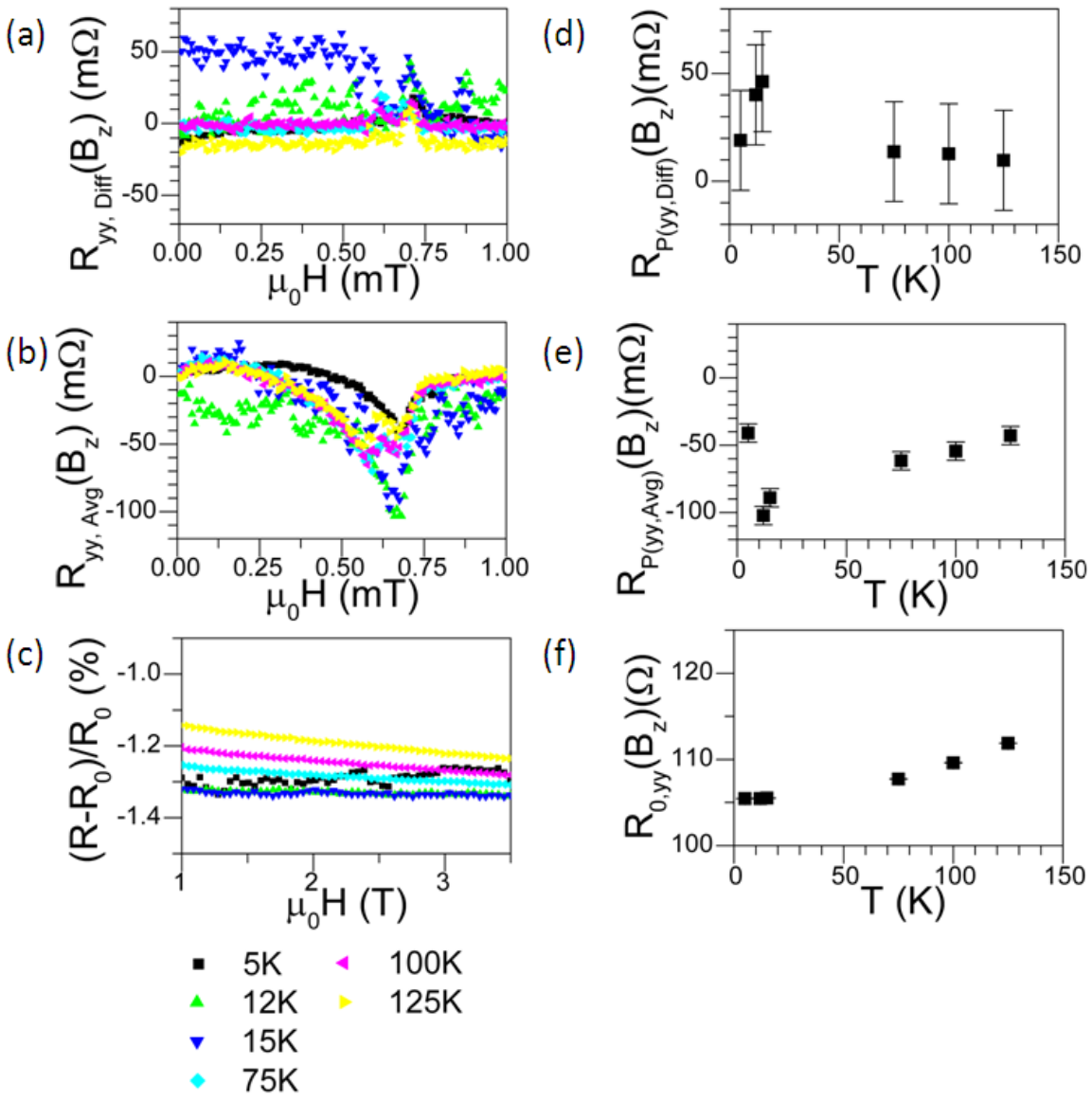

Figure 5.9 Reversible and irreversible components of $R_{yy}(B_z)$. (a) The difference between the irreversible resistance change at positive and negative field, $R_{yy,Diff}(B_z)$. (b) $R_{yy,Avg}(B_z)$, the average irreversible change in the resistance. (c) Magnetoresistance at high fields normalised to the zero field resistance. (d) Temperature evolution of $R_{P(yy,Diff)}(B_z)$, the maximum peak height in (a). (e) $R_{P(yy,Avg)}(B_z)$, the maximum peak height in (b) versus temperature. (f) Temperature evolution of the zero field resistance, $R_{0,yy}(B_z)$.

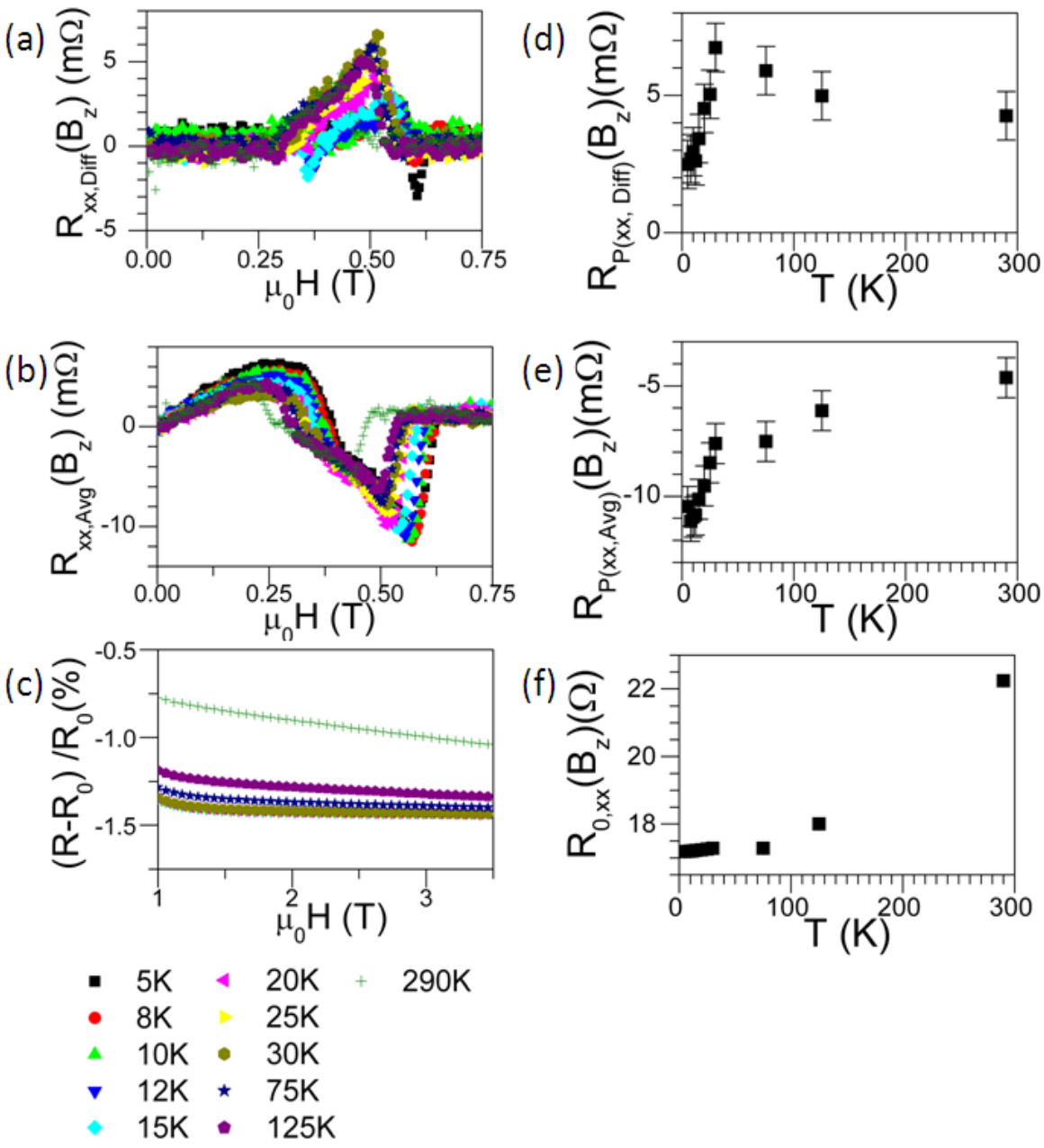

Figure 5.10 Reversible and irreversible components of $R_{xx}(B_z)$. (a) The difference between the irreversible resistance change at positive and negative field, $R_{xx,Diff}(B_z)$. (b) $R_{xx,Avg}(B_z)$, the average irreversible change in the resistance. (c) Magnetoresistance at high fields normalised to the zero field resistance. (d) Temperature evolution of $R_{P(xx,Diff)}(B_z)$, the maximum peak height in (a). (e) $R_{P(xx,Avg)}(B_z)$, the maximum peak height in (b) versus temperature. (f) Temperature evolution of the zero field resistance, $R_{0,xx}(B_z)$.

5.1.2 In-Plane 180° Magnetic Reversal

In-plane magnetoresistance curves at 5K and 50K for all relative configurations are shown in figure 6.8(a)-(l).The magnetisation reversal of honeycomb artificial spin ice is field direction dependent. The array switches by nucleation of domain wall at the edges which then propagate through the array leaving a trail of switched bars behind. At higher fields the magnetic moments of the bars start to curl away from the long axis as the force of the external field exceeds the shape anisotropy constraints. Both mechanisms are reflected in the magnetoresistance measurements; the low field sharp peaks are associated with the sum of the different ice rule states which change due to the domain wall propagation. The slow background curvature reflects the slow curling of the magnetic moments away from the long axis.

Figures 5.12(a) and (b) show the dominating vertex configuration, out of the 5 possible states (illustrated in figure 5.12 (1)-(5)), at low fields when the external field was applied along the x-direction when the current was applied perpendicular and parallel to the field direction respectively. The artificial spin ice array at 5K was seen to switch via domain wall propagation below $\sim \pm 50$ mT. At fields above $\sim \pm 50$ mT the magnetic moments slowly curl away from the long axis of the diagonal nanobars while still being parallel to the horizontal bar. Hence the current is parallel to the magnetisation direction of the horizontal bar and at an angle of 60° in the two diagonal bars leading to an overall low resistance state at high fields. All vertices are expected to be in state (2) (see vertex configurations in figure 5.12) at zero field after a saturation field in the -x-direction (state (1) in figure 5.12). This is a low resistance state in the case of $R_{yy}(B_x)$ and a high resistance state in case of $R_{xx}(B_x)$ as shown in figure 5.12(a) and figure 5.12(b) respectively. During the reversal $R_{xx}(B_x)$ was observed to drop until the cascades due to the domain walls have traversed through the array leaving a majority of the vertices in state (3) or (4). The following sharp resistance increase is associated with nucleation of domain walls from the partially switched vertices reversing the remaining bars, returning to all vertices to state (2).

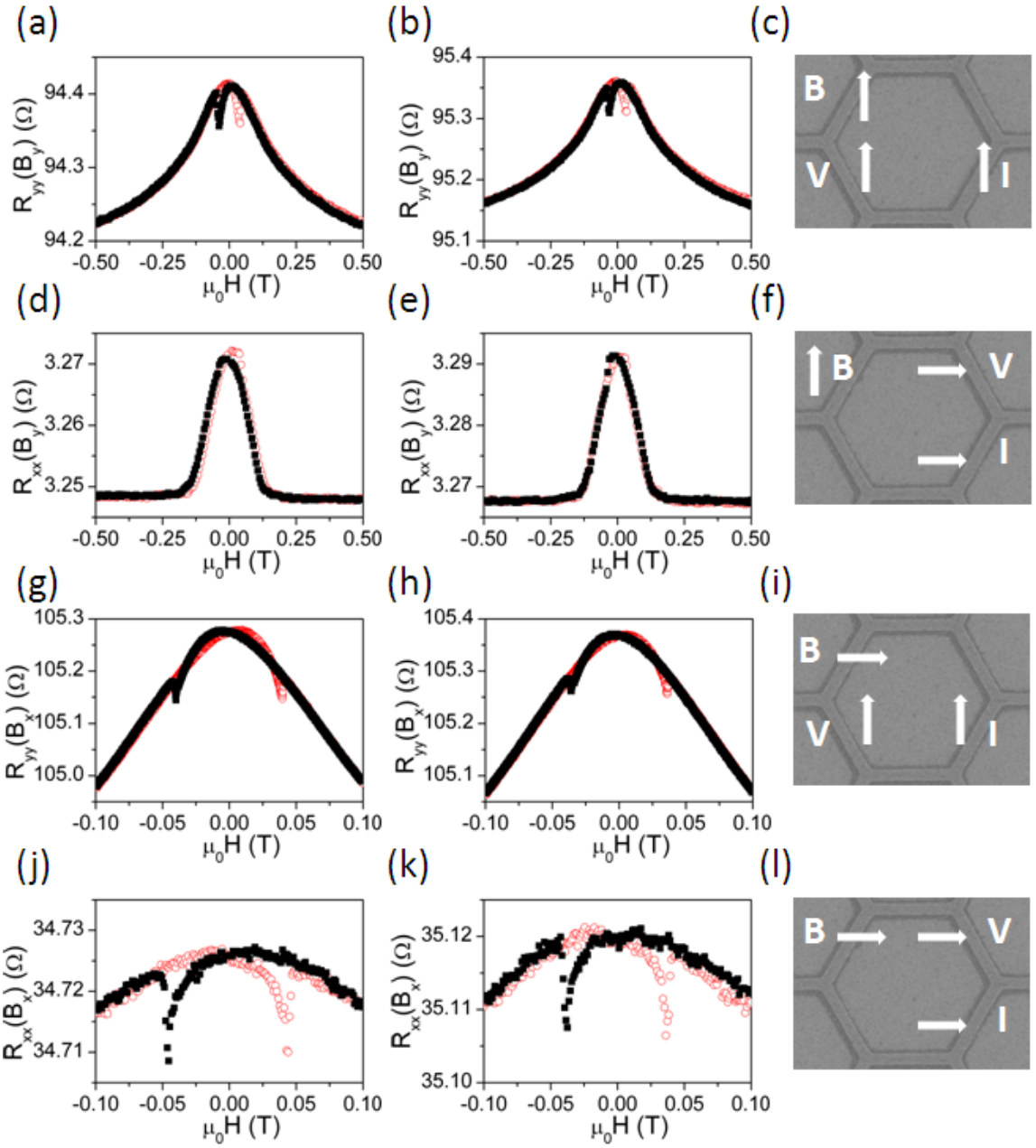

Figure 5.11 In plane magnetoresistance data. $R_{yy}(B_y)$ (a) 5 K, (b) 50 K, relative field current and voltage orientation shown in (c). $R_{xx}(B_y)$ (d) 5 K, (e) 50 K, relative field, current and voltage orientation shown in (f). $R_{yy}(B_x)$ (g) 5 K, (h) 50 K, relative field, current and voltage orientation shown in (i). $R_{xx}(B_x)$ (j) 5 K, (k) 50 K, relative field current and voltage orientation shown in (l).

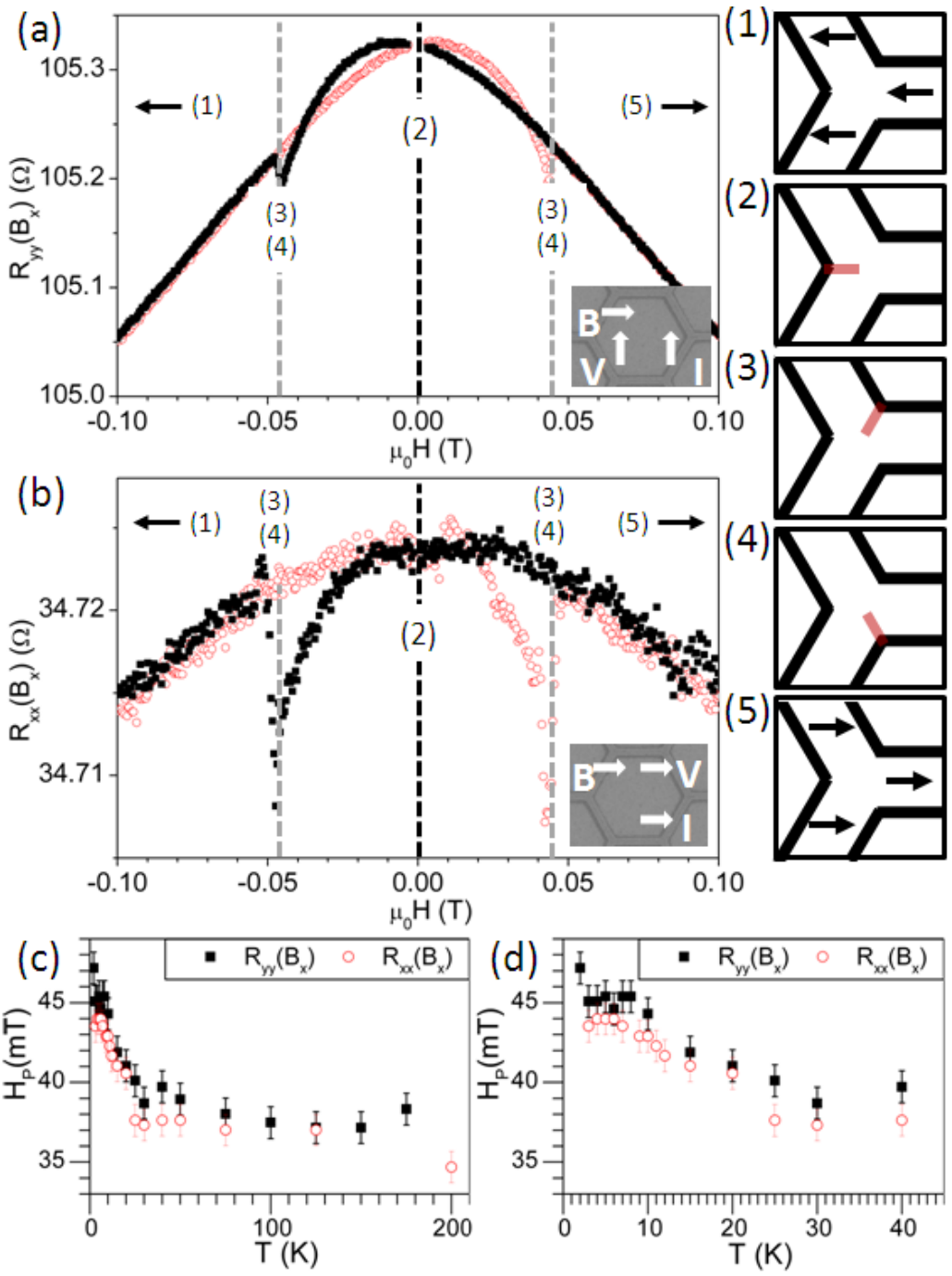

Figure 5.12 Vertex configuration during B_x 180° magnetic reversal. Mapping of the five vertex configurations to the distinct features observed in the magnetoresistance for (a) $R_{yy}(B_x)$ at3 K and (b) $R_{xx}(B_x)$ 3 K. The gray line highlights the field H_P at which the low field resistance peak reaches its maximum. (c) H_P versus temperature for $R_{yy}(B_x)$ and $R_{xx}(B_x)$. (d) Enlarged low temperature region of (c).

$R_{yy}(B_x)$ was seen to increase from the local minimum at zero field as the domain walls traversed across the array leaving vertices in state (3) or (4) in their wake. The temperature evolution of the peak position, the field of the local resistance minimum, is shown in figure 5.12(c). H_P was seen to increase with decreasing temperature. A sharp increase of H_P, by 7 mT occurred below $\sim$25 K. A maximum value of $H_P = 46\pm1$ mT was reached at 5K$\pm$1 K.

The raw magnetoresistance data, at all measured temperatures, is shown in appendix B.1. $R_{xx}(B_x)$ was measured at 3 K, 4 K, 5 K, 6 K, 7 K, 9 K, 10 K, 11 K, 12 K, 15 K, 20 K, 25 K, 30 K, 40 K, 50 K, 75 K, 125 K and 200 K (magnetic field sweep rate of 0.03 A/s equivalent to a data point every 30 Oe) and at 4 K, 5 K, 6 K, 10 K, 11 K and 20 K acquiring a data point every 0.2 Oe (sweep rate of 0.075 mA/s and a data averaging time of 0.5 s). $R_{yy}(B_x)$ was measured at sweep rate of 0.03 A/s at 2 K, 3 K, 4 K, 5 K, 6 K, 7 K, 8 K, 10 K, 15 K, 20 K, 25 K, 30 K, 40 K, 50 K, 75 K, 100 K, 125 K, 150 K and 175 K and at a sweep rate of 0.15 mA/s (a data point roughly every 0.8 Oe) at 2 K, 3 K, 4 K, 5 K, 6 K, 8 K, 10 K, 12 K, 15 K, 20 K, and 25 K.

The asymmetry of the irreversible magnetic reversal, due to domain wall nucleation and propagation, was evaluated by comparing the change of the resistance at positive field and negative field after the removal of the back ground introduced by the curling of the magnetisation away from the long axis. The temperature evolution of $R_{P(xx,Diff)}(B_x)$ and $R_{P(xx,Avg)}(B_x)$) is shown in figure 5.13 (a) and (b) respectively. No clear trend in the temperature dependence of $R_{P(xx,Diff)(B_x)}$ could be identified as the reversal features were to sharp for the sweep rate chosen, resulting in too few data points in the crucial field region. The external field was swept at a rate of 0.03 A/s and sampled around every 30 Oe. The amplitude of $R_{P(xx,Avg)(B_x)}$ was seen to initially increase to a maximum value of -53$\pm$2 mΩ at 10K and then was observed to decrease with increasing temperature. The zero field resistance in the magnetoresistance measurement geometry, $R_{0,xx}(B_x)$ was found to decrease with temperature reaching a residual resistance of 34.724$\pm$0.001 Ω (see figure 5.13(c)). $R_{xx}(B_x)$ was remeasured at temperatures below 20 K using a slower sweep rate. However, the magnetoresistance measurement was very noisy. $R_{0,xx}(B_x)$ at the base temperature, extracted

from the slow field ramp, was seen to be approximately 2 Ω lower. Similarly, $R_{P(xx,Avg)(B_x)}$ was observed to be around ∼-10 mΩ which is around 35 mΩ lower than the previously measured average peak height. This most likely a result of one of the five current contacts, shortened together at the edges, broke, changing the local current distribution and hence affected the signal size measured. At low temperatures the saturation magnetoresistance was measured to be around -0.26 % (see figure 5.13(d)).

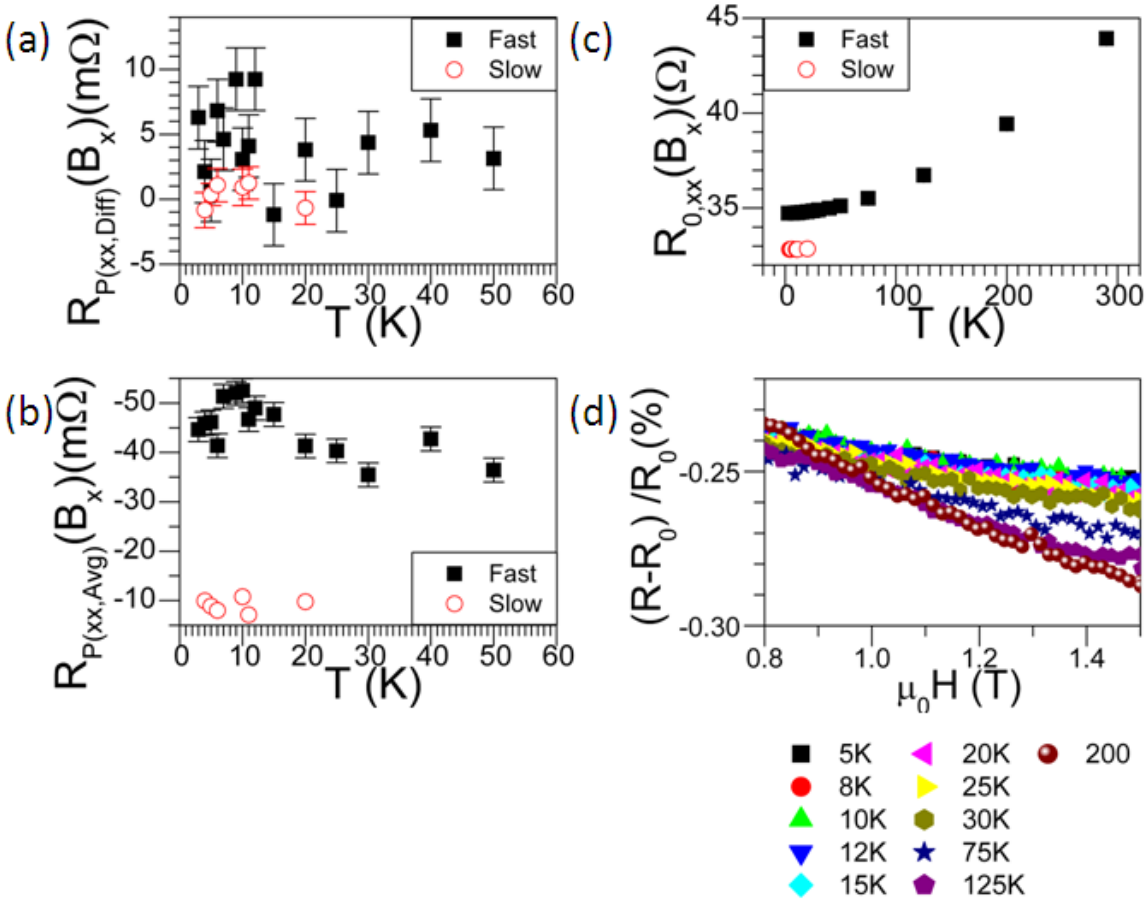

Figure 5.13 Reversible and irreversible components of $R_{xx}(B_x)$. (a) The temperature evolution of the maximum difference between the resistance change at positive and negative field due to domain wall propagation, $R_{P(xx,Diff)}(B_x)$. (b) The average peak height $R_{P(xx,Avg)}(B_x)$ versus temperature. (c) Temperature evolution of the zero field resistance, $R_{0,xx}(B_x)$. (d) Magnetoresistance at high fields normalised to the zero field resistance.

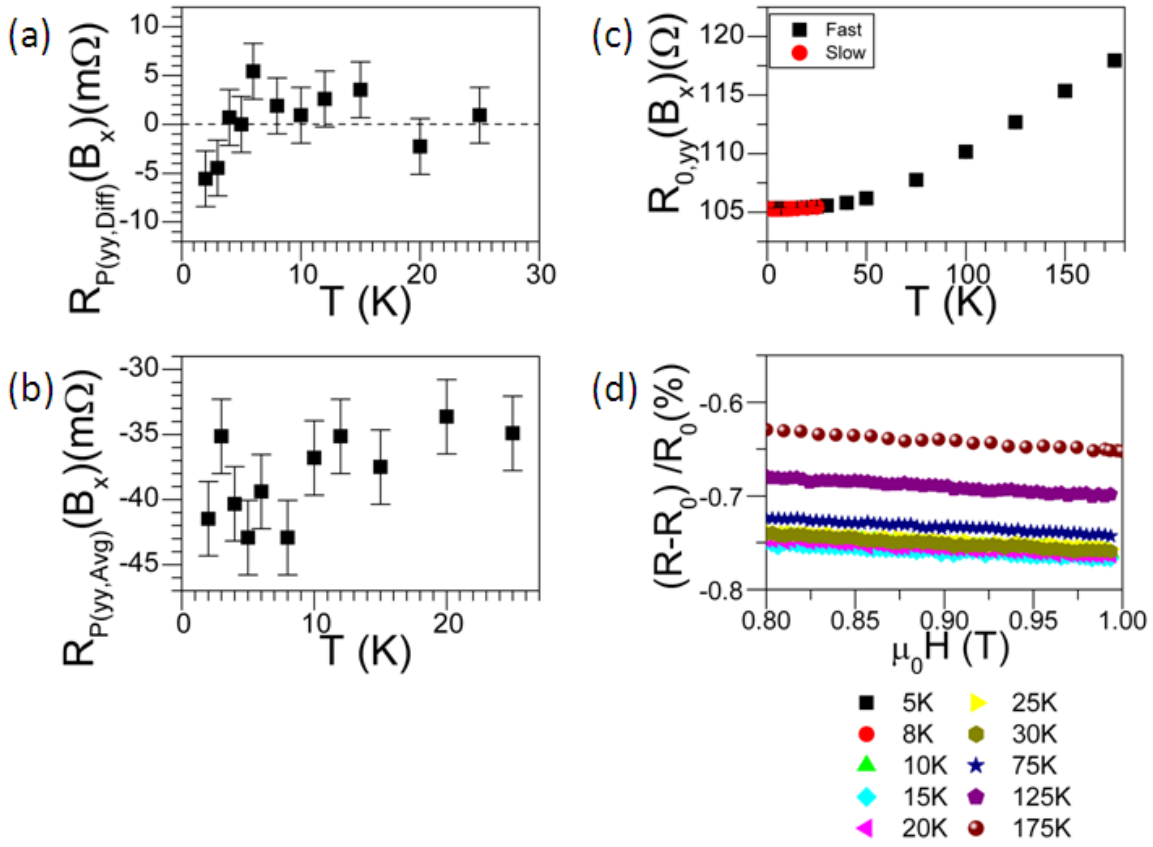

Figure 5.14 Reversible and irreversible components of $R_{yy}(B_x)$. (a) The temperature evolution of the maximum difference between the resistance change at positive and negative field due to domain wall propagation, $R_{P(yy,Diff)}(B_x)$. (b) The average peak height $R_{P(yy,Avg)}(B_x)$ versus temperature. (c) Temperature evolution of the zero field resistance, $R_{0,yy}(B_x)$. (d) Magnetoresistance at high fields normalised to the zero field resistance.

The temperature evolution of $R_{P(yy,Diff)}(B_x)$ and $R_{P(yy,Avg)}(B_x)$ is shown in figure 5.14 (a) and (b) respectively. The field was swept at a rate of 0.15 mA/s resulting in a data point roughly every 0.8 Oe. $R_{P(yy,Diff)}(B_x)$ was seen to be at a maximum of -5.57±2.85 mΩ at 2K. The asymmetric signature vanished above 4 K. $R_{P(yy,Avg)}(B_x)$ was seen to fluctuate around -40±5 mΩ. The zero field resistance in the magnetoresistance measurement geometry, $R_{0,yy}(B_x)$ was found to decrease with temperature reaching a residual resistance of 105.324±0.001 Ω (see figure 5.14(c)). At low temperatures the saturation magnetoresistance was measured to be around -0.76 % (see figure 5.14(d)).

Figures 5.15(a) and (b) show the dominating vertex configuration, out of the 5 possible states (illustrated in figure 5.15 (1)-(5)), at 5 K during the magnetic reversal induced by an external magnetic field in the y-direction. The current was applied perpendicular and parallel to the field direction allowing the investigation of the field response of $R_{xx}(B_y)$ and $R_{yy}(B_y)$ respectively. The magnetic reversal at low fields is mediated by nucleation and propagation of domain walls; at high fields the Zeeman force exceeds the shape anisotropy and the magnetic moments curl away from the long axis in all three bars and align with the external field. This is evident in the slow changing resistance background. The artificial spin ice array at 5K was seen to switch via domain wall propagation at fields up to $\sim \pm 50$ mT. At high fields the magnetisation of the horizontal bars is aligned perpendicular to the current flow whereas the magnetisation of the diagonal bars are at 60° to the current flow (state (1) and (5) in figure 5.15). $R_{yy}(B_y)$ was seen to reach a constant minimum resistance at fields above ∼150 mT. The current flowing in the y-direction flows along the shortest path, hence one can assume that virtually no current passes through the horizontal bars. Therefore the resistance minimum occurs when the magnetisation in the diagonal bars are aligned parallel to the external field, at $\sim 150\ mT$. Retrospectively this means that the continuing drop in resistance above 150 mT observed in the $R_{xx}(B_y)$ orientation is associated with the magnetisation of the horizontal bar not having reached full alignment with the field.

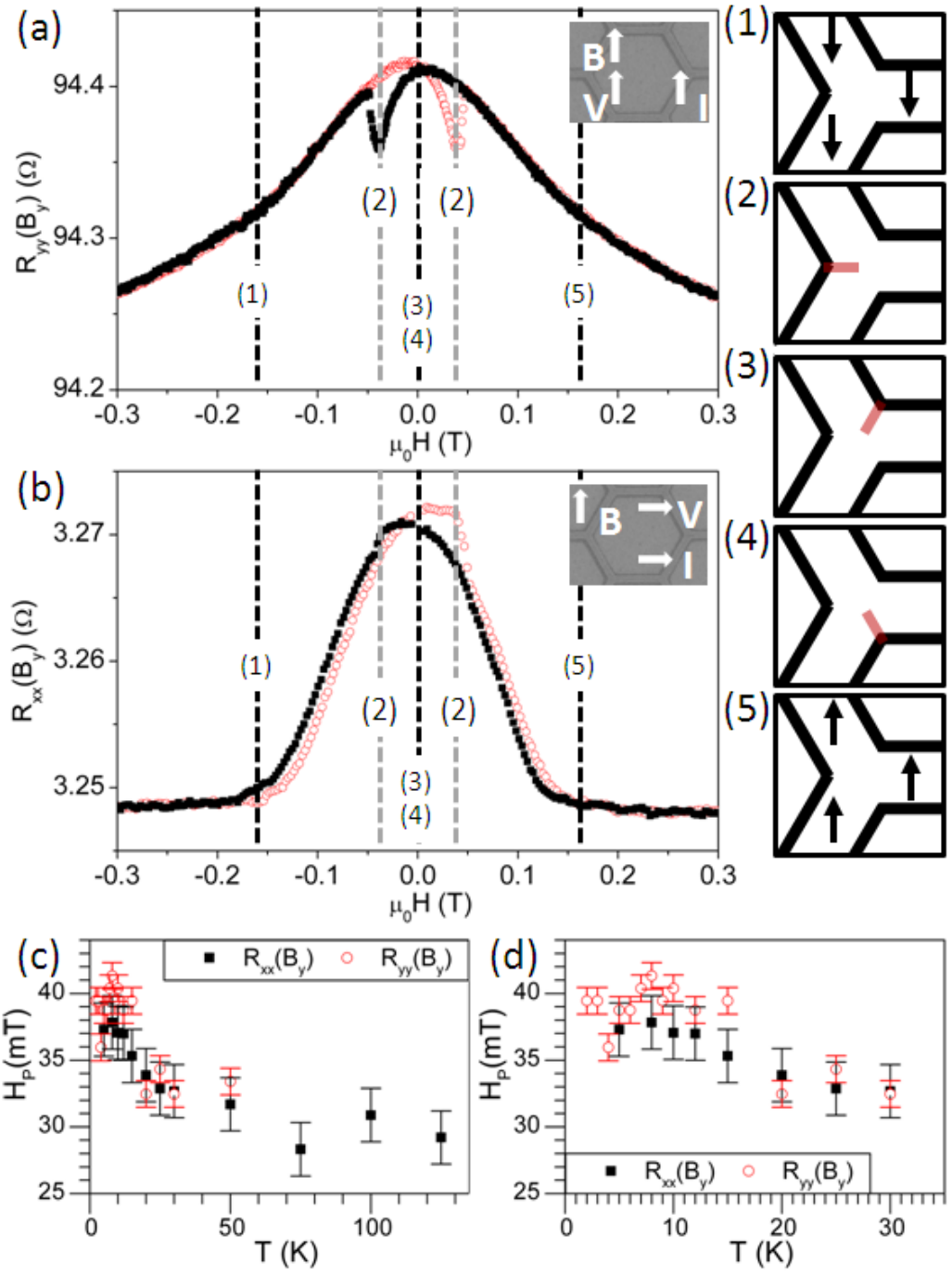

Figure 5.15 Vertex configuration during B_y 180° magnetic reversal. Mapping of the five vertex configurations to the distinct features observed in the magnetoresistance for (a) $R_{yy}(B_y)$ at 2 K and (b) $R_{xx}(B_y)$ at 5 K. The gray line highlights the field H_P at which the irreversible resistance peak reaches its maximum. (c) H_P versus temperature for $R_{yy}(B_y)$ and $R_{xx}(B_y)$. (d) Enlarged low temperature region of (c).

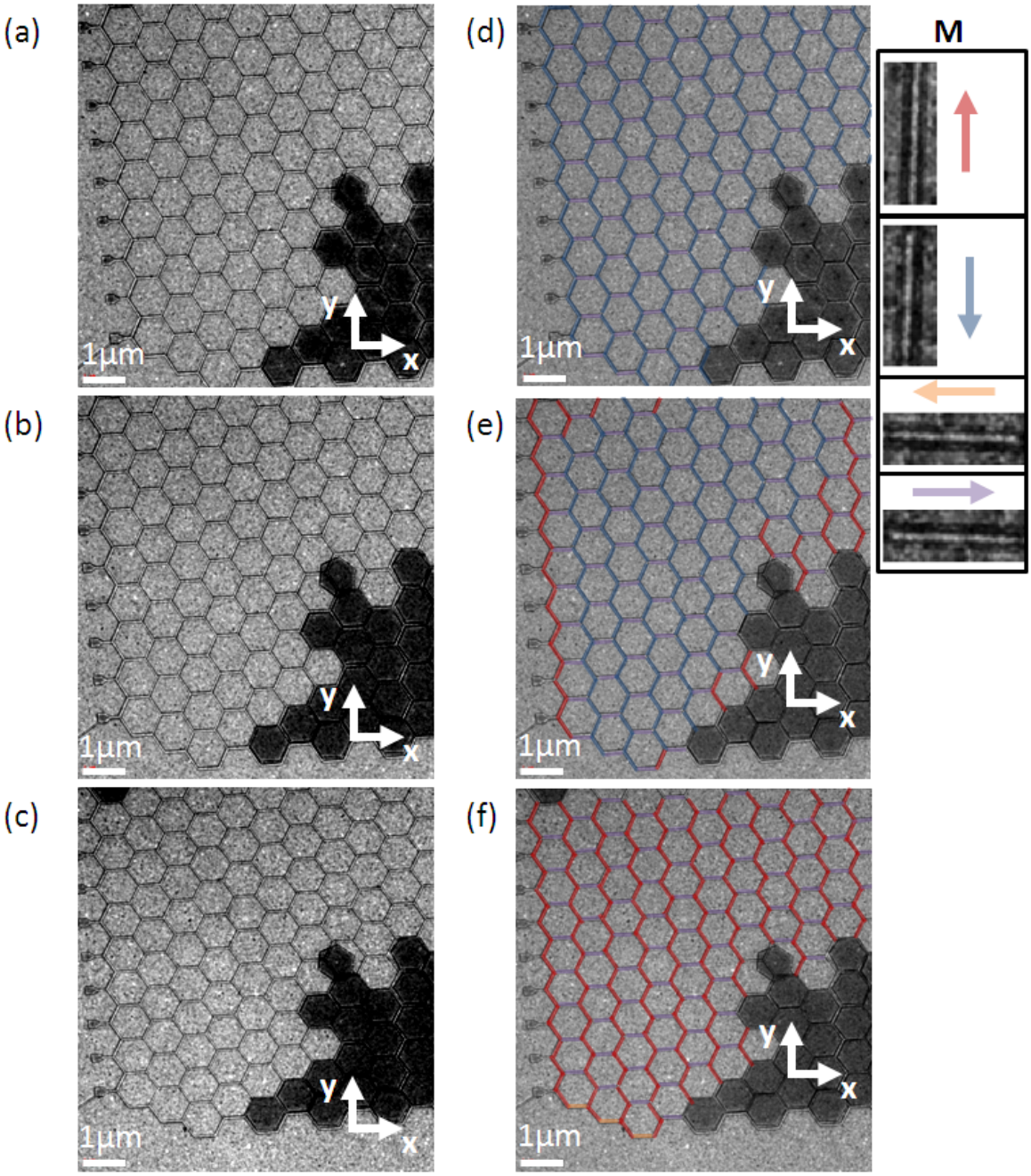

Figure 5.16 Room temperature magnetisation reversal of artificial spin ice in an external magnetic field applied perpendicular to the horizontal bars (along the y axis). After initial saturation in the -y direction a field of (a) 0 mT, (b) 12 mT and (c) 23 mT was applied. The magnetic contrast was imaged at remanence. (d) to (f) show magnetisation of (a) to (c), respectively, colour coded (Key on the right hand side). Images were taken by Dr. S. Felton.

Lorentz transmission electron microscopy measurements at room temperature showed that the 180° magnetic reversal of an artificial spin ice array induced by the application of a magnetic field in the y-direction is mediated by long chains of diagonal switching. Figure 5.16(a)-(c) shows LTEM images taken (by Dr. S. Felton) at remanence at different stages of the reversal. The majority of the horizontal bars were seen to remain in their original state, only a few were seen to reverse their magnetisation.The domain walls were observed to nucleate from the edges of the array. The first switched bar is seen at 8 mT. The first horizontal bars switch at 19.5 mT. It is unclear from the data if the initial magnetisation direction of the horizontal bars in the array is due to some unknown pre-measurement exposure to a magnetic field in the x-direction or a result of the external field along the y-axis.

From the transport measurements one can deduce that the vertices of the artificial spin ice array at zero field, after saturation in the y-direction, are in either state (3) or (4) (as depicted in figure 5.15), depending on the magnetisation direction of the horizontal bar. During the reversal vertices can be in state (2) (as depicted in figure 5.15) provided only one of the diagonal bars has switched. State (2) is a high resistance state in case of $R_{xx}(B_y)$ and a low resistance state in case of $R_{yy}(B_y)$, causing the local minimum observed in the latter and the local maximum observed in the former (see figure 5.15(a)). The peak position, H_P, in both configurations, was seen to increase with decreasing temperature. A sharp increase of H_P, by 5 mT occurred below around $\sim$20 K. A maximum value of $H_P = 40\pm2$ mT was reached at 8K$\pm$1 K.

The raw magnetoresistance data, at all measured temperatures, is shown in appendix B.1. $R_{xx}(B_y)$ was measured at 5 K, 8 K, 10 K, 12K, 15 K, 20 K, 25 K, 30 K, 50 K, 75 K, 100 K and 125 K. (magnetic field sweep rate of 0.03 A/m). $R_{yy}(B_y)$ was measured at sweep rate of 0.03 A/m at 2 K, 3 K, 4 K, 5 K, 6 K, 7 K, 8 K, 9 K, 10 K, 12 K, 15 K, 20 K, 25 K, 30 K and 50 K.

The temperature evolution of the asymmetry in the field dependent resistance, measured at constant temperature, was quantified by extracting the difference between

($R_{xx,Diff}(B_y)$) the resistance change induced by magnetic reversal through domain wall nucleation and propagation at positive field and negative field (see figure 5.17(a)). The average of the resistance change at positive and negative field ($R_{xx,Avg}(B_y)$) is seen in 5.17(b). The temperature evolution of the peak heights in figure 5.17(a) and (b) are shown in figures 5.17(d) and (e) respectively. $R_{P(xx,Diff)}(B_y)$, an indicator that there is a Hall contribution to the signal, reaches a maximum at 10 K of -3.5±0.5 mΩ and vanishes at 15 K. $R_{P(xx,Avg)}(B_y)$ followed a similar trend; starting at 2.5±0.5 mΩ at 5K $R_{P(xx,Avg)}(B_y)$ was observed to increase to a maximum of 5.5±0.5 mΩ at 12K and decreased back to around 2.0±0.5 mΩ by 30 K. $R_{P(xx,Avg)(B_y)}$ remained constant above 30 K. The saturation magnetoresistance was -0.7% (see figure 5.17 (c)). The zero field resistance in the magnetoresistance measurement geometry, $R_{0,xx}(B_y)$ was found to decrease with temperature reaching a residual resistance of 3.271±0.001Ω (see figure 5.17(f)).

Figure 5.18(b) shows the average height of the peak caused by the domain wall propagation at positive and negative fields $R_{P(yy,Avg)}(B_y)$ measured at all temperatures. The temperature evolution of $R_{P(yy,Diff)}(B_y)$, the difference in peak height, is plotted in figure 5.18(a). $R_{P(yy,Diff)}(B_y)$ was seen to initially decrease down to around -10 mΩ at 4 K. Within 2K $R_{P(yy,Diff)}(B_y)$ increased to around 10 mΩ and was then seen to decrease reaching values around zero above 25K. The amplitude of $R_{P(yy,Avg)}(B_y)$ was seen to stay constant at around -43 mΩ between 2 K and 10 K above which it was seen to increase up to a maximum value of -51.0±1.8 mΩ at 20 K. The zero field resistance in the magnetoresistance measurement geometry, $R_{0,yy}(B_y)$ was found to decrease with temperature reaching a residual resistance of 94.412±0.001 Ω (see figure 5.18(c)). The saturation magnetoresistance was ∼-0.2% (see figure 5.17 (c)). The magnetoresistance was seen to have a slight negative slope of gradient ∼0.05 T^{-1} at high fields.

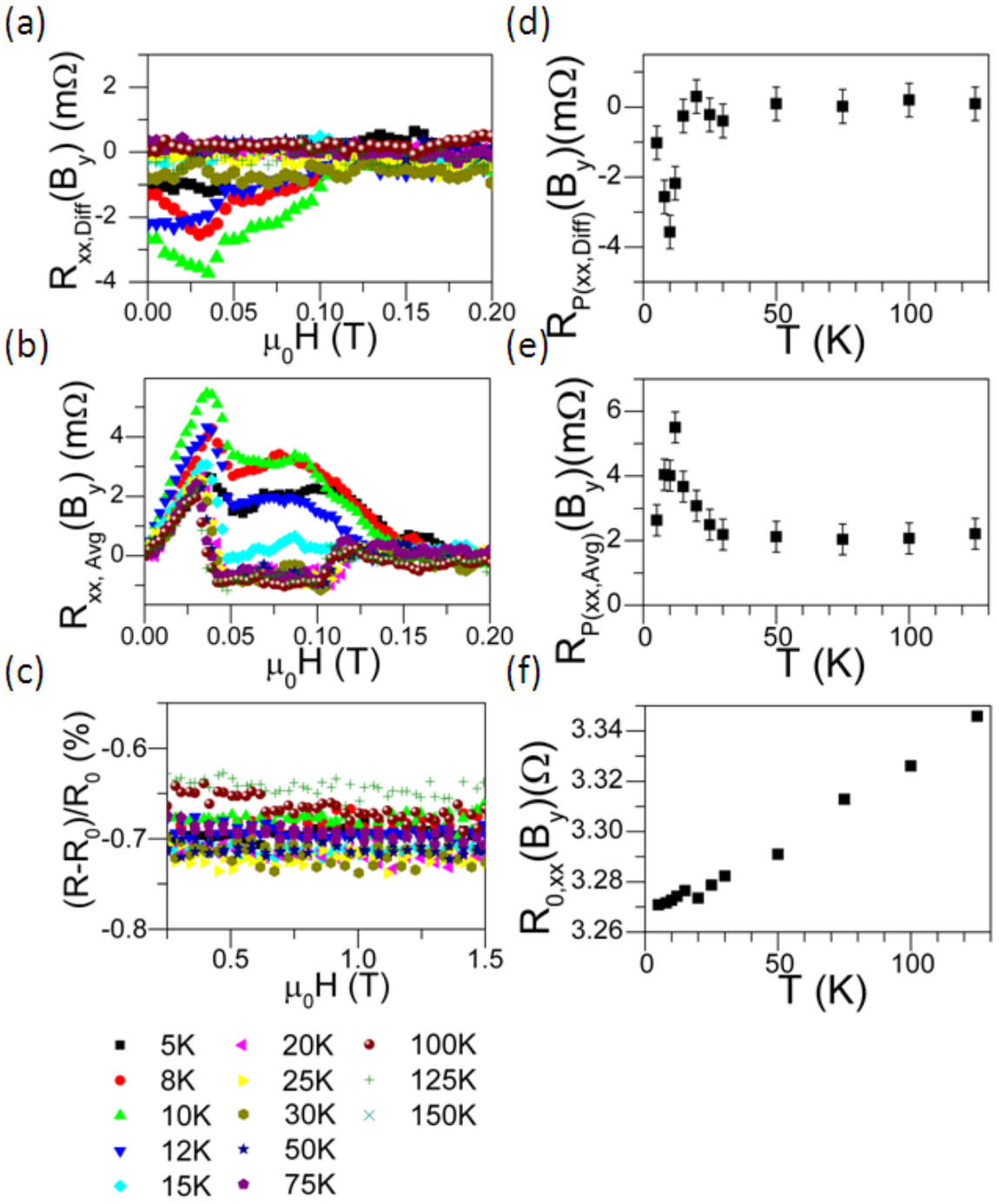

Figure 5.17 Reversible and irreversible components of $R_{xx}(B_y)$. (a) The difference between the resistance change at positive and negative field due to domain wall nucleation and propagation, $R_{xx,Diff}(B_y)$. (b) $R_{xx,Avg}(B_y)$, the average change in resistance due to domain wall propagation. (c) Magnetoresistance at high fields normalised to the zero field resistance (d) Temperature evolution of $R_{P(xx,Diff)}(B_y)$, the maximum peak height in (a). (e) $R_{P(xx,Avg)}(B_y)$, the maximum peak height in (b) versus temperature. (f) Temperature evolution of the zero field resistance, $R_{0,xx}(B_y)$.

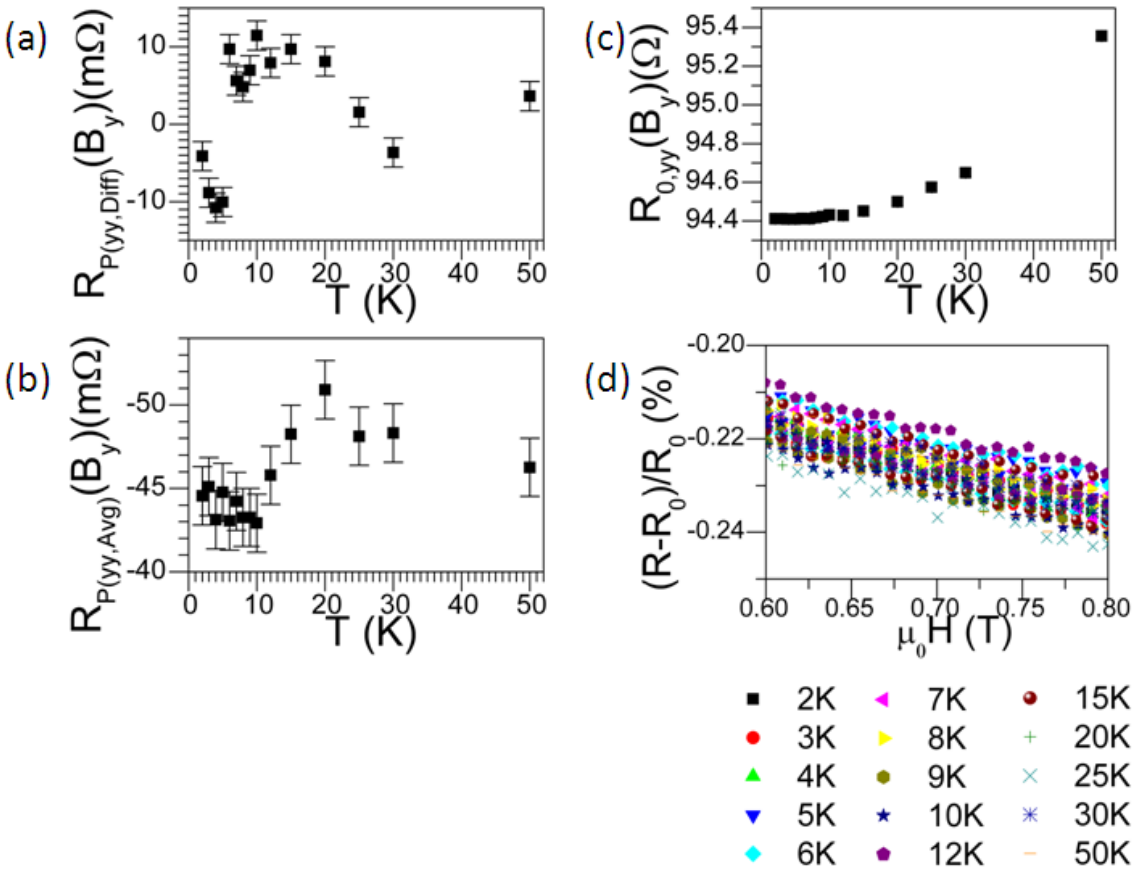

Figure 5.18 Reversible and irreversible components of $R_{yy}(B_y)$. (a) The temperature evolution of the maximum difference between the resistance change at positive and negative field due to domain wall propagation, $R_{P(yy,Diff)}(B_y)$. (b) The average peak height $R_{P(yy,Avg)}(B_y)$ versus temperature. (c) Temperature evolution of the field resistance, $R_{0,yy}(B_y)$. (d) Magnetoresistance at high fields normalised to the zero field resistance (c).

5.1.3 Discussion

The normalised zero field resistance R_0, extracted from the artificial spin ice resistance measurements, can be seen in figure 5.19(a); a good agreement was found between the artificial spin ice and a thin film of permalloy, irrespectively of the measurement configuration. The thin film resistivity was fitted to the Matthiesen's rule (see chapter 2.4.5 for details), including a temperature independent contribution, a contribution caused by phonon scattering (ρ_{ph}) and a contribution due to spin disorder scattering (ρ_{ferro}) (See figure 5.19(b)(Top)). Good agreement between data and simulation was found. The maximum contribution to the resistivity due to spin disorder (ρ_{para}) was extracted to be 3 $\mu\Omega$cm. As a rough approximation, ρ_{para} is given by $\rho_{para} \sim (\rho_{\uparrow} + \rho_{\downarrow})/4$, where $\rho_{\uparrow}$ and $\rho_{\uparrow}$ are the resistivity of the up and down current carriers. This results in ρ_{para} to be $\sim$20 $\mu\Omega$cm and $\sim$15 $\mu\Omega$cm for nickel and iron respectively [44]. The ρ_{para} extracted from the 90 nm thin film of permalloy resistivity data agrees reasonably well with the values estimated for bulk nickel and iron. The dominant contribution to the zero field resistivity was found to be caused by phonon scattering (See figure 5.19(b)); The onset of the phonon scattering was found to be $\sim$30 K. The onset of significant spin disorder scattering was seen to be $\sim$150 K and was simulated to increase with increasing temperature. At 290 K 30 % of the resistivity is caused by spin disorder scattering (see figure 5.19(c)), this is in good agreement with data published by Raquet *et al.* who reported the magnetic contribution to the resistivity to be 30 % for nickel and 15 % for iron [103].

The 5 K zero field resistances are listed in table 5.1. The zero field resistance estimate, $R_{0,Calc}$, was calculated using the resistivity of of a single permalloy bar and assuming the honeycomb artificial spin ice can be simplified into a network of series resistors in parallel (see figure 5.19(d)). The resistance for a w =100 nm wide, l =1000 nm long and t =18 nm thick nanowire was estimated to be 138 Ω at 5 K. Despite its simplicity this model predicted resistances of the right order of magnitude. The higher zero field resistance of $R_{xx}(B_x)$ is most likely caused by one of the ten current electrodes (five on each side) breaking which

resulted in a change of the current path and hence a shift in the resistance background. At zero applied field, the honeycomb artificial spin ice behaves like a collection of ferromagnetic bars.

The temperature dependence of the field, at which the irreversible peak was observed, is shown in figure 5.19(e) normalised to 5 K. Within the error of the measurement, the H_P of the different magnetoresistance orientations was seen to follow the same temperature trend. H_P was seen to reduce with temperature. About 15 % reduction occurs within the first 30 K. Between 30 K and 290 K H_P was seen to decrease by a further 15 %. The low temperature region is replotted in figure 5.19(f) for one configuration in B_x, B_y and B_z. A roughly constant maximum of H_P was observed at temperatures below 8 K. A distinct change in the switching field evolution with temperature is seen below 30 K. This transition coincides with the onset of phonon scattering. There is an indication of a further change in the temperature dependence of H_P around 150 K which coincides with the onset of spin disorder. However, more data points are needed to confirm this high temperature evolution. On the other hand, below 30 K the zero field resistivity was found to be constant, hence any changes to H_P cannot be a mere reflection of temperature induced changes in lattice and spin vibration. The change of H_P below 30 K suggest a fundamental change in the magnetic reversal.

Above magnetic saturation, where the resistance change with increasing field is reversible, the resistance was measured to drop linearly with increasing field. The percentage change of the anisotropic magnetoresistance (ΔR_0) for all six configurations is shown in figure 5.20(a). ΔR_0 is the extrapolated intercept of the high field linear dependence. At 5 K, ΔR_0 was extracted to be $\sim$ -0.2 %, $\sim$-0.7 % and $\sim$-1.4 % in the case of $R_{yy}(B_y)$ and $R_{xx}(B_x)$, $R_{yy}(B_x)$ and $R_{xx}(B_y)$ and $R_{yy}(B_z)$ and $R_{xx}(B_z)$ respectively. The key factors, in determining the overall resistance drop with increasing field, were identified to be the angle θ between the magnetisation and the current in the two diagonal bars and the over all current direction (along either the x- or y axis). If the current is applied along the y-direction, then the majority of the current flow is expected to be in the diagonal bars, as they form the shortest

path between the current electrodes. Therefore, the resistance change in the diagonal bars affect ΔR_0 more significantly than a reorientation of the magnetisation in the horizontal bar. Despite the horizontal bar of the $R_{yy}(B_y)$ configuration being in a low resistance state at saturation the high resistance state of the diagonal bars ($\theta = 30°$) was seen to dominate ΔR_0; When ignoring the magnetisation state of the horizontal bar ΔR_0 would be expected to increase by a factor of $\times 3$ when changing θ from 30° to 60°. Experimentally an increase of $\sim$4.2 is observed. The opposite is the case when the current is applied along the x-axis. ΔR_0 extracted from $R_{xx}(B_y)$ was observed to be a factor of $\sim \times$ 3.2 larger in comparison to ΔR_0 extracted from $R_{xx}(B_x)$,despite the diagonal bars changing from a low resistance state ($\theta = 60°$) to a high resistance state ($\theta = 30°$). This can be attribute to a change in θ of 90°. See figure 5.20(b) for an illustration of the relative changes between the magnetisation and the current direction caused by the external magnetic field. ΔR_0 was seen to decrease with increasing temperature. With increasing temperature the anisotropic magnetoresistance is masked by the isotropic phonon and spin disorder scattering. The slope (ΔR_{Slope}) of the linear high field resistance dependence is shown in figure 5.20(c). ΔR_{Slope} was observed to be around 0 %/T at 5 K for $R_{xx}(B_x)$, $R_{xx}(B_y)$, $R_{yy}(B_z)$ and $R_{xx}(B_z)$. On the other hand ΔR_{Slope} extracted from $R_{yy}(B_x)$, $R_{yy}(B_y)$ were measured to be around -0.1 %/T. The slope was seen to become more negative with increasing temperature irrespective of the configuration. This temperature high field slope trend with temperature was also observed by Raquet *et al* in case of nickel and iron [103] and was attributed to a damping of collective spin excitations. However, a qualitative comparison of the changes in resistance with increasing field and with temperature require resistance measurements up to 10-20 T in order to fully capture the factual form.

Figure 5.21(a) shows the temperature evolution of $R_{P(xx,Avg)}$ extracted from the in plane measurement configurations. The low temperature details of 5.21(a) are shown in figure 5.21(b). In-plane $R_{P(Avg)}$ was found to change below $\sim$20 K (see figure 5.21(d) and (e)). On the other hand, the temperature evolution of the zero field resistance was observed to be constant below $\sim$30 K. Whereas, the changes in $R_{P(xx,Avg)}$ above 30 K can be attributed

to a washing out of the anisotropic magnetoresistance due to phonon and spin disorder scattering, below 30 K this is not the case. Therefore, we attribute these low temperature features to changes in the overall arrangement of the vertex domain walls, marking a change in the magnetisation reversal of artificial spin ice reversal. The changes in $R_{P(Avg)}$, with the exception of $R_{yy}(B_z)$, coincide with changes in the H_P which is a further indication that fundamental changes in the magnetisation reversal occur below 30 K. The temperature evolution of $R_{yy}(B_z)$ and $R_{xx}(B_z)$ is shown in figures 5.21(c) and 5.21(f). $R_{xx}(B_z)$ shows a similar temperature dependence to the in-plane $R_{P(Avg)}$, whereas $R_{yy}(B_z)$ suggest a different behaviour. However, more measurements at temperatures between 30 K and 75 K and above 125 K are needed to confirm this change.

Artificial Honeycomb Spin Ice Arrays				
Configuration	$R_0(5K)$	$R_{0,Calc}$	$N_{Avg,Series}$	$N_{Avg,Parallel}$
$R_{xx}(B_z)$	17.185±0.001Ω	58±23Ω	40	95
$R_{xx}(B_y)$	3.271±0.001Ω	30±23Ω	20	95
$R_{xx}(B_x)$	34.724±0.001Ω	30±23Ω	20	95
$R_{yy}(B_z)$	105.454±0.001Ω	92±26Ω	36	54
$R_{yy}(B_x)$	105.324±0.001Ω	92±26Ω	36	54
$R_{yy}(B_y)$	94.412±0.001Ω	92±26Ω	36	54

Table 5.1 Table listing the zero field resistance for all artificial spin ice samples and their estimated resistance assuming a simple resistor model.

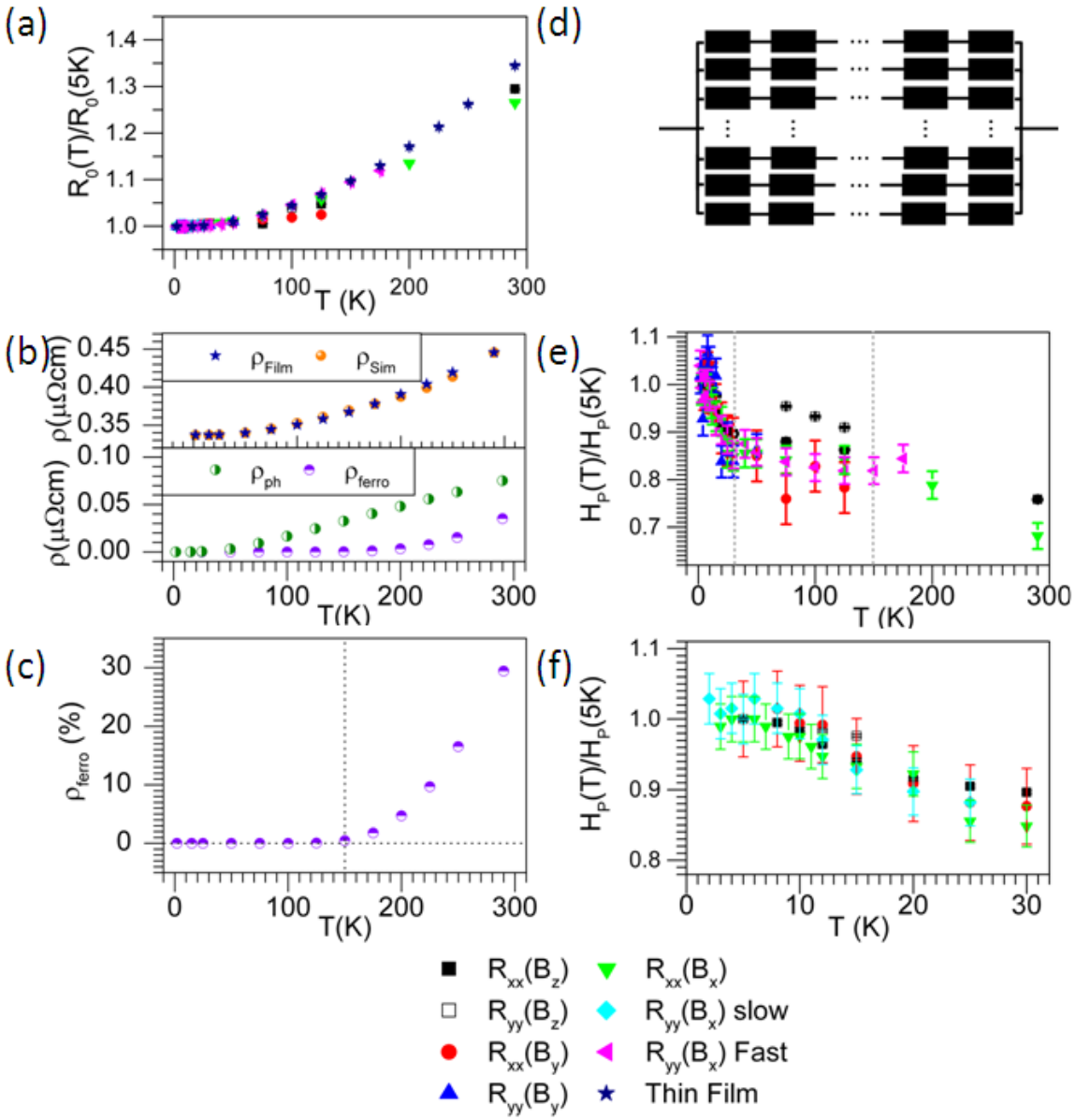

Figure 5.19 Temperature dependence of R_0 (a) shows the zero resistance normalised to its 5 K value. (b) Top: Resistivity of 90 nm thick evaporated permalloy film compared to simulated resistivity. Bottom: Extracted phonon (ρ_{ph}) and spin disorder (ρ_{ferro}) contribution to the resistivity. (c) percentage of the ρ_{ferro} contribution to the total resistivity. (d) Illustration of simple resistor model describing honeycomb artificial spin ice. (e) H_P normalised to its 5 K value versus temperature. (f) Low temperature region of (c).

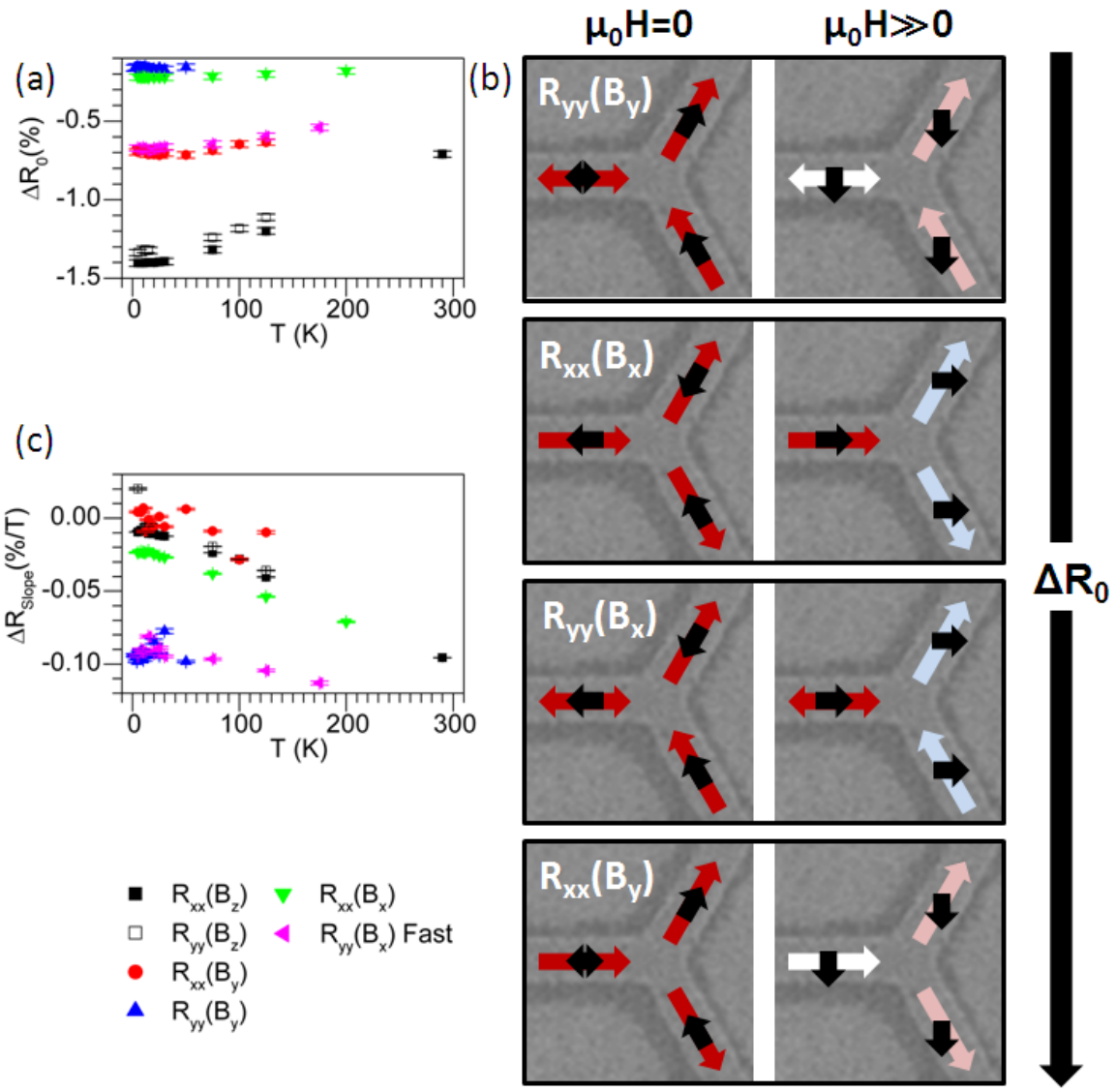

Figure 5.20 Reversible component of the anisotropic magnetoresistance. (a) Percentage change in the anisotropic magnetoresistance between zero field and magnetic saturation at high fields (ΔR_0) with respect to temperature. (b) Schematics of the angle between the current and the magnetization at zero field and fields above magnetic saturation. Black arrows indicate the magnetization direction with respect to the bars. The arrows ranging in colour from red to white, indicate the average current direction, where the colour indicates high or low resistance states. θ listed in order of decreasing resistance: $\theta = 0^\circ$ red, $\theta = 30^\circ$ light red, $\theta = 60^\circ$ light blue and $\theta = 90^\circ$ white. (c) Temperature dependence of the slope of the linear high field dependence of the resistance.

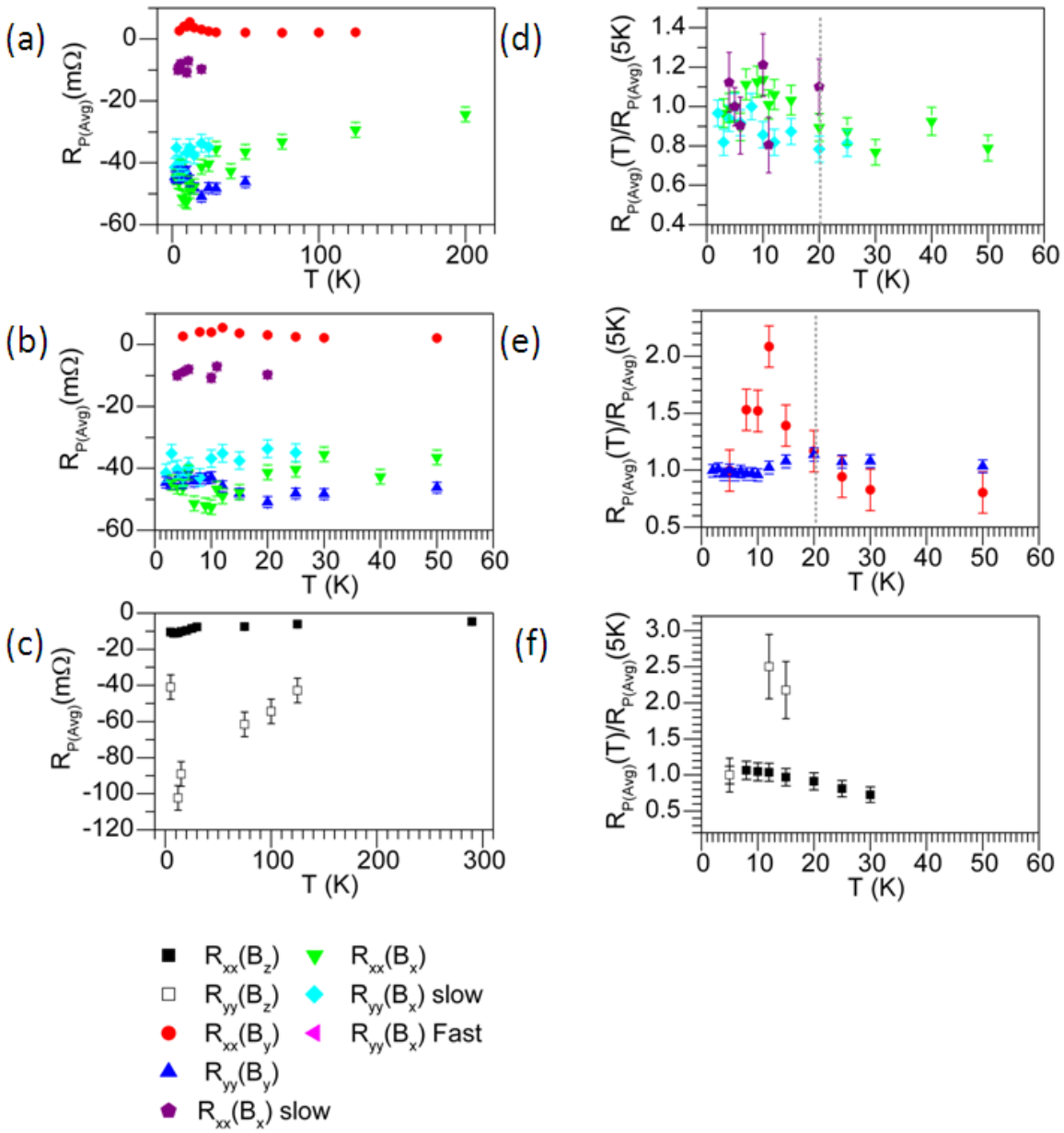

Figure 5.21 Temperature dependence of $R_{P(Avg)}$: (a) with an in-plane applied field, (b) low temperature region of (a) and (c) with an out of plane applied field. Temperature evolution of $R_{P(Avg)}$ normalised to 5K:(d) in-plane applied field in the x-direction, (e) in-plane applied field in the y-direction, (f) out of plane applied field.

5.2 Hall Resistance

5.2.1 Out of Plane 180° Magnetic Reversal

Figure 5.22 (a) and (b) shows the anomalous Hall resistance data $R_{xy}(B_z$ at 5 K and 75 K respectively. The current was applied in the x direction while the magnetic field was applied in the z-direction. Measuring the voltage perpendicular to both measures the charge built up due to the Lorentz force which when converted into a resistance is the so called anomalous Hall resistance. Figure 5.22(d) and (e) show the anomalous Hall resistance $R_{yx}(B_z)$ at 5 K and 100 K respectively. Schematics of both measurement configurations are shown in figure 5.22(c) and (f).

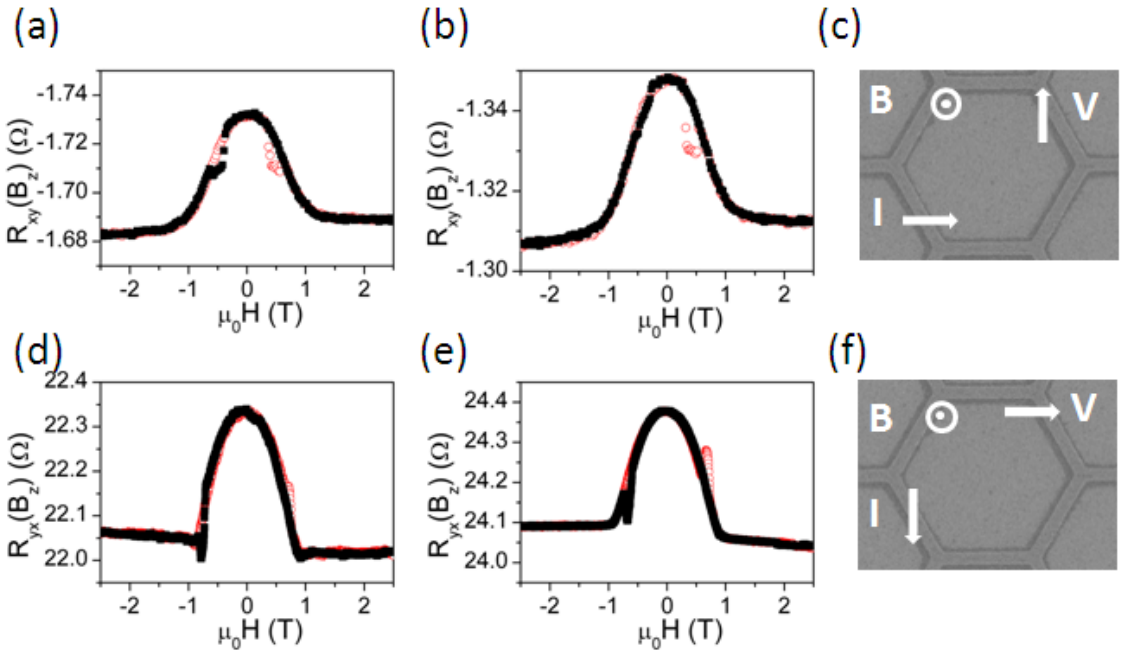

Figure 5.22 Out of plane Hall resistance data. $R_{xy}(B_z)$ (a) 5 K, (b) 75 K, relative field current and voltage orientation shown in (c). $R_{yx}(B_z)$ (d) 5 K, (e) 100 K, relative field, current and voltage orientation shown in (f).

The raw anomalous Hall resistance data at all measured temperatures can be found in appendix B.1.7. $R_{xy}(B_z)$ was measured at 5 K, 8 K, 10 K, 12 K, 15 K, 20 K, 25 K, 30 K, 75 K, 125 K and 290 K. $R_{yx}(B_z)$ was measured at 5 K, 12 K, 15 K, 75 K, 100 K and 125 K. During both measurements, the magnetic field was swept at a rate of 0.7 A/s which resulted in a data point roughly every 4.61 mT.

Both $R_{xy}(B_z)$ and $R_{yx}(B_z)$ exhibit a bell shaped magnetoresistance contribution between $\pm 1\ T$. This mixing of the Hall signal and the magnetoresistance is most likely due to a slight offset in the voltage electrodes. The difference between the irreversible resistance change at positive fields and negative fields of $R_{xy}(B_z)$ for all measured temperatures is shown in figure 5.23(a). Figure 5.23(b) shows $R_{xy,Avg}$ for all temperatures.

$R_{P(xy,Diff)}(B_z)$ was observed to initially decrease from -3.0±0.6 mΩ at 5 K down to a minimum of -1.4±0.6 mΩ at 12 K. After the initial decrease a maximum was reached at 75 K of -6.5±0.6 mΩ, after which $R_{P(xy,Diff)}(B_z)$ was seen to decrease slowly as the temperature approached 290 K. On the other hand, the average height of the irreversible peaks $R_{P(xy,Avg)}(B_z)$ was observed to be at a constant maximum level of 12.2±1.0 mΩ below temperatures of 10 K. Above 10 K $R_{P(xy,Avg)}(B_z)$ decreased rapidly to 7.9±1.0 mΩ until 30 K where $R_{P(xy,Avg)}(B_z)$ was seen remain constant until 120 K. At 290 K $R_{P(xy,Avg)}(B_z)$ was measured to be 5.6±1.0 mΩ. The temperature evolution of $R_{P(xy,Avg)}(B_z)$ and $R_{P(xx,Avg)}(B_z)$ was observed to follow the same trend.

The reversible and irreversible components extracted from $R_{yx}(B_z)$are shown in figure 5.24(a) to (c). $R_{P(yx,Diff)}(B_z)$ remained at a constant minimum level of -61.1±0.3 mΩ between 5 K and 12 K, above which an increase with temperature was observed reaching a value of -101.7±0.3 mΩ at 75 K (see figure 5.24(d)). An initial increase in $R_{P(yx,Avg)}(B_z)$ was observed from -39±4 mΩ at 5 K to a maximum of -65±4 mΩ at 15 K. Above 15 K $R_{P(yx,Avg)}(B_z)$ decreased and was observed to change sign between 100 K and 125 K (see figure 5.24(e)). At 125 K $R_{P(yx,Avg)}(B_z)$ was observed to be 30±4 mΩ. The change of $R_{P(yx,Avg)}(B_z)$ and $R_{P(yy,Avg)}(B_z)$ with temperature followed the same trends.

The intercept, extracted from the reversible part of $R_{yx}(B_z)$ (figure 5.24(c)) and $R_{xy}(B_z)$

(figure 5.23(c)), $R_{yx,Sat}(B_z)$ (figure 5.24(f)) and $R_{xy,Sat}(B_z)$ (figure 5.23(f)) was found to be negative through the measured temperature range. This is in agreement with the expected sign of the anomalous Hall of $Ni_{80}Fe_{20}$ ($\pm$ 2%) as published by Soffer *et al.* [61].

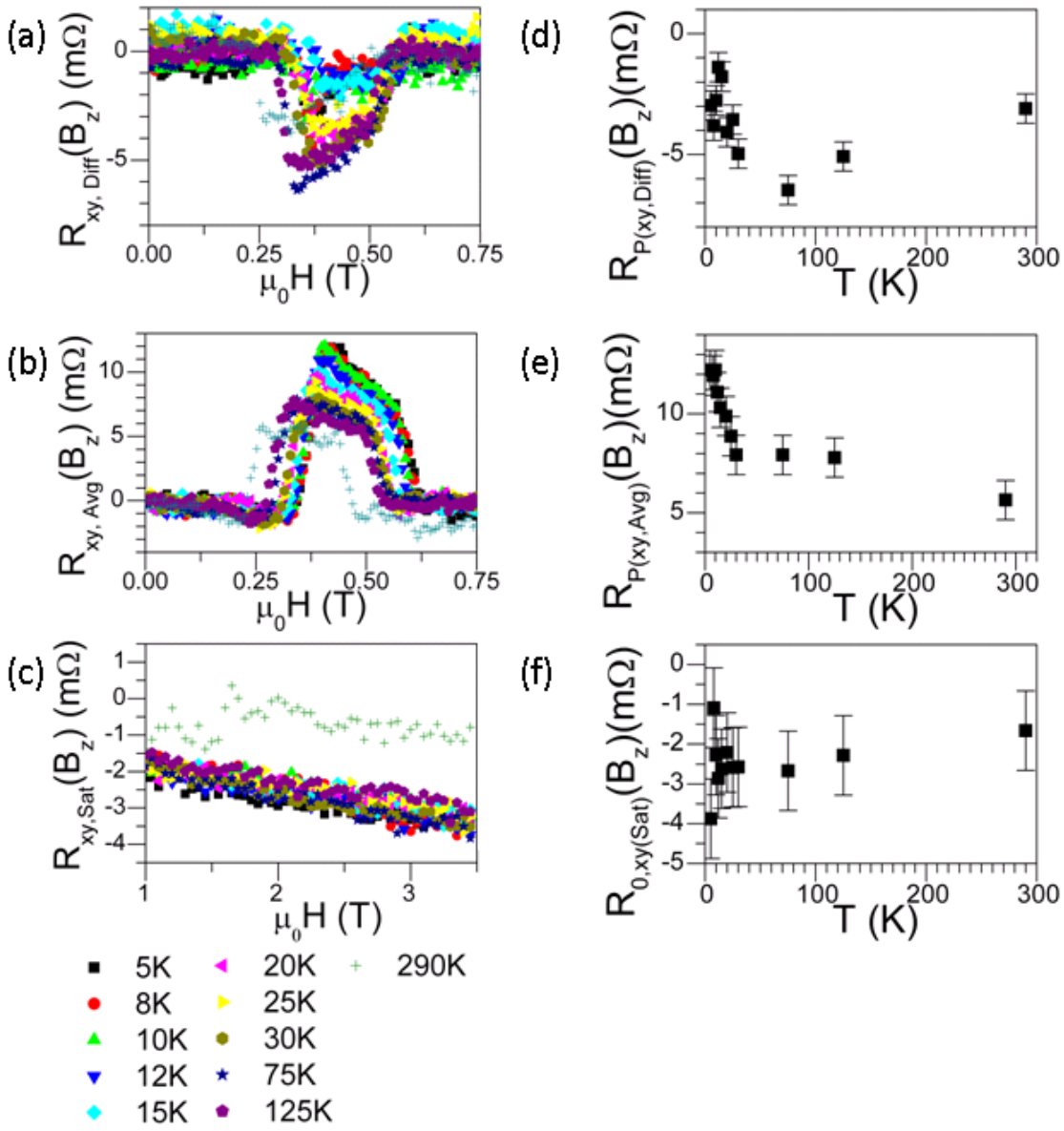

Figure 5.23 Reversible and irreversible components of $R_{xy}(B_z)$. (a) The difference between the irreversible resistance change at positive and negative field, $R_{xy,Diff}(B_z)$. (b) $R_{xy,Avg}(B_z)$, the average irreversible change in the resistance. (c) The high field reversible component $R_{xy,Sat}(B_z)$. (d) Temperature evolution of $R_{P(xy,Diff)}(B_z)$, the maximum peak height in (a). (e) $R_{P(xy,Avg)}(B_z)$, the maximum peak height in (b) versus temperature. (f) Intercept, extrapolated from $R_{xy,Sat}(B_z)$, $R_{0,xy(Sat)}(B_z)$ versus temperature.

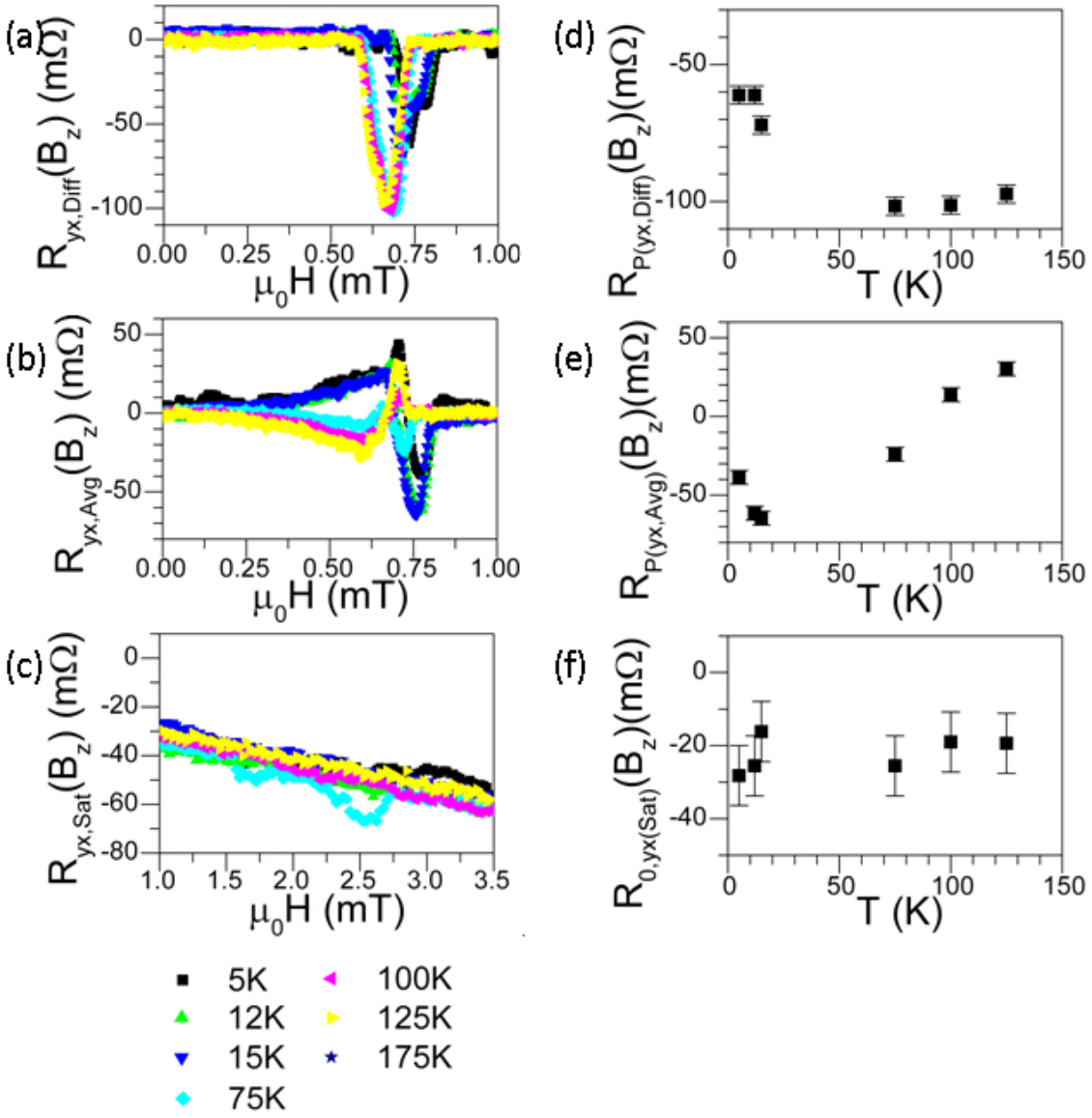

Figure 5.24 Reversible and irreversible components of $R_{yx}(B_z)$. (a) The difference between the irreversible resistance change at positive and negative field, $R_{yx,Diff}(B_z)$. (b) $R_{yx,Avg}(B_z)$, the average irreversible change in the resistance. (c) The high field reversible component $R_{yx,Sat}(B_z)$). (d) Temperature evolution of $R_{P(yx,Diff)}(B_z)$, the maximum peak height in (a). (e) $R_{P(yx,Avg)}(B_z)$, the maximum peak height in (b) versus temperature. (f) Intercept, extrapolated from $R_{yx,Sat}(B_z)$ $R_{0,yx(Sat)}(B_z)$ versus temperature.

5.2.2 In-plane Plane 180° Magnetic Reversal

The Hall resistance curves acquired during the in-plane magnetic reversal are shown in figure 5.25 for all measured configurations. $R_{yx}(B_y)$ measured at 5 K (figure 5.25(a)) and $R_{xy}(B_y)$ measured at 5 K (figure 5.25(d)) show a clear asymmetry in the low field region dominated by domain wall nucleation and propagation.

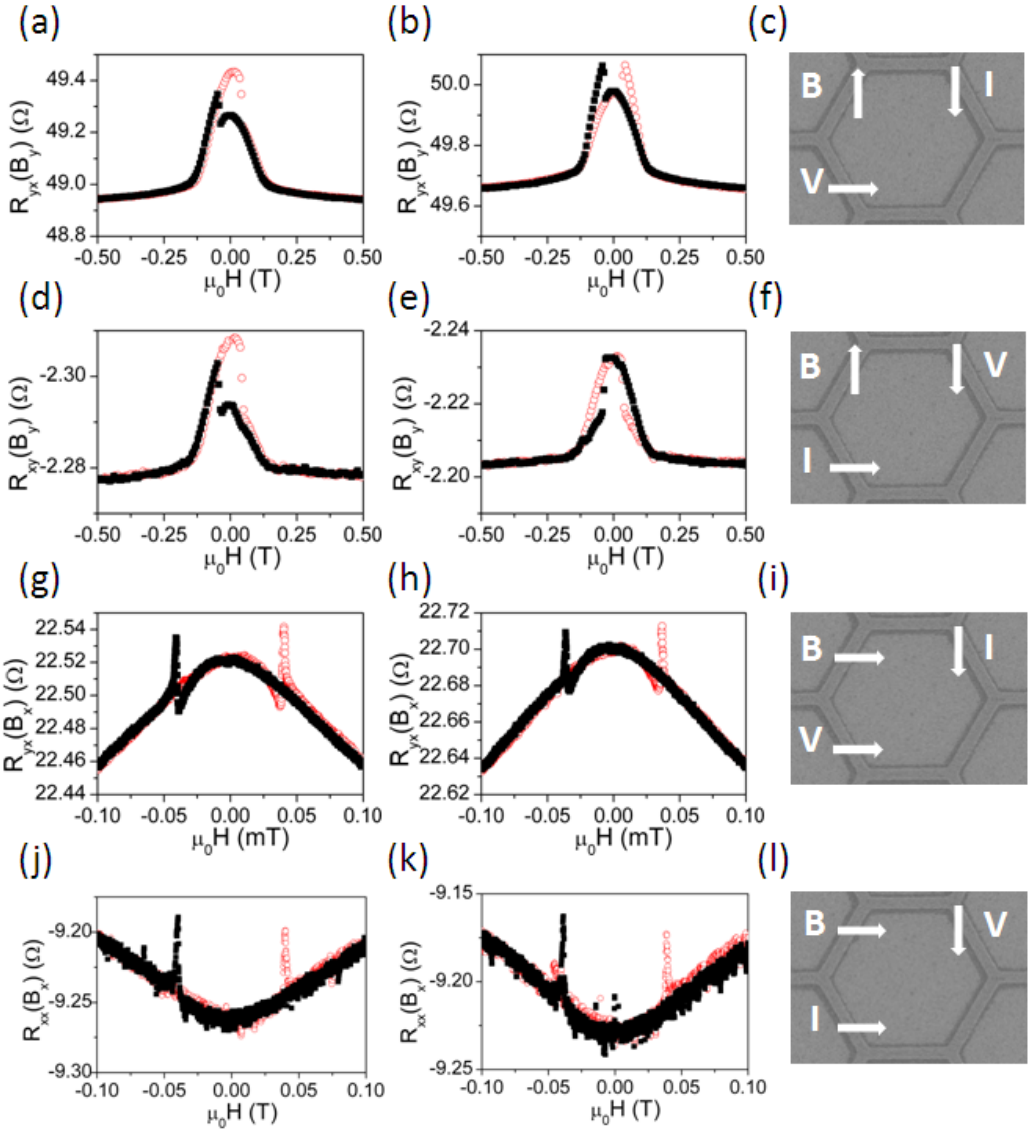

Figure 5.25 In-plane Hall resistance data. $R_{yx}(B_y)$ at (a) 5 K and (b) 50 K, relative field current and voltage orientation shown in (c). $R_{xy}(B_y)$ at (d) 5 K and (e) 50 K, relative field, current and voltage orientation shown in (f). $R_{yx}(B_x)$ at (g) 5 K and (h) 20 K, relative field current and voltage orientation shown in (i). $R_{xy}(B_x)$ at (j) 5 K and (k) 50 K, relative field, current and voltage orientation shown in (l).

At higher temperatures this asymmetry is not observed in either configuration (figure 5.25(b) and (e)). At 5 K a similar but more subtle asymmetry is observed in $R_{yx}(B_x)$ (figure 5.25(g)). $R_{xy}(B_x)$ at 5 K and 50 K is shown in figure 5.25(j) and (k) respectively.

The raw Hall resistance data at all measured temperatures can be found in appendix B.2.2. $R_{xy}(B_x)$ was measured at 8 K,10 K, 12 K, 15 K, 20 K, 25 K, 30 K, 40 K, 50 K, 100 K, 125 K and 175 K. The external field was swept at a rate of 0.03 A/s and sampled around every 30 Oe. Due to the large field steps the subtleties of the resistance change with the domain wall movement was not captured. Therefore only the reversible component of the Hall resistance was extracted and analysed (see figure 5.26(c) and (d)). The measurements were repeated at a rate of 0.01 A/s (a data point roughly every 5.0$\pm$0.3 Oe) in an attempt to resolve the peak in the irreversible part of the magnetic reversal in more detail. The low temperature regions were measured again at an even slower sweep rate at 4 K, 5 K, 6 K, 10 K, 11 K and 20 K acquiring a data point every 0.2 Oe. $R_{xy}(B_x)$ was measured at 3 K, 4 K, 5 K, 6 K, 7 K, 9 K, 10 K, 11 K, 12 K, 15 K, 20 K, 25 K, 30 K, 40 K, 50 K, 75 K, 125 K and 200 K. Similarly $R_{yx}(B_x)$ was measured at a rate of 0.03 A/s at 2 K,3 K, 4 K, 5 K, 6 K, 7 K, 8 K, 10 K, 15 K, 20 K, 25 K, 30 K, 40 K, 50 K, 75 K,100 K, 125 K, 150 K and 175 K and at a rate of 0.15 mA/s (field steps of roughly 0.8$\pm$0.2 Oe) at 2 K, 3 K, 4 K, 5 K, 6 K, 8 K, 10 K, 12 K, 15 K, 20 K, and 25 K.

The irreversible and reversible components of $R_{xy}(B_x)$ are shown in figure 5.26. The difference in the peak height at positive and negative field $R_{P(xy,Diff)}(B_x)$ is plotted in figure 5.26(a). However, field steps of 5.0$\pm$0.3 Oe are still to large to resolve the exact detail of the peak (solid black squares). $R_{P(xy,Diff)}(B_x)$ acquired every 0.2 Oe shows a decrease between 4 K and 6 K from an initial value of -5.8$\pm$2.5 mΩ down to 0.3$\pm$2.5 mΩ and then was seen to increase again between 10 K and 20 K (open red circle). However, $R_{xy}(B_x)$ was not measured at enough temperatures to resolve details. $R_{P(xy,Avg)}(B_x)$ was seen to increase with temperature until a maximum at 10$\pm$2 K of around 90 mΩ was reached. Above 10 K the average resistance change decreased rapidly; around 40 mΩ within 40 K. Between 50 K and 200 K a further decrease in $R_{P(xy,Avg)}(B_x)$ of roughly 10 mΩ was observed.

The reversible component $R_{xy,Sat}(B_x)$ was measured to be field independent (see figure 5.26(c)). The intercept, $R_{0,xy(Sat)}(B_x)$, was extracted to be 0 mΩ for all temperatures within the limits of the error (see figure 5.26(f)). Hence, no anomalous Hall signature was observed for an in plane measurement, as expected.

The irreversible and reversible components of $R_{yx}(B_x)$ are shown in figure 5.27. The sharp positive peak was labeled peak 1 and the broad negative peak was referred to as peak 2 (see figure 5.25(g) and (h)). $R_{P(yx,Diff)}(B_x)$ and $R_{P(yx,Avg)}(B_x)$ for both peak 1 and 2 can be seen in figure 5.27(a) and (b) respectively. $R_{P1(yx,Diff)}(B_x)$ showed an increase from 1±1 mΩ to 6±1 mΩ between 2 K and 3 K and then steadily decreased down to 2±1 mΩ. $R_{P1(yx,Diff)}(B_x)$ was observed to jump from 2±1 mΩ to 8±1 mΩ between 6 K and 8 K. By 10 K $R_{P1(yx,Diff)}(B_x)$ was measured to be 3±1 mΩ. Above 15 K $R_{P1(yx,Diff)}(B_x)$ vanished. The value of $R_{P1(yx,Diff)}(B_x)$ at 8 K seems to be an abnormality. Ignoring this point reveals a sharp increase between 2 K and 3 K then a rapid decrease until 6 K above which $R_{P1(yx,Diff)}(B_x)$ was seen to remain approximately constant at a small non zero value until its disappearance at 15 K. $R_{P2(yx,Diff)}(B_x)$ was observed to stay roughly constant at around -3±1 mΩ until it decreased to zero between 15 K and 20 K. $R_{P1(yx,Avg)}(B_x)$ was seen to increase from 26±1 mΩ at 2 K to 36±1 mΩ at 8 K above which $R_{P1(yx,Avg)}(B_x)$ decreased back down to a value around 26±1 mΩ at 15 K. At temperatures above 15 K $R_{P1(yx,Avg)}(B_x)$ was observed to remain approximately constant. On the other hand, $R_{P2(yx,Avg)}(B_x)$ was seen to stay approximately constant between 2 K and 15 K at a value of approximately -13 mΩ fluctuating only slightly by 2 mΩ. At temperatures above 15 K a slight decrease in $R_{P2(yx,Avg)}(B_x)$ to 10 mΩ was found.

The reversible component $R_{yx,Sat}(B_x)$ was found to be field independent. $R_{0,yx(Sat)}(B_x)$ for all temperatures was measured to be 0 mΩ within the limits of the error. Again, as expected for an in-plane measurement, no anomalous Hall signature was observed.

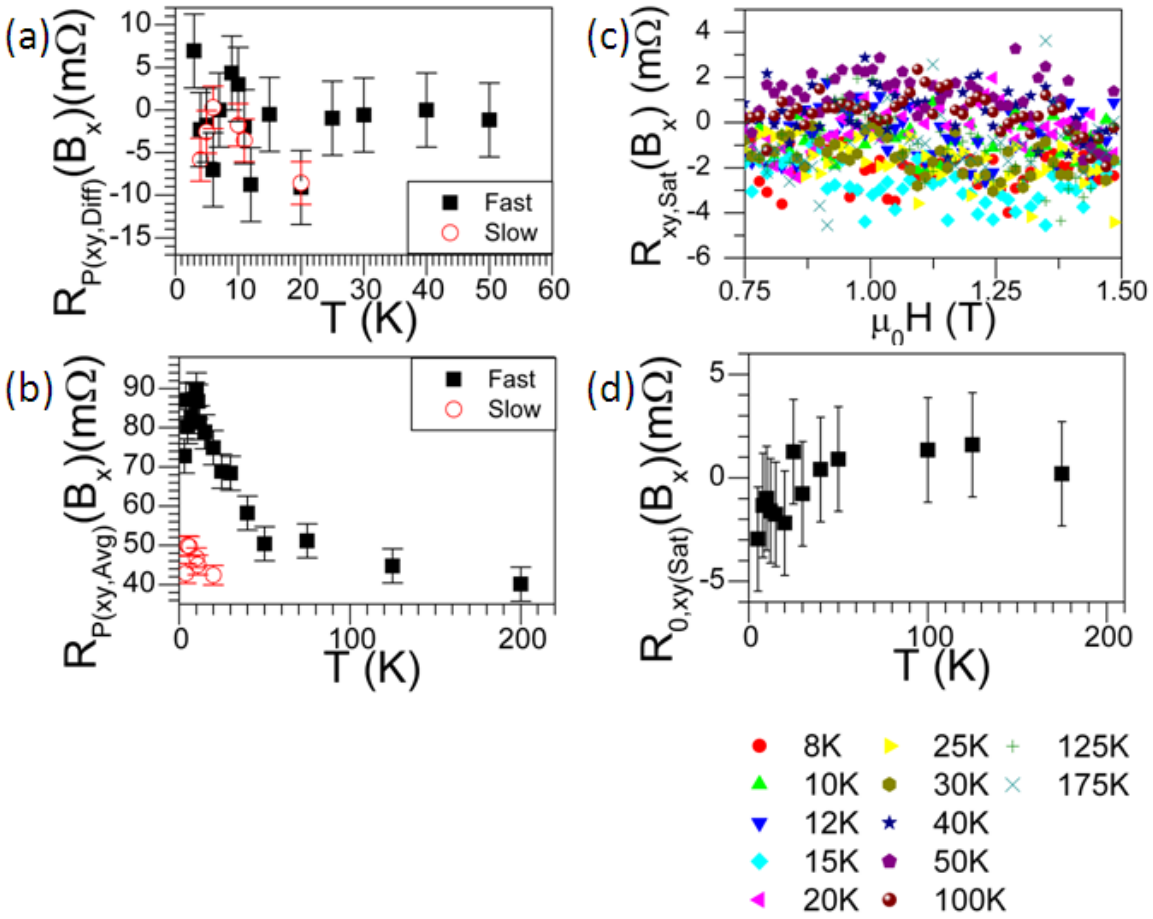

Figure 5.26 Reversible and irreversible components of $R_{xy}(B_x)$. (a) Temperature evolution of the sharp positive peak in $R_{xy}(B_x)$, $R_{P(xy,Diff)}(B_x)$. (b) $R_{P(xy,Avg)}(B_x)$ versus temperature of the sharp positive peak in $R_{xy}(B_x)$. (c) The high field reversible component $R_{xy,Sat}(B_x)$. (d) $R_{0,xy(Sat)}(B_x)$ versus temperature.

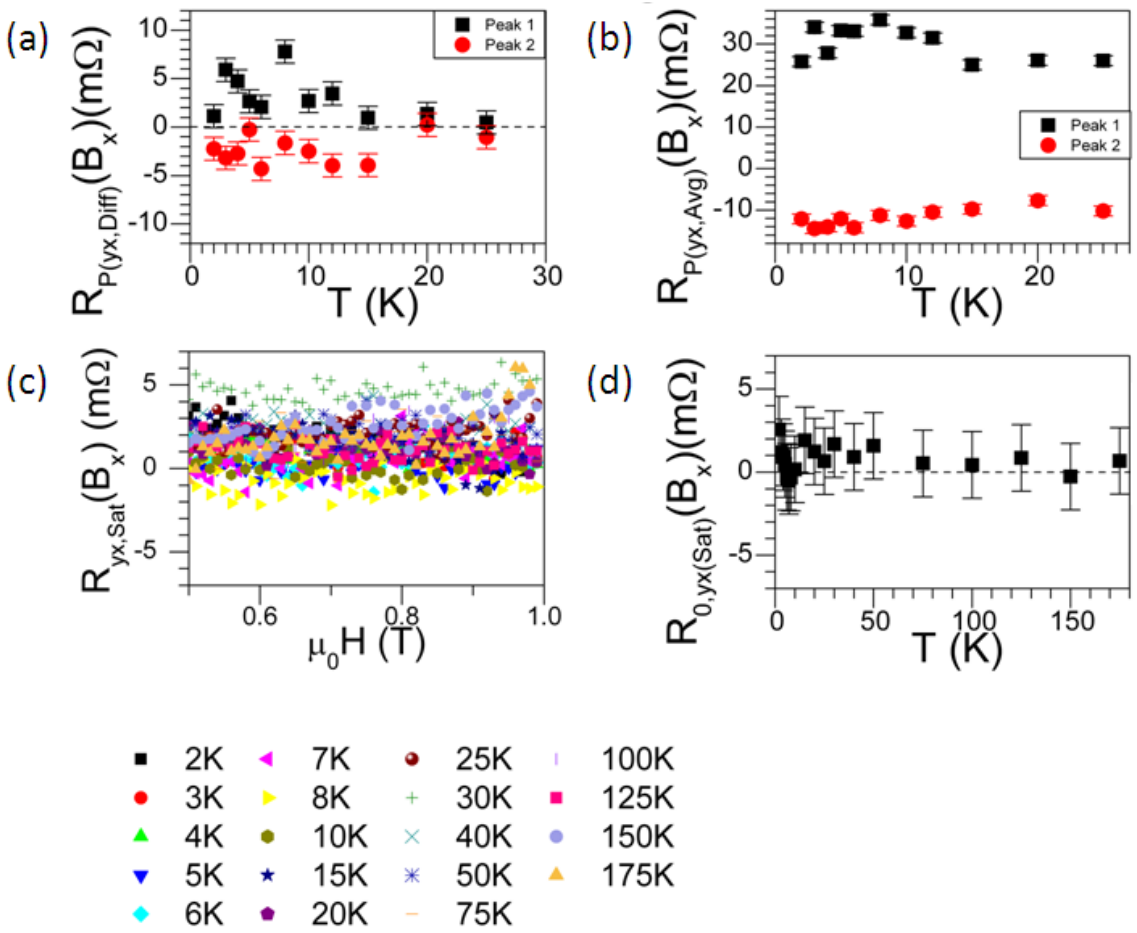

Figure 5.27 Reversible and irreversible components of $R_{yx}(B_x)$. (a) Temperature evolution of $R_{yx}(B_x)$, $R_{(yx,Diff)}(B_x)$. (b) $R_{P(yx,Avg)}(B_x)$ versus temperature. Peak 1 refers to the sharp positive peak and Peak 2 refers to the broader peak at lower fields in $R_{yx}(B_x)$. (c) The high field reversible component $R_{yx,Sat}(B_x)$. (d) $R_{0,yx(Sat)}(B_x)$ versus temperature.

Figure 5.28 shows the irreversible and reversible component of $R_{xy}(B_y)$. The two irreversible components $R_{xy,Diff}(B_y)$ and $R_{xy,Avg}(B_y)$ are shown in figure 5.28(a) and (b) respectively. The temperature evolution height of the peaks observed in $R_{xy,Diff}(B_y)$ and $R_{xy,Avg}(B_y)$, $R_{P(xy,Diff)}(B_y)$ and $R_{P(xy,Avg)}(B_y)$ show distinct features (see figures 5.28(d) and (e)). $R_{P(xy,Diff)}(B_y)$ decreases with temperature vanishing between 12 K and 20 K. At 5 K $R_{P(xy,Diff)}(B_y)$ was found to be 14.9$\pm$0.4 mΩ and $R_{P(xy,Avg)}(B_y)$ was measured to be -1.8$\pm$0.6 mΩ. Between 8 K and 10 K $R_{P(xy,Avg)}(B_y)$ changed sign reaching a maximum at 25 K of 11.4$\pm$0.6 mΩ. A slight decrease of $R_{P(xy,Avg)}(B_y)$ with increasing of temperature was observed reaching a value of 8.5$\pm$0.6 mΩ at 125 K.

The reversible component $R_{xy,Sat}(B_y)$ was measured to be field independent. The intercept, $R_{0,xy(Sat)}(B_y)$, was extracted to be 0 mΩ.

Figure 5.29(a), (b) and (c) show the irreversible components $R_{yx,Diff}(B_y)$, $R_{yx,Avg}(B_y)$ and the reversible high field component $R_{yx,Sat}(B_y)$ for $R_{yx}(B_y)$ respectively. The temperature evolution of $R_{P(yx,Diff)}(B_y)$ is shown in figure 5.29(d). $R_{P(yx,Diff)}(B_y)$ decreased from a maximum value of 168.7$\pm$1.6 mΩ at 3 K with increasing temperature, vanishing at between 12 K and 15 K. 65% of the decrease occurred between 9 K and 12 K. $R_{P(yx,Avg)}(B_y)$ was observed to be at a minimum at 3 K of 24.8$\pm$1.6 mΩ increasing with increasing temperature reaching 127.4$\pm$1.6 mΩ by 12 K. $R_{P(yx,Avg)}(B_y)$ was found to stay approximately constant above 12 K.

$R_{yx,Sat}(B_x)$ was found to be field independent. $R_{0,yx(Sat)}(B_y)$ for all temperatures was found to be approximately 0 mΩ within the limits of the error as expected for an in plane measurement, indicating the absence of an anomalous Hall signature.

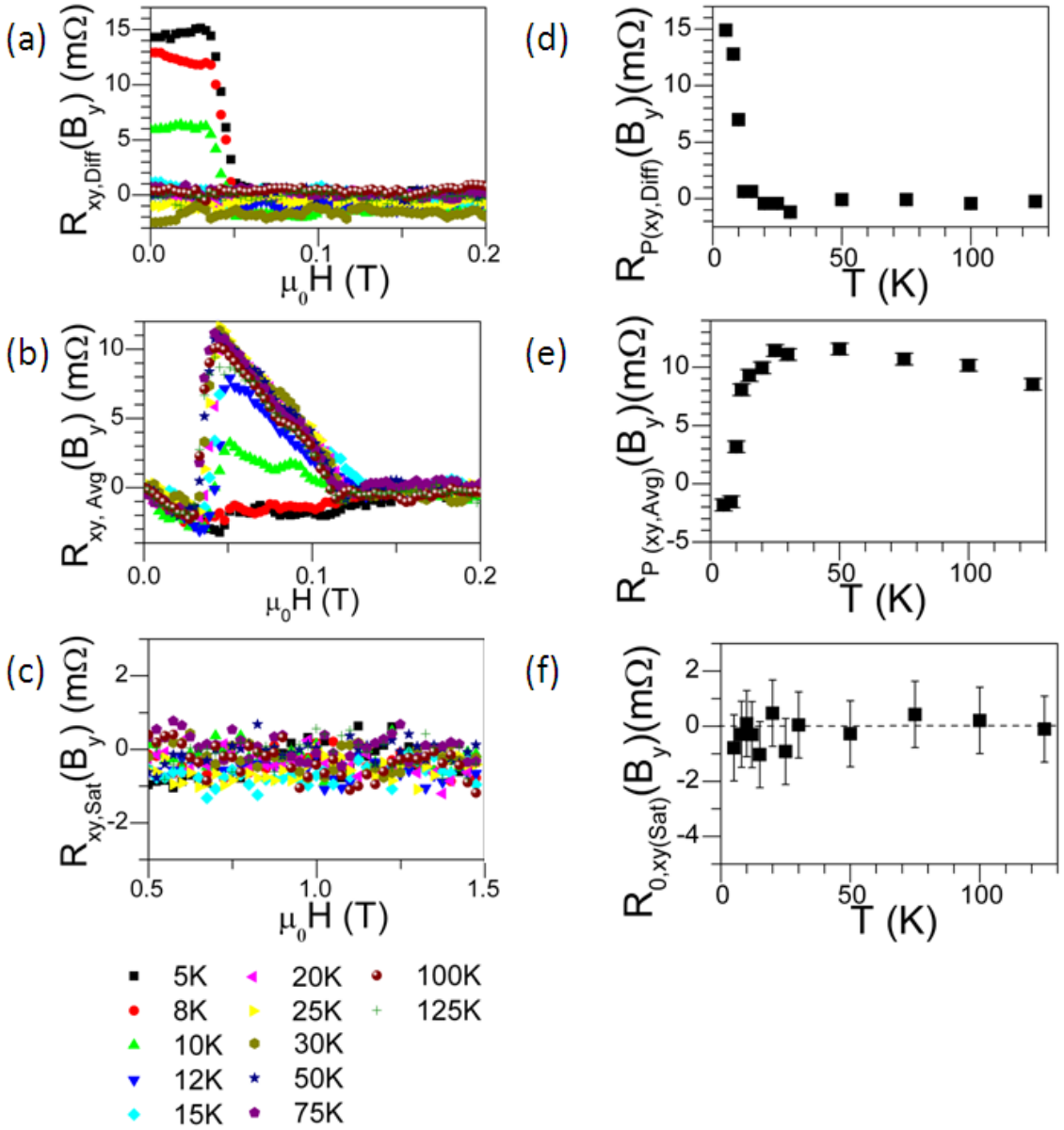

Figure 5.28 Reversible and irreversible components of $R_{xy}(B_y)$. (a) The difference between the irreversible resistance change at positive and negative field, $R_{xy,Diff}(B_y)$. (b) $R_{xy,Avg}(B_y)$, the average irreversible change in the resistance. (c) The high field reversible component $R_{xy,Sat}(B_y)$). (d) Temperature evolution of $R_{P(xy,Diff)}(B_y)$, the maximum peak height in (a). (e) $R_{P(xy,Avg)}(B_y)$, the maximum peak height in (b) versus temperature. (f) $R_{0,xy(Sat)}(B_y)$ versus temperature.

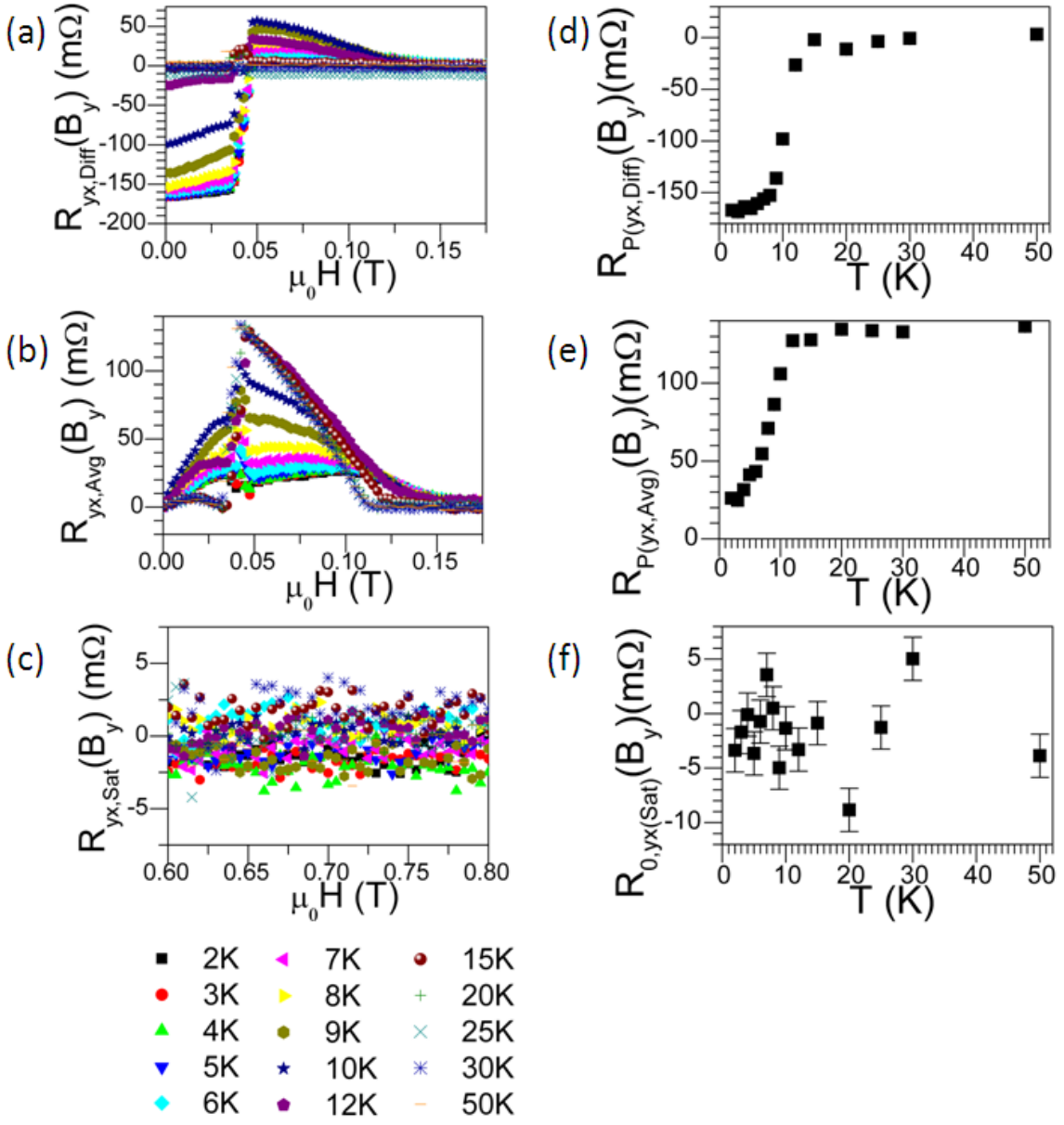

Figure 5.29 Reversible and irreversible components of $R_{yx}(B_y)$. (a) The difference between the irreversible resistance change at positive and negative field, $R_{yx,Diff}(B_y)$. (b) $R_{yx,Avg}(B_y)$, the average irreversible change in the resistance. (c) The high field reversible component $R_{yx,Sat}(B_y)$). (d) Temperature evolution of $R_{P(yx,Diff)}(B_y)$, the maximum peak height in (a). (e) $R_{P(yx,Avg)}(B_y)$, the maximum peak height in (b) versus temperature. (f) $R_{0,yx(Sat)}(B_y)$ versus temperature.

5.2.3 Discussion

Figure 5.30 shows the temperature dependence of the asymmetry in the Hall resistance. Normalizing $R_{P(Diff)}$ to 5 K shows that the evolution of temperature dependent feature is dependent on the applied field direction. The asymmetry in the in-plane Hall resistance vanishes above approximately 15 K. However, whereas $R_{P(xy,Diff)}(B_y)$ and $R_{P(yx,Diff)}(B_y)$ increase rapidly below 15 K, the evolution of $R_{P(xy,Diff)}(B_x)$ and $R_{P(yx,Diff)}(B_x)$ below 15 K seems more complicated, possibly showing a double peak. In order to resolve the details of the asymmetry in the B_x configuration measurements at more temperatures are needed. $R_{P(xy,Diff)}(B_z)$ and $R_{P(yx,Diff)}(B_z)$ was seen to increase with temperature, showing a maximum between 30 K and 75 K.

Permalloy artificial spin ice shows similar asymmetric features at low temperatures to cobalt artificial spin ice [3]. This is most likely due to a fundamental change in the magnetic switching mediated via domain walls. The low temperature increase in the average peak height acquired in the in-plane magnetoresistance geometries $R_{P(Avg)}$ hints at a change in the dominating vertex magnetisation states. Such a magnetisation change could be due to vertex dipole interactions starting to influence the magnetic reversal at temperatures below T^{II}_{ice}. Using equation 5.3 the ratio of the ordering temperature of cobalt, $T^{II}_{ice,Co}$, and permalloy, $T^{II}_{ice,Py}$, is given by

$$\frac{T^{II}_{ice,Co}}{T^{II}_{ice,Py}} = \left(\frac{M_{Co}}{M_{Py}}\right)^2 \sim 3 \tag{5.9}$$

hence a transition temperature of 17K is expected for permalloy artificial spin ice. The experimentally observed ratio is using $T^{II}_{ice,Co} = 50 \pm 10$ K and $T^{II}_{ice,Py} = 15 \pm 3$ K:

$$\frac{T^{II}_{ice,Co}}{T^{II}_{ice,Py}} \sim 3.3 \pm 0.9, \tag{5.10}$$

which agrees with the ratio expected from theory.

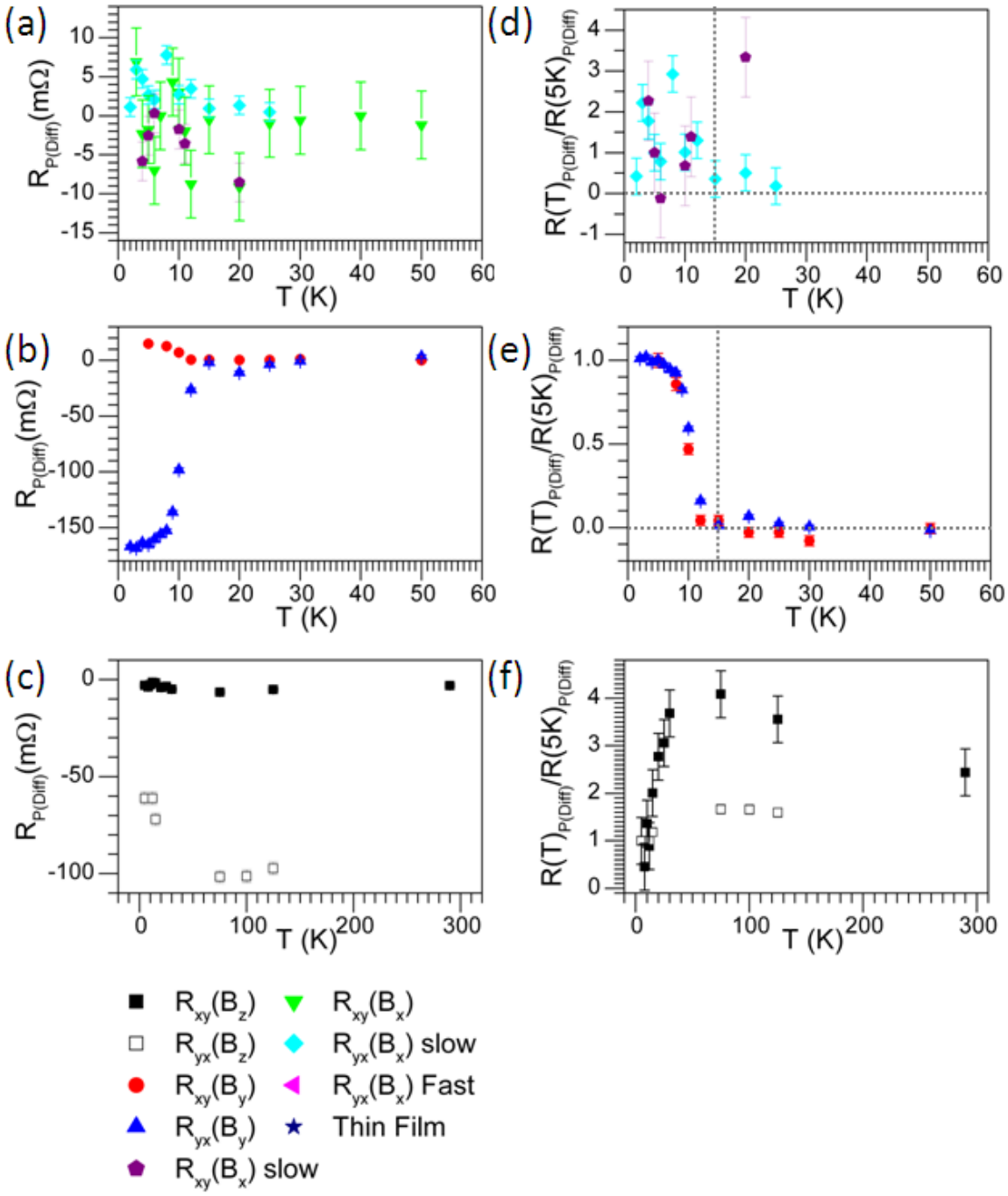

Figure 5.30 Temperature dependence of $R_{P(Diff)}$. $R_{P(Diff)}$ extracted from the Hall resistance measurement obtained during the magnetic reversal due to the applied field in the (a) x-direction, B_x (b) y-direction, B_y and (c) z-direction, B_z. (d), (e) and (f) show $R_{P(Diff)}$ plotted in (a), (b), and (c) normalised to 5 K respectively.

In the case of 180° magnetic reversal due to an applied magnetic field in the x-direction OOMMF simulations show the formation of magnetisation loops forming close to the edges 5.31(a)-(e). The following parameters were used to simulate the permalloy artificial spin ice: $M = 800 \times 10^3$ Am^{-1}, $A = 1.4 \times 10^{-11}$ Jm^{-1}, and a mesh cell size of $[x,y,z] = [5nm, 5nm, 18nm]$. The minimum magnetisation configuration was calculated every 5 mT. These loop states fix the vertex domain wall states at the edges of the array and hence one can identify low resistance current path (see figure 5.31(h) and (i) for loops at the top and bottom edge). The low resistance current path, anticlockwise loops at the top (A_{Top}) and clockwise loops at the bottom (C_{Bottom}), ensure a deflection of the current towards the edges. Clockwise loops at the top (C_{Top}) and anticlockwise loops at the bottom (A_{Bottom}) would result in a deflection of the current carriers towards the center of the array. Hence a charge built-up can only occur if $(A_{Bottom} - C_{Top}) - (C_{Bottom} - A_{Top})$ is non-zero.

In the case of 180° magnetic reversal due to an applied magnetic field in the y-direction the loop states cannot form at zero applied field. However, the asymmetry observed is apparent at and around zero fields (see figure 5.25(a)-(f)). Similar resistance shifts have been observed in the resistance of cobalt zigzag nanowires when a magnetic field at 40° to the wires was applied [104]. The zigzag wire consists of 30 nanowires, 15 at 45° and 15 at -45° to the x-axis. Applying a field at ±40° causes the magnetisation of the 15 45° nanobars to change the magnetisation direction with the external magnetic field while the magnetisation of the remaining 15 segments is essentially undisturbed at low fields. Therefore there is a two fold degenerate zero field state depending on the saturation direction.

In the B_y magnetic reversal of the honeycomb artificial spin ice, the magnetisation of the diagonal bars will follow the general direction of the field, providing initial saturation along y. However, the magnetisation of the horizontal bars at zero field is more ambiguous, the magnetic moment will either be parallel to the x- or -x-direction. The similarity between the Hall resistance feature and the resistance change measured in zigzag wires fuel the assumption that the magnetisation of the horizontal bar does not change under the application of the magnetic field at temperatures below 15 K. Possible configurations

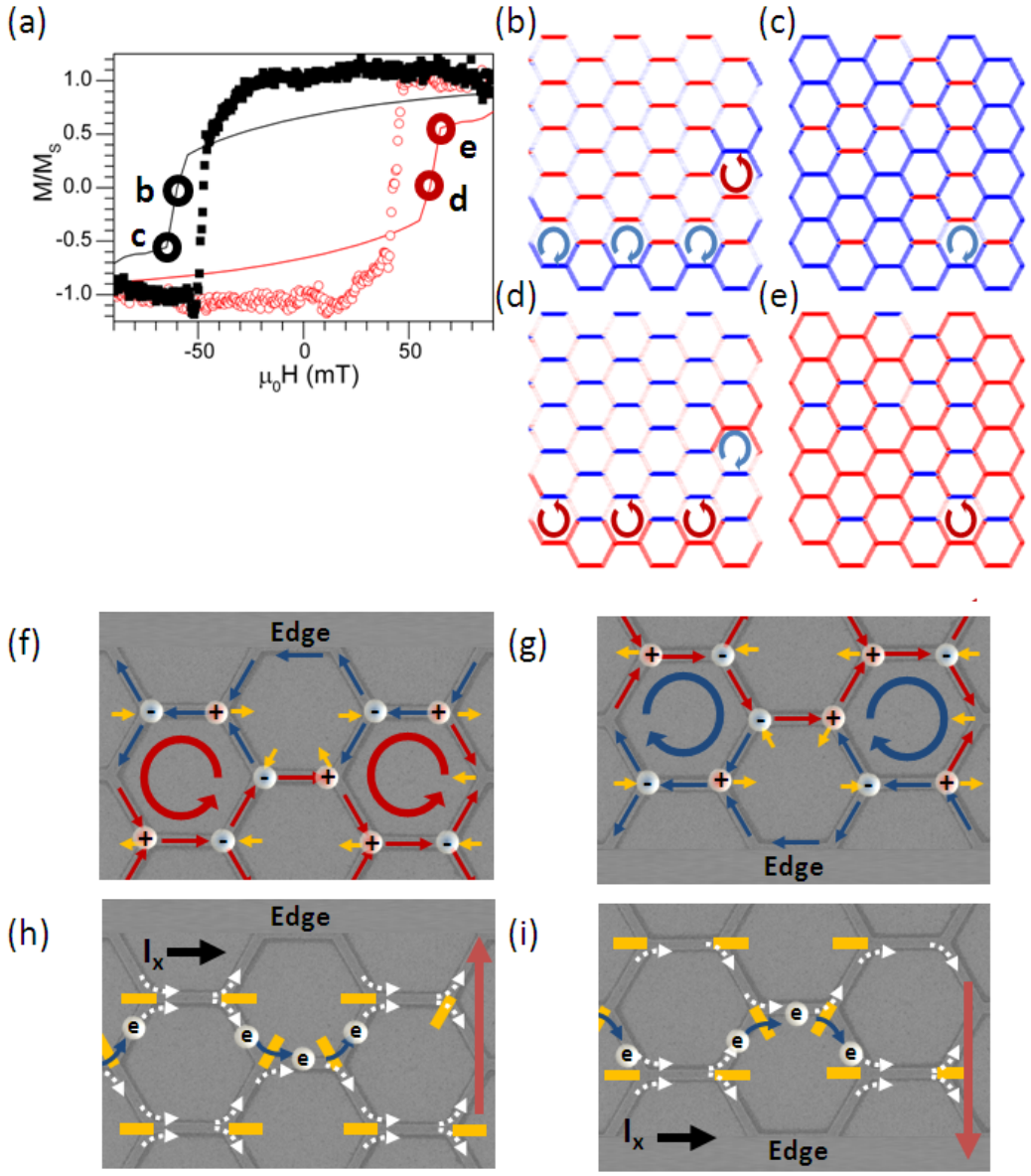

Figure 5.31 Low current path due to domain wall configuration in the B_x magnetic reversal. (a) Normalised magnetisation versus external field calculated by OOMMF (solid lines) in comparison to the 2 K normalised magnetisation determined from the magnetoresistance measurement (black solid squares, red open circles). (b) to (e) OOMMF simulations at selected points along the reversal (as indicated on the MH loop). Vertex dipole arrangement for magnetisation loops close to the top edge (f) and bottom edge (g). The low resistance current path (blue arrows) associated with states (f) and (g). Domain walls are marked with an orange rectangle. The red arrow indicates the average deflection of the charge carriers.

at zero field after saturation in -y and +y are shown in figure 5.32(a) and (b) respectively. The systematic arrangement of the domain walls could cause a deflection of the current carriers towards the edges for both a current along x (figure 5.32(c) and (d)) and a current along y (figure 5.32(e) and (f)).

The charge deflection towards or away from the edge due to low resistance path is expected to be quite small. The difference in resistance of current passing through a single nanowire with a domain wall and without a domain wall is $\Delta R \sim 0.03\% - 0.04$ [50]. The asymmetry constitutes 0.03% of the arrays resistance in permalloy.

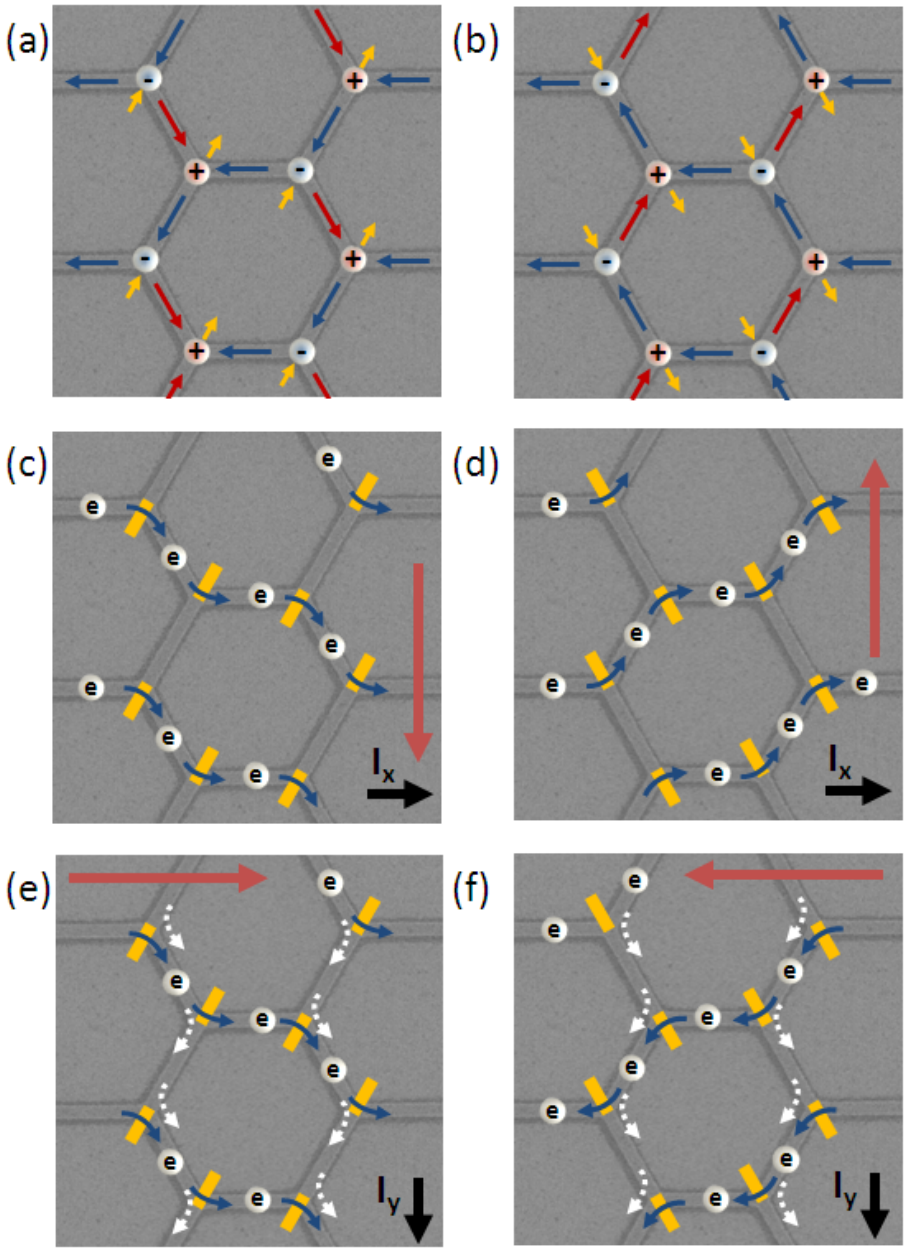

Figure 5.32 Low current path due to domain wall configuration in the B_x magnetic reversal. (a) vertex dipole arrangement at zero fields after saturation in the (a) -y-direction and (b) +y-direction. Low resistance current path for a current applied in the x-direction for (c) magnetisation state as shown in (a) and (d) magnetisation state as shown in (b). Low resistance current path for a current applied in the y-direction for (e) magnetisation state as shown in (a) and (f) magnetisation state as shown in (b). Domain walls are marked with an orange rectangle and the low resistant path is marked by blue arrows. The red arrow indicates the average deflection of the charge carriers.

5.3 Conclusion

The field dependent resistance of a permalloy honeycomb artificial spin ice array was measured between 2 K and 290 K for a series of Hall and magnetoresistance geometries. The array consisted of bars of width 118±2 nm, length 1000±10 nm and thickness 18±2 nm. An asymmetry in the in-plane Hall resistances was observed below 15 K. The occurrence was correlated with a change in the magnetoresistance peak height and a change in the peak field. The height of the magnetoresistance peak was thought to be due to the ratio of high and low resistance vertices in the array; a change in the magnetisation reversal would influence the ratio and hence would be observed as a change in the average peak height. Therefore the field dependent asymmetry in the Hall resistance is likely to be caused by a change in the magnetisation reversal below 15±2 K. Figure 5.33 shows the onset of the field inversion asymmetry of the in-plane configurations. For comparison $R_{P(xy,Diff)}(B_x)$ extracted from measurements on cobalt artificial spin ice, with an onset temperature of 50 K, is shown as well [3]. Field inversion asymmetry is a distinctive signature of the Hall effect. However, in artificial spin ice the magnetisation lies in the sample plane a crucial requirement of the Hall effect. We attribute the asymmetry to an ordered arrangement of the vertex domain wall at low temperatures, creating low resistance paths.

A phase transition was predicted to occur for dipoles on a honeycomb lattice [102] with a transition temperature which was expected to scale with the bar dimensions and the square of the saturation magnetisation M_{sat}^2. By comparing artificial spin ice array fabricated from cobalt and permalloy while keeping the bar dimensions constant allows the verification of the transferability of the long range dipole model onto artificial spin ice. The experimentally obtained ratio between the transition of the cobalt and permalloy honeycomb artificial spin ice (3.3±0.9) agreed with the theory.

The work in this chapter confirms, that the observed changes in the field dependent resistance, far below the Curie temperature, is a characteristic feature of artificial spin ice and not singular to cobalt artificial spin ice.

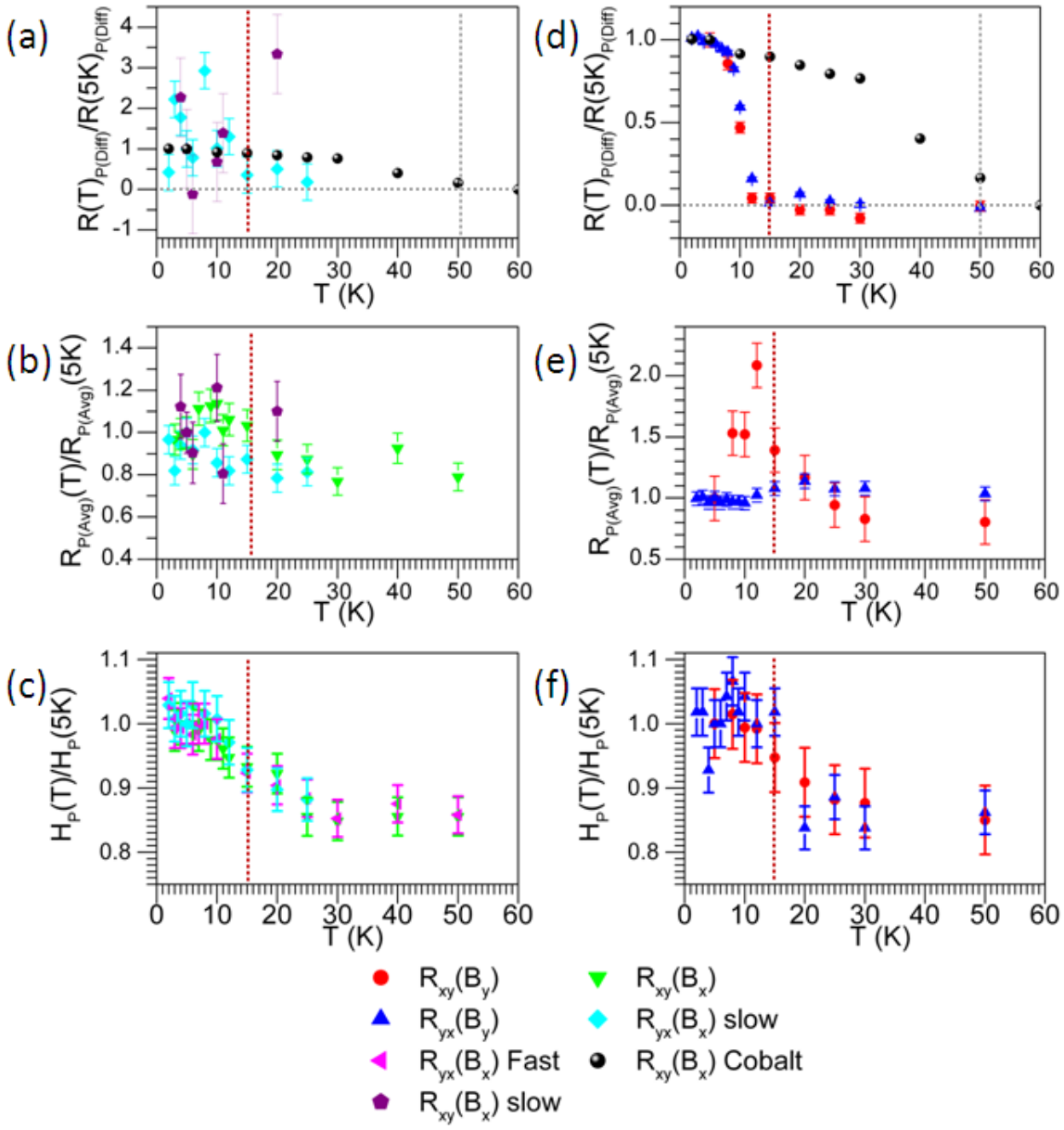

Figure 5.33 Comparison of features extracted from in-plane magnetoresistance measurement under field application in the x-direction normalised to 5 K (a) $R_{P(Diff)}$, (b) $R_{P(Avg)}$ and (c) H_P. Comparison of features extracted from in-plane magnetoresistance measurement under field application in the y-direction normalised to 5 K (a) $R_{P(Diff)}$, (b) $R_{P(Avg)}$ and (c) H_P. The normalised temperature dependence of $R_{P(xy,Diff)}(B_x)$ was added to (a) and (b). Red (gray) dotted line indicates transition temperature for permalloy (cobalt).

Chapter 6

Three Dimensional Artificial Spin Ice

In the preceding chapters the geometrical frustration of two dimensional honeycomb and square artificial spin ice has been investigated in detail. However, both these geometrical frustrated structures have drawbacks: the former possesses a non zero magnetic charge background due to an odd number of wires joining at each vertex and the latter due to non-equivalent interactions between the four nearest neighbours. In this chapter we consider the magnetic behaviour of a potential three dimensional artificial spin ice, magnetic inverse opals, which potentially eliminates two major disadvantages of the former artificial spin ice nanostructures. Permalloy inverse opals, with a void diameter of 300 nm, were investigated through room temperature magnetometry, scanning transmission X-ray microscopy and Lorentz transmission electron microscopy. The magnetic reversal of quasi two and three dimensional permalloy inverse opals was studied at low temperatures by means of electrical transport. The measurements suggest that three dimensional permalloy inverse opal is indeed a geometrical frustrated artificial spin ice.

Three dimensional inverse opals are ordered macroporous structures heavily studied for their usability for a range of applications, including surface enhanced Raman spectroscopy [105] and nanoplasmonics [106]. The fabrication process of such structures by electrochemical deposition through self assembled ordered templates was pioneered by Bartlett *et al.* [107]. The inverse opals are constructed by growing a metal around fcc closed packed templates of polystyrene spheres. The metal, in this case permalloy, can be electrochemically grown around the crystalline template which is then removed to leave the inverse structure. The template consists of repeating layers A, B and C. Each sphere is surrounded by 12 neighbors: three in the layer below (layer A), six in the same layer (layer B) and three in the layer above (layer C). Figure 6.1(b) depicts the top down view of layer A, B and C, coloured blue, green and orange respectively. The dotted squares show the top down interstices running through the layers; The orange box encases the narrow free space running through aligned holes in layer A and B, framed by the two subsequent C layers, the green and the blue box highlight the opening running through layer C and A and B and C respectively. Figure 6.1(c) shows a schematic of the connective voids in gray joined at the vertices (colour coded spheres). The position of the spherical junctions are highlighted in figure 6.1(b). As the metal is grown around a spherical template the bars will possess concave edges and their joints will mirror a concaved tetrahedrons. Figure 6.1(d) shows a projection of two connected vertices (c) onto the pyrochlore lattice. The sizes of the nanobars and vertices can be estimated considering spheres nesting in the voids of the spherical template. The largest space available enclosed by the template forms the vertices (see figure 6.1(e), red sphere enclosed by blue template spheres); the biggest sphere able to fit in the space has a diameter of $d = 0.225a$ (red circle in figure 6.1(f)), where a is the radius of the template spheres. The wire diameter of the can be estimated by considering the maximum diameter of a sphere which still fits through the narrowest space framed by the surrounding spheres (blue circle in 6.1(f)).The maximum available diameter of the connective bars is then $d = 0.155a$. The center to center distance between vertices is given by $L = 2a\sqrt{3/8} = 1.224a$. Thus a length to width ratio of $L/w \sim 8$ is achieved.

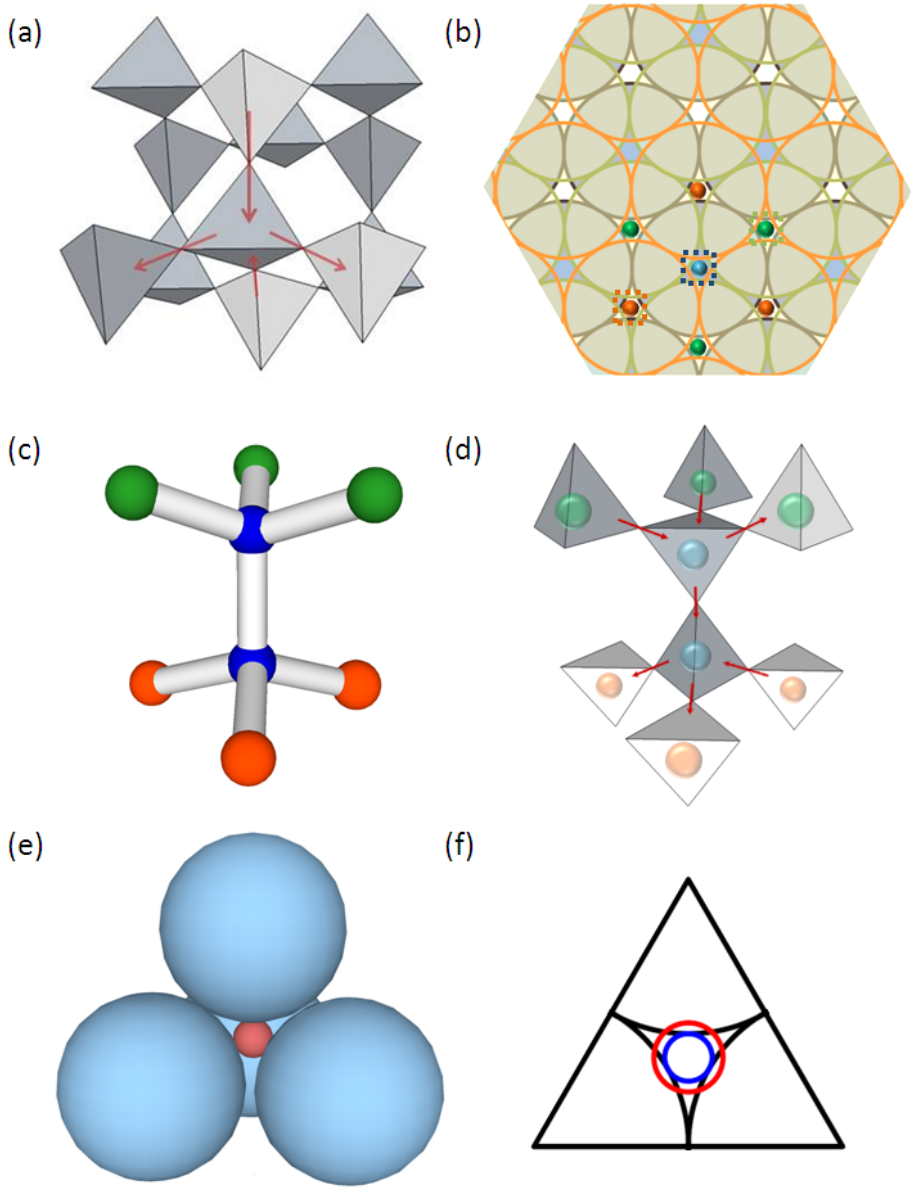

Figure 6.1 The inverse opal and pyrochlore lattice. (a) Pyrochlore lattice shown as corner sharing tetrahedron. The spin of the rare earth atoms located at the four corners of each tetrahedron points along the easy axis between the tetrahedron centers. (b) Top down view of close packed arrangement of spheres with radius a (bottom layer blue, middle layer green and top layer orange). (c) Inverse opal approximated as spherical nanoparticles connected by cylindrical nanowires of length $L = a\sqrt{3/8}$. (d) Projection of the nanoparticle arrangement onto the pyrochlore lattice. (e) The size of the nanoparticles is determined by the largest possible in-sphere (red) fitting into the void of the closed packed template (blue). (f) Cut through the basal plane of (e) showing the maximum wire diameter (blue circle) and the in-sphere diameter (red circle).

6.1 Fabrication

All structures discussed in this chapter where grown by Chahat Kansal, a research master student (graduated in August 2011) if not otherwise stated. Complete details on their growth are given in her Masters thesis: *Ordered Macroporous Structures as Artificial Spin Ice Systems* [108]. Polystyrene sphere templates were self-assembled using a Langmuir-Blodgett technique [109]. The polystyrene sphere suspension, consisting of 300 nm diameter spheres, was added drop-wise onto the surface of deionised water. Self-assembly of an ordered monolayer was achieved through an alteration of the surface tension under the addition of a few drops of sodium dodecyl sulfate. The ordered layer of spheres was transfered onto a substrate and annealed at 80 °C prior to electrochemical deposition of permalloy. STXM samples were grown on gold coated ($\sim$10 nm) 100nm thick Si/Si_3N_4 membranes, LTEM samples were grown on gold coated ($\sim$10 nm) 30nm thick Si/Si_3N_4 membranes and transport samples were grown on indium tin oxide coated glass slides (surface resistivity of 8-12 Ω/cm^2). Permalloy was grown through the template by electrochemical deposition from a NiSO4 and FeSO4 aqueous electrolyte. A three electrode set up was utilised, using a Pt mesh as the counter electrode and an Ag/AgCl reference electrode. A fixed potential of -1.0 V was maintained throughout the deposition. The thickness of the films was controlled by regulating the amount of charge passed during deposition. The colloidal spheres were selectively removed by dissolution in toluene. Energy dispersive X-Ray analysis using the INCA software showed an alloy composition of 25$\pm$2 wt % Fe and 75$\pm$2 wt % Ni.

Figures 6.2 shows SEM images of permalloy inverse opals fabricated on indium tin oxide coated glass around (a) a monolayer template and (b) a three dimensional template. The monolayer sample is henceforward referred to as the quasi 2D inverse opal whereas the inverse opal grown around the three dimensional template is referred to as 3D inverse opal. Both samples show general order, however, defects in the ordering can be seen in both samples, including filled cracks in the 3D sample. The origin of these defects is most

likely due to disorder in the self assembly or a consequence of imperfect monodispersity. Local ordering can clearly inset figures of figure 6.2. The lower magnification in figure 6.2(b) allows for the observation of domain formation due to the drying cracks common in the self assembly method. The crack characteristics are heavily dependent on the growth parameter chosen [110].

The quasi two dimensional transport sample pore diameter was measured to be 227$\pm$30 nm which indicates that the metal was grown around the sphere template to a thickness of 248$\pm$15 nm. The sphere diameter was found to be 279$\pm$30 nm. Magnetometry measurements estimate the three dimensional sample to be approximately 6.3 layers thick. Figure 6.2(b) shows an average top layer pore diameter of 250$\pm$30 nm which translates into a filling of up to 0.35a around the top layer sphere, which is in agreement with the VSM measurement. The two top layers of the three multilayer transport sample can be seen in the inset of 6.2(b). The bright top layer and the three small dark voids which are the visual third of the three spherical voids caused by the three lower layer neighbors.

The lattice constant for both the quasi 2D and the 3D samples were measured to be 279$\pm$15 nm. The slight deviation from the sphere diameter of 300 nm is most likely due to shrinkage during the template drying process [106].

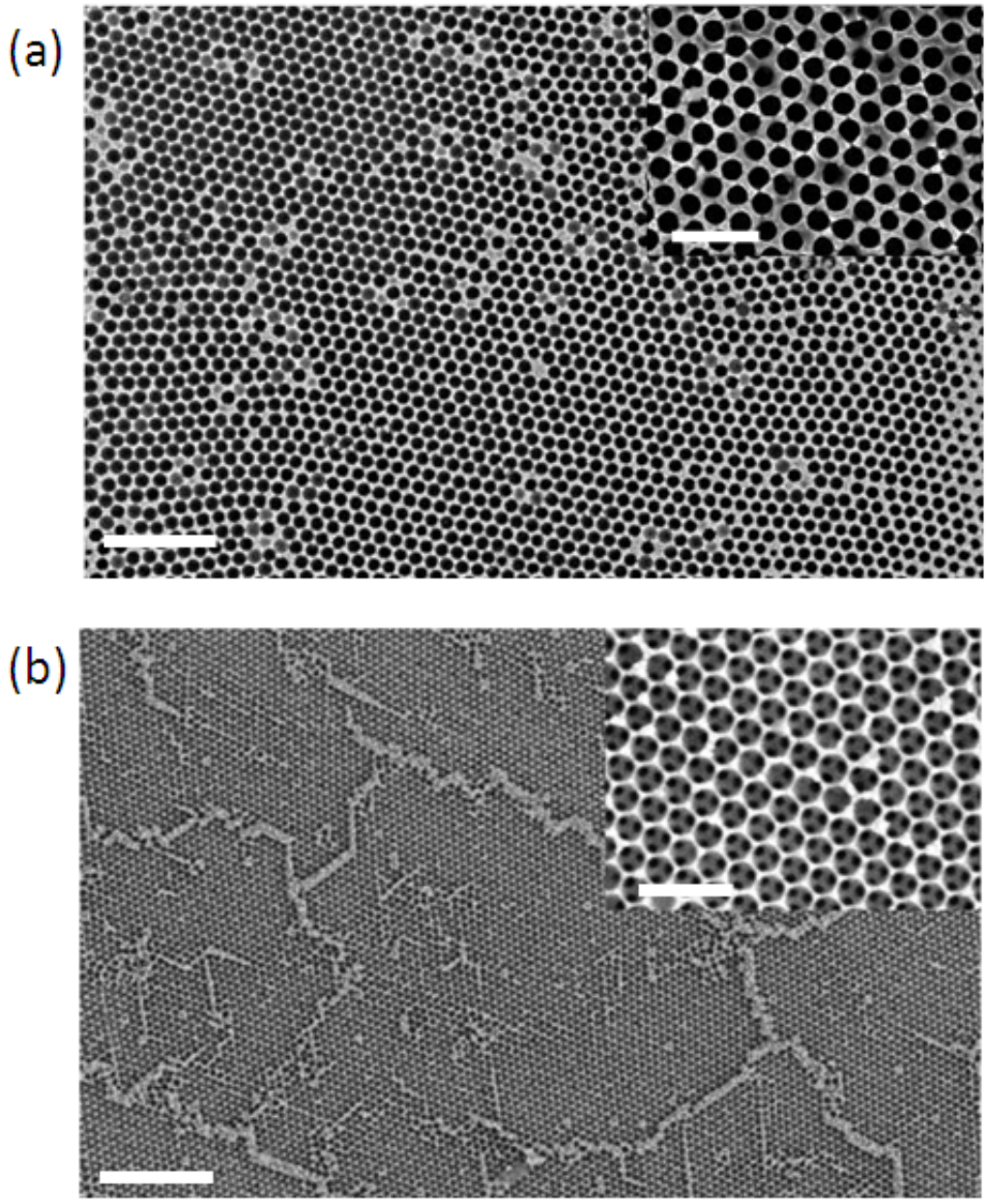

Figure 6.2 SEM images of monolayer and multilayer permalloy inverse opals (a) Quasi two dimensional inverse opal grown around self-assembled template consisting of 300 nm polystyrene spheres (scale bar 2 μm). (b) Three dimensional inverse opal grown around self-assembled template consisting of 300 nm spheres (Scale bar 4 μm). Scale bar of both insets 0.9 μm. Short range order is seen for both structures. SEM images were taken by Chahat Kansal

6.2 Magnetisation

6.2.1 Bulk Vibrating Sample Magnetometry

Figure 6.3(a) shows the angular dependence of the coercive field, H_C, for the quasi 2D (red circles) and the 3D (green, triangles) inverse opal structures shown in figure 6.2(a) and (b) respectively. For comparison, the coercive field of an unpatterned, electrochemically deposited film, is shown (purple triangle). No angular dependence was observed for the inverse opals; The coercive fields were found to be 10$\pm$2 Oe for the unpatterned film, 61$\pm$5 Oe for the quasi 2D inverse opal and 87$\pm$2 Oe for the 3D inverse opal. This magnetic hardening with patterning is to be expected as the magnetic reversal is strongly dependent on nucleation and pinning of domain walls [44]; adding voids into a thin film adds regular pinning sites and spatial dependent shape anisotropy [111]. The normalised remanent magnetisation is shown in figure 6.3(b) with respect to the angle. The dependence of the remanence with angle was seen to be isotropic, hence the direction of the applied field does not significantly influence the coercive field or the magnetic remanence. However, magnetic inverse opal structures, quasi two dimensional, three dimensional, and lithographically fabricated anti-dot arrays (two dimensional inverse opals equivalent with with cylindrical holes) have been studied for their compatibility with magnetic storage [1, 112, 113]. It was found that anti-dot arrays with cylindrical holes arranged on a rhomboid lattice, equivalent to the quasi 2D void arrangement of the inverse opals, expressed a six fold anisotropic symmetry where the hard and easy axis were separated by 30° [1, 112, 113]. Figure 6.3(c) shows the typical magnetisation versus external field curve for the quasi 2D and the 3D inverse opals. In the case of the quasi 2D sample 79$\pm$2 Oe were needed to change the magnetisation from a state of zero net magnetisation to a reversible state. 313$\pm$2 Oe were needed to achieve closure of the hysteresis loop starting from a net zero magnetised state. In the idealised case of cylindrical holes on a rhombic lattice the reversible part of the hysteresis loop was reach by applying 25 Oe along the easy axis or 150 Oe along the hard axis according to data published by Wang *et al.* [1]. Wang *et al.* inves-

tigated a pore diameter of 250 nm separated by 400 nm (center to center nearest neighbor). Therefore, both inverse opals are magnetically harder than unpatterned films. The three dimensional inverse opal switches at two distinct rates; 83 % switches in the first 118±2 Oe, while the remaining 17 % switches under the application of an additional 282±2 Oe. It is likely that the second stage involves switching the vertical bars which require higher energies to switch as the applied field and the shape anisotropy forced magnetic easy axis are at right angles to each other. The magnetic switching of the quasi 2D inverse opal will be dominated by domain wall nucleation and more importantly, pinning at lattice defects and drying cracks common in these structures due to the self assembly. The most likely cause for the lack of the magnetic anisotropy expected for these structures is the presence of the permalloy filled cracks (see figure 6.2(b)) combined with the fact that the ordered domains, separated by the cracks, are not necessarily orientated along the same axis.

Figure 6.3(d) shows the out of plane magnetisation loop. Magnetic saturation of the quasi 2D inverse opal and the thin film occurs at 1.5±0.2 T whereas the 3D inverse opal saturates at 2.0±0.2 T. The lack of a hysteresis loop and the large fields required to saturate in all cases indicates that the out of plane axis runs along the magnetically hard axis.

The magnetic reversal of inverse opals, in particular for the in-plane case, depends on the ratio between the pore diameter and the lattice constant under which de Groot *et al.* published a cross over at a ratio of $D/A = 0.7$ [114], shape anisotropy considerations dominate over the exchange. At ratios larger than 0.7 the shape anisotropy aligns the magnetic moments along the long axis of the bars [114]. Investigations into monolayer magnetic inverse opals have confirmed, via magnetic force microscopy, that the cross-over results in artificial spin ice behaviour [115]. The lattice constant is fixed by the template sphere diameter ($A = 2a$) used and the pore diameter (D) is linked to the thickness changes. If $D/A > 0.7$ the thickness of the film results in the possibility of the moments deviating from the true in-plane configuration as the constraint of the surface on the magnetic moments is reduced. However at ratios $D/A < 0.7$ exchange considerations result in the magnetic moments 'flowing' around the voids [114]. The reduced thickness leads to the magnetic

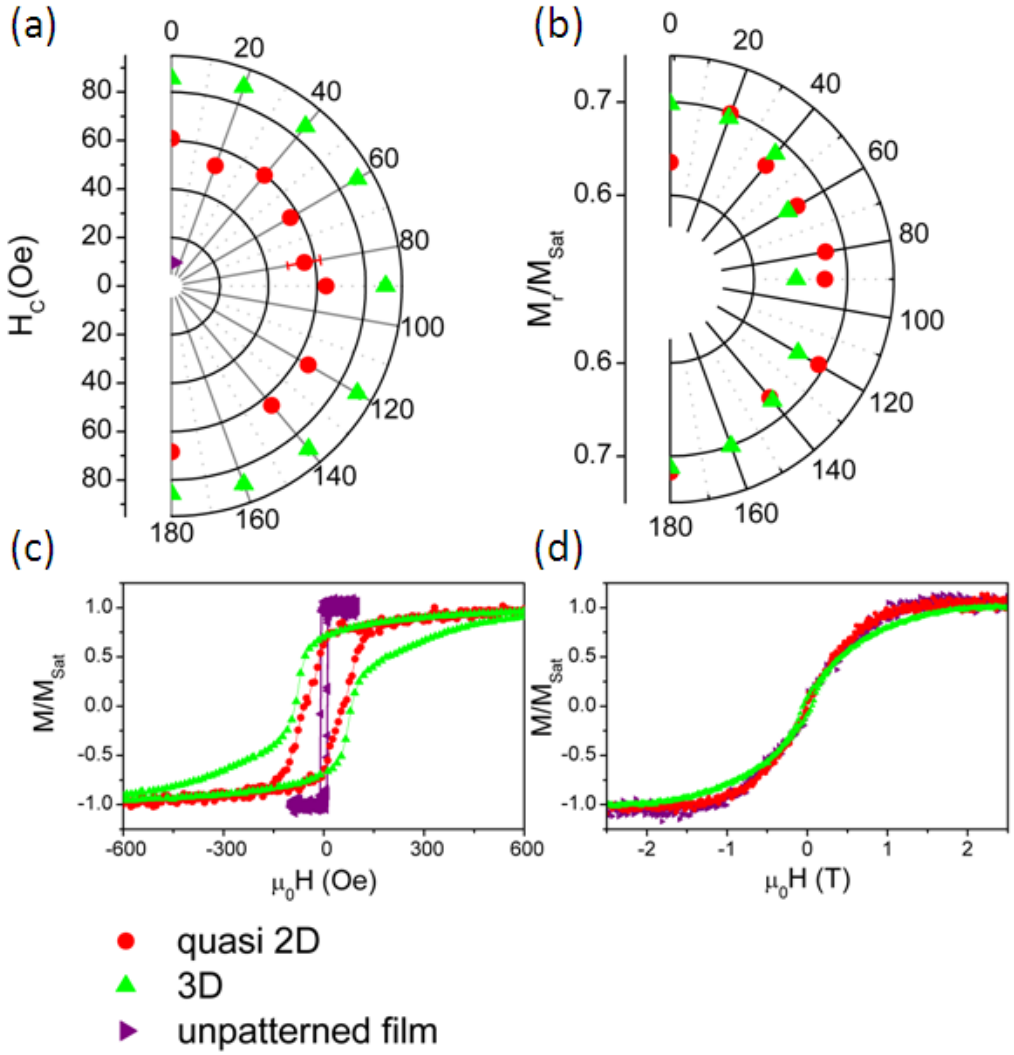

Figure 6.3 Bulk VSM measurement of permalloy inverse opal samples. the magnetic field was applied in the sample plane. (a) Angle dependence of the coercive field. (b) Angle dependence of the normalised remanence M_r/M_{Sat}. Typical normalised magnetisation versus applied field curves for quasi 2D, 3D inverse opal and unpatterned permalloy film (c) magnetic field applied in-plane (d) magnetic field applied out of plane.

Permalloy inverse opal structures					
Sample	A (nm)	D (nm)	D/A	t (nm)	t/D
Quasi 2D	279±15	227±30	0.8	248±15	0.9
3D	279±15	250±30	0.9	1092±87	NA
STXM quasi 2D	279±15	142±18	0.5	18±15	0.1
LTEM quasi 2D	279±15	216±18	0.8	51±15	0.2
LTEM 3D	279±15	242±16	0.9	NA	NA

Table 6.1 Table summarizing the relevant length scales of the inverse opal samples studied, where A refers to the lattice constant D to the pore diameter and t to the calculated sample thickness.

moments being confined in the plane. According to de Groot *et al.* a steep increase in the coercive field is expected for inverse opals with ratios of $D/A > 0.7$ [114]. At ratios below 0.10 ± 0.05 the holes have virtually no influence on H_C [114]. Above a ratio of 0.2 the coercive field increases and stays constant for ratios in the range of $0.2 < D/A < 0.7$ [114]. An increase in H_C by a factor of $\times 5.5$ was calculated between a ratio of 0.7 and 0.9.

The lattice constant A and pore diameter D were measured using SEM. Table 6.1 lists the relevant length scales of the samples measured in this thesis. According to the measured d/a ratio of the quasi 2D inverse opal and the 3D inverse opal an increase of coercivity by a factor of 1.4 is expected, while an increase by a factor of 1.3 was observed. However, according to de Groot *et al.*, the thickness to pore diameter ratio t/d adds a sinusoidal fluctuation onto H_C, whose amplitude depends on the layer number [114,116]. The fluctuation of the coercive field, which is thickness dependent, decreases with increasing layer numbers. The sample thickness of the top layer of the multilayer sample or the monolayer thickness was calculate using the spherical geometry of the void. However, the symmetry of the void with respect to above or below the half way point leads to two possible thicknesses for each pore diameter. A significant change in H_C is only expected in the case of a

quasi 2D sample with thickness 52±15 nm and 248±15 nm. The coercive field is expected to differ by a factor of $\sim \times 2$ in the case of a thickness change of 196 nm. The contribution to the coercive field due to the thickness diameter ratio of a 248±15 nm monolayer is closer to the contribution to the coercive field of a 3D inverse opal with 2 or 3 layers. Hence it is reasonable to assume that the monolayer inverse opal has an average thickness 248±15 nm. This agrees with results from VSM measurements which estimate a layer number of 2.2 for the quasi 2D inverse opal and 6.3 for the 3D inverse opal (a void volume fraction of 74 % was assumed [117]. The discrepancy between the SEM measurements, which show a monolayer sample in the quasi 2D case, is most likely due to the filled cracks which are detected in the bulk VSM measurement.

6.2.2 Scanning Transmission X-Ray Microscopy

Figure 6.4 shows the magnetic reversal of a quasi 2D permalloy inverse opal sample. The magnetic field was applied along the x-axis and the images were taken at remanence. The reversal is mediated by the nucleation of domain walls from random nucleation sites in the film and their subsequent propagation (see figure 6.4(a)-(d). The zoomed in magnetic image in figure 6.4(f) shows that the reversal runs along the 0° easy axis of the cylindrical holes in a permalloy film on a rhombic lattice, as described by Adeyeye *et al.* [112]. OOMMF simulations confirm this trend (see figure 6.5). Cylindrical holes in a 60 nm thick permalloy film were simulated (Exchange stiffness $A = 13 \times 10^{-12}$ Jm^{-1}, $\alpha = 0.5$ and $M_{Sat} = 800$ kAm^{-1}, mesh size $[x,y,z] = [5,5,30]$ nm). The reversal along the spherical anti dot array is mediated via domains running along the magnetically easy directions, 0° and ±60° (see blue and red arrows pointing along the easy and hard axis , respectively, of the quasi 2D anti-dot array in figure 6.5(a)). Figure 6.4(f) shows that the ordering has defects; overall the holes are close packed with only a few dislocations, however there are multiple close packed areas at angles to each other. The reversal of two domains at an angle to each other can be seen, both occurring along the 0° easy axis. The magnetisation reversal in the anti-dot regime is confirmed by the diameter versus lattice constant ratio of 0.5 (see table

Permalloy inverse opal structures	
Sample	$H_C(mT)$
Quasi 2D	6.1±0.2
STXM quasi 2D	10.4±0.5
OOMMF anti-dot	20.5±0.7

Table 6.2 Table summarizing the coercive fields of the quasi 2D inverse arrays.

6.1. The quasi 2D inverse opal imaged via STXM was 18±15 nm thick leading to $d/a = 0.5$. The VSM measurements were performed on a 248±15 nm thick sample with $d/a = 0.9$.

The magnetisation versus applied field can be seen in figure 6.6. The magnetisation for the quasi 2D structure measured using STXM (black squares) was extracted by comparing the amount of black and white contrast seen in the XMCD contrast images. Hence it is a rough estimate of magnetisation along the x axis. For comparison figure 6.6(a) shows the bulk magnetisation measured on the quasi 2D inverse opal grown on a indium tion oxide coated glass substrate. Figure 6.6(b) shows the quasi 2D STXM magnetisation in comparison to the cylindrical anti-dot simulation. The coercive fields are summarised in table 6.2. The quasi 2D inverse opal measured using STXM is a factor of $\sim \times 3$ thinner and is magnetically harder by a factor $\sim \times 1.7$. According to de Groot *et al.* the thicker sample should be a factor of $\times 4$ harder as the shape anisotropy dominates in a sample of $d/a = 0.9$. The magnetisation versus applied field, extracted from the localised STXM images of the thin inverse opal, is sharp; Complete reversal is achieved within 3.5 mT. On the other hand, the broad transition between negative and positive saturation indicates that the 248±15 nm thick inverse opal is comprised of multiple domains rotated with respect to each other mixing easy and hard axis states; Complete reversal is achieved within approximately 16 mT. The magnetometry measurements averaged the magnetisation over the whole sample whereas the STXM images are spatially localised.

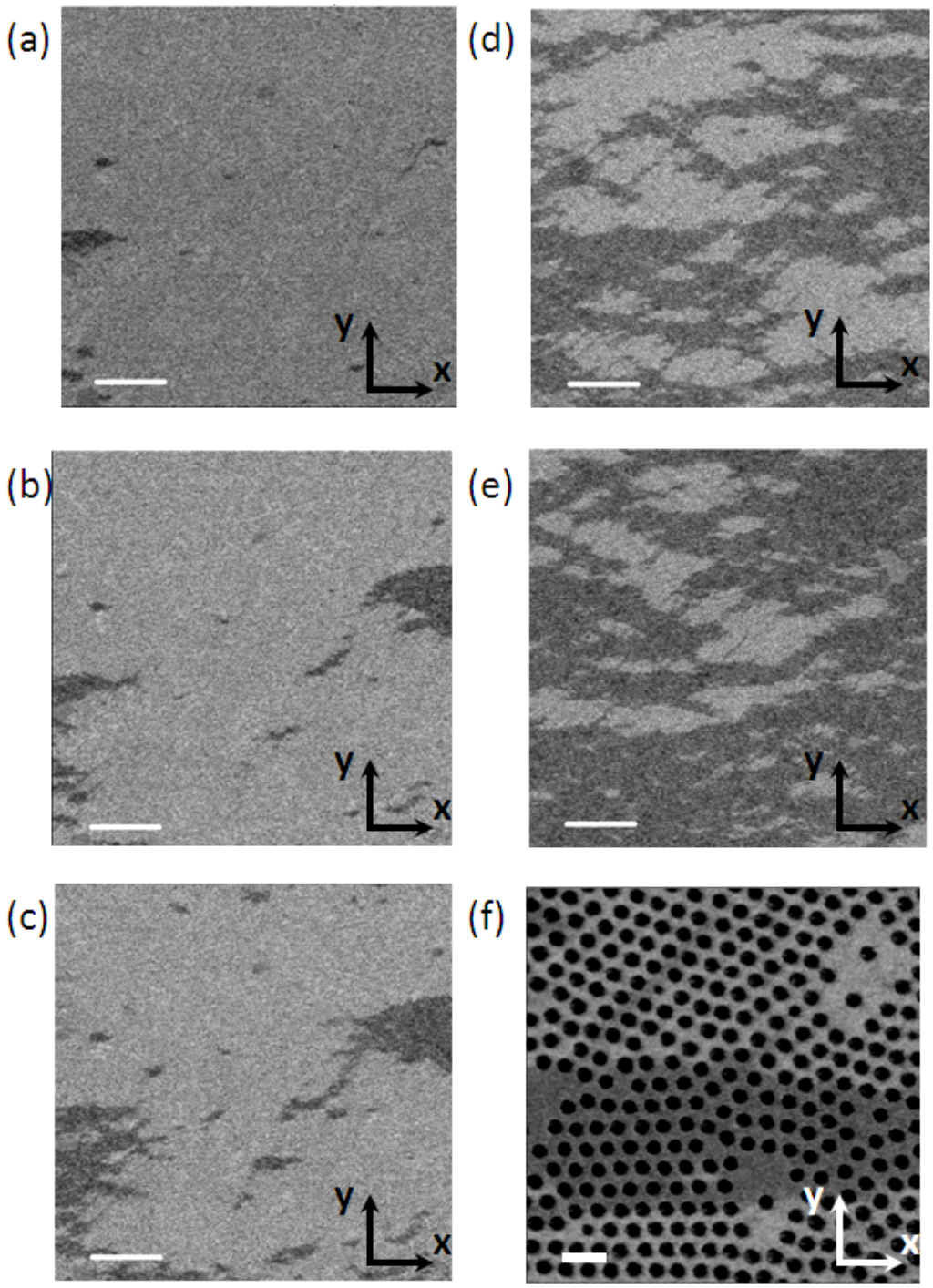

Figure 6.4 Magnetic reversal images of permalloy quasi 2D inverse opal reversing in the anti-dot fashion. Magnetic contrast of STXM images taken at remanence after the application of (a) -8.45 mT, (b) -8.8 mT, (c) -18.4 mT and (d) -9.8 mT along the x-axis. (e) Magnetic contrast after re-saturation at 25 mT in the x direction and subsequent application of -10 mT. The scale bar in (a) to (e) is 5 μm. (f) Expanded view of a region in (e) (scale bar 500 nm).

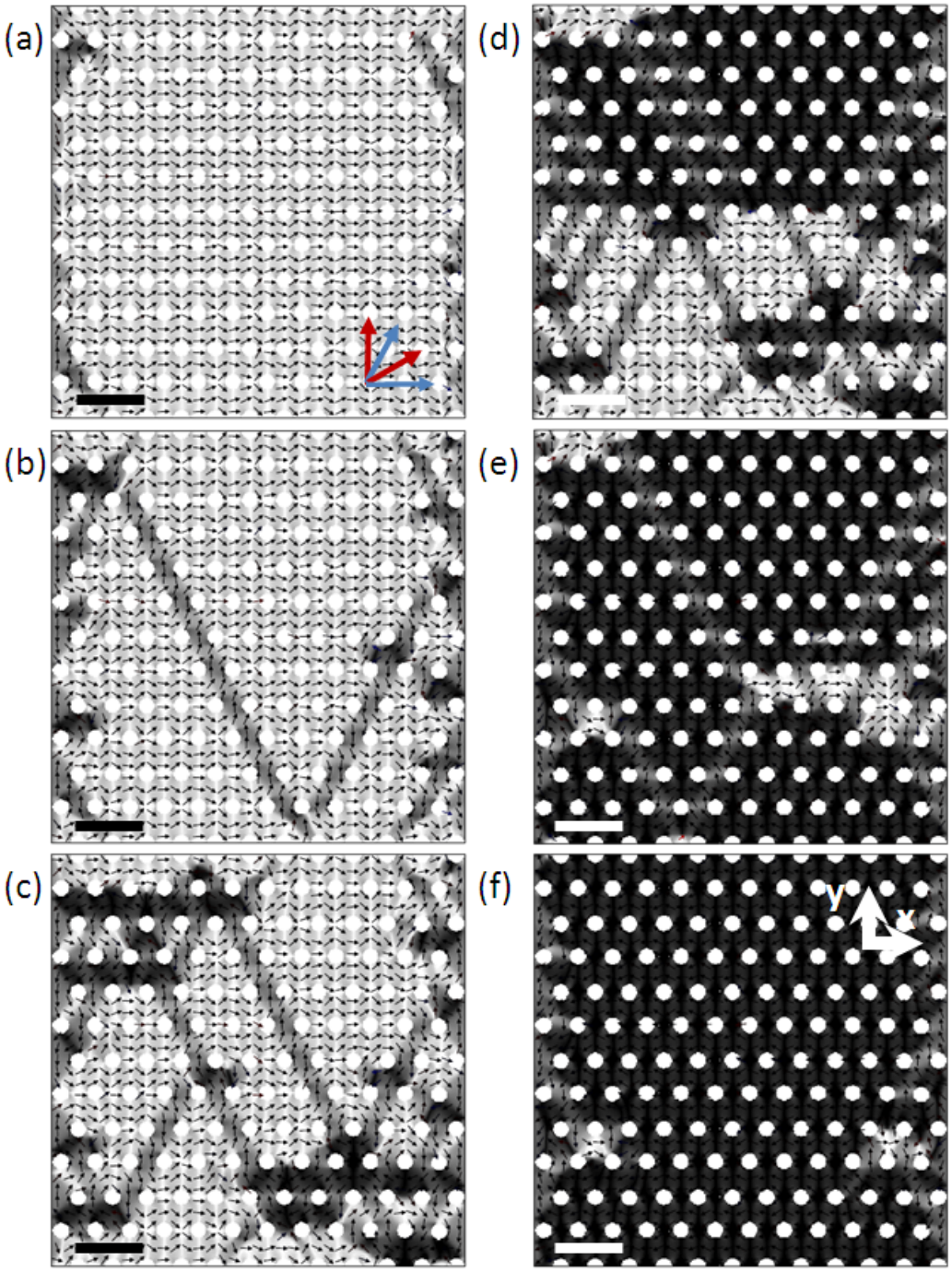

Figure 6.5 OOMMF simulation of cylindrical holes in a permalloy thin film on a rhombic lattice. Simulations were performed using a hole diamter of 142 nm and a nearest neighbour distance of 300 nm. The magnetic field was applied along the x axis. (a) 0mT, (b) -16 mT, (c) -20 mT, (d) -24 mT, (e) -28 mT and (f) -30 mT. The blue and red arrows in (a) indicate the magnetic easy and hard axis separated by 30°. Scale bars are 600 nm

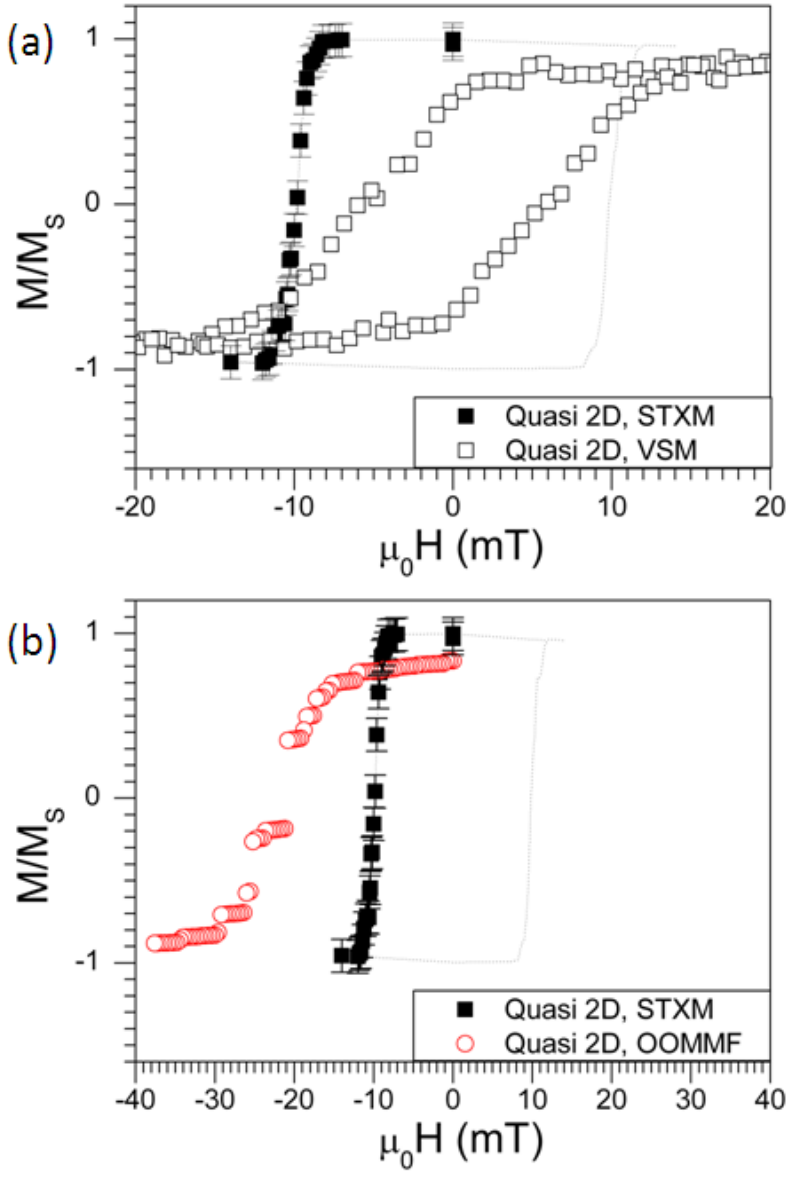

Figure 6.6 Normalised magnetisation versus applied field loops for quasi 2D inverse opals. (a) Normalised MH loop showing estimated magnetisation from STXM images (solid squares) and bulk VSM measurement. (b) Normalised magnetisation calculated by OOMMF (red open circles) and normalised magnetisation from STXM images (as in (a)).

6.2.3 Lorentz Transmission Electron Microscopy

The use of magnetic inverse opal as three dimensional artificial spin ice was investigated using LTEM by imaging the magnetic state of a slice (thickness <100 nm) cut from a multilayer permalloy inverse opal grown around a 300 nm sphere diameter template, using LTEM. The TEM images were taken by Dr. Solveig Felton and the sample was grown by Dr. Amy Cruickshank. Figure 6.7 (a) shows the slice cut. Figure 6.7(b) and (c) show the in focus and the out of focus LTEM images. The magnetisation configuration of the bars in the out of focus image (figure 6.7(c)) is depicted in figure 6.7(d). The blue and green circles enclose two ice rule violations. The LTEM images show that locally the three dimensional inverse opal slice acts as a spin ice. The bar length to width ratio of around 8 is large enough to ensure Ising like behaviour.

The Lorentz TEM contrast was simulated by S.K. Walton using the MALTS simulation package developed by Walkton *et al.* [118]. The OOMMF simulation, used as an input for the MALTS simulator package, and the simulated LTEM contrast are shown in figures 6.7(e) and (f) respectively. Cylindrical holes in a 40 nm thick permalloy film were simulated using OOMMF (Exchange stiffness $A = 13 \times 10^{-12}$ Jm^{-1}, $\alpha = 0.5$ and $M_{Sat} = 800$ kAm^{-1}, mesh size $[x, y, z] = [5, 5, 40]$ nm). The schematic in figure 6.7(g) shows a simplified picture of the Lorentz contrast.

Although LTEM on a slice, taken from a three dimensional permalloy inverse opal, showed artificial spin ice behaviour, as the slice had to be less than 100 nm, in order for the electrons to able to travel through the slice, it is not obvious if this spin ice behaviour is preserved in the bulk inverse opal. Electrical transport measurements allow us to evaluate the bulk magnetisation behaviour of the inverse opals; shedding light on the question: Are magnetic inverse opals three dimensional artificial spin ices?

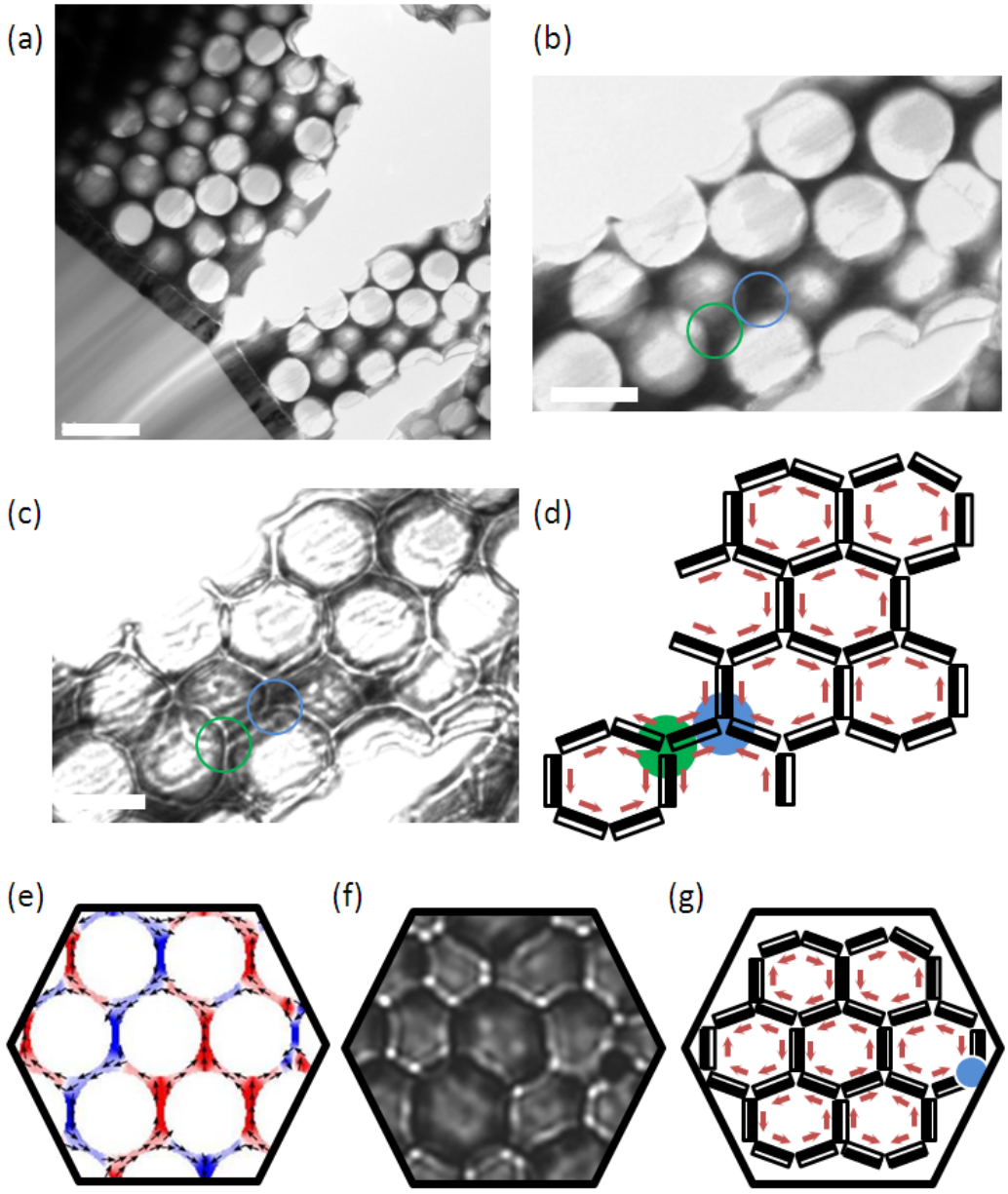

Figure 6.7 Lorentz TEM of slice cut from three dimensional permalloy inverse opal. (a) Infocus image of the three dimensional slice. Scale bare 0.2 μm. (b) Zoomed in area of the slice. Scale bar 0.4 μm. (c) Lorentz contrast of area shown in (b) (defocus 100 μm). (c) Magnetisation state of bars. (e) OOMMF simulation of cylindrical holes in a 40 nm permalloy film on a rhombic lattice. (f) Simulated Lorentz TEM contrast of (e). (g) Schematics showing the magnetisation state of the bars in (e) and (f)

6.3 Magnetotransport

Magnetotransport measurements are well suited to studying the temperature dependence of the magnetisation reversal of two dimensional artificial spin ice. A unique characteristic asymmetry was identified at low temperatures, the onset temperature of which was found to be dependent on the materials saturation magnetisation. Therefore, magnetotransport measurements as a function of temperature, allow the identification of the magnetic inverse opals as an artificial spin ice candidate.

The resistance of the quasi two dimensional and three dimensional magnetic inverse opals was investigated as a function of temperature and field direction. A four electrode setup was used; The electrical contacts where placed at the corners of the sample, allowing the resistance to be measured either parallel to the current or perpendicular.

Figure 6.8 shows the low and high temperature magnetoresistance data. The quasi 2D inverse opal magnetoresistance taken at 25 K and 290 K is shown in figure 6.8(a) and (b) respectively. The magnetic field was applied out of plane while the voltage was measured parallel to the current flow. Figure 6.8(c) and (d) show the resistance change with applied field for a three dimensional permalloy inverse opal at 25 K and 100 K respectively using the same measurement configuration.

The magnetoresistance was observed to be at a minimum during magnetic saturation of the quasi two dimensional and the three dimensional inverse opal when the external magnetic field was applied out of plane (see figure 6.8(a)-(f)). This is consistent with the current being perpendicular to the magnetisation of the inverse opal. More precisely, in the case of the 3D inverse opal structure the current and the magnetisation are at an angle of 0° (one bar) and 60° (3 bars) to each other. In the case of an in-plane magnetic field, magnetic saturation is a high resistance state as the current and the magnetisation are parallel to each other (see figure 6.8(g)-(l)). More precisely, in the case of the 3D inverse opal structure the current and the magnetisation are at an angle of 90° (one bar) and 30° (3 bars) to each other. This is in agreement with the typical anisotropic magnetoresistance.

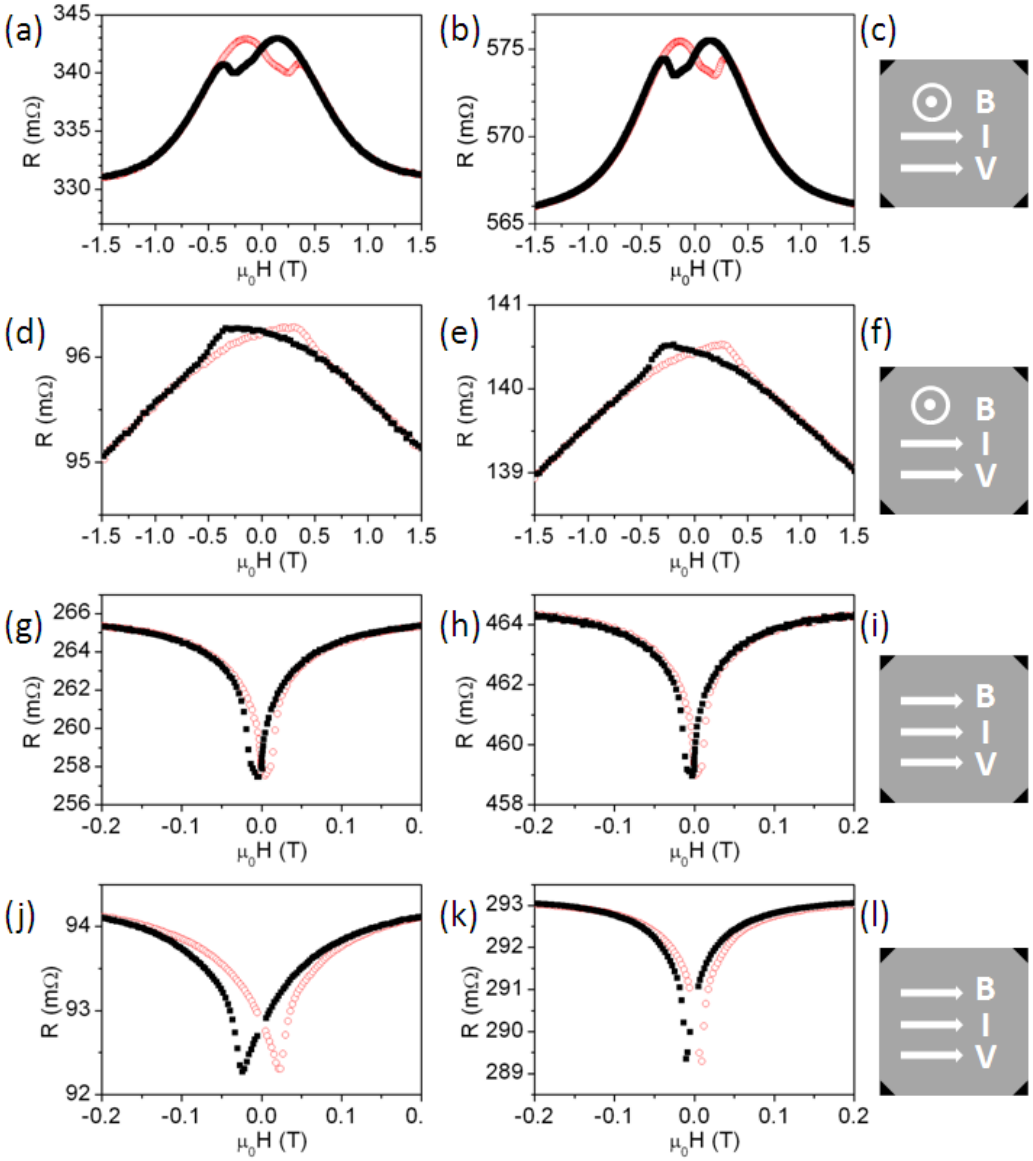

Figure 6.8 Out of plane magnetoresistance of a quasi 2D inverse opal at (a) 25 K and (b) 290 K. The relative field, current and voltage orientation are shown in (c). Out of plane magnetoresistance of a 3D inverse opal at (d) 25 K and (e) 100 K. The relative field, current and voltage orientation are shown in (f). In-plane magnetoresistance of a quasi 2D inverse opal at (g) 2 K and (h) 290 K. The relative field, current and voltage orientation are shown in (i). In-plane magnetoresistance of a 3D inverse opal at (j) 20 K and (k) 290 K. The relative field, current and voltage orientation are shown in (l).

Figure 6.9 shows a comparison between bulk VSM and magnetoresistance data taken at 290 K (apart from the out of plane 3D inverse opal transport measurement which was taken at 100 K). Figure 6.9(a) and (b) show the data taken during the in-plane magnetic reversal. The low resistance state coincides with a zero net magnetised state of the inverse opal, occurring at a field of 6.1±0.5 mT and 8.7±0.2 mT in case of the quasi 2D and 3D inverse opal respectively. Figure 6.9(c), shows irreversible features at low field which are not mirrored in the magnetometry data. VSM measures the stray field emitted by a sample; observing a change in the electrical transport without a mirroring change in the magnetometry data requires a local change in the angle between the magnetic moments and the current without a net change in the overall stray fields emitted by the sample. Similar behaviour has been observed in the magnetic reversal of a single nickel nanowire (30 nm diameter) [119] and of a single permalloy nanowire (200 nm diameter) [120].

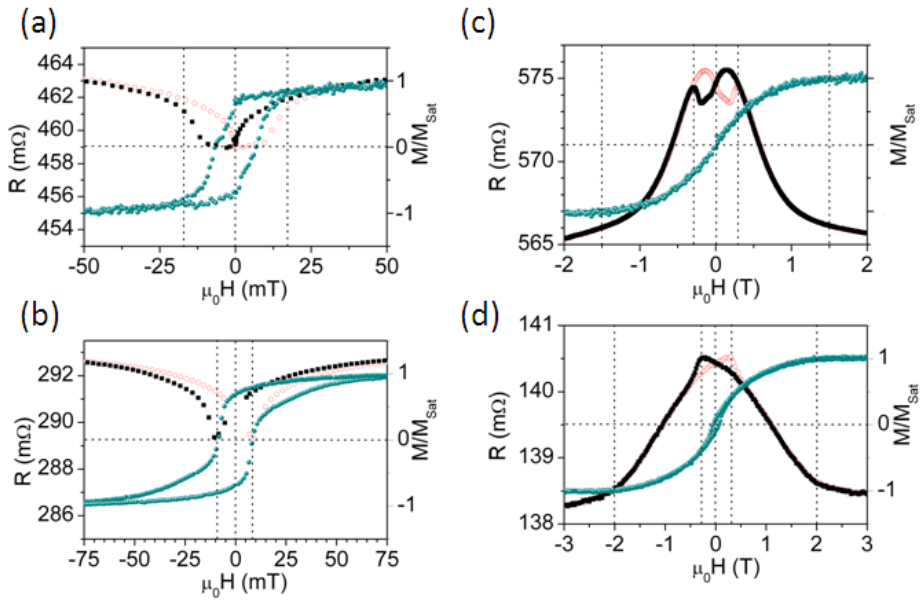

Figure 6.9 Comparison between in-plane magnetometry (green spheres) and magnetoresistance (black solid squares and red open circles, the down and up sweep respectively) data for (a) 290 K quasi 2D inverse opals, (b) 290 K 3D inverse opals. Comparison between out of plane magnetometry (green spheres) and magnetoresistance (black solid squares and red open circles, the down and up sweep respectively) data for (c) 290 K quasi 2D inverse opals, (d) 290 K 3D inverse opals (resistance data was acquired at 100 K).

6.3.1 In-Plane 180° Magnetic Reversal

The temperature evolution of the irreversible component extracted from the raw resistance data of the quasi two dimensional and the three dimensional inverse opals are shown in figure 6.10(a)-(d) and (e)-(h) respectively. In both cases the external field was applied parallel to the current flow.

The average field dependent irreversible resistance change, $R_{xx,Avg}$, extracted for the quasi two dimensional permalloy inverse opal is shown in figure 6.10(a). The temperature evolution of the maximum peak height, $R_{P(xx,Avg)}$, is shown in figure 6.10(b). The maximum amplitude of $R_{P(xx,Avg)}$ was observed to be at 2 K, -3.00$\pm$0.09 mΩ, and then was observed to decrease with increasing temperature. Three distinct regimes can be identified. Between 2 K and 25 K, $R_{P(xx,Avg)}$ was seen to decrease rapidly; 0.2 mΩ over 23 K. The rapid decrease is followed by a slow decrease between 25K and 175K; 0.2 mΩ over 150 K. Between 175 K and 290 K, $R_{P(xx,Avg)}$ was seen to decrease by 0.65 mΩ over a range of 115 K. Figure 6.10(c) shows the temperature evolution of the zero field resistance $R_{0,xx}$. $R_{0,xx}$ was found to decrease with temperature. Below 25 K the zero field resistance reaches a constant value of 259.12$\pm$0.13 mΩ. Figure 6.10(d) shows the temperature evolution of the field at which the irreversible resistance peak reaches its maximum (H_P). H_P was seen to decrease with increasing temperature from 9.4$\pm$0.5 mT at 2 K to 5.9$\pm$0.5 mT at 290 K.

$R_{xx,Avg}$ extracted for the three dimensional inverse opal is shown in figure 6.10(d). The temperature evolution of height of the peaks in figure 6.10(d) is plotted in figure 6.10(e). At 20 K $R_{P(xx,Avg)}$ was found to be -1.64$\pm$0.05 mΩ. $R_{P(xx,Avg)}$ reached a maximum amplitude at 30 K of -2.044$\pm$0.05 mΩ. Between 30 K and 150 K the amplitude of $R_{P(xx,Avg)}$ was observed to decrease by 0.29 mΩ, a rate of roughly 0.0024 mΩ/K. A further reduction of $R_{P(xx,Avg)}$ by 0.78 mΩ is observed between 150 K and 225 K. $R_{P(xx,Avg)}$ decreased by approximately 0.0104 mΩ/K above which $R_{P(xx,Avg)}$ was seen to stay constant at a value of -0.97$\pm$0.05 mΩ. The temperature evolution of the zero field resistance $R_{0,xx}$ is shown in figure 6.10(f). $R_{0,xx}$ was found to decrease with temperature reaching a constant value of

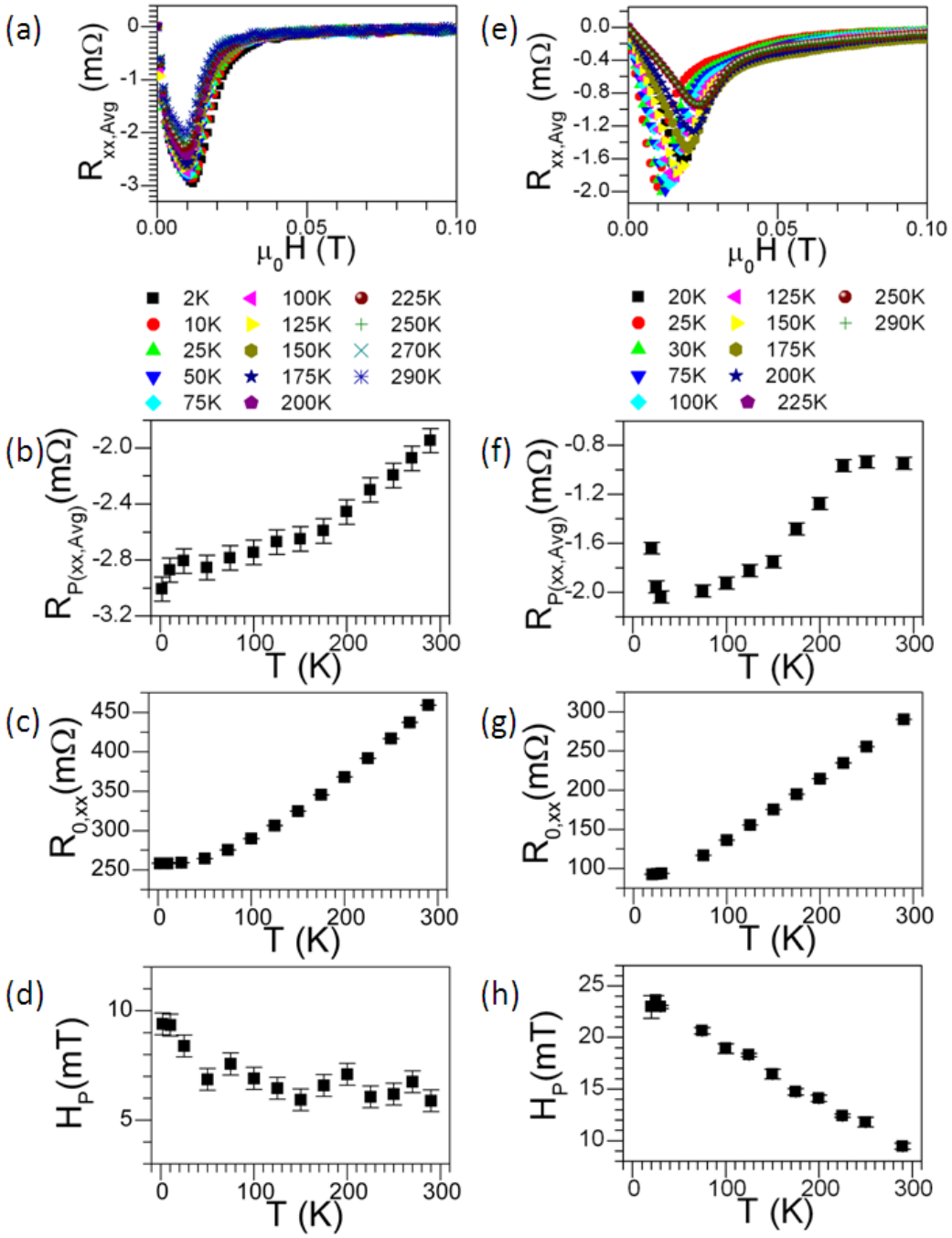

Figure 6.10 Irreversible in-plane magnetoresistance of quasi 2D permalloy inverse opals: (a) $R_{xx,Avg}$, (b) temperature evolution of peak height $R_{P(xx,Avg)}$ in (a), (c) zero field resistance, $R_{0,xx}$, versus temperature and (d) H_P versus temperature. Irreversible in-plane magnetoresistance of 3D permalloy inverse opals: (e) $R_{xx,Avg}$, (f) temperature evolution of peak height $R_{P(xx,Avg)}$ in (e), (g) zero field resistance, $R_{0,xx}$, versus temperature and (h) H_P versus temperature.

92.81±0.01 mΩ below 25 K. H_P was seen to decrease with increasing temperature from 23.0±0.5 mT at 30 K to 9.5±0.5 mT at 290 K (see figure 6.10(h)).

6.3.2 Out of Plane 180° Magnetic Reversal

Figure 6.11 (a)-(d) shows the average peak and zero field resistance information extracted from the irreversible part of the raw magnetoresistance measurement of the quasi 2D inverse opal. The equivalent information extracted from the three dimensional inverse opal is shown in figure 6.11(e)-(h). In both cases the external field was applied out of the plane.

The average field dependent irreversible resistance change, $R_{xx,Avg}$, extracted for the quasi two dimensional permalloy inverse opal is shown in figure 6.11(a). The peak seen in the irreversible component of the resistance measurement of the quasi two dimensional inverse opal magnetoresistance measurement was measured to be negative. On the other hand, $R_{xx,Avg}$ extracted from the magnetoresistance of the three dimensional inverse opal was seen to be positive. During the irreversible magnetisation reversal, the resistance was seen to decrease in the case of the quasi two dimensional sample whereas the resistance of the three dimensional inverse opal increased during the irreversible magnetisation change.

The maximum peak height of the quasi two dimensional inverse opal was observed to be -2.09±0.09 mΩ at 2 K. At 25 K $R_{P(xx,Avg)}$ was observed to be at a maximum value of -2.62±0.09 mΩ. between 25 K and 150 K $R_{P(xx,Avg)}$ was observed to slightly decrease and then increase again forming a local minimum at 87.5±12.5 K. Above 150K $R_{P(xx,Avg)}$ was found to linearly decrease from -2.54±0.09 mΩ to -1.93±0.09 mΩ at a rate of roughly 0.0044 mΩ/K. $R_{0,xx}$ was found to decrease with temperature reaching a constant value of 332.17±0.11 mΩ below 25K. A jump of 10 mΩ was observed between 25 K and 20 K. The peak field H_P was seen to decrease with increasing temperature from 243±2 mT at 25 K to 188±5 mT at 290 K (see figure 6.11(d)).

$R_{P(xx,Avg)}$ extracted from the irreversible component of the magnetoresistance data from the three dimensional inverse opal was measured to increase with increasing temperature. At 2 K a maximum peak height of 0.16±0.04 mΩ was observed, increasing to 0.23±0.04 mΩ

at 100 K. The zero field resistance $R_{0,xx}$ was seen to increase with increasing temperature. At 2K $R_{0,xx}$ was observed to be 92.83±0.13 mΩ. H_P was seen to decrease with increasing temperature from 331±6 mT at 2 K to 275±9 mT at 290 K (see figure 6.11(h)).

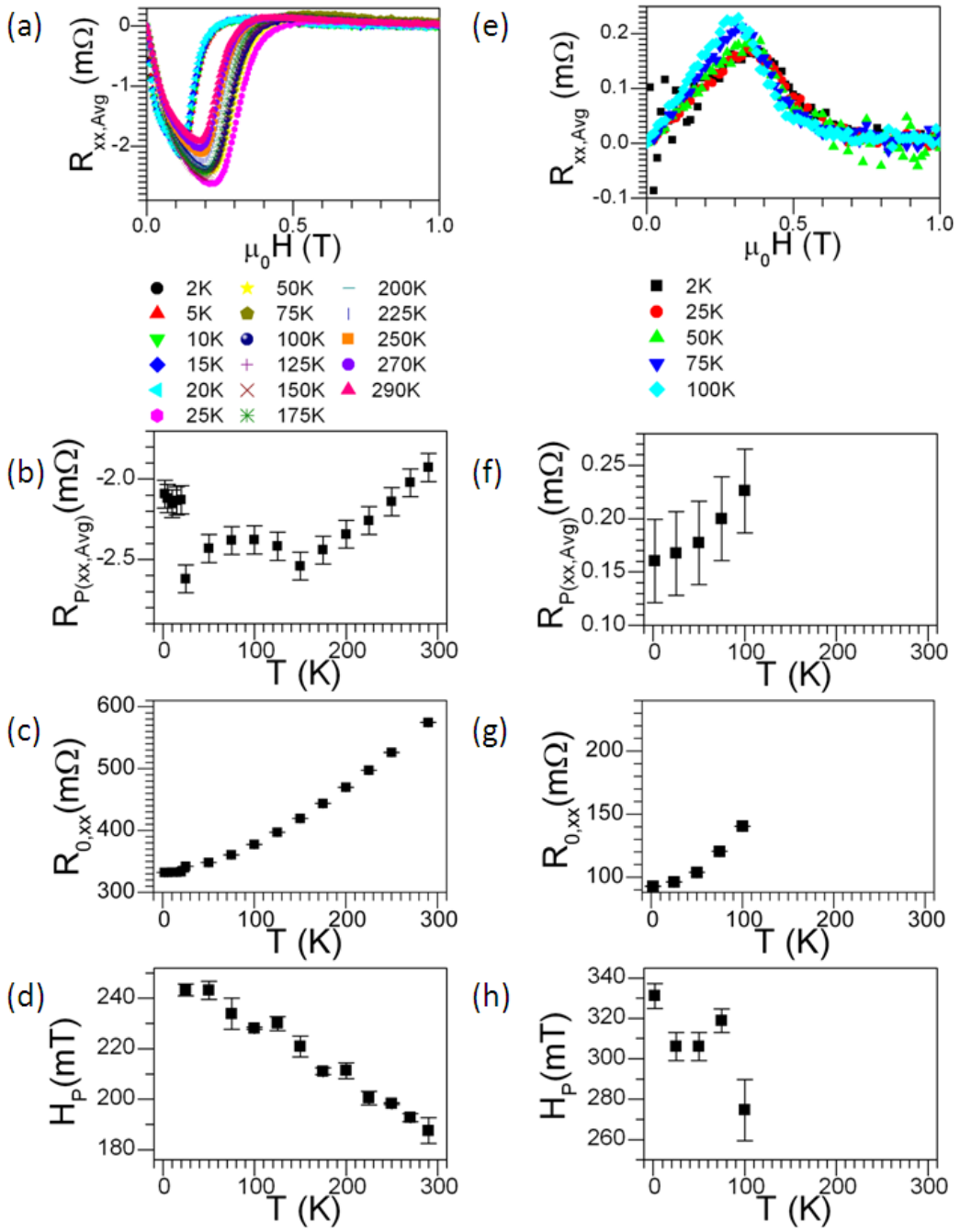

Figure 6.11 Irreversible out of plane magnetoresistance of quasi 2D permalloy inverse opal: (a) $R_{xx,Avg}$, (b) temperature evolution of peak height $R_{P(xx,Avg)}$ in (a), (c) zero field resistance, $R_{0,xx}$, versus temperature and (d) H_P versus temperature. Irreversible out of plane magnetoresistance of 3D permalloy inverse opals: (e) $R_{xx,Avg}$, (f) temperature evolution of peak height $R_{P(xx,Avg)}$ in (e), (g) zero field resistance, $R_{0,xx}$, versus temperature and (h) H_P versus temperature.

6.3.3 Discussion

Figure 6.12(a) shows the temperature dependence of the zero field resistance extracted from the in-plane and out of plane magnetoresistance measurements for the inverse opal samples. $R_{0,xx}$ was seen to decrease with temperature reaching a constant value below 25 K. The residual resistance was seen to be higher for the quasi two dimensional inverse opal. The residual resistance is caused by temperature independent lattice imperfections, surface scattering, grain boundaries, impurity and other defect sites [119]. An increase in scattering is expected to occur for smaller grains [119]. As both inverse opals were grown following the same methodology the average grain size and the impurity content can be assumed to be equivalent and hence the difference in the residual resistance is most likely caused by changes in the surface scattering and lattice defects. The grain sizes were evaluated by C. Kansal and was found to be 10.6±0.5 nm (for details see Master thesis by Chahat Kansal [108]) for samples grown around a 300 nm diameter sphere template. A reduction of the residual resistance is expected with increasing wire diameter and a minimum is reached when bulk material properties are recovered [121, 122]. The residual resistance to room temperature ratio increases as the diameter of the nanowires increases [122]. Figure 6.12(b) shows a residual resistance ration of ∼3 for three dimensional inverse opals and ∼1.8 for the quasi two dimensional counterpart. The quasi 2D inverse opal followed the same trend as a 75±10 nm thick electrochemically grown thin film, whereas the temperature dependence of the 3D inverse opal was seen to deviate from the thin film behaviour. The thin film and the 3D inverse opal zero field resistance was fitted to the Matthiesen's rule (see chapter 2.4.5 for details), including a temperature independent contribution, a contribution caused by phonon scattering ($R_{ph} \propto \rho_{ph}$) and a contribution due to spin disorder scattering ($R_{ferro} \propto \rho_{ferro}$) (See figure 6.13(a)(Top) and (b)(Top) respectively). Good agreement between data and simulation was found. In both cases the dominant contribution to the zero field resistivity was found to be caused by phonon scattering with an onset of ∼30 K (See figure 6.13(a)(Bottom) and (b)(Bottom)). The onset of significant

spin disorder scattering was seen to be ∼150 K and was found to increase with increasing temperature 6.13(b) and (d) for the case of the thin film and the 3D inverse opal respectively. However, whereas approximately 21 % of the temperature dependent resistance, measured for the thin film, is due to spin disorder a contribution of only approximately 3 % was measured in the case of the 3D inverse opal. This reduction in spin disorder might be cause by the patterning which will introduce increased surface scattering. The influence of the slightly conductive substrate (needed for electrochemical deposition) was assumed to negligible due to the large difference in the conductance; for indium tin oxide $\sigma_{xx} \sim 10^4\ \Omega^{-1}cm^{-1}$ [123] whereas the conductivity of nickel and iron is typically of the order of $10^5 < \sigma_{xx} < 10^6\ \Omega^{-1}cm^{-1}$ [57]. The normalised resistance of indium tin oxide on glass, extracted from temperature dependent mobility and carrier concentration measurements by Kikuchi *et al.* [123], was found to be temperature independent. Hence the zero field resistance changes with temperature can be assumed to be dominated by the magnetic material.

H_P versus field is shown in figure 6.12(c). The out of plane peak field was found to be approximately 5× larger than the in-plane field. This shows that the magnetic easy axis of the inverse opals lies in the plane irrespective of its dimensionality. The in-plane shape anisotropy of the quasi two dimensional inverse opal results in such an in-plane easy axis. In the case of the three dimensional inverse opal the in-plane easy axis is a result of the bar arrangement: three bars are at 30° to the in-plane axis whereas only one bar is perpendicular, hence overall the shape anisotropy ensures an in-plane easy axis. However, the out of plane H_P measured for 2D honeycomb permalloy artificial spin ice was found to be around 700-800 mT which is a factor of approximately 2.5× larger. This indicates that in contrast to truly two dimensional structures magnetic inverse opals support out of plane magnetisation more readily. H_P, normalised to 25 K, is shown in figure 6.12(d). A linear decrease of H_P with increasing temperature was observed. The change of H_P with temperature was found to be independent of the direction of the field application. A noticeable difference in the linear slope was observed between quasi two dimensional and the three dimensional

inverse opal which is a reflection of the change in the high temperature slope of the zero field resistance. H_P extracted from the in-plane 290 K electrical transport was seen to agree with the coercive fields H_C extracted from 290 K magnetisation versus applied field curves.

$R_{P(xx,Avg)}$ in-plane and out of plane for quasi 2D inverse permalloy opals and 3D inverse permalloy opals are plotted in figure 6.12(e) and (f) respectively. The dotted lines mark changes in the temperature behaviour of $R_{P(xx,Avg)}$. In the quasi two dimensional case $R_{P(xx,Avg)}$ showed the same temperature behaviour down to 25 K below which a clear divergence in the in-plane and out of plane $R_{P(xx,Avg)}$ was seen (see figure 6.12(f)). Three distinct changes in the temperature evolution of $R_{P(xx,Avg)}$, extracted from the three dimensional inverse opal, were observed (see figure 6.12(g)-(h)). The changes at 30 K and 150 K coincide with the onset of the phonon and spin disorder scattering. However, the origin of the third change in the temperature evolution, observed in the case of the 3D inverse opal, is unclear.

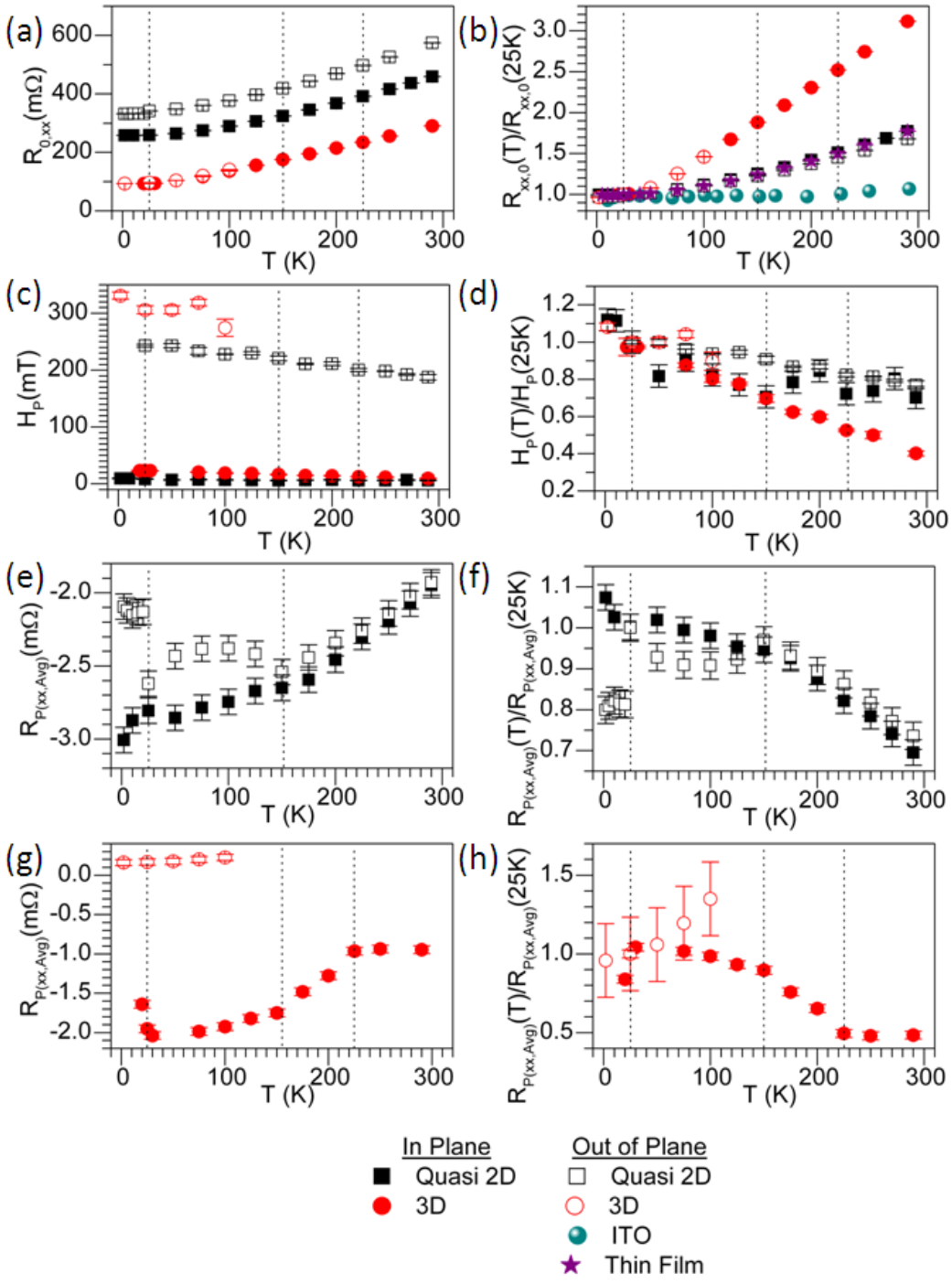

Figure 6.12 Temperature dependence of (a) $R_{0,xx}$, (b) $R_{0,xx}$ normalised to 25 K, (c) H_P, (d) H_P normalised to 25 K, (e) quasi 2D permalloy inverse opal $R_{P(xx,Avg)}$, (f) quasi 2D inverse opal $R_{P(xx,Avg)}$ normalised to 25 K, (g) 3D permalloy inverse opal $R_{P(xx,Avg)}$ and (h) 3D permalloy inverse opal $R_{P(xx,Avg)}$ normalised to 25 K. Dashed lines mark the temperature at which changes in the temperature evolution of $R_{P(xx,Avg)}$ occurred. The temperature dependence of the indium tin oxide coated glass resistance was extracted from mobility and carrier concentrations published by Kikuchi *et al.* [123].

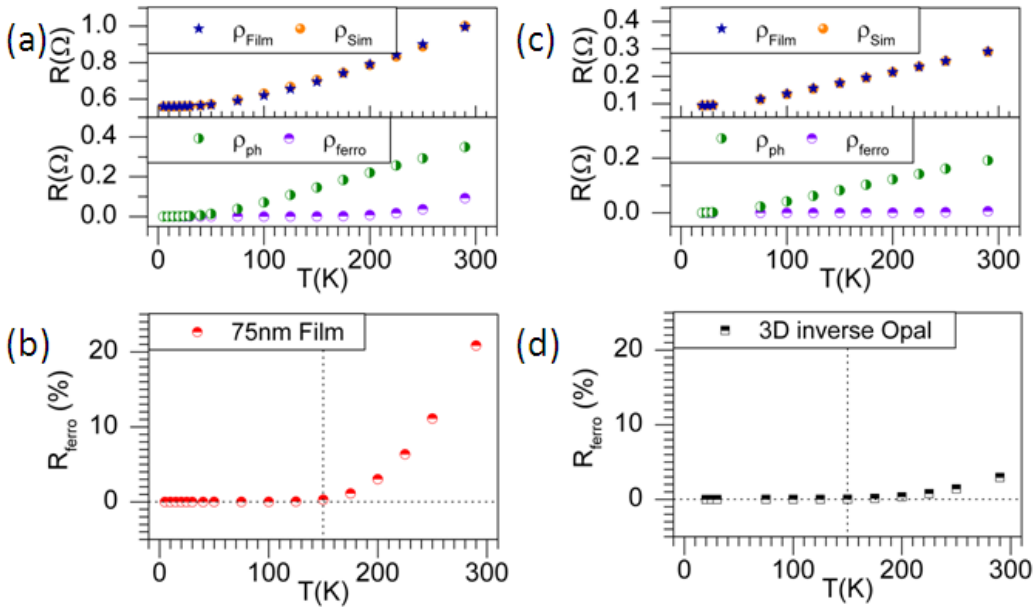

Figure 6.13 Temperature dependence of the zero field resistance. (a) (Top) comparison between zero field resistance of a 75±10 nm thick electrochemically deposited film and simulations. (Bottom) breakdown of the zero field resistance into its phonon (ρ_{ferro}) and spin disorder contribution (ρ_{ferro}). (b) ρ_{ferro} extracted from the 75±10 nm permalloy film versus temperature. (c) (Top) comparison between zero field resistance of 3D permalloy inverse opal and simulations. (Bottom) breakdown of the zero field resistance into its phonon (ρ_{ferro}) and spin disorder contribution (ρ_{ferro}). (b) ρ_{ferro} extracted from the 2D permalloy inverse opal versus temperature.

6.4 Hall Resistance

The Hall resistance of a quasi two dimensional magnetic permalloy inverse opal and a three dimensional inverse opal was measured at temperatures ranging from 2 K to 290 K. The anomalous Hall of the quasi two dimensional inverse opal taken at 2 K and 290 K are shown in figures 6.14(a) and (b) respectively. The field was applied along the out of plane axis and was swept at a rate of 0.7 A/s resulting in a data point roughly every 4.61 mT. 5 K and 290 K anomalous Hall data measured in the three dimensional inverse opal is shown in figure 6.14(d) and (e) respectively.

The low temperature (2 K) and high temperature (290 K) planar Hall data of the quasi two dimensional inverse opal are shown in figures 6.14(g)-(h). The three dimensional inverse opal planar Hall data is shown in figure 6.14(j) and (k) at 3 K and 290 K respectively. In the planar Hall configuration the current was applied between diagonally opposite corners of the sample, the voltage was measured perpendicular to the current flow and the field was applied at a 45° angle to the current. The field was swept at a rate of 0.03 A/s. Even though the external field is applied in-plane, due to the three dimensionality of the inverse opals, the low field magnetisation can have out of plane components leading to the possibility of observing an anomalous Hall effect contribution to the resistance measurement.

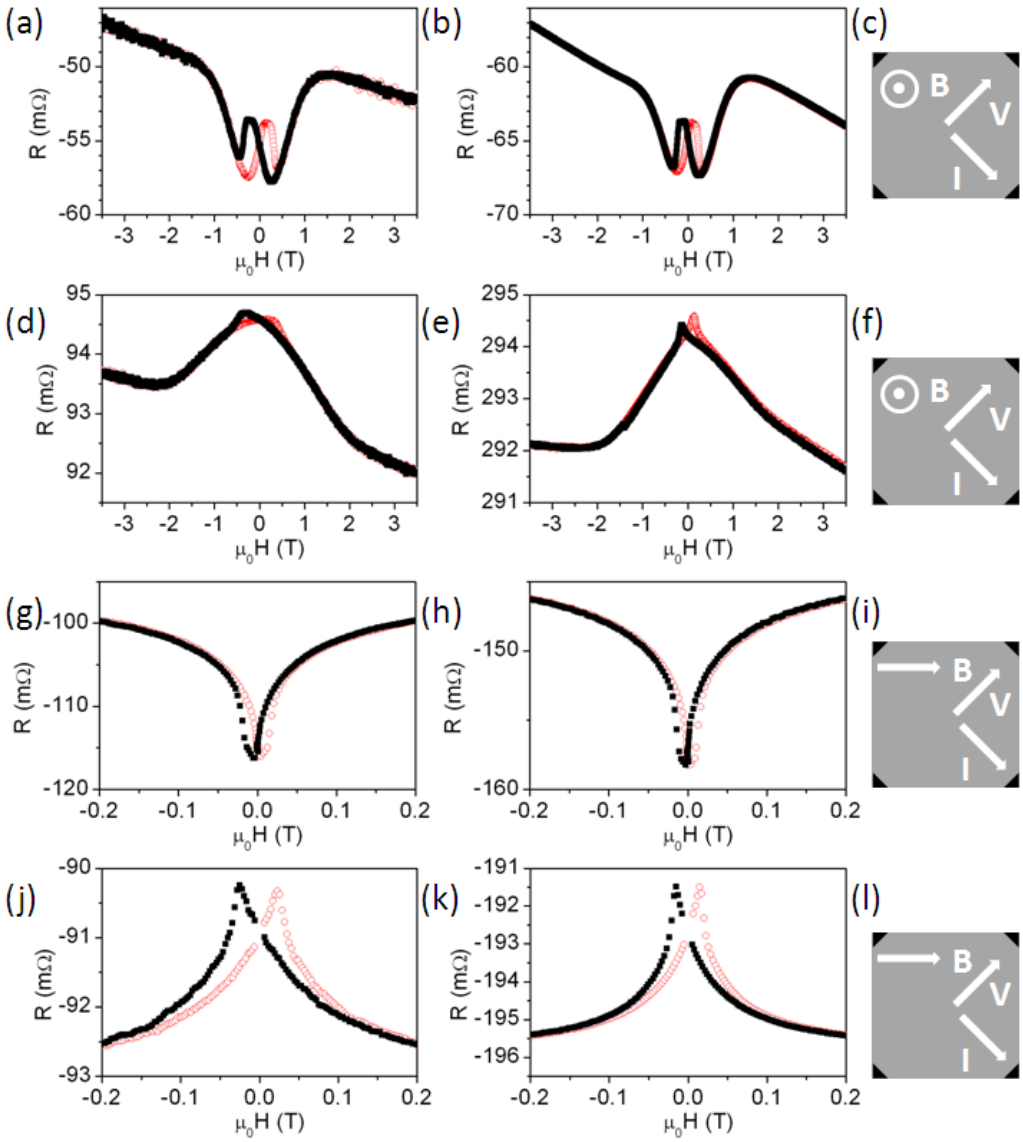

Figure 6.14 Anomalous Hall resistance of the quasi 2D inverse opal at (a) 2 K and (b) 290 K. The relative field, current and voltage orientation are shown in (c). Anomalous Hall resistance of the 3D inverse opal at (d) 5 K and (e) 290 K. The relative field, current and voltage orientation are shown in (f). In-plane Hall resistance of the quasi 2D inverse opal at (g) 2 K and (h) 290 K. The relative field, current and voltage orientation are shown in (i). In-plane Hall resistance of the 3D inverse opal at (j) 3 K and (k) 290 K. The relative field, current and voltage orientation are shown in (l).

6.4.1 In-Plane 180° Magnetic Reversal

The asymmetry of the resistance sweeps was evaluated for the irreversible part of the planar Hall resistance and is shown in figure 6.15(a) in case of the quasi two dimensional inverse opal and figure 6.15(c) in case of the three dimensional inverse opal. $R_{P(xy,Diff)}$ is the difference between the up and the down sweep resistance at positive fields and at negative fields. The temperature evolution of the height of the peak observed in figure 6.15(a) and (c) is shown in figure 6.15(b) and (d) respectively.

$R_{P(xx,Diff)}$ extracted from the irreversible part of the quasi two dimensional planar Hall data, is shown in figure 6.15(b). A maximum at 2 K of -0.65$\pm$0.04 mΩ was observed. $R_{P(xx,Diff)}$ was seen to decrease rapidly with increasing temperature staying approximately constant at a value of -0.10$\pm$0.04 mΩ at 25 K and above.

$R_{P(xx,Diff)}$ extracted from the irreversible part of the three dimensional planar Hall data, is shown in figure 6.15(d). A maximum at 5K of 0.12$\pm$0.01 mΩ was observed. $R_{P(xx,Diff)}$ was seen to decrease rapidly with increasing temperature reaching a value of 0.09$\pm$0.01 mΩ at 25 K. Between 125 K and 175 K $R_{P(xx,Diff)}$ was observed to stay constant at 0.05$\pm$0.01 mΩ.

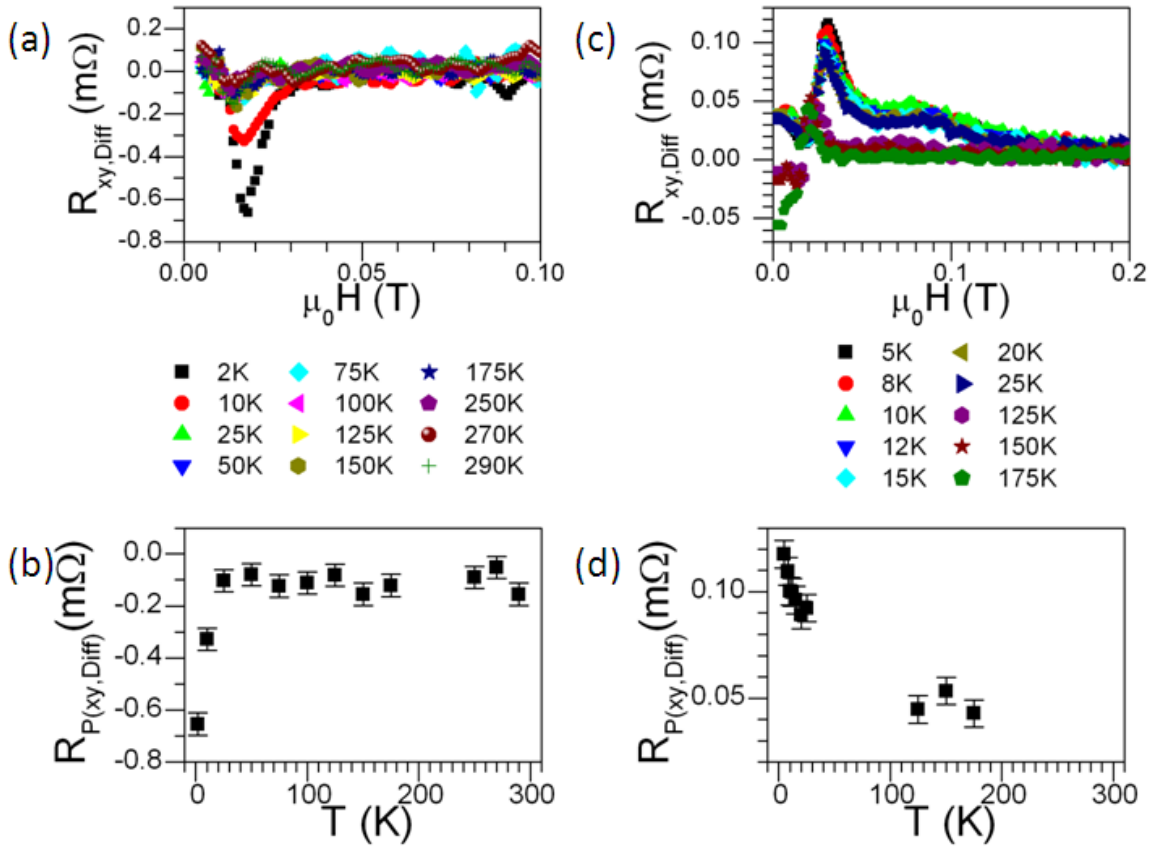

Figure 6.15 Irreversible part of the quasi 2D in-plane Hall resistance data: (a) $R_{xy,Diff}$, (b) temperature evolution of peak height $R_{P(xy,Diff)}$ in (a). Irreversible in-plane Hall resistance of the 3D inverse opal: (c) $R_{xy,Diff}$, (d) temperature evolution of peak height $R_{P(xy,Diff)}$ in (c).

6.4.2 Out of Plane 180° Magnetic Reversal

The reversible component $R_{xy,Sat}$ of the out of plane Hall measurement extracted from the two dimensional and three dimensional inverse opal transport data is shown in figure 6.16(a) and (c) respectively. The reversible Hall resistance component allows the extraction of the intercept, $R_{0,xy(Sat)}$, obtained by fitting a line through the high field data, which is proportional to the anomalous Hall coefficient R_S. $R_{0,xy(Sat)}$ extracted from the quasi two dimensional inverse opal anomalous Hall resistance is shown in figure 6.16(b). $R_{0,xy(Sat)}$ extracted from the three dimensional inverse opal anomalous Hall resistance is shown in figure 6.16(f). In both cases $R_{0,xy(Sat)}$ was found to be positive. The sign is consistent with Soffer *et al.*'s observation for Ni_xFe_{1-x} compositions below $x = 0.8$ [61]. An increase with increasing temperature was observed.

The irreversible component $R_{xy,Diff}$ extracted from the quasi 2D and the 3D inverse opal Hall resistance is shown in figure 6.16(c) and (g). $R_{P(xy,Diff)}$ are shown in figure 6.16(d) and (h) for both samples. The peak asymmetry observed in the quasi 2D inverse opal is at a maximum of 0.44 ± 0.05 mΩ at 2 K and was seen to vanish between 15 K and 20 K. No apparent asymmetry was observed in the irreversible peaks measured on the 3D inverse opal below 225 K. A non zero $R_{P(xy,Diff)}$ might be observed for 225 K and 250 K, however not enough temperatures were measured around 225 to 290 K to exclude a non systematic shift in the resistance measurement caused by factors such as: temperature fluctuations during the measurement.

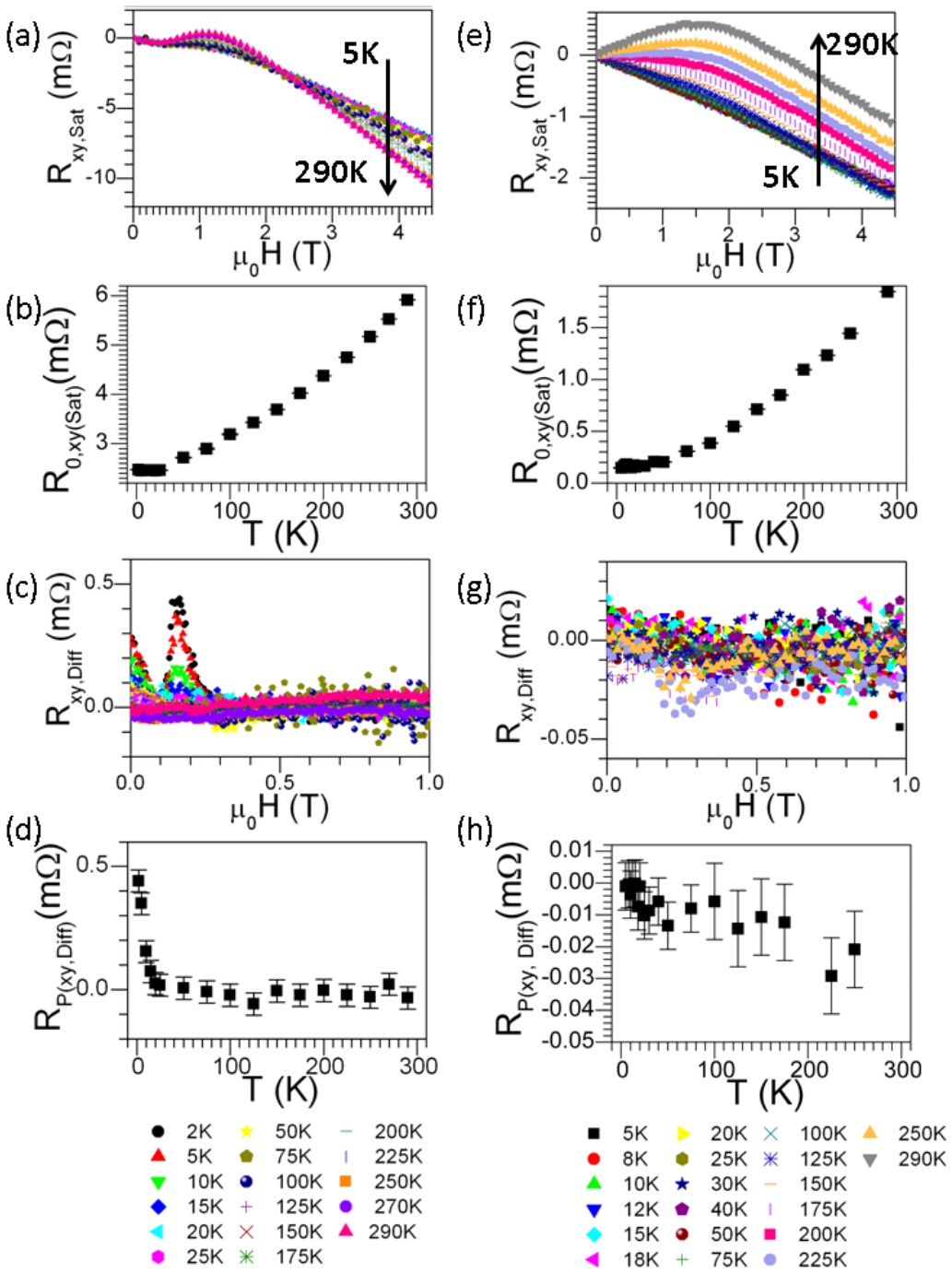

Figure 6.16 Reversible part of the quasi 2D anomalous Hall resistance data: (a) $R_{xy,Sat}$, (b) temperature evolution of high field linear fit intercept with the x-axis $R_{P(xy,Sat\,\mu_0 H=0)}$ of data in (a). Irreversible part of the quasi 2D anomalous Hall resistance data: (c) $R_{xy,Diff}$ and (d) $R_{P(xy,Diff)}$. Reversible part of the 3D anomalous Hall resistance data: (e) $R_{xy,Sat}$, (f) temperature evolution of high field linear fit intercept with the x-axis $R_{0,xy(Sat)}$ of data in (e). Irreversible part of the 3D anomalous Hall resistance data: (g) $R_{xy,Diff}$ and (h) $R_{P(xy,Diff)}$.

6.4.3 Discussion

The temperature dependence of the asymmetry in the irreversible part of the Hall resistance caused by the application of an in-plane applied field, $R_{P(xy,Diff)}$, is shown in figure 6.17(a). Figure 6.17(b) shows the the in-plane temperature evolution of $R_{P(xy,Diff)}$ normalised to 10 K. The in-plane $R_{P(xy,Diff)}$ extracted from two dimensional honeycomb artificial spin ice was plotted along side the permalloy inverse opal data. The in-plane Hall resistance of quasi two dimensional magnetic inverse opals, exhibits evidence of the characteristic anomaly of two dimensional honeycomb artificial spin ice at low temperature. However, whereas the asymmetry vanished for two dimensional honeycomb artificial spin ice above 15 K the asymmetry observed in quasi two dimensional inverse opals reaches a constant level of 35 % of the 10 K value above 15±5 K. Three dimensional permalloy inverse opals showed a 30 % decrease of $R_{P(xy,Diff)}$ between its maximum value at 5 K and 15 K. Between 15 K and 25 K $R_{P(xy,Diff)}$ was observed to remain constant. A further reduction of $R_{P(xy,Diff)}$ by approximately 50 % was observed to occur between 25 K and 125 K. $R_{P(xy,Diff)}$ extracted from the quasi two dimensional and the three dimensional inverse opal collapsed to a constant level of 35 % of the 10 K value at high temperatures. This is a clear distinction between the inverse opals and the honeycomb artificial spin ice. The origin of this distinction is most likely found in the geometrical differences.

Due to the three dimensionality and the curvatures, evaluating the expected behaviour of the magnetic inverse opals is far from straight forward. Structurally, the most similarities are found between the quasi two dimensional inverse opal and the honeycomb artificial spin ice. Approximating the in-plane wires by cylindrical nanowires with an estimated diameter of around $d = w_{\parallel} = a/2 = 75$ nm and a length of $L_{\parallel} = 1.155a$ results in a length to width ratio of $L/w \sim 2.3$ (see figure 6.18(a)). Figure 6.18(b) shows a comparison between the cylindrical wire approximation and the actual concave triangular shape of the wires. The true picture deviates further away from the cylindrical approximation the closer one gets to the vertices.

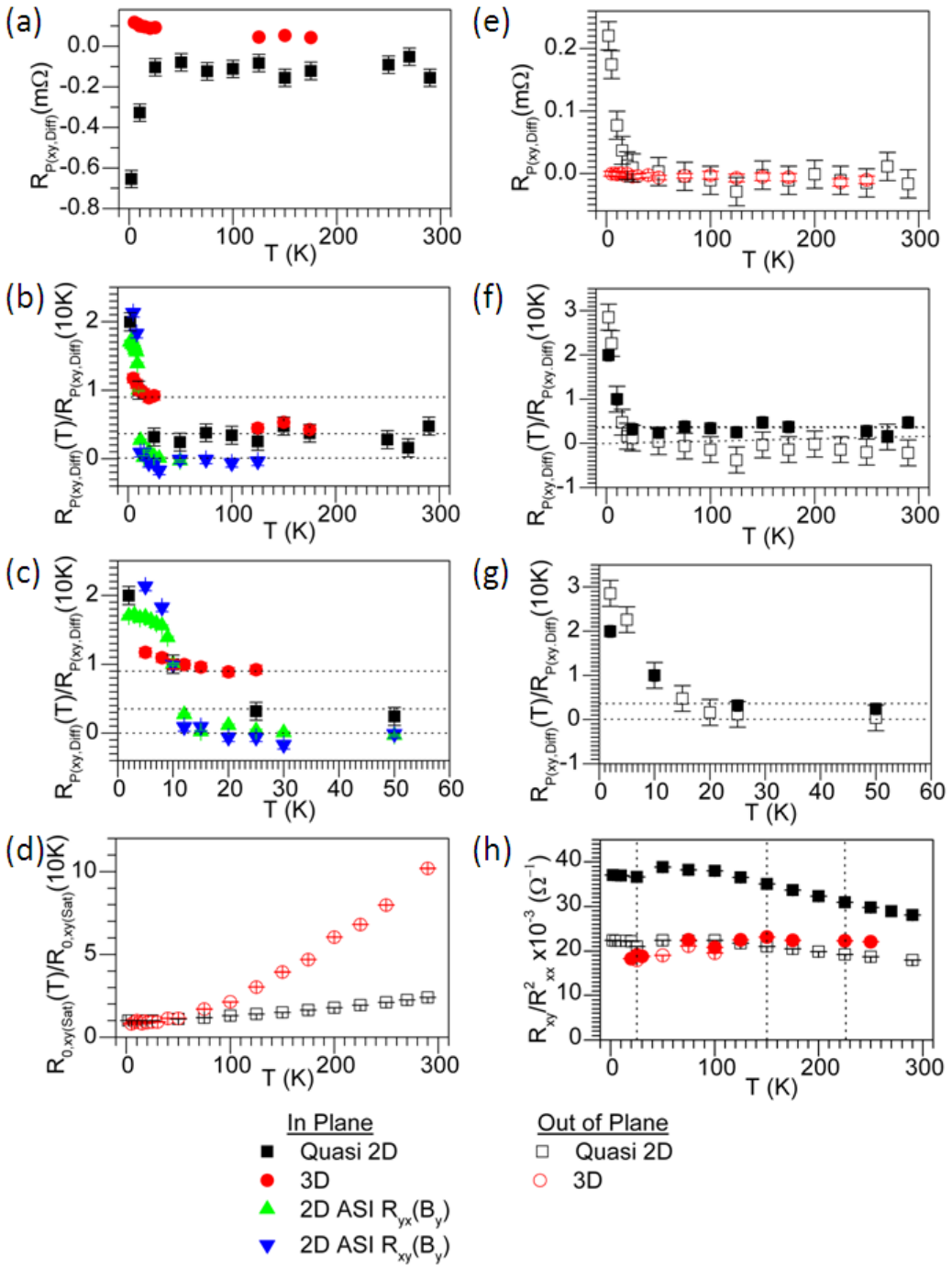

Figure 6.17 Temperature dependence of normalised Hall resistance data. (a) $R_{P(xyDiff)}$ field applied in-plane. (b) $R_{P(xyDiff)}$ field applied in-plane normalised to 10 K. (c) low temperature region of (b). (d) $R_{0,xy(Sat)}$ normalised to the 10K value. (e) $R_{P(xyDiff)}$ field applied out plane. (f) Comparison between $R_{P(xyDiff)}$ normalised to 10 K extracted from in-plane and out of plane Hall resistance measurement of the quasi two dimensional inverse opal. (g) low temperature region of (f). (h) Hall conductance R_{xy}/R_{xx}^2. ASI refers to the 2D honeycomb artificial spin ice measured in chapter 5.

If one tries to calculate a relative transition temperature for the quasi two dimensional artificial spin ice ($T^{II}_{ice,q2D}$) in comparison to the truly two dimensional artificial honeycomb spin ice using Möller and Moessner model then

$$\frac{T^{II}_{ice,q2D}}{T^{II}_{ice,Py}} \sim 35 \tag{6.1}$$

using $q = (M_{Sat} \times Area) = M_{Sat}\pi a^2$ for the cylindrical wires. Hence one would expect a transition temperature around 524 K. However, if one approximates the quasi two dimensional inverse opal to consist of rectangular wires of width 100 nm then the wire would have a height equal to $a/4$ (see figure 6.18(c)) which would lead to a ordering temperature ratio of

$$\frac{T^{II}_{ice,q2D}}{T^{II}_{ice,Py}} \sim 25 \tag{6.2}$$

hence an ordering temperature of around 375 K. The transition temperature is, therefore, extremely dependent on the wire shape and dimensions. A high transition temperature could explain the non zero asymmetry up to room temperature. However, it is important to keep in mind that the transition temperature in Möller and Moessner model is only expected to scale with $T^{II}_{ice} \propto q^2/a$ assuming the deviation from a perfect Ising model is small; Due to the curvature of the bars connecting the vertices, a large deviation from a true Ising state close to the vertex is to be expected. Nevertheless, the rough estimate of the transition temperature agrees with experiments.

$R_{P(xy,Diff)}$ extracted from the out of plane Hall resistance measurement exhibited a peak at low temperatures and was seen to vanish at 15 K. This is in contrast with the two dimensional honeycomb artificial spin ice possessing a small out of plane $R_{P(xy,Diff)}$ below 15 K which was seen to increase with increasing temperature. The most obvious difference between the two structures is the sample thickness. The quasi two dimensional magnetic inverse opal was found to be 248$\pm$15 nm thick which is in stark contrast to the 18 nm of the honeycomb artificial spin ice. The increased thickness will allow some deviation from the

in-plane magnetisation configuration especially at the vertices. Approximating the filled void at the vertex of the permalloy quasi 2D inverse opal as a perpendicular cylindrical nanowire leads to a wire of diameter $d = w_{\perp} = 0.154a$ and length $L = t = 248 \pm 15$ nm (see figure 6.18(d)). This leads to a length to width ratio of $L/w \sim 10.7$, a large enough ratio for an expected shape anisotropy, neglecting any deviation from this simplistic picture.

VSM measurements showed that the easy axis of the inverse opal is in the plane, hence overall the in-plane approximation dominates the magnetic response. However, it is conceivable that after a saturation field out of plane, the vertices will retain an out of plane magnetisation at zero field which will influence any further switching. Zhang *et al* showed that magnetostatically interacting single domain ferromagnetic islands with magnetisation normal to the plane on a honeycomb lattice possess an unique ground state if nearest neighbour interactions dominate [124]. This ground state takes the form of antiferromagnetic alignment of adjacent vertices [124]. It is possible that this preferential antiferromagnetic alignment of the out of plane magnetisation ensures time reversal symmetry breaking ordering at low temperatures which breaks the symmetry of the current flow, leading to the observed asymmetry in the resistance peaks.

However, if out of plane magnetisation is allowed, then one would expect an anomalous Hall contribution to the transport signal, in-plane as well as out of plane. Figure 6.17(d) shows $R_{0,xy(Sat)}$ normalised to 10 K extracted from the out of plane transport data. An increase with temperature was observed. The unusual non-zero resistance peak asymmetry associated with the in-plane Hall resistance was observed to be temperature independent above 15 K, hence $R_{P(xy,Diff)}$ does not show the temperature evolution expected from the anomalous Hall contribution and it is not likely to be the sole cause for the non-vanishing electrical transport signature.

A striking similarity was observed between the low temperature evolution of the in-plane asymmetry and the out of plane asymmetry of the quasi two dimensional permalloy inverse opal Hall resistance (see figure 6.17(g)). This might indicate that the low temperature peaks in the quasi two dimensional inverse opal are caused by the same effect. Hence,

at low temperatures there might be some antiferromagnetic ordering of an out of plane magnetisation at the vertices affecting the transport.

This might also be the cause for the reduced rate of change with temperature of the low temperature peak observed in the case of the truly three dimensional permalloy inverse opal. The three dimensional inverse opals possess a well defined shape anisotopy controlled nanowire along the out of plane axis. Hence a stronger influence on the electrical transport is to be expected which could lead to a stabilization of the effect up to higher temperatures.

The similarities of the irreversible transport features between the quasi two dimensional inverse opal and the two dimensional honeycomb artificial spin ice suggests that a quasi two dimensional inverse opals with a d/a ratio of 0.8 is geometrically frustrated. The characteristic asymmetry of artificial spin ice at low temperatures was found to be a factor of 10 smaller in the quasi 2D inverse opals in comparison with the truly 2D artificial spin ice. This could be a result of the inverse opal being an assembly of ordered domains rotated at an arbitrary angle to each other whereas the order of the measured honeycomb artificial spin ice is 'single domain'. The magnitude of the low temperature Hall signature observed for the honeycomb artificial spin ice was seen to be extremely angle dependent. The disorder in the domain orientation with respect to the field will thus result in an averaging over many different switching fields and current and magnetisation angles which is likely to lead to the observed suppression of the low temperature asymmetry.

Furthermore, the similarities between the quasi two dimensional inverse opal and the three dimensional inverse opal leads to the conclusion that the three dimensional inverse opal is indeed a three dimensional artificial spin ice. This result is in agreement with the localised Lorentz TEM measurements on thin slices of the inverse opal structure. However more high temperature measurements are needed to fully investigate the decay of $R_{P(xy,Diff)}$ with temperature.

The preservation of the artificial spin ice electrical transport signature in the magnetic inverse opals is surprising considering the structural defects.

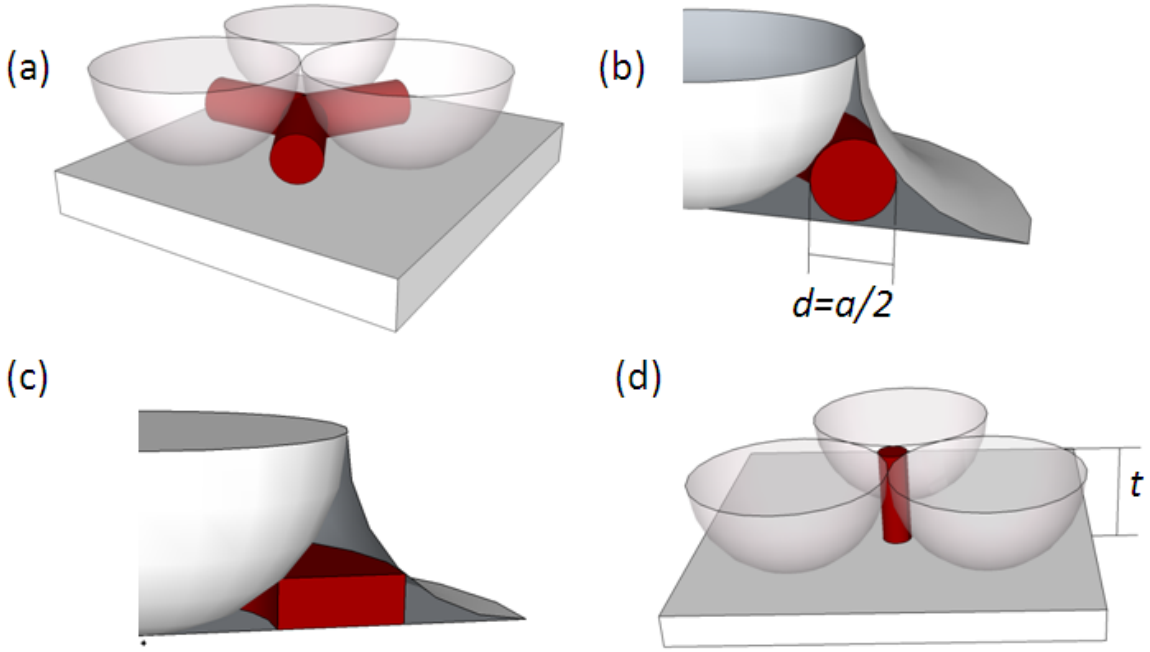

Figure 6.18 Quasi 2D inverse opal cylindrical wire approximation. (a) In plane wires (diameter $d = w_{\parallel} = a/2$ nm with a vertex to vertex length of $L_{\parallel} = 1.155a$), (b) Comparison between cylidrical wire approximation and true shape. (c) Comparison between a rectangular wire approximation and true shape (wire width is 100 nm and wire diameter is $a/4$). (d) Out of plane wire (diameter $w_{\perp} = 0.154a$ with a vertex to vertex length of $L_{\parallel} = t$ where t is the thickness of the sample.

Figure 6.17(h) shows the temperature dependence of $R_{0,xy(Sat)}$ taking into account the change in the longitudinal resistance. The longitudinal conductivity of permalloy nanowire is around $10^5\ \Omega^{-1}\mathrm{cm}^{-1}$ [119] hence the anomalous Hall conductivity is expected to be independent of the longitudinal conductivity [57]. This results in $\rho_{xy} \propto \rho_{xx}^2$ which implies that $R_{xy} \propto R_{xx}^2$. R_{xx} was observed to be larger for the quasi two dimensional inverse opal in comparison with the three dimensional inverse opal, therefore R_{xy} is expected to be larger as well. Experimentally R_{xy} was found to be larger for the quasi two dimensional sample. R_{xx} was observed to increase with temperature which is reflected in the observed increase of R_{xy} with temperature. However, if the anomalous Hall conductivity remains in the same scaling regime then R_{xy}/R_{xx}^2 is expected to be constant with temperature, whereas R_{xy}/R_{xx}^2 calculated from the three dimensional data was seen to be linear with temperature. However R_{xy}/R_{xx}^2 of the two dimensional inverse opal deviated from constant above 150 K (a change of 20 % was observed). The cause of this is not clear but could lie in the contraction of the substrate and the permalloy with temperature aggravating structural defects like cracks which will in turn have an influence on $R_{0,xx}$. Furthermore, an overall increase of R_{xy}/R_{xx}^2 was seen for R_{xy}/R_{xx}^2 calculated using $R_{0,xx}$ extracted from the in-plane measurement and $R_{0,xx}$ extracted from the out of plane measurement. This change is most likely explained by the not well defined sample area causing the resistance measured to be different between different corners of the sample. It is important to note that the temperature behaviour has not changed, hence the sample properties are identical, only the absolute value has shifted.

6.5 Conclusion

The magnetic properties of permalloy inverse opals with void diameter of around 300 nm were studied at room temperature using angle dependent VSM, STXM and LTEM. The influence of temperature on the magnetic switching of magnetic inverse opals (quasi two dimensional and three dimensional) was investigated indirectly using magnetoresistance

and Hall resistance measurements.

The magnetometry and the STXM data showed that the samples consisted of ordered domains rotated to each other masking any angle dependence of the magnetic reversal. LTEM measurements performed on a slices through multilayer three dimensional permalloy inverse opal showed magnetic behaviour dominated by the shape anisotropy and magnetic frustration due to interactions at the vertices.

The electrical transport showed atypical low temperature behaviour similar to permalloy and cobalt honeycomb artificial spin ice. However, the structural defects and the change of the angle between the field and the nanostructure of the individual domains resulted in a reduction of the effect.

Overall permalloy inverse opals, grown around a fcc closed packed self assembled polystyrene sphere template, shows great potential as a truly three dimensional artificial spin ice on a macroscopic scale.

Chapter 7

Conclusion and Future Work

7.1 Conclusion

In this thesis the mechanism of the magnetic reversal in artificial spin ice was investigated. The understanding of the magnetic domain wall propagation through a complex network, as presented by the artificial spin ice structure, was furthered at room temperature as well as low temperatures. The findings where used to investigate the potential of magnetic inverse opals as a artificial spin ice which can extended from a two dimensional structure into a three dimensional construct.

At room temperature, the influence of the domain wall structure and the proximity of, comparatively large ferromagnetic features in contact with the array, were investigated. The chirality, of the propagating domain walls, was found to have a crucial effect on the array reversal, by influencing the passage through each vertex. It was postulated that the domain wall chirality experiences the energy landscape, created by the moment configuration of the vertices, in different ways. For an accurate description of the field driven magnetic reversal, domain wall considerations have to be added to the magnetic charge model developed to prior to this work. Soft ferromagnetic pads, connected to the edges of the artificial spin ice increased the likelihood of long cascades in the early stages of the magnetic reversal, however a manipulation of the edge thickness was found to be needed

to increase the probability of such events to a significant level. Both, the domain wall structure, the chirality, and soft ferromagnetic pads connected to the array, showed potential in controlling aspects of the magnetic reversal.

Electrical transport measurements allowed an insight into the magnetic reversal of artificial spin ice not easily accessibly with imaging techniques. The work presented in this thesis confirmed the unusual Hall signature at low temperatures to be a generic feature of artificial spin ice structures, eliminating the possibility of its origin lying in material properties. The onset temperature was found to scale with the ferromagnetic bar dimensions and the saturation magnetisation. A fundamental change in the magnetic reversal of the artificial spin ice was postulated to be the cause of the unusual feature. Its origin was argued to lie in anisotropic magnetoresistance arguments.

The magnetic behaviour of permalloy inverse opals was investigated using a variety of characterisation techniques. Similarities to published work on anti-dot arrays and electrical transport measurements of two dimensional permalloy artificial spin ice suggests that inverse opals indeed are frustrated magnets.

The unusual temperature signature of ferromagnetic artificial spin ice was found to be surprisingly resistant to substrate changes and fabrication defects.

7.2 Future Work

7.2.1 Magnetic Charge Carrier Control in Artificial Spin Ice

The controlling influence of the domain wall chirality was deduced to originate in a change of the energy landscape depending on the chirality, however the exact shape could not be determined by the measurements. Such energy landscape can be experimentally deduced by injecting a known chiral transverse domain wall into a single junction and probing the fields needed to push the wall into the vertex; extracting the propagation fields and the fields needed to pull the domain wall out again. Spatially resolved magneto-optical Kerr effect has been shown to allow such deterministic measurements [93]. Direct experimental

confirmation of the energy landscape and propagation direction of up and down transverse domain walls through a single artificial spin ice vertex can be achieved by following a similar approach to D. Petit *et al.* [93]. A mapping of the exact energy landscape would be the logical next step in characterising the field driven magnetic reversal of artificial spin ice.

A further exploration into the control of magnetic reversal could involve the combination of domain wall injection and chirality control. To such an extend, the injection of domain walls with known chirality will be required. This would enable, for example, the creation of ice rule violations during the early stages of the magnetic switching where the implications of said violation can be observed without the interference of other switching cascades. It has been shown that fashioning the beginning of a nanowire into a C shape allows the creation of a domain wall of known chirality. However, a rotation of the external magnetic field is needed to create and push the domain wall around the bend into the horizontal part of the wire. OOMMF simulations shows that triangular injection pads are a promising structure to achieve the nucleation of transverse domain walls of controlled chirality without the field rotation.

7.2.2 Magnetotransport of Two Dimensional Artificial Spin Ice

Electrical transport measurements suggest that there is change in the magnetic behaviour of artificial spin ice below a critical temperature which is dependent on the saturation magnetisation (details found in chapter 5). The next step into investigating this unusual behaviour would be the direct imaging of the magnetic state through the reversal at low temperatures. However, imaging at temperatures below 50 K and 15 K are challenging as most experimental set ups (PEEM, STXM and LTEM) are currently limited to liquid nitrogen temperatures. Magnetic force microscopy at temperatures down to 4 K are possible using an attocube scanning probe microscope in conjunction with a cryostat. However, magnetic force microscopy measures the stray field emitted by the sample, in case of artificial spin ice the stray field at the vertices, hence magnetic force microscopy can only

distinguish between a $+q$, a $-q$, a $+3q$ and a $-3q$ state but cannot resolve the state of the individual three bars of each vertex. Despite this limitation magnetic force microscopy in conjunction with magnetisation versus field measurements will be able to confirm the transition and might help further our understanding of the observed phenomenon.

Furthermore, if the unusual behaviour of the honeycomb artificial spin ice is indeed a reflection of vertex dipole interactions then a tuning of the temperature should be achievable through changing the nanowire dimensions. For example a transition temperature of 30 K is expected for honeycomb artificial spin ice constructed from 18 nm thick, 100 nm wide and 500 nm long bars. This potential dependence on the transition temperature could allow the creation of an artificial spin ice with a high enough transition temperature allowing the direct magnetisation imaging with conventional liquid nitrogen cool-able equipment such as LTEM, e.g. 18 nm thick, 200 nm wide and 500 nm long bars should lead to a critical temperature of 120 K.

Investigating the current flow through a single vertex, especially the change in resistance due to the vertex domain wall position, could help shed light on the question anisotropic magnetoresistance effects can cause a current asymmetric current distribution.

7.2.3 Three Dimensional Artificial Spin Ice

The findings of chapter 6 suggest that permalloy inverse opals indeed acts like frustrated artificial spin ice whose dimensionality can be tuned by altering the thickness. The origin of the low temperature increase in the asymmetry, was proposed to be due to antiferromagnetic ordering of the out of plane magnetic moments situated at the vertices due to the thickness. The electrical transport of truly three dimensional inverse opals exhibited a non vanishing asymmetry of the irreversible in-plane Hall resistance peaks, however then low temperature peak showed a slower decay to the constant high temperature level.

Further signal to noise improvement and investigation of angle dependence will require electrical transport measurement on a single domain in order to avoid disorder introduced by the characteristic drying cracks and randomisation due to the disorder in the

domain orientation with respect to each other.

A further development could include electroetching of permalloy inverse opals allowing the manipulation of the bar dimensions leading to the control over the shape anisotropy and the area deviating from the Ising approximation. The layer dependence could also be systematically investigated including various thicknesses between one and three layers and considerably thicker samples e.g. 20 layers. This would allow the probing of the significance of the vertical bar on the magnetic reversal.

A further development could include electroetching of permalloy inverse opals allowing the manipulation of the bar dimensions leading to the control over the shape anisotropy and the control over the area deviating from the Ising approximation.

Bibliography

[1] R.F. Wang, C. Nisoli, R.S. Freitas, J. Li, W. McConville, B.J. Cooley, M.S. Lund, N. Samarth, C. Leighton, V.H. Crespi, and P. Schiffer. Artificial 'spin ice' in a geometrically frustrated lattice of nanoscale ferromagnetic islands. *Nature*, 439:303–306, 2006.

[2] Yi Qi, T. Brintlinger, and John Cumings. Direct observation of the ice rule in an artificial kagome spin ice. *Phys. Rev. B*, 77:094418, Mar 2008.

[3] W.R. Branford, S. Ladak, D.E. Read, K. Zeissler, and L.F. Cohen. Emerging chirality in artificial spin ice. *Science*, 335:1597–1600, 2012.

[4] Blundell. *Magnetism in Condensed Matter*. Oxford University Press, Oxford, UK, first edition, 2001.

[5] L.J. Pauling. The structure and entropy of ice and other crystals with some randomness of atomic arrangement. *J. Am. Chem. Soc*, 57:2680, 1935.

[6] A.P. Ramirez, A Hayashi, R.J. Cava, R.J. Siddharthan, and B.S. Shastry. Zero-point entropy in 'spin ice'. *Nature*, 399:333, 1999.

[7] M. J. Harris, S. T. Bramwell, D. F. McMorrow, T. Zeiske, and K. W. Godfrey. Geometrical frustration in the ferromagnetic pyrochlore $Ho_2Ti_2O_7$. *Phys. Rev. Lett.*, 79:2554–2557, Sep 1997.

[8] S T Bramwell and M J Harris. Frustration in ising-type spin models on the pyrochlore lattice. *Journal of Physics: Condensed Matter*, 10(14):L215, 1998.

[9] K Matsuhira, Y Hinatsu, K Tenya, and T Sakakibara. Low temperature magnetic properties of frustrated pyrochlore ferromagnets $Ho_2Sn_2O_7$ and $Ho_2Ti_2O_7$. *Journal of Physics: Condensed Matter*, 12(40):L649, 2000.

[10] H. Kadowaki, Y. Ishii, K. Matsuhira, and Y. Hinatsu. Neutron scattering study of dipolar spin ice $Ho_2Sn_2O_7$: Frustrated pyrochlore magnet. *Phys. Rev. B*, 65:144421, Mar 2002.

[11] S. Rosenkranz, A.P. Ramirez, A. Hazashi, R.J. Cava, and R. Siddharthan. Crystal-field interaction in the pyrochlore magnet $Ho_2Ti_2O_7$. *Journal of Applied Physics*, 87(9):5914, 2000.

[12] S. T. Bramwell, M. J. Harris, B. C. den Hertog, M. J. P. Gingras, J. S. Gardner, D. F. McMorrow, A. R. Wildes, A. L. Cornelius, J. D. M. Champion, R. G. Melko, and T. Fennell. Spin correlations in $Ho_2Ti_2O_7$: A dipolar spin ice system. *Phys. Rev. Lett.*, 87:047205, Jul 2001.

[13] T. Fennell, O. A. Petrenko, B. Fåk, S. T. Bramwell, M. Enjalran, T. Yavors'kii, M. J. P. Gingras, R. G. Melko, and G. Balakrishnan. Neutron scattering investigation of the spin ice state in $Dy_2Ti_2O_7$. *Phys. Rev. B*, 70:134408, Oct 2004.

[14] Byron C. den Hertog and Michel J. P. Gingras. Dipolar interactions and origin of spin ice in ising pyrochlore magnets. *Phys. Rev. Lett.*, 84:3430–3433, Apr 2000.

[15] M. Tanaka, E. Saitoh, H. Miyajima, T. Yamaoka, and Y. Iye. Magnetic interactions in a ferromagnetic honeycomb nanoscale network. *Phys. Rev. B*, 73:052411, Feb 2006.

[16] E. Saitoh, H. Tanaka, M.and Miyajima, and T. Yamaoka. Domain-wall trapping in a ferromagnetic nanowire network. *Journal of Applied Physics*, 93(7444):7444–7446, 2003.

[17] R.F. Wang, J. Li, W. McConville, C. Nisoli, and X. Ke. Demagnetization protocols for frustrated interacting nanomagnet arrays. *Journal of Applied Physics*, 101:09J104, 2007.

[18] C. Nisoli, R. Wang, J. Li, W.F. McConville, P.E. Lammert, P. Schiffer, and V.H. Crespi. Ground state lost but degeneracy found: The effective thermodynamics of artificial spin ice. *Phys. Rev. Lett.*, 98:217203, May 2007.

[19] J.P. Morgan, A. Stein, S Langridge, and C.H. Marrows. Thermal ground-state ordering and elementary excitations in artificial magnetic square ice. *Nature Physics*, 7:75–79, 2011.

[20] E. Mengotti, L. J. Heyderman, A. Fraile Rodríguez, A. Bisig, L. Le Guyader, F. Nolting, and H. B. Braun. Building blocks of an artificial kagome spin ice: Photoemission electron microscopy of arrays of ferromagnetic islands. *Phys. Rev. B*, 78:144402, Oct 2008.

[21] S. Ladak, D. Read, T. Tyliszczak, W.R. Branford, and L.F. Cohen. Monopole defects and magnetic coulomb blockade. *New Journal of Physics*, 13(2):023023, 2011.

[22] J. Li, X. Ke, S. Zhang, D. Garand, C. Nisoli, P. Lammert, V. H. Crespi, and P. Schiffer. Comparing artificial frustrated magnets by tuning the symmetry of nanoscale permalloy arrays. *Phys. Rev. B*, 81:092406, Mar 2010.

[23] G. Möller and R. Moessner. Artificial square ice and related dipolar nanoarrays. *Phys. Rev. Lett.*, 96:237202, Jun 2006.

[24] V. Kapaklis, U.B. Arnalds, A. Harman-Clarke, E.T. Papaioannou, M. Karimipour, P. Korelis, A. Taroni, P.C.W. Holdsworth, S.T. Bramwell, and B. Hjörvarsson. Melting artificial spin ice. *New Journal of Physics*, 14(3):035009, 2012.

[25] E. Mengotti, L.J. Heyderman, A. Fraile Rodríguez, F. Nolting, R.V. Hugli, and H. Braun. Real-space observation of emergent magnetic monopoles and associated dirac strings in artificial kagome spin ice. *Nature Physics*, 7:68–74, Jan 2011.

[26] L. A. S. Mól, W. A. Moura-Melo, and A. R. Pereira. Conditions for free magnetic monopoles in nanoscale square arrays of dipolar spin ice. *Phys. Rev. B*, 82:054434, Aug 2010.

[27] Y. Qi. *Artificial Spin Ice (PhD Thesis)*. University of Maryland, USA, 2008.

[28] X. Ke, J. Li, C. Nisoli, Paul E. Lammert, W. McConville, R. F. Wang, V. H. Crespi, and P. Schiffer. Energy minimization and ac demagnetization in a nanomagnet array. *Phys. Rev. Lett.*, 101:037205, Jul 2008.

[29] C. Nisoli, J. Li, X. Ke, D. Garand, P. Schiffer, and V.H. Crespi. Effective temperature in an interacting vertex system: Theory and experiment on artificial spin ice. *Phys. Rev. Lett.*, 105:047205, Jul 2010.

[30] C. Nisoli. On thermalization of magnetic nano-arrays at fabrication. *New Journal of Physics*, 14(3):035017, 2012.

[31] A. S. Wills, R. Ballou, and C. Lacroix. Model of localized highly frustrated ferromagnetism: the *kagomé* spin ice. *Phys. Rev. B*, 66:144407, Oct 2002.

[32] G. Chern, P. Mellado, and O. Tchernyshyov. Two-stage ordering of spins in dipolar spin ice on the kagome lattice. *Phys. Rev. Lett.*, 106:207202, May 2011.

[33] N. Rougemaille, F. Montaigne, B. Canals, A. Duluard, D. Lacour, M. Hehn, R. Belkhou, O. Fruchart, S. El Moussaoui, A. Bendounan, and F. Maccherozzi. Artificial kagome arrays of nanomagnets: A frozen dipolar spin ice. *Phys. Rev. Lett.*, 106:057209, Feb 2011.

[34] S. Ladak, D. E. Read, G.K. Perkins, L.F. Cohen, and W.R. Branford. Direct observation of magnetic monopole defects in an artificial spin-ice system. *Nature Physics*, 6:359–363, Apr 2010.

[35] A. Schumann and H. Zabel. Magnetic dipole configurations on honeycomb lattices: effect of finite size and boundaries. *Philosophical Transactioons of the Royal Society A*, 370:5783–5793, 2012.

[36] S. Ladak, D.E. Read, W.R. Branford, and L.F. Cohen. Direct observation and control of magnetic monopole defects in an artificial spin-ice material. *New Journal of Physics*, 13(6):063032, 2011.

[37] S.A. Daunheimer, O. Petrova, O. Tchernyshyov, and J. Cumings. Reducing disorder in artificial kagome ice. *Phys. Rev. Lett.*, 107:167201, Oct 2011.

[38] P.V. Hügli, G. Duff, B.O. OConchuir, E. Mengotti, A.F. Rodríguez, F. Nolting, L.J. Heyderman, and H.B. Braun. Artificial kagome spin ice: dimensional reduction, avalanche control and emergent magnetic monopoles. *Philosophical Transactioons of the Royal Society A*, 370:5767–5782, 2012.

[39] S Ladak, S.K. Walton, K Zeissler, T. Tyliszczak, D.E. Read, W.R. Branford, and L.F. Cohen. Disorder-independent control of magnetic monopole defect population in artificial spin-ice honeycombs. *New Journal of Physics*, 14(4):045010, Dec 2012.

[40] C. Castelnovo, R. Moessner, and L. Sondhi. Magnetic monopoles in spin ice. *Nature*, 451:42–45, Jan 2008.

[41] S.T. Bramwell, S.R. Giblin, S. Calder, R. Aldus, D. Prabhakaran, and T. Fennell. Measurement of the charge and current of magnetic monopoles in spin ice. *Nature*, 461:956–960, Oct 2009.

[42] O. Tchernyshyov. Magnetic monopoles: No longer on thin ice. *Nature Physics*, 6:323–324, May 2010.

[43] P. Mellado, O. Petrova, Y. Shen, and O. Tchernyshyov. Dynamics of magnetic charges in artificial spin ice. *Phys. Rev. Lett.*, 105:187206, Oct 2010.

[44] J.M.D. Coey. *Magnetism and Magnetic Materials*. Cambridge University Press, Cambridge, UK, 2010.

[45] R.C. O'Handley. *Modern Magnetic Materials Principles and Applications*. John Wiley and Sons, New York, USA, 2000.

[46] A. Hubert and R. Schafer. *Magnetic Domains: The Analysis of Magnetic Microstructures*. Springer, New York, USA, 2000.

[47] A. Hirohata, H.T. Leung, Y.B. Xu, C.C. Yao, W.Y. Lee, and J.A.C. Bland. Magnetic domain evolution in permalloy mesoscopic dots. *IEEE Transaction on Magnetics*, 35:3886, 1999.

[48] T.Y. Chung and S.Y. Hsu. magnetization reversal in single domain permalloy wires probed by magnetotransport. *Journal of Applied Physics*, 103:07C506, Oct 2008.

[49] R.D. McMichael and M.J. Donahue. Head to head domain wall sctructures in thin magnetic strips. *IEEE Trans. Mag*, 33:4167–4169, 1997.

[50] L. Thomas and S. Parkin. *Current Induced Domain Wall Motion in Magnetic Nanowires*. John Wiley Sons Ltd, second edition, 2007.

[51] N.L. Schryer and L.R. Walker. The motion of 180° domain walls in uniform dc magnetic fields. *Journal of Applied Physics*, 45:5406, 1974.

[52] D. Atkinson, D.A. Allwood, G. Xiong, M.D. Cooke, C.C. Faulkner, and R.P. Cowburn. Magnetic domain-wall dynamics in a submicrometre ferromagnetic structure. *Nature Materials*, 2:85–87, 2003.

[53] M. Hayashi, L. Thomas, C. Rettner, R. Moriya, and S.S.P. Parkin. Direct observation of the coherent precession of magnetic domain walls propagating along permalloy nanowires. *Nature Physics*, 3:21, 2007.

[54] R.S. Popovic. *Hall Effect Devices*. IOP Publishing Ltd, Bristol, UK, second edition, 2004.

[55] E.H. Hall. On a new action of the magnet on electric currents. *American Journal of Mathematics*, 2:287, 1879.

[56] C.M. Hurd. *The Hall Effect in Metals and Alloys*. Plenum Press, New York, USA, 1972.

[57] S. Onoda, N. Sugimoto, and N. Nagaosa. Quantum transport theory of anomalous electric, thermoelectric, and thermal hall effects in ferromagnets. *Phys. Rev. B*, 77:165103, Apr 2008.

[58] N.P. Ong and W. Lee. Geometry and the anomalous hall effect in ferromagnets, foundations of quantum mechanics in the light of new technology, arxiv:cond-mat/0508236. In *Proceedings of ISQM_Tokyo 05*, page 121, 2006.

[59] M.V. Berry. Quantal phase factors accompanying adiabatic changes. *Proc. R. Soc. Lond. A*, 392:45–57, Mar 1984.

[60] F. Wolff-Fabris, P. Pureur, J. Schaf, V. Vieira, and I.A. Campbell. The chiral anomalous hall effect in pdfe and aufe alloys. *Physica B: Condensed Matter*, 403(5âĂŞ9):1373 – 1374, 2008.

[61] S. Soffer, J.A. Dreesen, and E.M. Pugh. Hall effects, resistivity, and thermopower in fe and $fe_{1-x}ni_x$, for x=0 to 0.2. *Physical Review*, 140:A668–A675, May 1965.

[62] L.K. Bogart and D. Atkinson. Domain wall anisotropic magnetoresistance in planar nanowires. *Applied physics Letters*, 94(042511):042511, 2009.

[63] M. Hayashi, L. Thomas, R. Rettner, R. Moriya, X. Jiang, and S.S.P. Parkin. Dependence of current and field driven depinning of domain walls on their structure and chirality in permalloy nanowires. *Physical Review Letters*, 97(207205):207205, 2006.

[64] H.P. Myers. *Introductory Solid State Physics*. Taylor and Francis, London, UK, 1990.

[65] G.K. White and S.B. Woods. Electrical and thermal resistivity of the transition elements at low temperatures. *Philosophical Transactions of the Royal Society A*, 251:273–302, 1959.

[66] Digital Instrumetns Inc. *Dimension 3100 Instruction manual*. Digital Instruments Inc, 1997.

[67] S Foner. Versatile and sensitive vibrating-sample magnetometer. *Review of Scientific Instruments*, 30(7):548, Jan 1959.

[68] J. Mallison. Magnetometer coils and reciprocity. *Journal of Applied Physics*, 37:2514, Jan 1966.

[69] S.R. Hoon. An inexpensive, sensitive vibrating sample magnetometer. *Eu. J. Phys.*, 4:61, Jan 1983.

[70] H. Hopster and H.P. Oepen. *Magnetic Microscopy of Nanostructures*. Springer, Berlin, Germany, 2005.

[71] E. Beaurepaire, H. Bulou, A. Scheurer, and J.P. Kappler. *Magnetism: A Synchrotron Radiation Approach*. Springer, Berlin, Germany, 2006.

[72] E. Beaurepaire, H. Bulou, A. Scheurer, and J.P. Kappler. *Magnetism and synchrotron Radiation*. Springer, Berlin, Germany, 2010.

[73] A.F. Rodriguez, A. Kleibert, J. Bansmann, and F. Nolting. Probing single magnetic nanoparticles by polarization-dependent soft x-ray absorption spectromicroscopy. *Journal of Physics D: Applied Physics*, 43(474006), 2010.

[74] P.W. Hawkes. *Science of Microscopy*. Springer, New York, USA, 2008.

[75] J.N. Schapman. The investigation of magnetic domain structures in thin foils by electron microscopy. *Journal of Physics D: Applied Physics*, 17:623, 1984.

[76] N. Ida. *Engineering Electromagnetics, Second Edition*. Springer, New York, USA, 2004.

[77] G. Bertotti, I.D. Mayergoyz, and C. Serpico. *Nonlinear Magnetization Dynamics in Nanosystems*. Elservier Ltd, Oxford, UK, 2009.

[78] Y. Nakatani, A Thiaville, and J. Miltat. Faster magnetic walls in rougher wires. *Nature Materials*, 2:521, 2003.

[79] M.J. Donahue and D.G. Porter. *OOMMF 1.2a3 User's Guide*. Interagency Report NISTIR 6376, National Institute of Standards and Technology, Gaithersburg, Maryland, USA, 2002.

[80] B Hillebrands and K. Ounadjela. *Spin Dynamics in Confined Magnetic Structures*. Springer, New York, USA, 2002.

[81] A. Vansteenkiste and B. Van de Wiele. Mumax: a new high-performance micromagnetic simulation tool. *Journal of Magnetism and Magnetic Materials*, 323(21):2585, 2011.

[82] W.C. Uhlig and J. Shi. Systematic study of the magnetization reversal in patterned co and nife nanolines. *Applied Physics Letters*, 84:759, 2004.

[83] D.A. Allwood, G. Xiong, C.C. Faulkner, D. Atkinson, D. Petit, and R.P. Cowburn. Magnetic domain-wall logic. *Science*, 309:1688, 2005.

[84] M. Hayashi, L. Thomas, R. Moriya, C. Rettner, and S.S.P. Parkin. Current-controlled magnetic domain-wall nanowire shift register. *Science*, 320:209, 2008.

[85] S.S.P. Parkin, M. Hayashi, and L. Thomas. Magnetic domain-wall racetrack memory. *Science*, 320:190, 2008.

[86] M. Klaui. head-to-head domain walls in magnetic nanostructures. *J. Phys.: Condens. Matter*, 20:1, 2008.

[87] P. Ping Liu, E. Fullerton, O. Gutfleisch, and D.J. Sellmyer. *Nanoscale Magnetic Materials and Applications*. Springer, New York, USA, 2009.

[88] G.P. Wiederrecht. *Handbook of Nanoscale Optics and Electronics*. 2010.

[89] L. Brillouin. *Science and information Theory*. Dover Publications Inc., New York, USA, 2004.

[90] K. Zeissler, D.E. Walton, S.K. Read, Tyliszczak, L.F. Cohen, and Branford. The non-random walk of chiral magnetic charge carriers in artificial spin ice. *Scientific Reports*, 3:1–7, 2013.

[91] A.L. Comrey and H.B. Lee. *Elementray Statistics A problem Solving Approach*. Lulu com, USA, 2007.

[92] E.R. Lewis, D. Petit, L. Thevenard, A.V. Jausovec, L. O'Brien, E.R. Read, and R.P. Cowburn. Magnetic domain wall pinning by a curved conduit. *Applied Physics Letters*, 95:152505, 2009.

[93] D. Petit, A. Jausovec, H.T. Zeng, E. Lewis, L. O'Brien, D. Read, and R.P. Cowburn. Mechanism for domain wall pinning and potential landscape modification by artificially patterned traps in ferromagnetic nanowires. *Phys. Rev. B*, 79:214405, Jun 2009.

[94] M. Heumann, T. Uhlig, and J. Zweck. True single domain and configuration-assisted switching of submicron permalloy dots observed by electron holography. *Phys. Rev. Lett.*, 94:077202, Feb 2005.

[95] H.T. Zeng, D. Petit, L. OâĂŹBrien, D. Read, E.R. Lewis, and R.P. Cowburn. The influence of wire width on the charge distribution of transverse domain walls and their stray field interactions. *Journal of Magnetism and Magnetic Materials*, 322(14):2010 – 2014, 2010.

[96] L. O'Brien, A. Beguivin, D. Petit, A. Fernandez-Pacheco, D. Read, and R.P. Cowburn. Domain wall interactions at a cross-shaped vertex. *Philosophical Transaction of the Royal Society A*, 370:5794–5805, 2012.

[97] J. Yang, C. Nistor, G. S. D. Beach, and J. L. Erskine. Magnetic domain-wall velocity oscillations in permalloy nanowires. *Phys. Rev. B*, 77:014413, Jan 2008.

[98] J. Lee, K. Lee, S. Choi, K.Y. Guslienko, and S. Kim. Dynamic transformations of the internal structure of a moving domain wall in magnetic nanostripes. *Phys. Rev. B*, 76:184408, Nov 2007.

[99] M.T. Bryan, T. Schrefl, and D.A. Allwood. Dependence of transverse domain wall dynamics on permalloy nanowire dimensions. *Magnetic IEEE Transactions*, 46:1135, May 2010.

[100] E. R. Lewis, D. Petit, A.-V. Jausovec, L. O'Brien, D. E. Read, H. T. Zeng, and R. P. Cowburn. Measuring domain wall fidelity lengths using a chirality filter. *Phys. Rev. Lett.*, 102:057209, Feb 2009.

[101] S.H. Liou, R.F. Sabiryanov, S.S. Jaswal, J.C. Wu, and Y.D. Yao. Magnetic domain patterns of rectangular and elliptic arrays of small permalloy elements. *Journal of Magnetism and Magnetic Materials*, 226-230:1270–1272, Feb 2001.

[102] G. Möller and R. Moessner. Magnetic multipole analysis of kagome and artificial spin-ice dipolar arrays. *Phys. Rev. B*, 80:140409, Oct 2009.

[103] B. Raquet, M. Viret, E. Sondergard, O. Cespedes, and R. Mamy. Electron-magnon scattering and magnetic resistivity in 3*d* ferromagnets. *Phys. Rev. B*, 66:024433, Jul 2002.

[104] T. Taniyama, I. Nakatani, T. Namikawa, and Y. Yamazaki. Resistivity due to domain walls in co zigzag wires. *Phys. Rev. Lett.*, 82:2780–2783, Mar 1999.

[105] P.M. Tessier, O.D. Velev, A.T. Kalabur, J.F. Rabolt, A.M. Lenhoff, and E.W. Kaler. Assembly of gold nanostructured films templated by colloidal crystals and use in surface-enhanced raman spectroscopy. *J. Am. Chem. Soc.*, 122:9554–9555, 2000.

[106] R. Zhu, M. McLachlan, S. Reyntjens, F. Tariq, M.P. Ryan, and D.W. McComb. Controlling the electrodeposition of mesoporous metals for nanoplasmonics. *Nanoscale*, 1:355–359, 2009.

[107] P.N. Bartlett, P.R. Birkin, and M.A. Ghanem. Electrochemical deposition of macroporous platinum, palladium and cobalt films using polystyrene latex sphere templates. *Chem. Commun.*, pages 1671–1672, 2000.

[108] C. Kansal. *PhD Thesis: Ordered Macroporous Structures as Artificial Spin Ice Systems*. Imperial College London, London, UK, 2011.

[109] B. van Duffel, R.H.A. Ras, F.C. de Schryver, and R.A. Schoonheydt. Langmuir-blodgett deposition and optical diffraction of two-dimensional opal. *Journal of Materials Chemistry*, 11:3333–3336, 2001.

[110] M.A. McLachlan, N.P. Johnson, R.M. De La Rue, and D.W. McComb. Thin film photonic crystals: synthesis and characterisation. *Journal of Materials Chemistry*, 14:114–150, 2004.

[111] R.P. Cowburn, A.O. Adeyeye, and J.A.C. Bland. Magnetic switching and uniaxial anisotropy in lithographically defined anti-dot permalloy arrays. *Journal of Magnetism and Magnetic Materials*, 173:193, 1997.

[112] A.O. Adeyeye, S. Goolaup, , N. Singh, W. Jun, C.C. Wang, S. Jain, and D. Tripathy. Reversal mechanism in ferromagnetic nanostructures. *IEEE Transaction on Magnetics*, 44:1935–1940, 2008.

[113] N.G. Deshpande, M.S. Seo, X.R. Jin, S.J. Lee, Y.P. Lee, J.Y. Rhee, and K.W. Kim. Tailoring of magnetic properties of patterned cobalt antidots by simple manipulation of lattice symmetry. *Applied Physics Letters*, 96:122503, 2010.

[114] P.A.J. de Groot, A.A. Zhukov, R. Boardman, G. Bordignon, H Fangohr, and P.N. Bartlett. Geometrical multilayers: Coercivity in magnetic 3-d nanostructures. *Journal of Magnetism and Magnetic Materials*, 310:e846–e848, 2007.

[115] F. Haering, U. Wiedwald, T. Häberle, L. Han, A. Plettl, B. Koslowski, and P. Ziemann. Geometry-induced spin-ice structures prepared by self-organization on the nanoscale. *Nanotechnology*, 24(5):055305, 2013.

[116] A.A Zhukov, A.V. Goncharov, P.A.J. de Groot, M.A. Ghanem, I.S. El-Hallag, P.N. Bartlett, R. Boardman, H. Fangohr, V. Novosad, and G. Karapetrov. Oscillatory thickness dependence of the coercive field in three-dimensional anti-dot arrays from self-assembly. *Journal of Applied Physics*, 97:10J701, 2005.

[117] G. Subramanian, V. N. Manoharan, J. D. Thorne, and D. J. Pine. Ordered macroporous materials by colloidal assembly: A possible route to photonic bandgap materials. *Advanced Materials*, 11(15):1261–1265, 1999.

[118] S.K. Walton, K. Zeissler, W.R. Branford, and S. Felton. Malts: A tool to simulate lorentz transmission electron microscopy from micromagnetic simulations. *IEEE Transactions on Magnetics*, 49:1–6, 2013.

[119] Y Rheem, B-Y Yoo, B K Koo, W P Beyermann, and N V Myung. Synthesis and magnetotransport studies of single nickel-rich nife nanowire. *Journal of Physics D: Applied Physics*, 40(23):7267, 2007.

[120] Y. Rheem, B. Yoo, W.P. Beyermann, and N.V. Myung. Magnetotransport studies of a single nickle nanowire. *Nanotechnology*, 18(1):015202, 2007.

[121] M. Venkata Kamalakar and A. K. Raychaudhuri. Low temperature electrical transport in ferromagnetic ni nanowires. *Phys. Rev. B*, 79:205417, May 2009.

[122] M. Venkata Kamalakar, A. K. Raychaudhuri, X. Wei, J. Teng, and P.D. Prewett. Temperature dependent electrical resistivity of a single strand of ferromagnetic single crystalline nanowire. *Appl. Phys. Lett.*, 95:013112, 2009.

[123] N. Kikuchi, E. Kusano, H. Nanto, A. Kinbara, and H. Hosono. Phonon scattering in electron transport phenomena of {ITO} films. *Vacuum*, 59:492 – 499, 2000.

[124] S. Zhang, J. Li, I. Gilbert, J. Bartell, M.J. Erickson, Y. Pan, P.E. Lammert, C. Nisoli, K. K. Kohli, R. Misra, V. H. Crespi, N. Samarth, C. Leighton, and P. Schiffer. Perpendicular magnetization and generic realization of the ising model in artificial spin ice. *Phys. Rev. Lett.*, 109:087201, Aug 2012.

Appendix A

Chirality Controlled Propagation of Magnetic Charge Carriers Raw Data

		PHC0,PHC1, PHC2 combined			PHC3	
Chain Length	y-Displacement	N_Y	N_Y/N	$N_Y/(NP_{n,m})$	N_Y	N_Y/N
0	0	410	1	1	30	1
1	-1	207	0.50	1.01	11	0.37
1	1	203	0.50	0.99	19	0.63
2	-2	101	0.25	1.01	2	0.07
2	0	167	0.42	0.83	10	0.33
2	2	134	0.33	1.33	18	0.6
3	-3	29	0.11	0.86	–	–
3	-1	96	0.36	0.95	1	0.06
3	1	92	0.34	0.91	6	0.35
3	3	52	0.19	1.55	10	0.59
4	-4	9	0.06	0.93	–	–
4	-2	33	0.21	0.85	1	0.13
4	0	48	0.31	0.83	4	0.5
4	2	47	0.30	1.21	3	0.38
4	4	18	0.12	1.86	–	–
5	-5	4	0.04	1.20	–	–
5	-3	9	0.08	0.54	–	–
5	-1	33	0.31	0.99	–	–
5	1	27	0.25	0.81	–	–
5	3	26	0.24	1.56	1	0.25
5	5	8	0.08	2.39	3	0.75
6	-6	1	0.01	0.77	–	–

Table A.1 Raw data of PHC0, PHC1, PHC2 and PHC3

		PHC0,PHC1, PHC2 combined			PHC3	
Chain Length	y-Displacement	N_Y	N_Y/N	$N_Y/(NP_{n,m})$	N_Y	N_Y/N
6	-4	6	0.07	0.77	–	–
6	-2	16	0.19	0.82	–	–
6	0	16	0.19	0.62	–	–
6	2	24	0.29	1.23	–	–
6	4	16	0.19	2.06	1	0.33
6	6	4	0.05	3.08	2	0.67
7	-7	1	0.02	1.94	–	–
7	-5	2	0.03	0.55	–	–
7	-3	6	0.09	0.55	–	–
7	-1	12	0.18	0.67	–	–
7	1	20	0.30	1.11	–	–
7	3	14	0.21	1.29	–	–
7	5	8	0.12	2.22	1	0.33
7	7	3	0.05	5.83	2	0.67
8	-4	3	0.06	0.54	–	–
8	-2	8	0.16	0.72	–	–
8	0	15	0.29	1.08	–	–
8	2	9	0.18	0.81	–	–
8	4	10	0.20	1.80	–	–
8	6	5	0.10	3.13	1	0.5
8	8	1	0.02	5.03	1	0.5
9	-5	2	0.05	0.71	–	–
9	-3	4	0.1	0.61	–	–
9	-1	10	0.25	1.02	–	–
9	1	9	0.23	0.91	–	–
9	3	7	0.18	1.07	–	–
9	5	5	0.13	1.78	–	–
9	7	2	0.05	2.84	–	–
9	9	1	0.025	12.82	–	–
10	-6	1	0.03	0.69	–	–
10	-4	2	0.06	0.52	–	–
10	-2	8	0.24	1.18	–	–
10	0	3	0.09	0.37	–	–
10	2	9	0.27	1.33	–	–
10	4	4	0.12	1.03	–	–
10	6	4	0.12	2.76	–	–
10	8	2	0.06	6.18	–	–
11	-5	1	0.04	0.52	–	–
11	-3	3	0.13	0.78	–	–
11	-1	3	0.13	0.55	–	–
11	1	8	0.33	1.48	–	–
11	3	3	0.13	0.78	–	–
11	5	3	0.13	1.55	–	–
11	7	1	0.04	1.55	–	–
11	9	2	0.08	15.43	–	–

Table A.1 Raw data of PHC0, PHC1, PHC2 and PHC3 continued

		PHC0,PHC1, PHC2 combined			PHC3	
Chain Length	y-Displacement	N_Y	N_Y/N	$N_Y/(NP_{n,m})$	N_Y	N_Y/N
12	-2	2	0.12	0.61	–	–
12	0	1	0.06	0.26	–	–
12	2	8	0.47	2.43	–	–
12	4	3	0.18	1.46	–	–
12	6	1	0.06	1.10	–	–
12	10	2	0.12	40.57	–	–
13	-3	2	0.14	0.91	–	–
13	1	2	0.14	0.68	–	–
13	3	6	0.43	2.73	–	–
13	5	2	0.14	1.64	–	–
13	7	1	0.07	3.15	–	–
13	9	1	0.07	7.52	–	–
14	-2	2	0.20	1.09	–	–
14	2	3	0.30	1.64	–	–
14	4	2	0.20	1.64	–	–
14	6	2	0.20	3.64	–	–
14	10	1	0.10	18.02	–	–
15	-1	2	0.25	1.27	–	–
15	3	3	0.38	2.46	–	–
15	5	1	0.13	1.41	–	–
15	7	1	0.13	3.51	–	–
15	9	1	0.13	11.57	–	–
16	-2	2	0.33	1.91	–	–
16	4	2	0.33	2.76	–	–
16	6	1	0.17	2.68	–	–
16	8	1	0.17	7.18	–	–
17	-3	2	0.40	2.71	–	–
17	3	2	0.40	2.71	–	–
17	9	1	0.20	13.25	–	–
18	-2	2	0.40	2.40	–	–
18	4	2	0.40	3.35	–	–
18	8	1	0.20	6.92	–	–
19	-1	2	0.50	2.84	–	–
19	3	1	0.25	1.75	–	–
19	7	1	0.25	5.22	–	–
20	0	1	0.25	1.42	–	–
20	6	1	0.25	3.52	–	–
21	-1	1	0.25	1.49	–	–
21	5	1	0.25	2.66	–	–

Table A.1 Raw data of PHC0, PHC1, PHC2 and PHC3 continued

		SHC1			SHC2		
Chain Length	y-Displacement	N_Y	N_Y/N	$N_Y/(NP_{n,m})$	N_Y	N_Y/N	$N_Y/(NP_{n,m})$
0	0	94	1	1	101	1	1
1	-1	41	0.44	0.87	47	0.47	0.93
1	1	53	0.56	1.13	54	0.53	1.07
2	-2	27	0.30	1.21	15	0.22	0.87
2	0	21	0.24	0.47	25	0.36	0.73
2	2	41	0.46	1.84	29	0.42	1.68
3	-3	8	0.15	1.16	1	0.03	0.25
3	-1	11	0.2	0.53	11	0.34	0.92
3	1	13	0.24	0.63	13	0.41	1.08
3	3	23	0.42	3.35	7	0.22	1.75
4	-4	3	0.11	1.78	–	–	–
4	-2	3	0.11	0.44	–	–	–
4	0	7	0.26	0.69	7	0.5	1.33
4	2	6	0.22	0.89	4	0.29	1.14
4	4	8	0.30	4.74	3	0.21	3.43
5	-5	1	0.09	2.91	–	–	–
5	-3	2	0.18	1.16	–	–	–
5	-1	1	0.09	0.29	2	0.25	0.8
5	1	3	0.27	0.87	3	0.38	1.2
5	3	2	0.18	1.16	1	0.13	0.8
5	5	2	0.18	5.82	2	0.25	8
6	-6	1	0.14	9.14	–	–	–
6	-4	1	0.14	1.52	–	–	–
6	-2	1	0.14	0.61	–	–	–
6	0	2	0.29	0.91	2	0.67	2.13
6	2	1	0.14	0.61	–	–	–
6	6	1	0.14	9.14	1	0.33	21.33
7	-5	1	0.25	4.57	–	–	–
7	-1	1	0.25	0.92	1	1	3.66
7	3	1	0.25	1.52	–	–	–
7	7	1	0.25	32.05	–	–	–
8	0	–	–	–	1	1	3.66
8	4	1	0.5	4.59	–	–	–
8	8	1	0.5	128	–	–	–
9	1	–	–	–	1	1	4.06
9	5	1	1	14.22	–	–	–
10	2	–	–	–	1	1	4.88
11	1	–	–	–	1	1	4.43

Table A.2 Raw data of SHC1 and SHC2

Chain Length	y-Displacement	Random Walk N_Y	Biasd Random Walk N_Y
0	0	1000	1000
1	-1	490	485
1	1	510	515
2	-2	242	363
2	0	507	270
2	2	251	367
3	-3	127	259
3	-1	370	258
3	1	379	228
3	3	124	255
4	-4	65	187
4	-2	259	215
4	0	361	230
4	2	246	181
4	4	69	187
5	-5	30	136
5	-3	166	175
5	-1	309	215
5	1	310	188
5	3	157	157
5	5	28	129
6	-6	17	97
6	-4	93	131
6	-2	243	210
6	0	307	175
6	2	241	164
6	4	82	128
6	6	17	95
7	-7	8	72
7	-5	47	101
7	-3	181	176
7	-1	262	175
7	1	286	161
7	3	160	138
7	5	49	108
7	7	14	69
8	-8	3	53
8	-6	28	77
8	-4	115	138
8	-2	220	163
8	0	269	160
8	2	233	154
8	4	103	125
8	6	25	81
8	8	4	49

Table A.3 Random walk and biased random walk simulation data

Chain Length	y-Displacement	Random Walk N_Y	Biasd Random Walk N_Y
9	-9	2	40
9	-7	15	64
9	-5	65	104
9	-3	173	134
9	-1	250	164
9	1	251	155
9	3	160	139
9	5	65	101
9	7	15	63
9	9	2	36

Table A.3 Random walk and biased random walk simulation data continued

		SHC2T		
Chain Length	y-Displacement	N_Y	N_Y/N	$N_Y/(NP_{n,m})$
0	0	33	1	1
1	-1	12	0.36	0.73
1	1	21	0.64	1.27
2	-2	8	0.29	1.14
2	0	10	0.36	0.71
2	2	10	0.36	1.43
3	-3	4	0.25	2
3	-1	5	0.31	0.83
3	1	4	0.25	0.67
3	3	3	0.19	1.5
4	-4	1	0.09	1.46
4	-2	2	0.18	0.73
4	0	4	0.36	0.97
4	2	3	0.27	1.09
4	4	1	0.09	1.46
5	-3	1	0.13	0.8
5	-1	4	0.5	0.4
5	1	1	0.13	0.4
5	3	1	0.13	0.8
5	5	1	0.13	4
6	-2	2	0.29	1.22
6	0	4	0.57	1.83
6	2	1	0.14	0.61
7	-3	1	0.25	1.52
7	-1	3	0.75	2.74
8	-4	1	0.33	3.06
8	-2	1	0.33	1.52
8	0	1	0.33	1.22
9	-3	1	0.5	3.05
9	-1	1	0.5	12.31
10	-4	1	1	8.53

Table A.4 Raw data of SHC2T

Appendix B

Two dimensional Artificial Spin Ice Raw Transport Data

B.1 Magnetoresistance

B.1.1 $R_{xx}(B_y)$

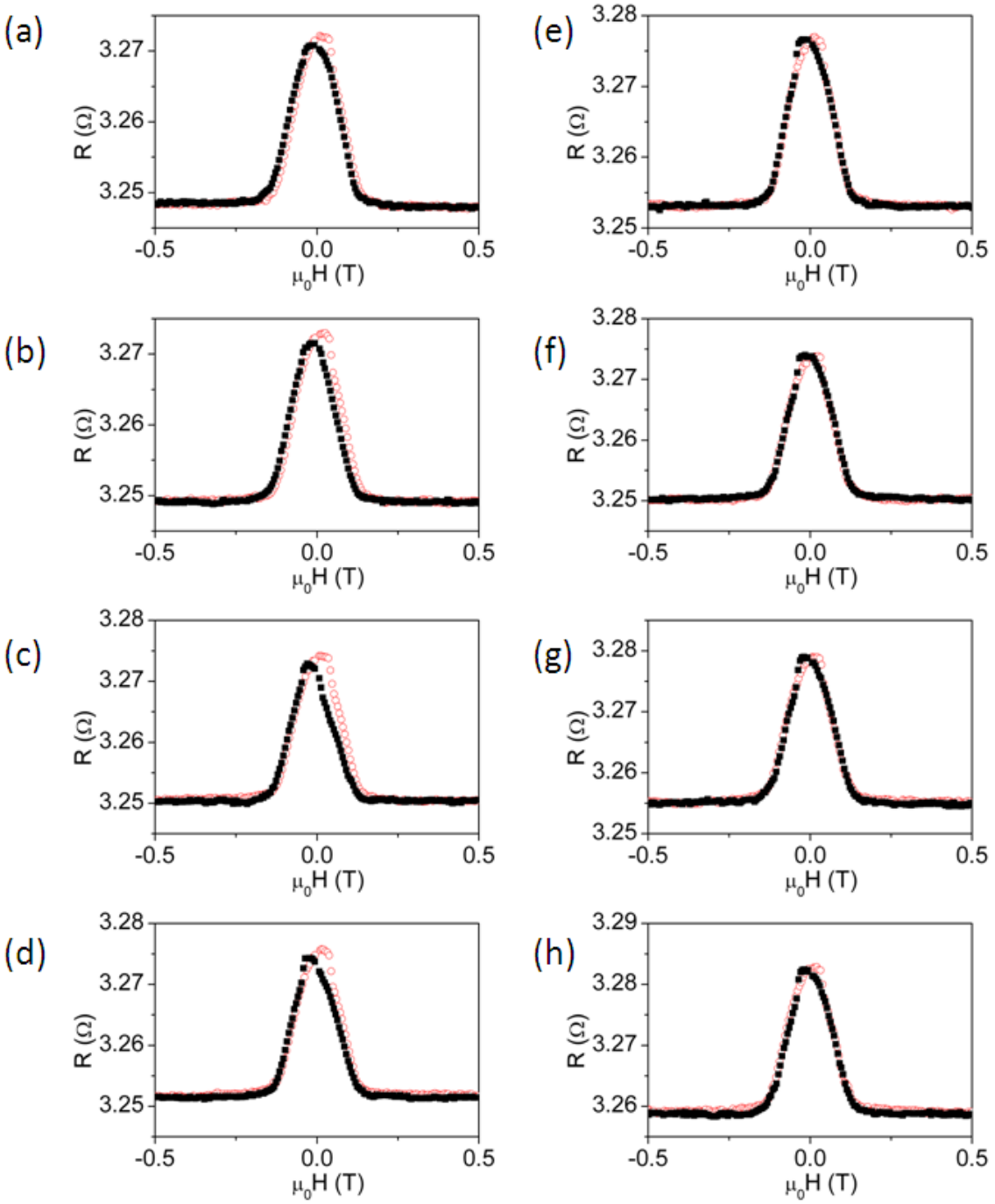

Figure B.1 Raw magnetoresistance data $R_{xx}(B_y)$. The magnetic field was applied along y and the current was applied along the x-direction. The voltage was measured parallel to the current path. The magnetic field was swept up (red open circles) and down (black filled squares). (a) 5 K, (b) 8 K, (c) 10 K, (d) 12 K, (e) 15 K, (f) 20 K, (g) 25 K, (h) 30 K.

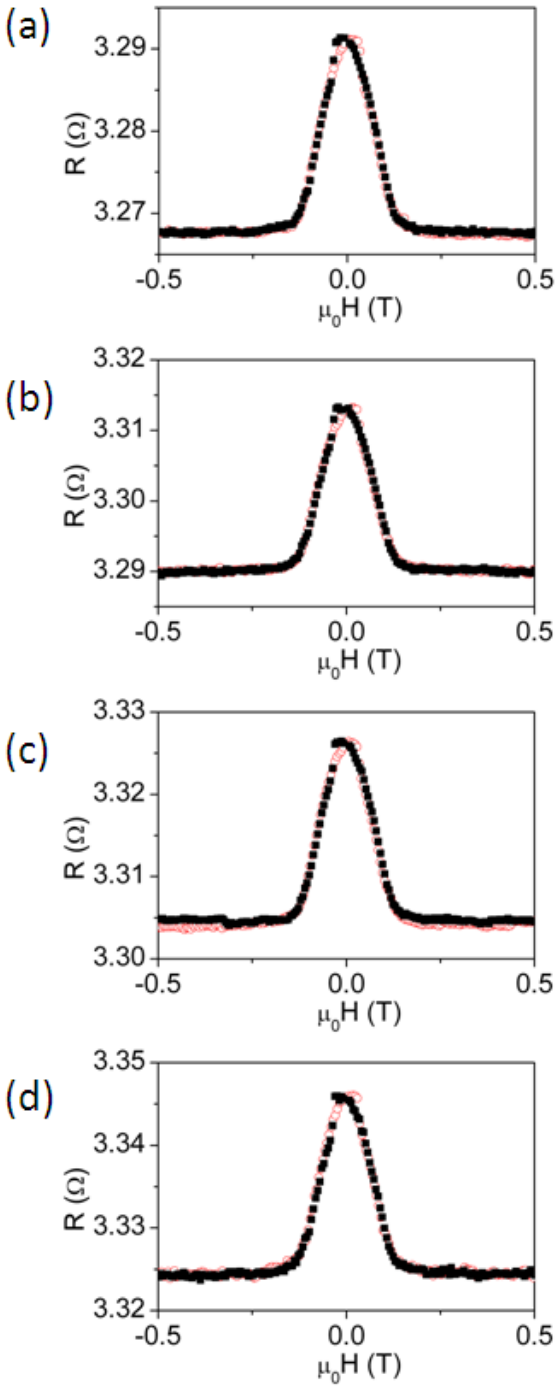

Figure B.2 Raw magnetoresistance data $R_{xx}(B_y)$. The magnetic field was applied along y and the current was applied along the x-direction. The voltage was measured parallel to the current path. The magnetic field was swept up (red open circles) and down (black filled squares). (a) 50 K, (b) 75 K, (c) 100 K, (d) 125 K.

B.1.2 $R_{yy}(B_y)$

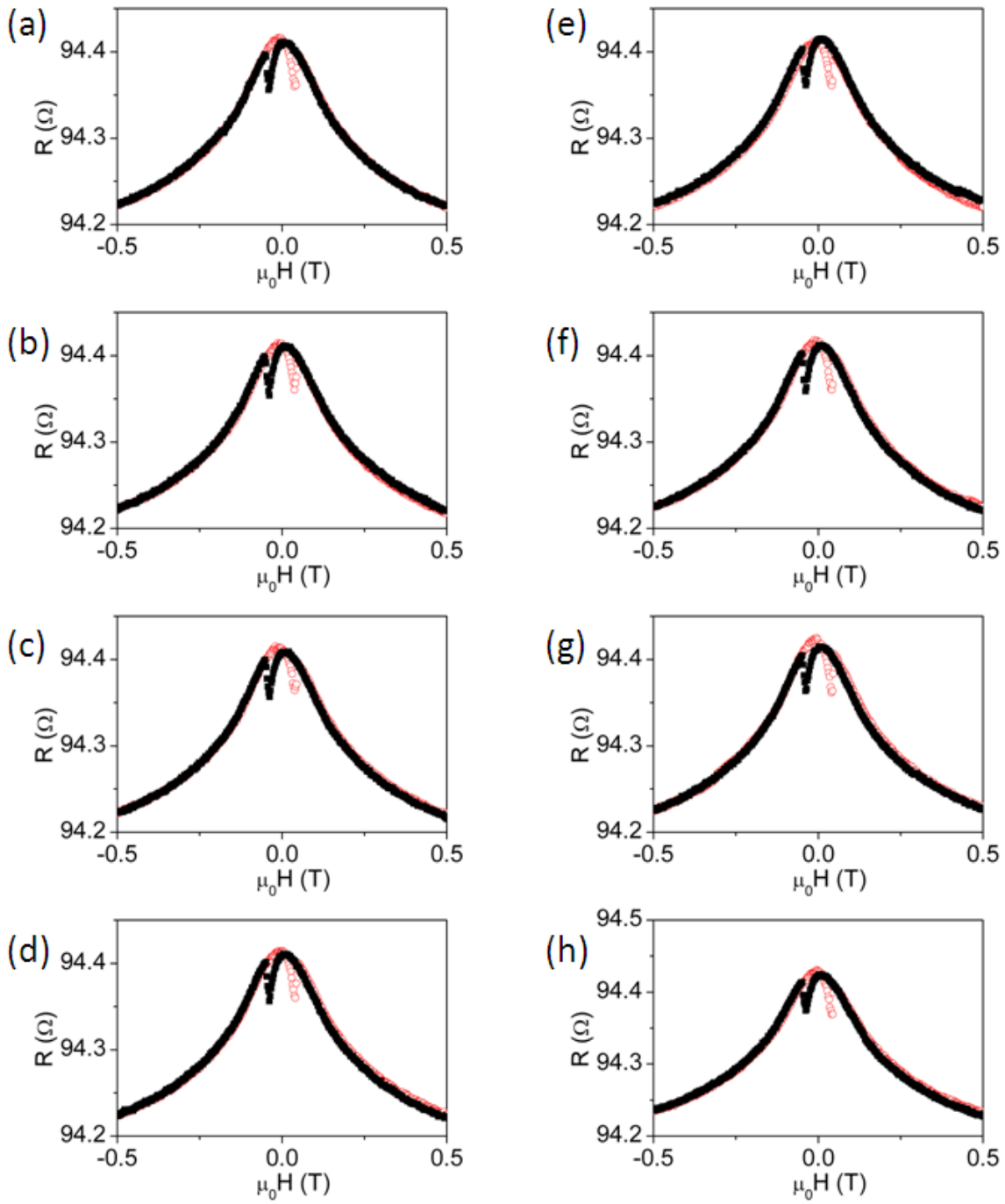

Figure B.3 Raw magnetoresistance data $R_{yy}(B_y)$. The magnetic field was applied along y and the current was applied along the y-direction. The voltage was measured parallel to the current path. The magnetic field was swept up (red open circles) and down (black filled squares). (a) 2 K, (b) 3 K, (c) 4 K, (d) 5 K, (e) 6 K, (f) 7 K, (g) 8 K, (h) 9 K.

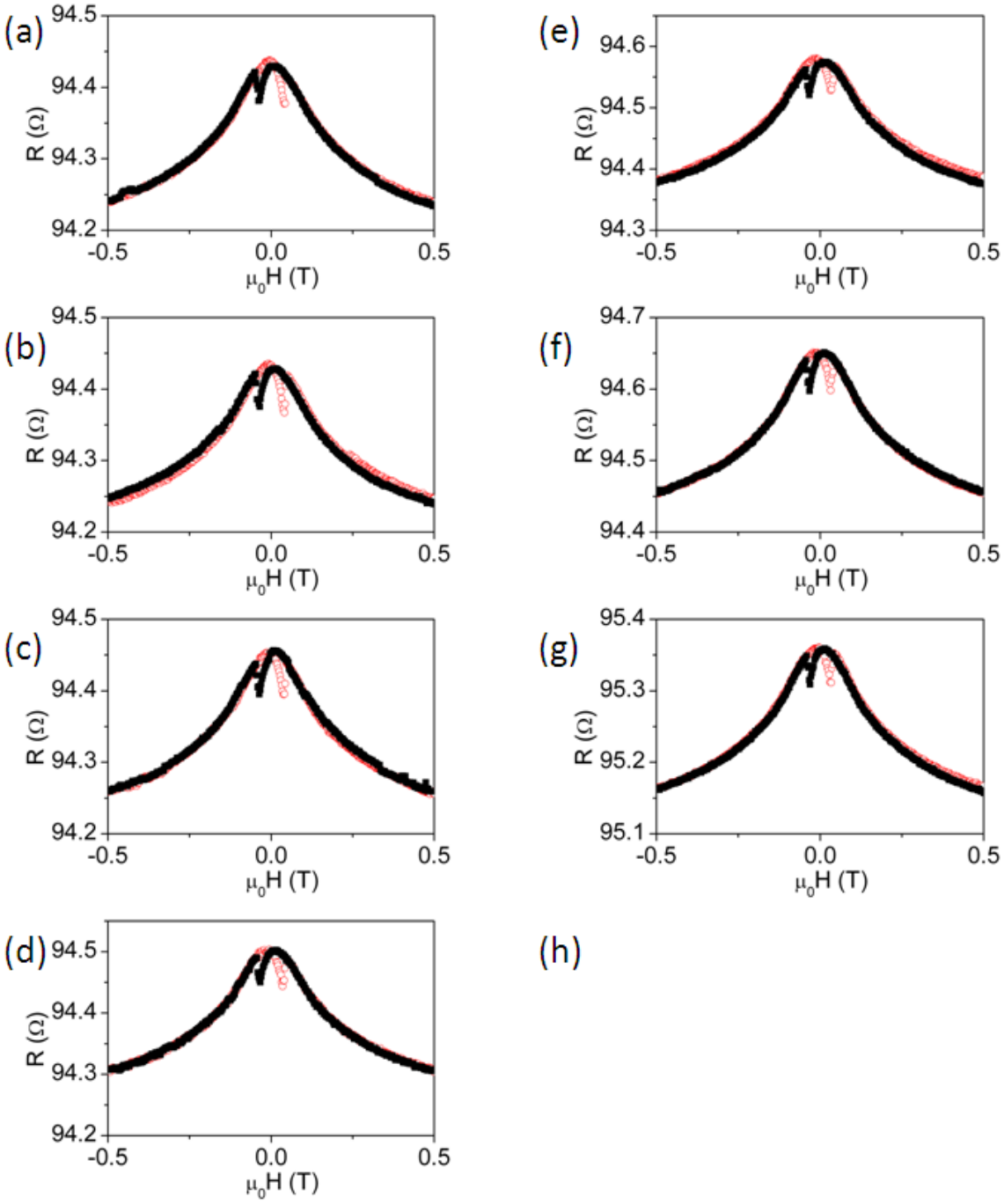

Figure B.4 Raw magnetoresistance data $R_{yy}(B_y)$. The magnetic field was applied along y and the current was applied along the y-direction. The voltage was measured parallel to the current path. The magnetic field was swept up (red open circles) and down (black filled squares). (a) 10 K, (b) 12 K, (c) 15 K, (d) 20 K, (e) 25 K, (f) 30 K, (g) 50 K.

B.1.3 $R_{xx}(B_x)$

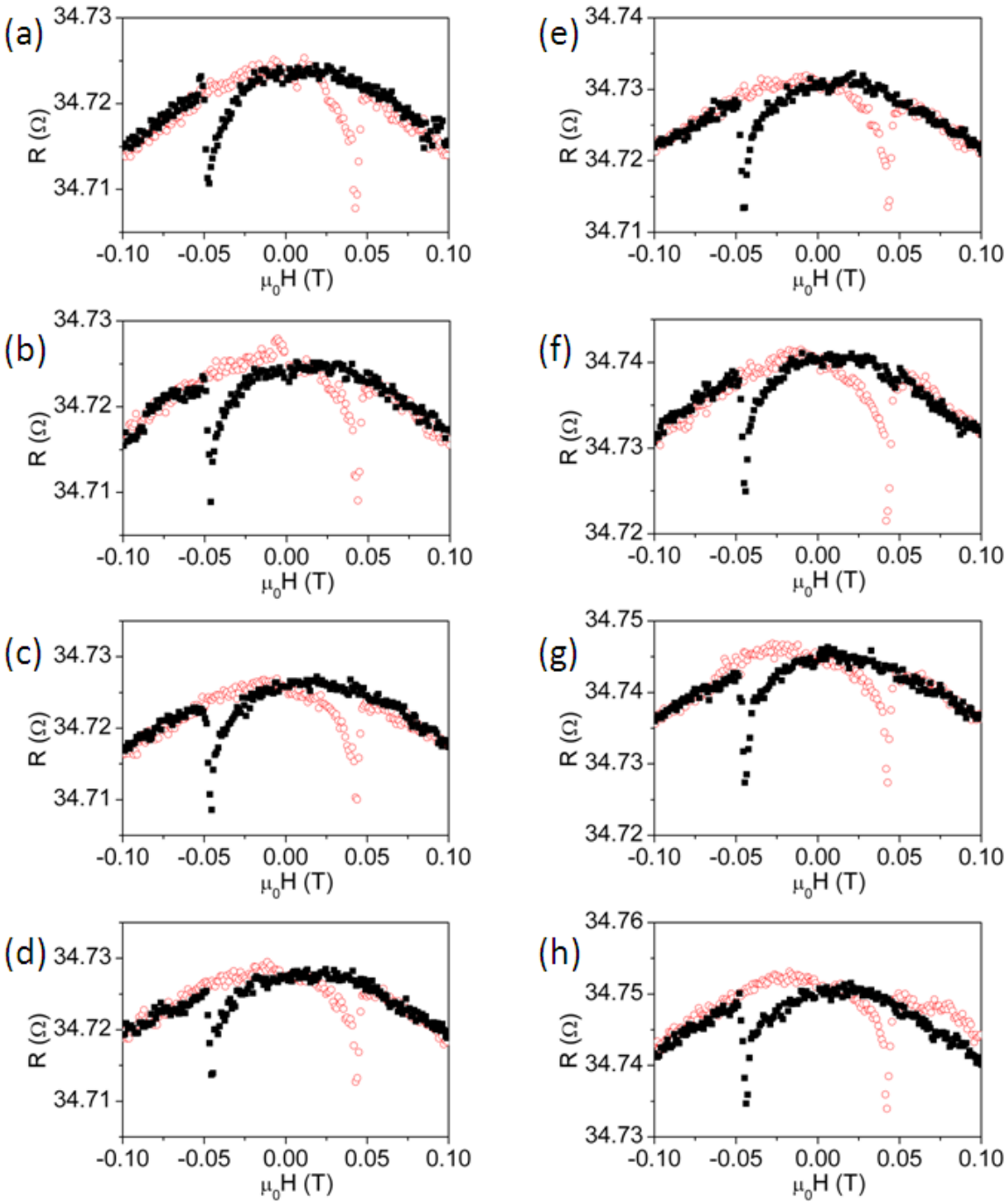

Figure B.5 Raw magnetoresistance data $R_{xx}(B_x)$. The magnetic field was applied along x and the current was applied along the x-direction. The voltage was measured parallel to the current path. The magnetic field was swept up (red open circles) and down (black filled squares). (a) 3 K, (b) 4 K, (c) 5 K, (d) 6 K, (e) 7 K, (f) 9 K, (g) 10 K, (h) 11 K.

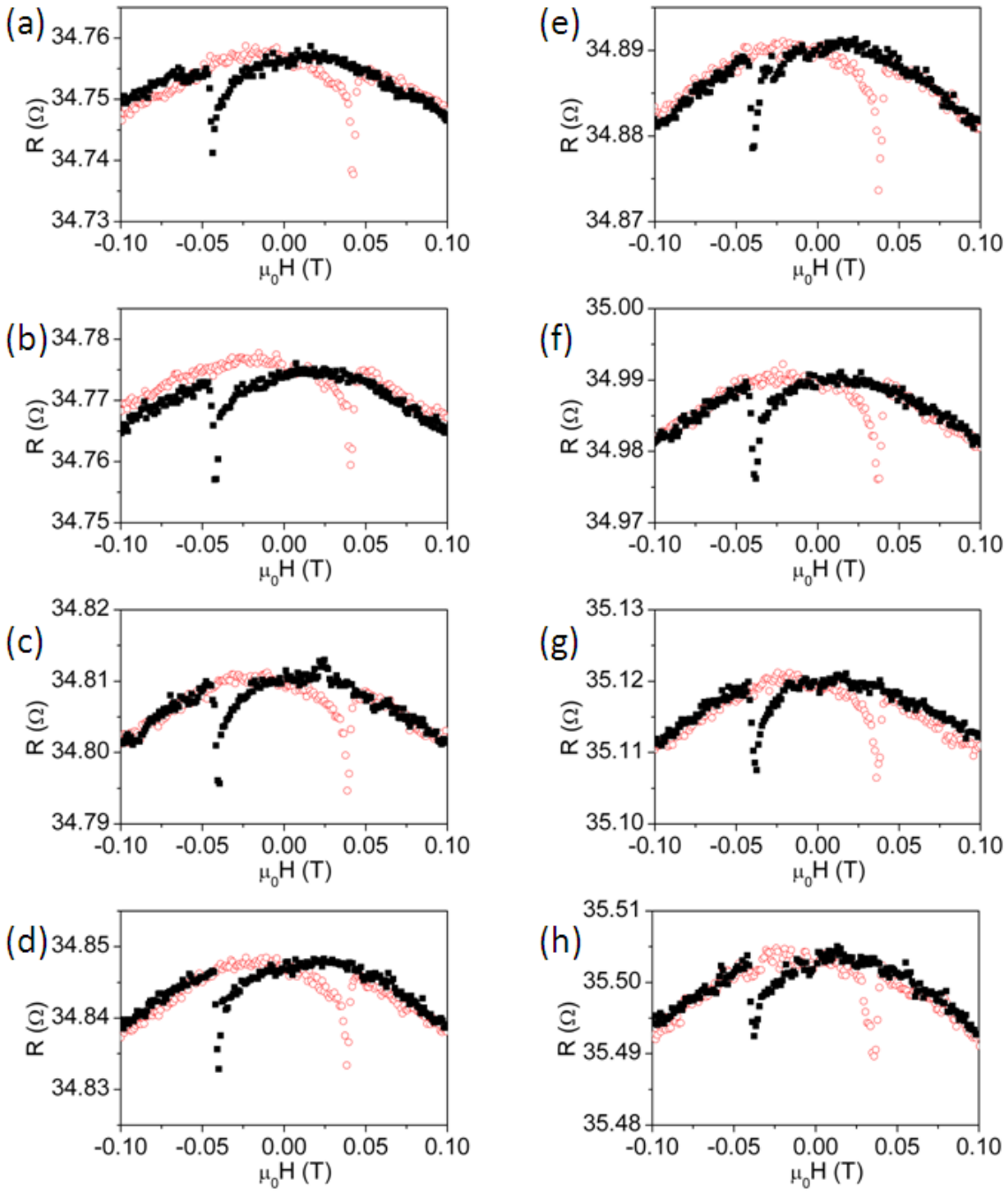

Figure B.6 Raw magnetoresistance data $R_{xx}(B_x)$. The magnetic field was applied along x and the current was applied along the x-direction. The voltage was measured parallel to the current path. The magnetic field was swept up (red open circles) and down (black filled squares). (a) 12 K, (b) 15 K, (c) 20 K, (d) 25 K, (e) 30 K, (f) 40 K, (g) 50 K, (h) 75 K.

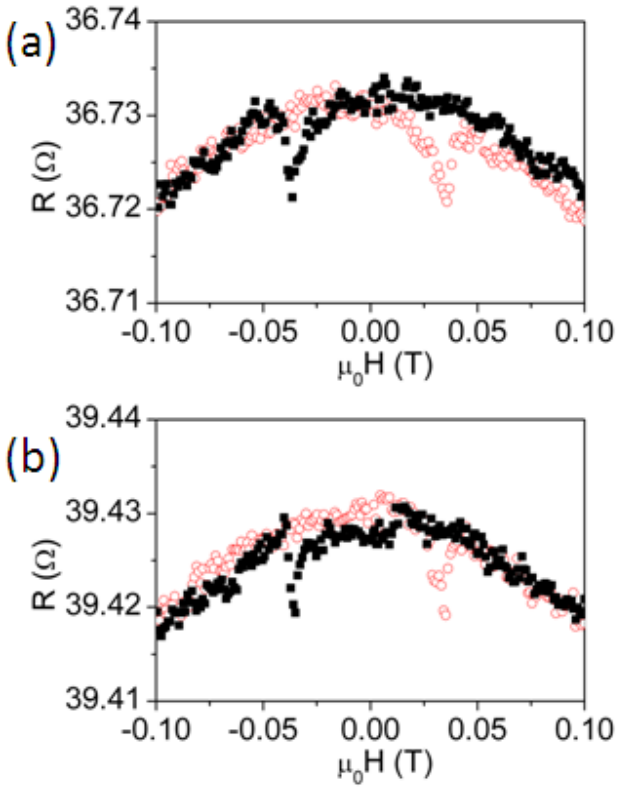

Figure B.7 Raw magnetoresistance data $R_{xx}(B_x)$. The magnetic field was applied along x and the current was applied along the x-direction. The voltage was measured parallel to the current path. The magnetic field was swept up (red open circles) and down (black filled squares). (a) 125 K, (b) 200 K.

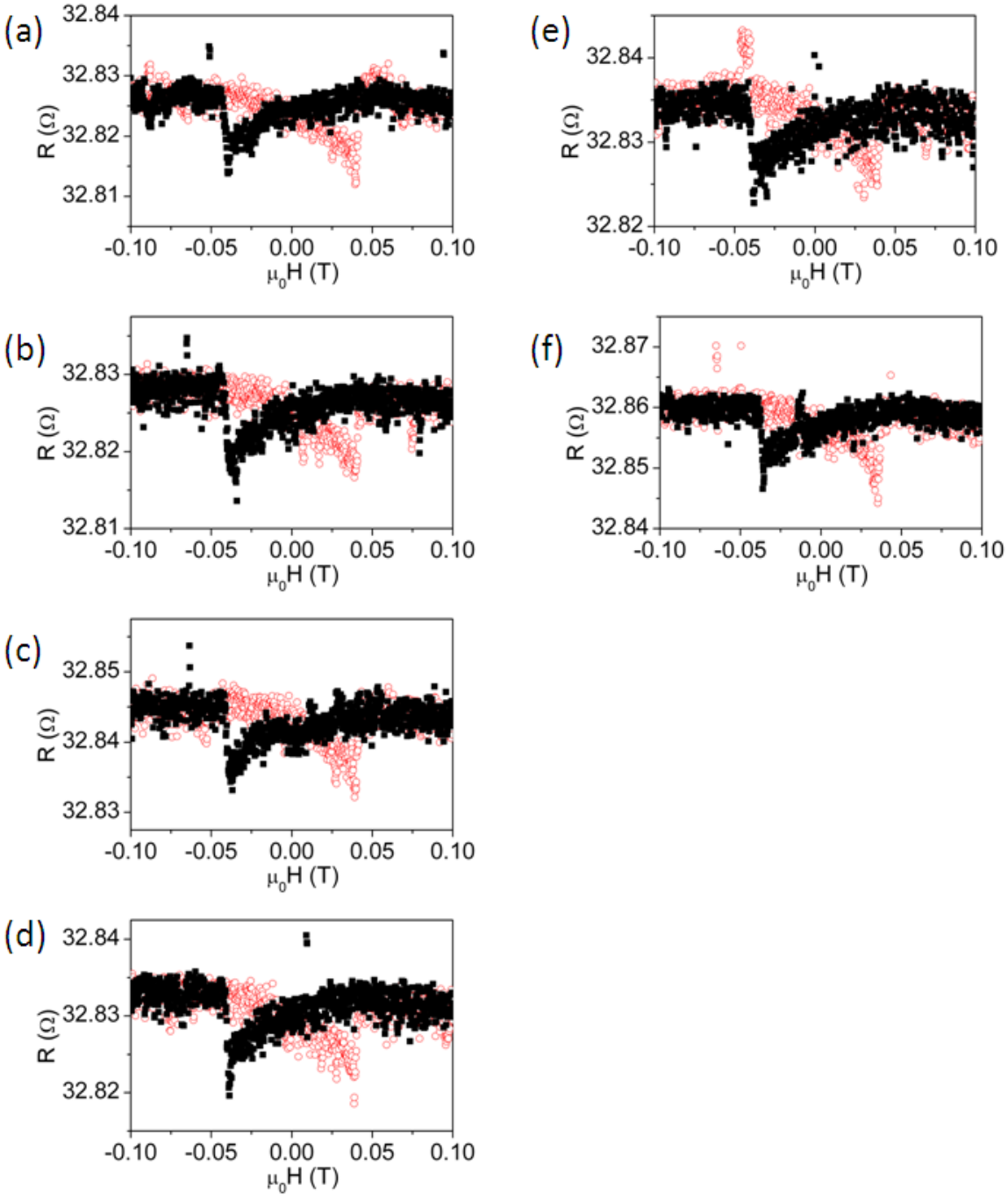

Figure B.8 Raw magnetoresistance data $R_{xx}(B_x)$. The magnetic field was applied along x and the current was applied along the x-direction. The voltage was measured parallel to the current path. The magnetic field was swept up (red open circles) and down (black filled squares). (a) 4 K, (b) 5 K, (c) 6 K, (d) 10 K, (e) 11 K and (f) 20 K.

B.1.4 $R_{yy}(B_x)$

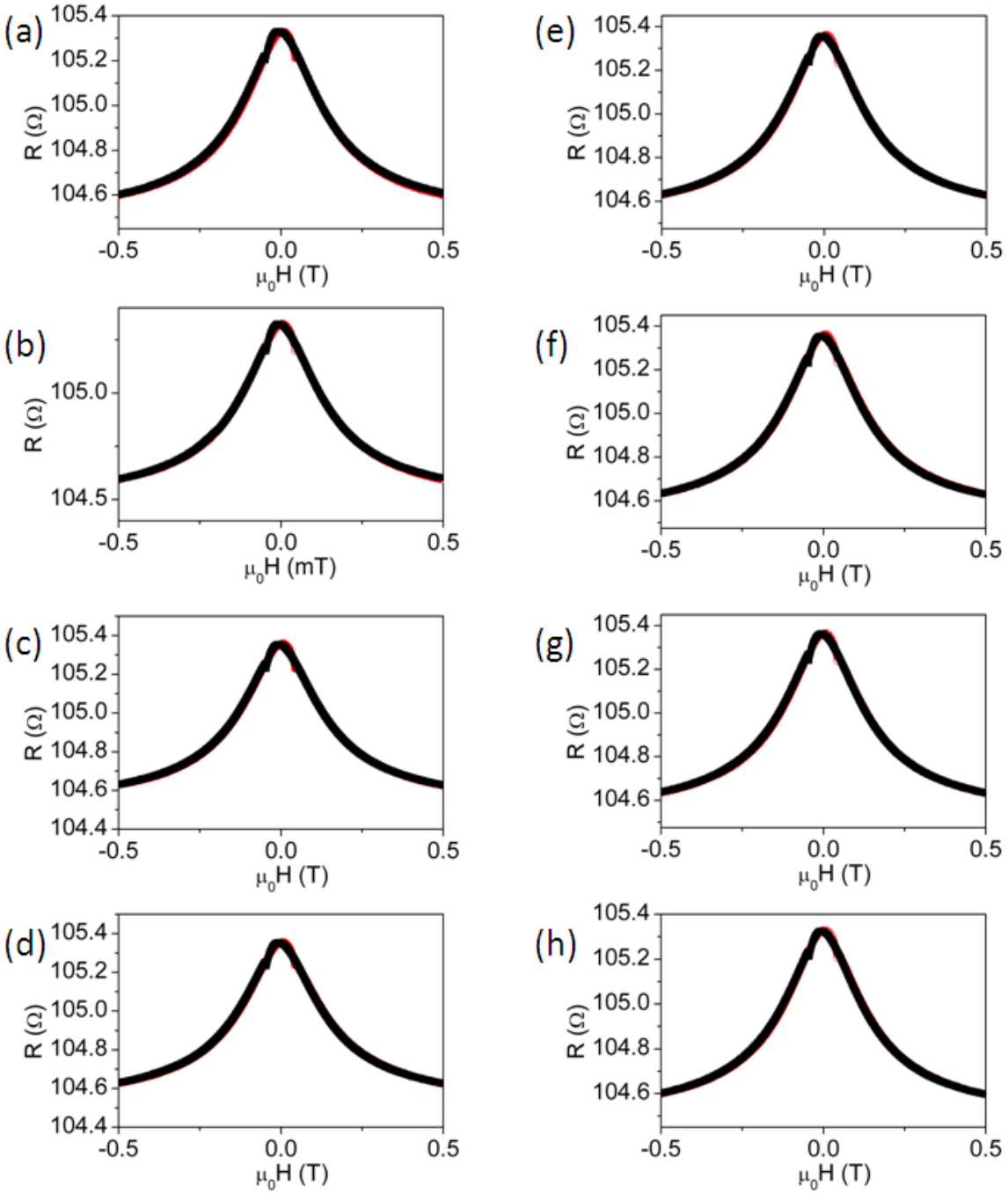

Figure B.9 $R_{yy}(B_x)$ configuration: the magnetic field was applied along x and the current was applied along the y-direction. The voltage was measured parallel to the current path. The magnetic field was swept up (red open circles) and down (black filled squares). (a) 2 K, (b) 3 K, (c) 4 K, (d) 5 K, (e) 6 K, (f) 7 K, (g) 8 K, (h) 10 K.

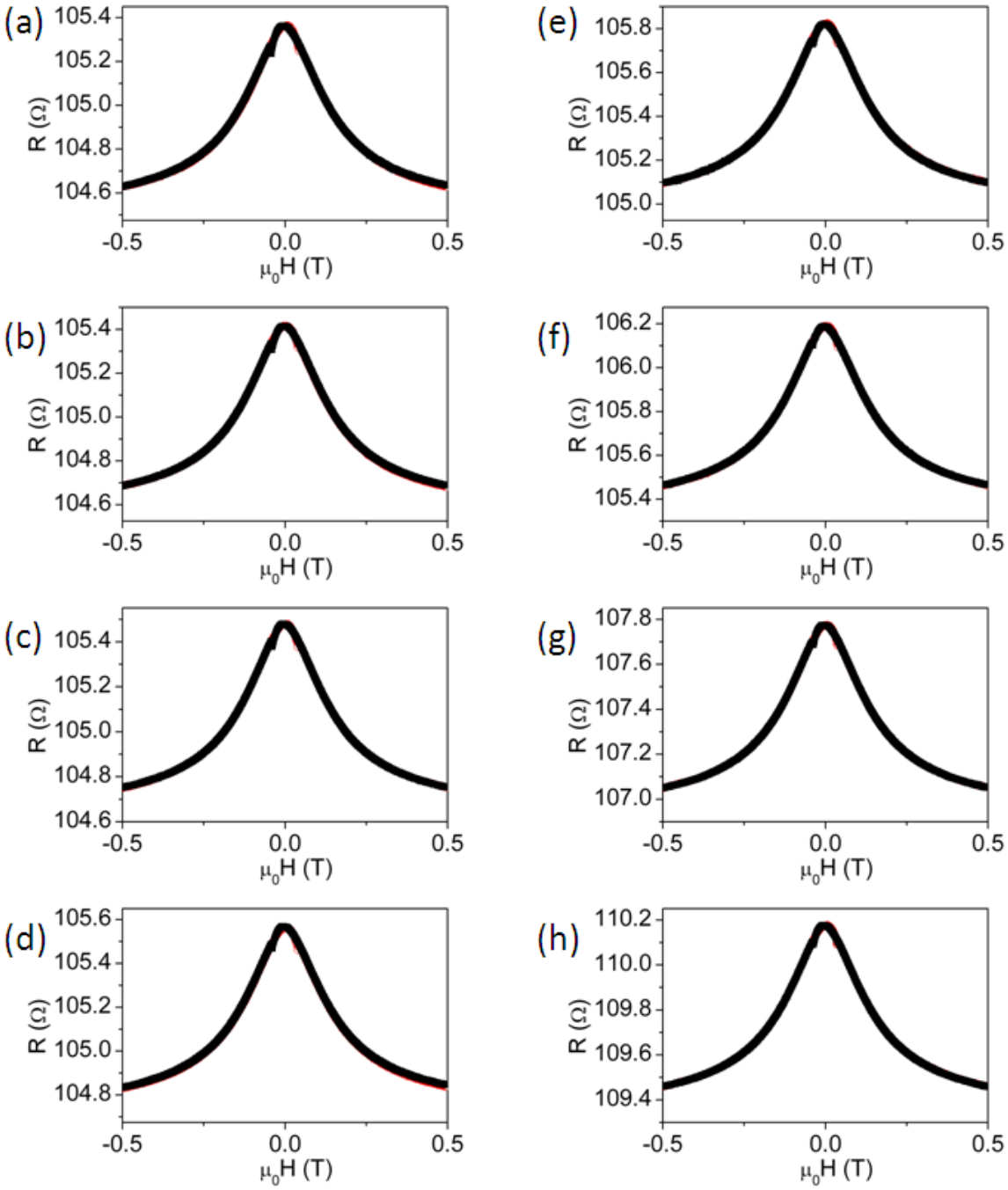

Figure B.10 $R_{yy}(B_x)$ configuration: the magnetic field was applied along x and the current was applied along the y-direction. The voltage was measured parallel to the current path. The magnetic field was swept up (red open circles) and down (black filled squares). (a) 15 K, (b) 20 K, (c) 25 K, (d) 30 K, (e) 40 K, (f) 50 K, (g) 75 K, (h) 100 K.

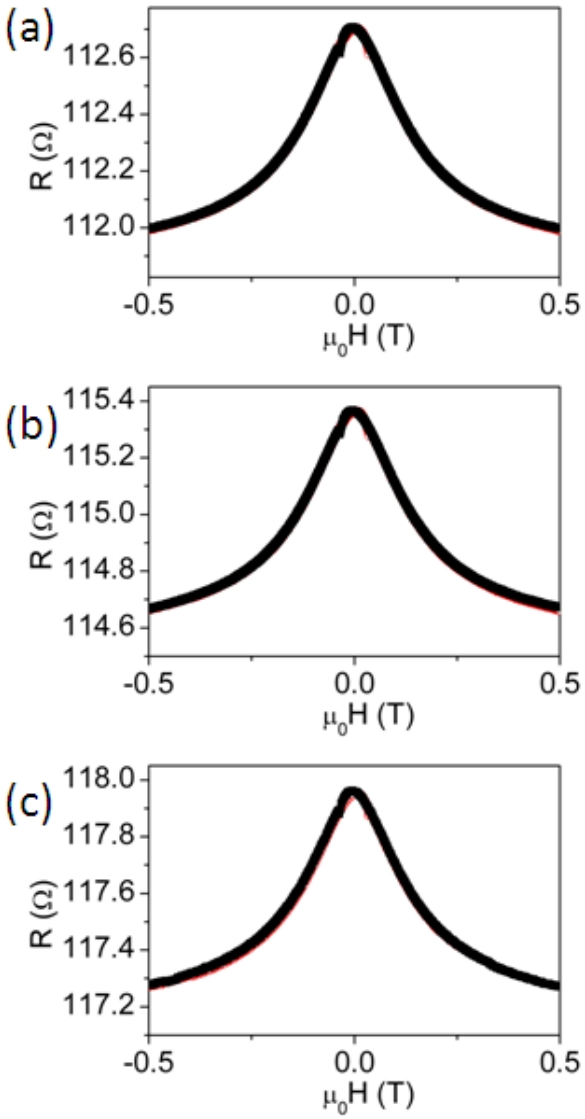

Figure B.11 $R_{yy}(B_x)$ configuration: the magnetic field was applied along x and the current was applied along the y-direction. The voltage was measured parallel to the current path. The magnetic field was swept up (red open circles) and down (black filled squares). (a) 125 K, (b) 150 K and (c) 175 K.

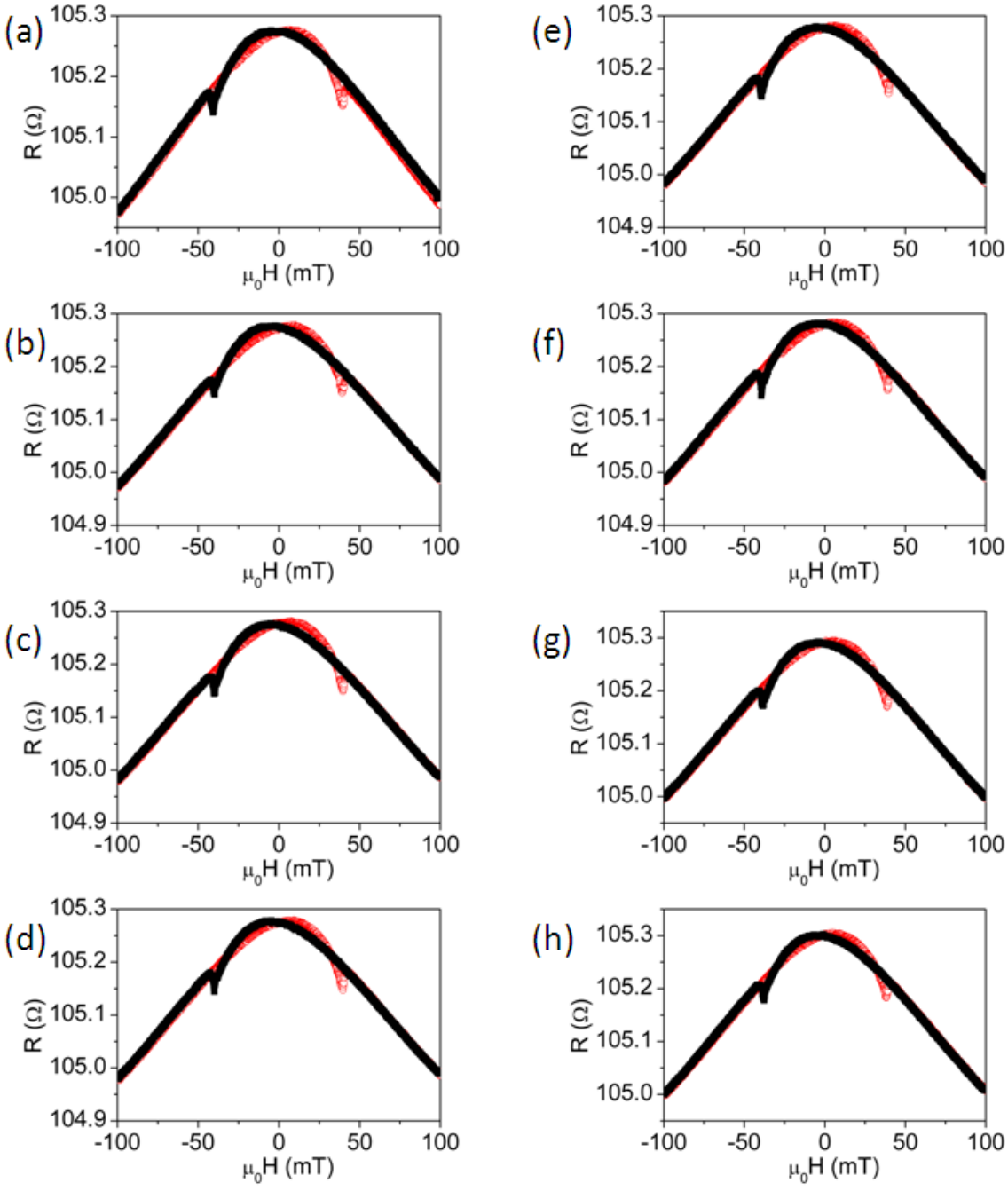

Figure B.12 $R_{yy}(B_x)$ configuration: the magnetic field was applied along x and the current was applied along the y-direction. The magnetic field was swept up (red open circles) and down (black filled squares). (a) 2 K, (b) 3 K, (c) 4 K, (d) 5 K, (e) 6 K, (f) 8 K, (g) 10 K, (h) 12 K.

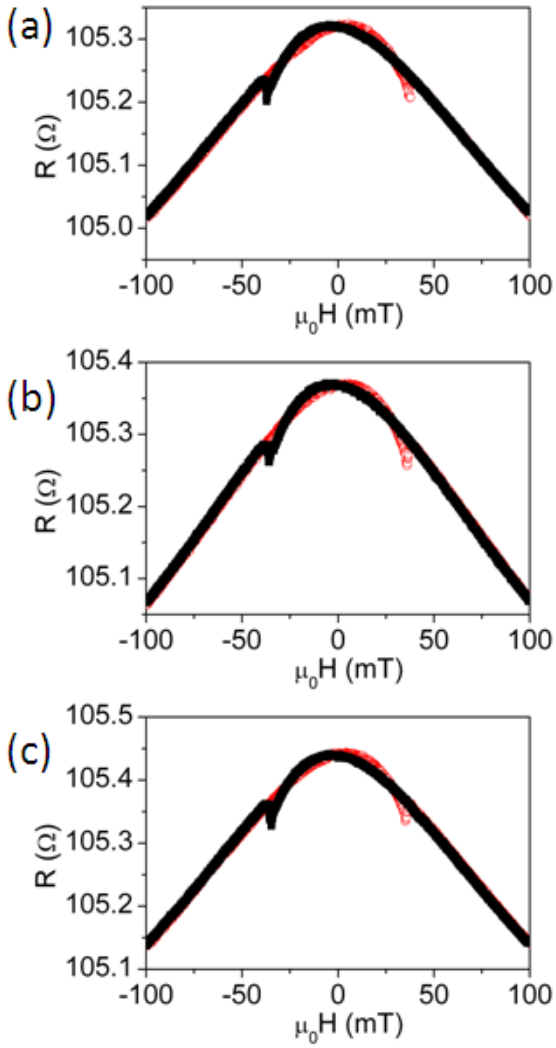

Figure B.13 $R_{yy}(B_x)$ configuration: the magnetic field was applied along x and the current was applied along the y-direction. The voltage was measured parallel to the current path. The magnetic field was swept up (red open circles) and down (black filled squares). (a) 15 K, (b) 20 K and (c) 25 K.

B.1.5 $R_{xx}(B_z)$

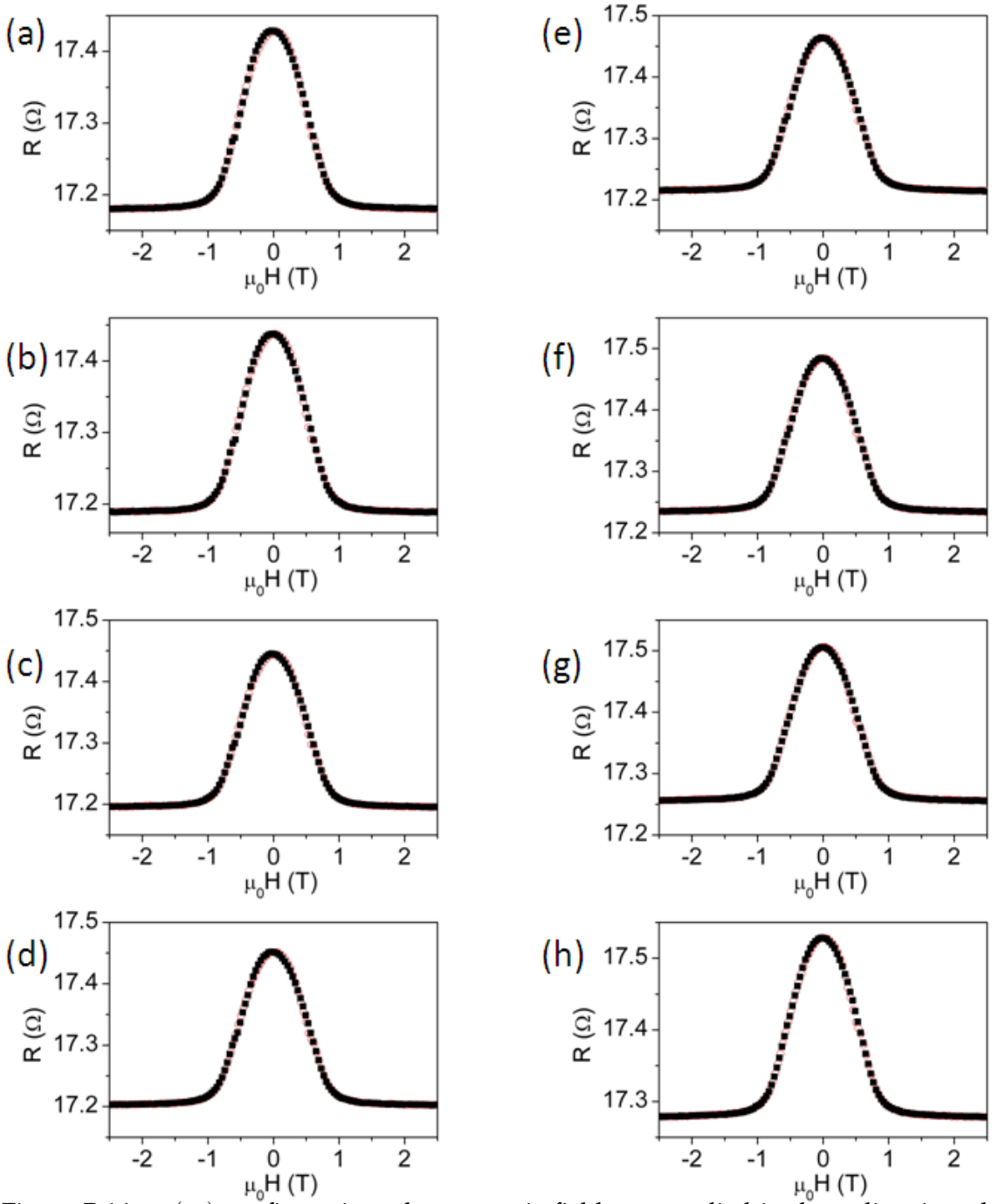

Figure B.14 $R_{xx}(B_z)$ configuration: the magnetic field was applied in the z-direction, the current was applied along the x-direction and the voltage was measured parallel to the current path. The magnetic field was swept up (red open circles) and down (black filled squares). (a) 5 K, (b) 8 K, (c) 10 K, (d) 12 K, (e) 15 K, (f) 20 K, (g) 25 K, (h) 30 K.

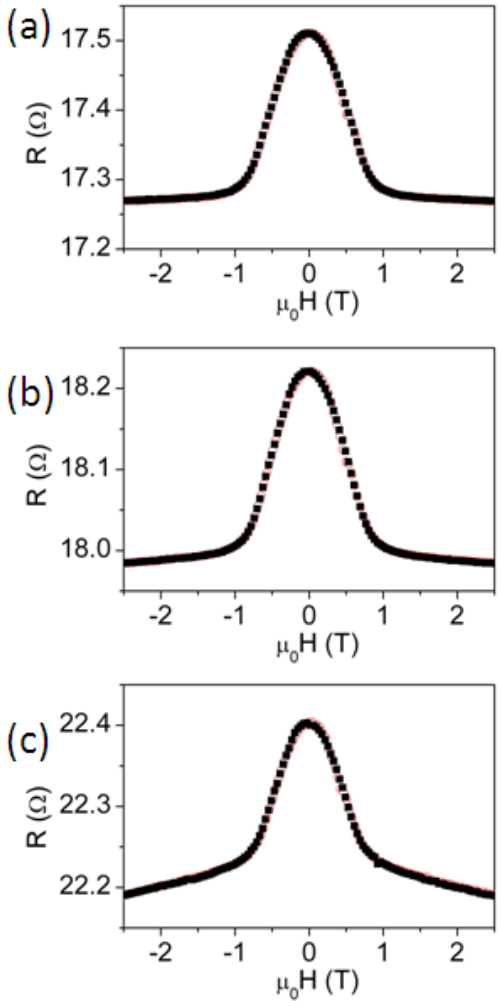

Figure B.15 $R_{xx}(B_z)$ configuration: the magnetic field was applied in the z-direction, the current was applied along the x-direction and the voltage was measured parallel to the current path. The magnetic field was swept up (red open circles) and down (black filled squares). (a) 75 K, (b) 125 K and (c) 290 K.

B.1.6 $R_{yy}(B_z)$

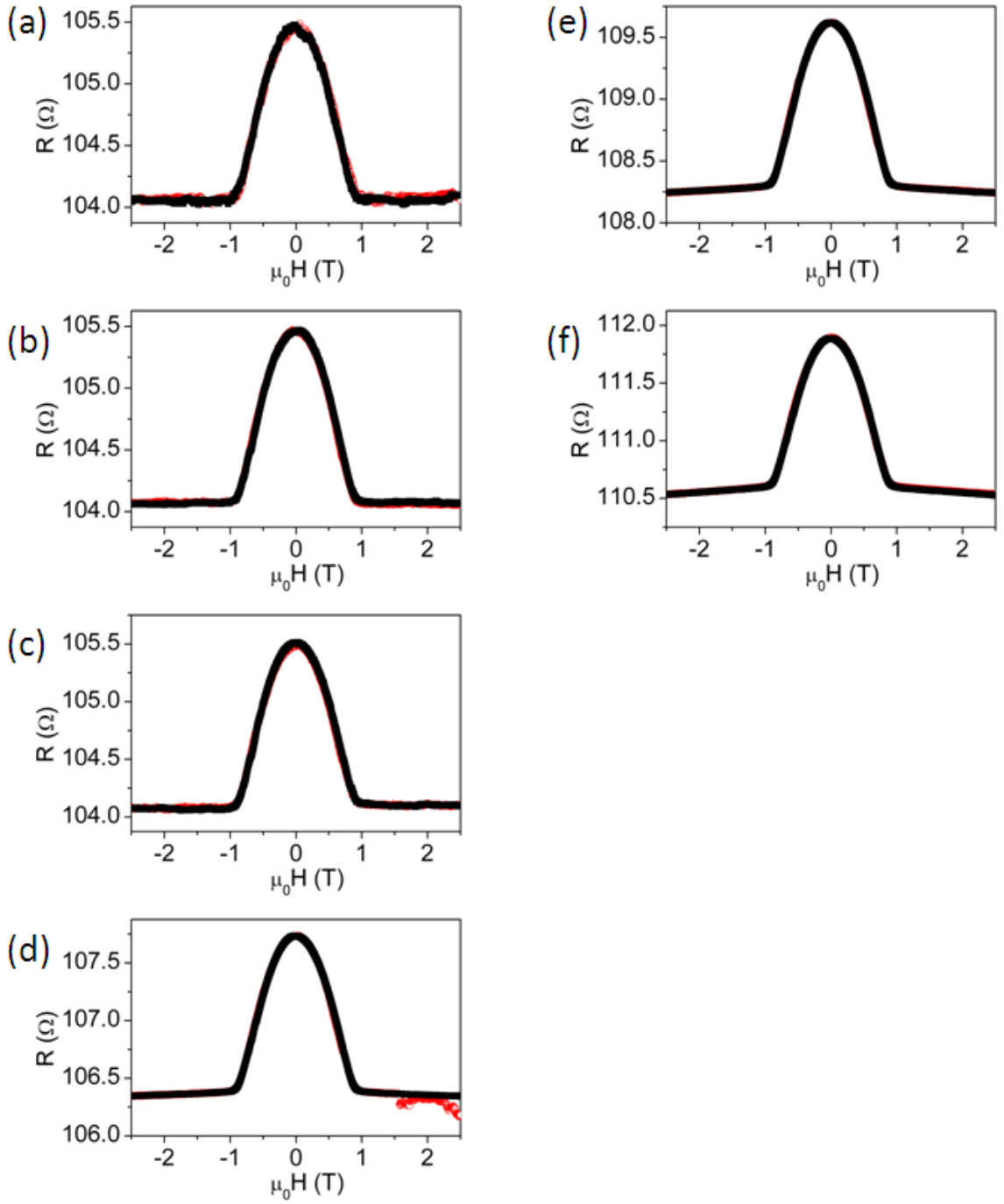

Figure B.16 $R_{yy}(B_z)$ configuration: the magnetic field was applied in the z-direction, the current was applied along the y-direction and the voltage was measured parallel to the current path. The magnetic field was swept up (red open circles) and down (black filled squares). (a) 5 K, (b) 9 K, (c) 12 K, (d) 15 K, (e) 75 K, (f) 100 K, (g) 125 K.

B.1.7 $R_{xy}(B_z)$

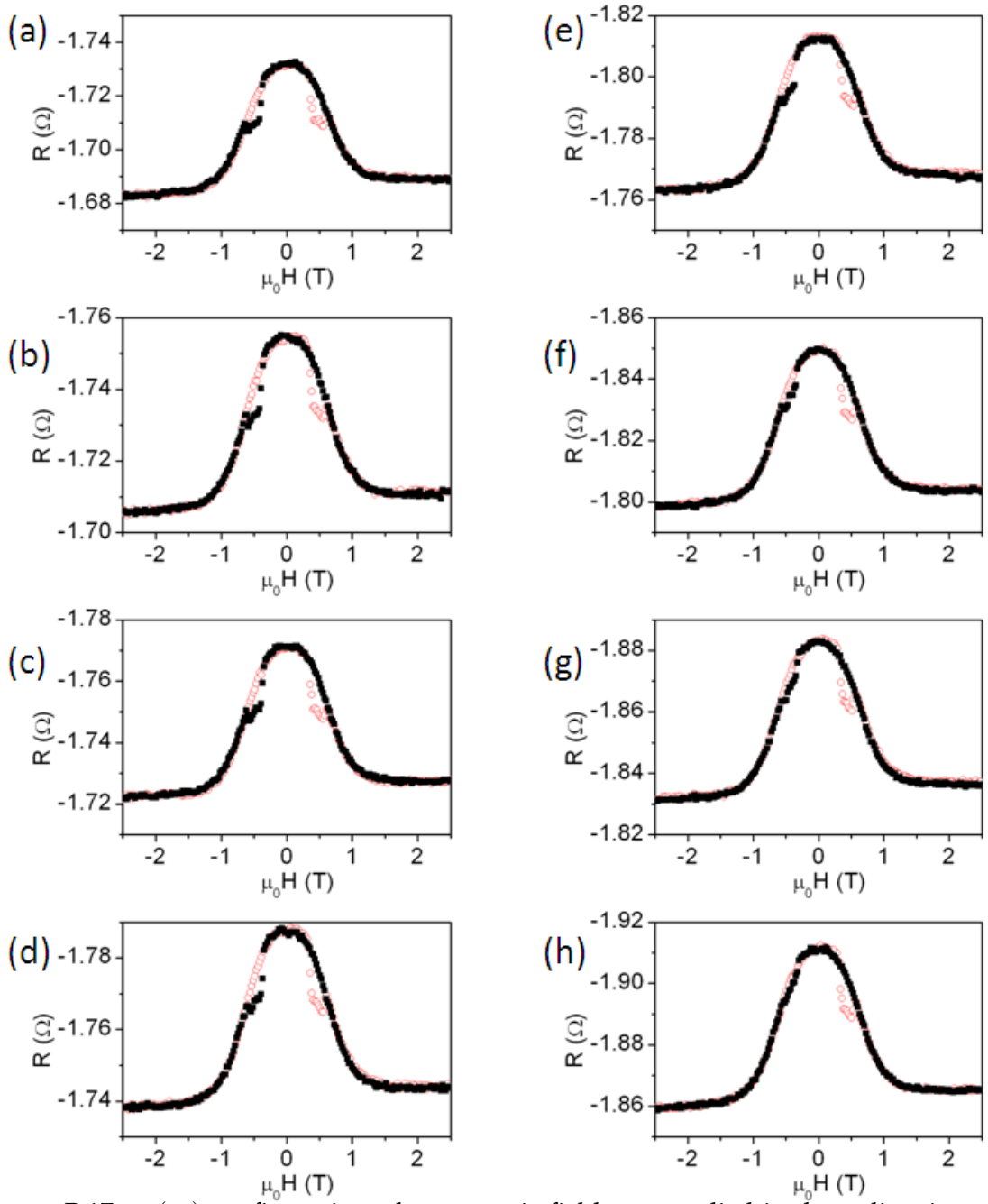

Figure B.17 $R_{xy}(B_z)$ configuration: the magnetic field was applied in the z-direction, the current was applied along the x-direction and the voltage was measured perpendicular to the current path. The magnetic field was swept up (red open circles) and down (black filled squares). (a) 5 K, (b) 8 K, (c) 10 K, (d) 12 K, (e) 15 K, (f) 20 K, (g) 25 K, (h) 30 K.

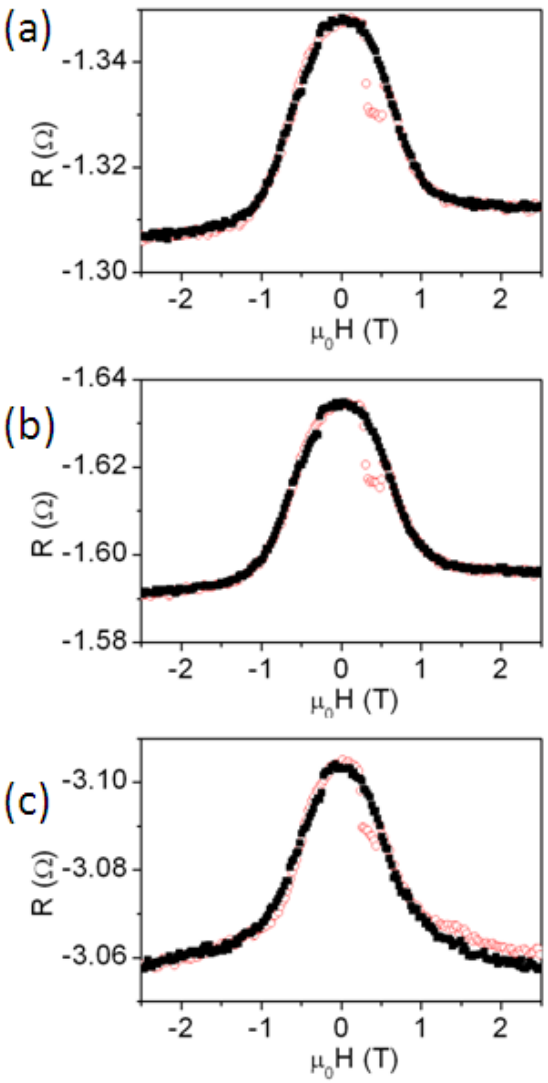

Figure B.18 $R_{xy}(B_z)$ configuration: the magnetic field was applied in the z-direction, the current was applied along the x-direction and the voltage was measured perpendicular to the current path. The magnetic field was swept up (red open circles) and down (black filled squares). (a) 75 K, (b)125 K, (c) 290 K.

B.2 Hall Resistance

B.2.1 $R_{yx}(B_z)$

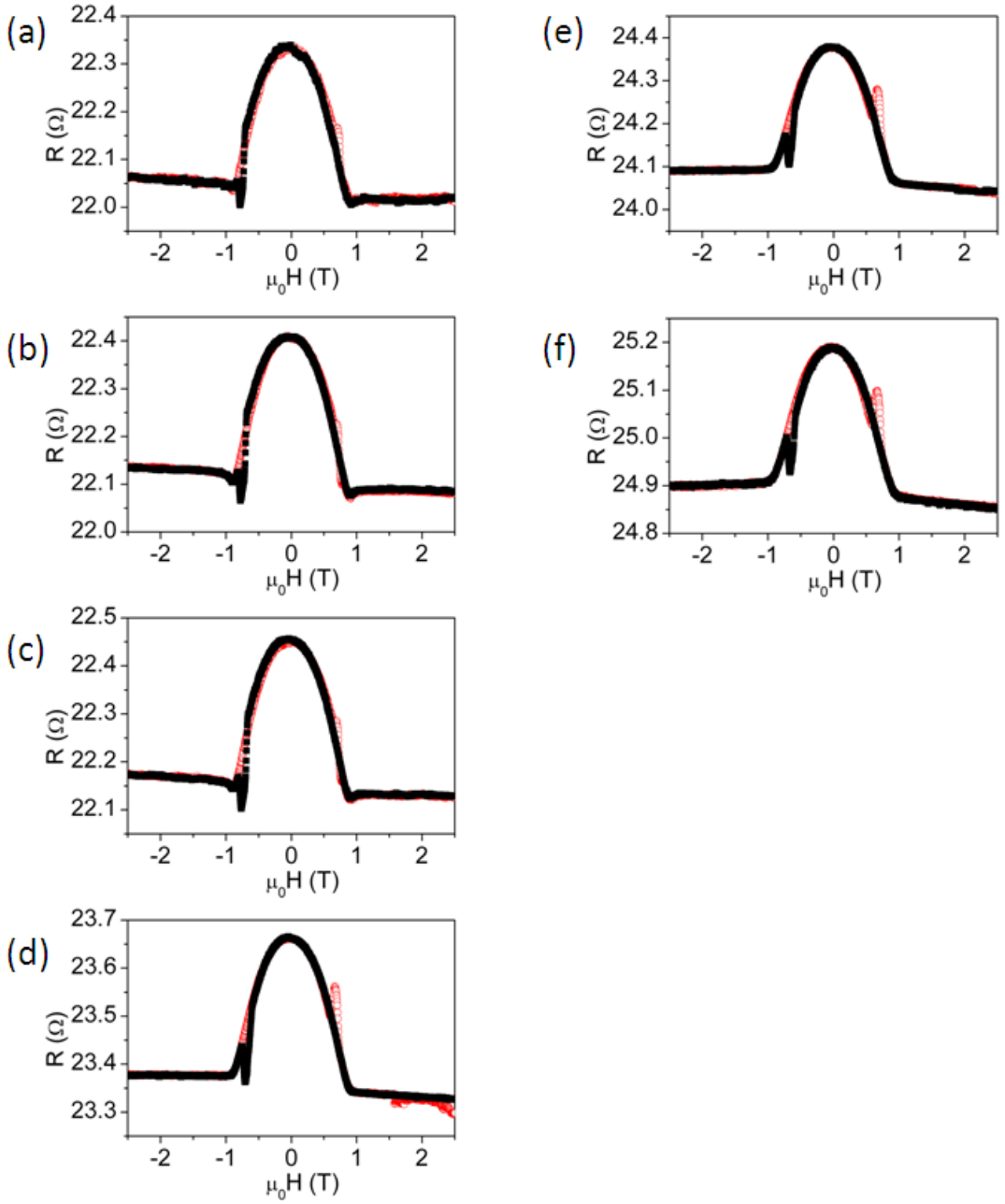

Figure B.19 $R_{yx}(B_z)$ configuration: the magnetic field was applied in the z-direction, the current was applied along the y-direction and the voltage was measured perpendicular to the current path. The magnetic field was swept up (red open circles) and down (black filled squares). (a) 5 K, (b) 12 K, (c) 15 K, (d) 75 K, (e) 100 K, (f) 125 K.

B.2.2 $R_{xy}(B_x)$

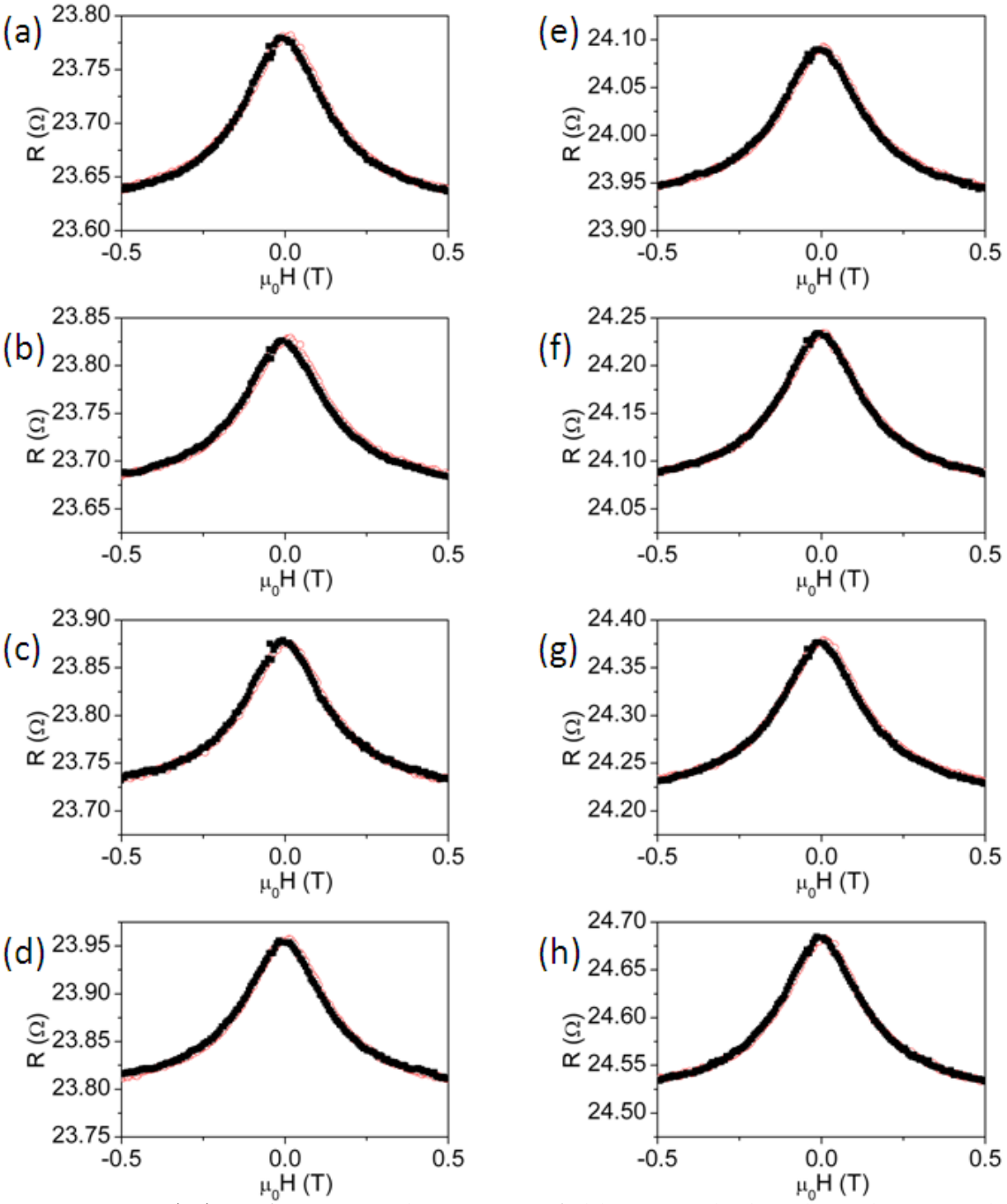

Figure B.20 $R_{xy}(B_x)$ configuration: the magnetic field was applied in the x-direction, the current was applied along the x-direction and the voltage was measured perpendicular to the current path. The magnetic field was swept up (red open circles) and down (black filled squares). (a) 8 K, (b) 10 K, (c) 12 K, (d) 15 K, (e) 20 K, (f) 25 K, (g) 30 K, (h) 40 K.

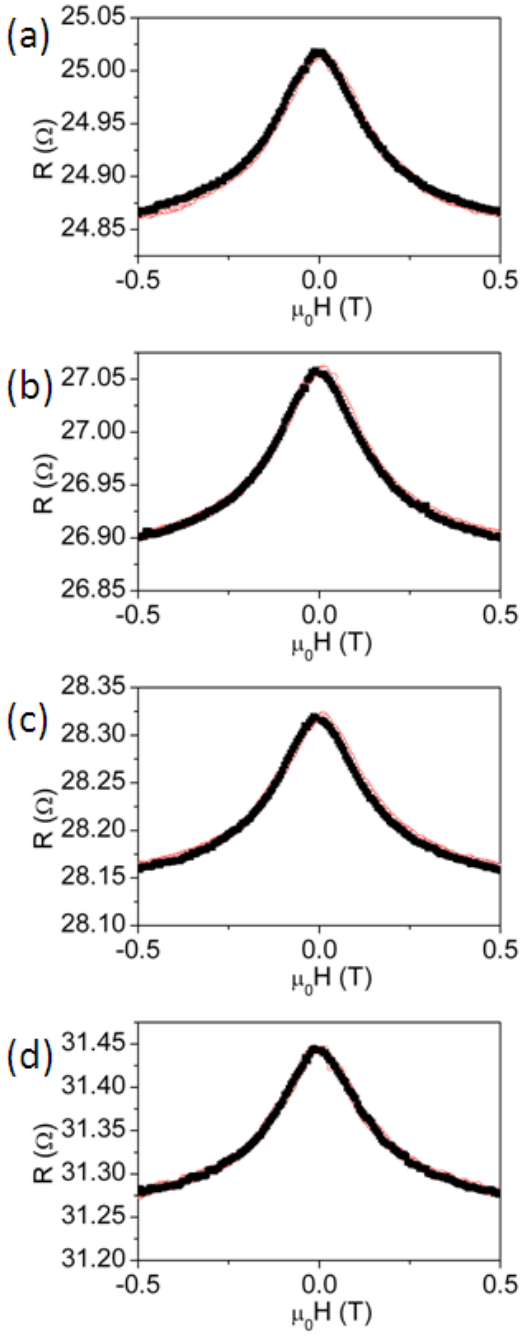

Figure B.21 $R_{xy}(B_x)$ configuration: the magnetic field was applied in the x-direction, the current was applied along the x-direction and the voltage was measured perpendicular to the current path. The magnetic field was swept up (red open circles) and down (black filled squares). (a) 50 K, (b) 100 K, (c) 125 K, (d) 175 K.

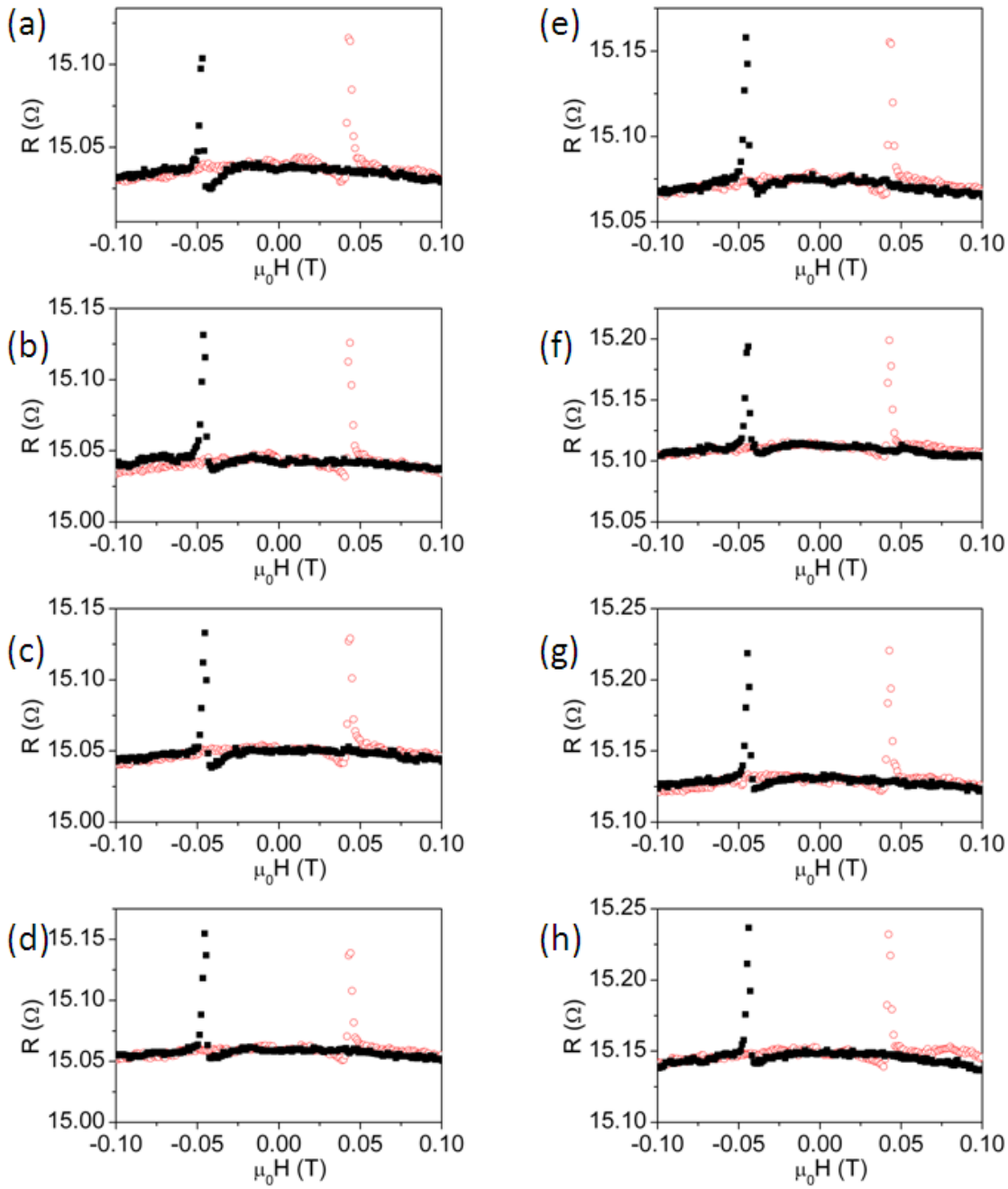

Figure B.22 $R_{xy}(B_x)$ configuration: the magnetic field was applied in the x-direction, the current was applied along the x-direction and the voltage was measured perpendicular to the current path. The magnetic field was swept up (red open circles) and down (black filled squares). (a) 3 K, (b) 4 K, (c) 5 K, (d) 6 K, (e) 7 K, (f) 9 K, (g) 10 K, (h) 11 K.

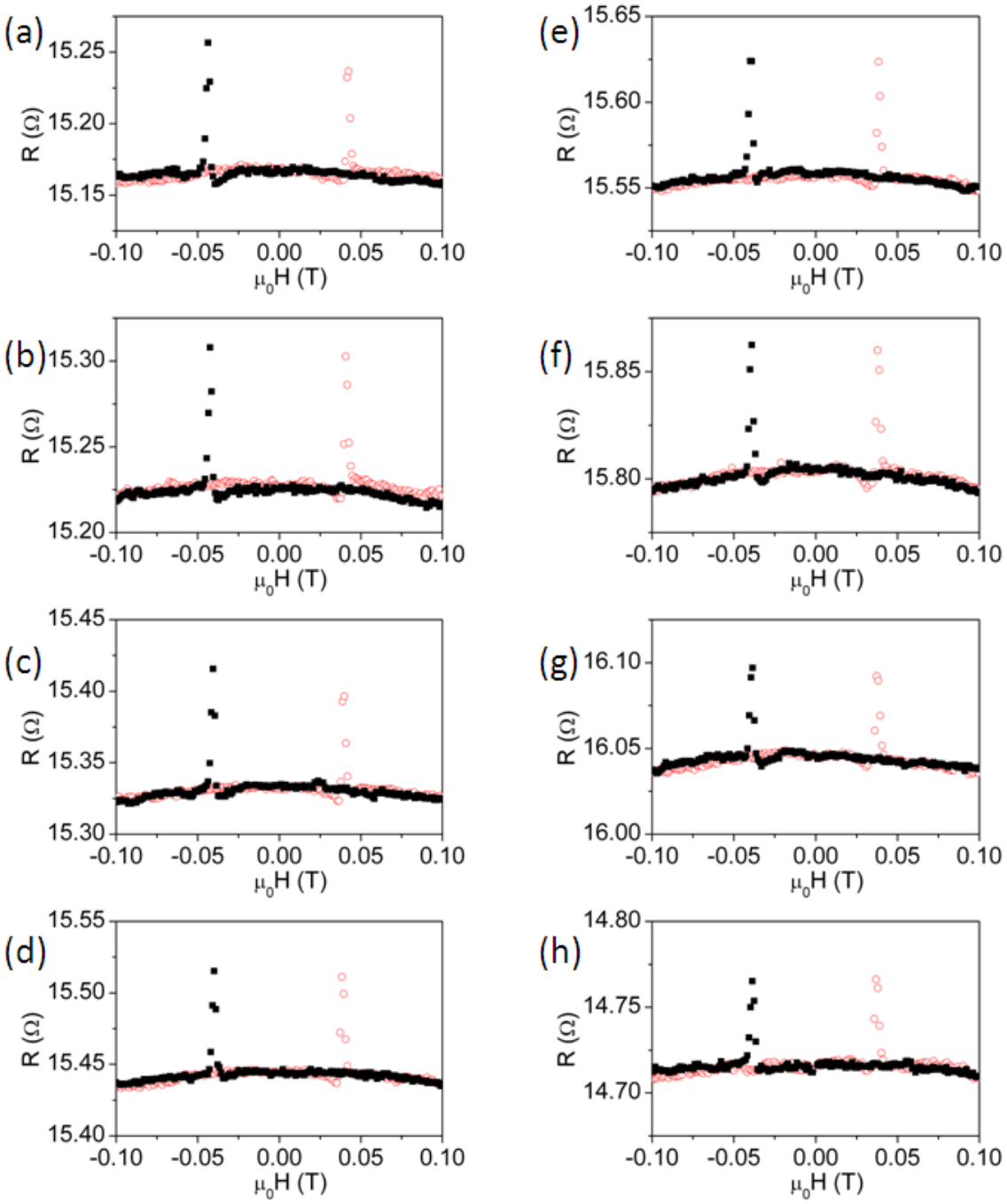

Figure B.23 $R_{xy}(B_x)$ configuration: the magnetic field was applied in the x-direction, the current was applied along the x-direction and the voltage was measured perpendicular to the current path. The magnetic field was swept up (red open circles) and down (black filled squares). (a) 12 K, (b) 15 K, (c) 20 K, (d) 25 K, (e) 30 K, (f) 40 K, (g) 50 K, (h) 75 K.

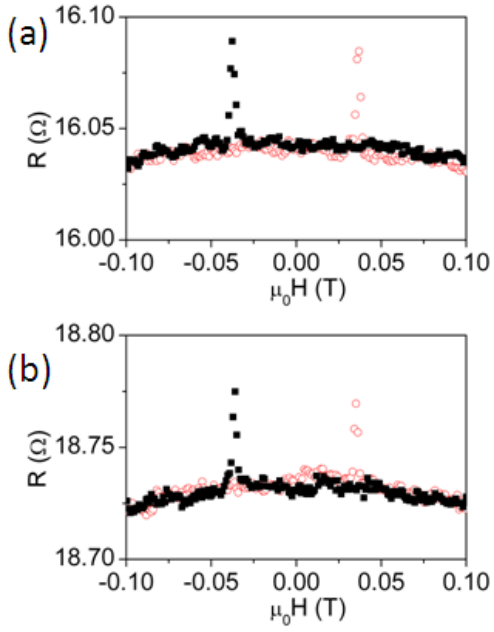

Figure B.24 $R_{xy}(B_x)$ configuration: the magnetic field was applied in the x-direction, the current was applied along the x-direction and the voltage was measured perpendicular to the current path. The magnetic field was swept up (red open circles) and down (black filled squares). (a) 125 K, (b) 200 K.

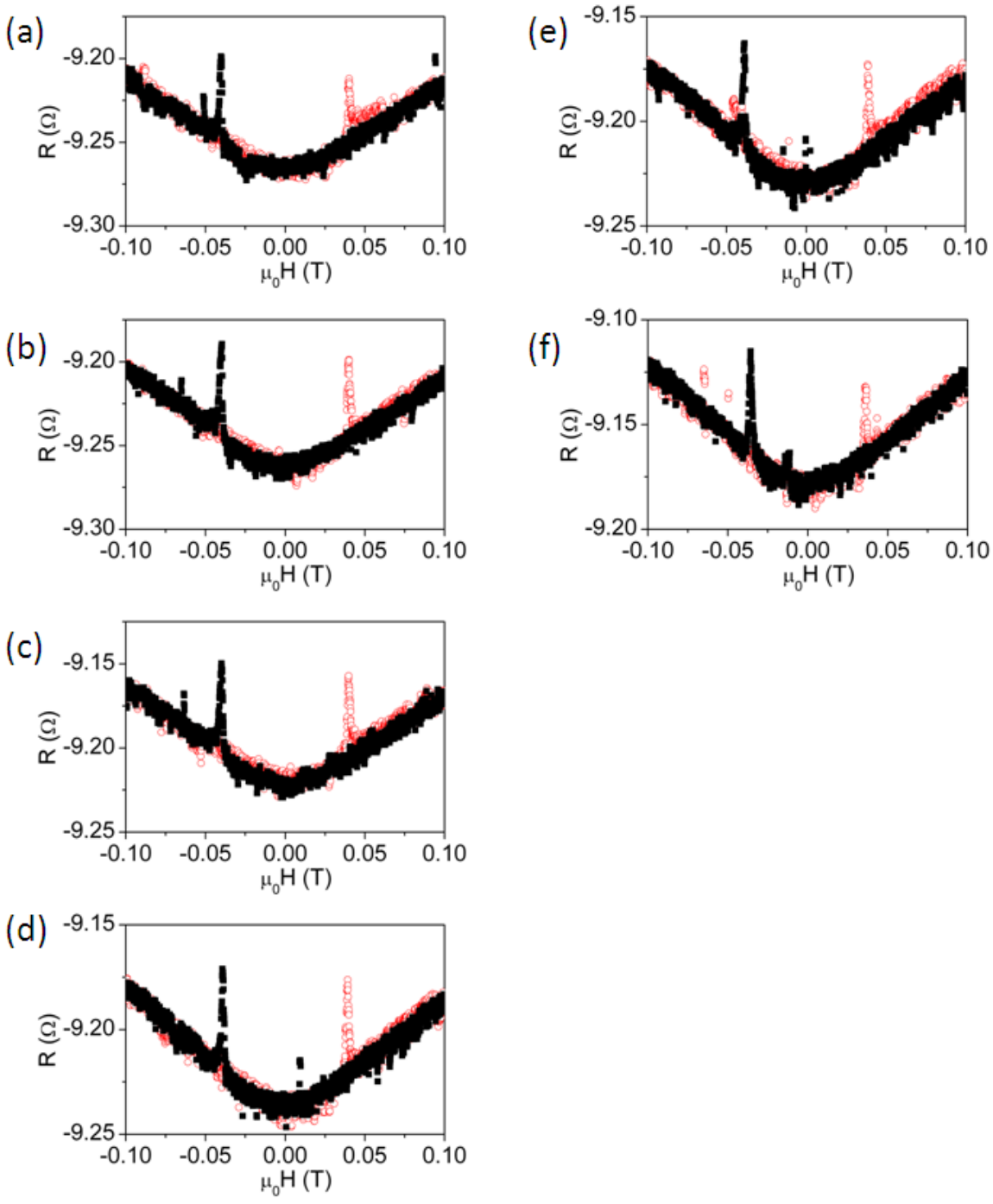

Figure B.25 Raw magnetoresistance data $R_{xy}(B_x)$. The magnetic field was applied along x and the current was applied along the x-direction. The voltage was measured perpendicular to the current path. The magnetic field was swept up (red open circles) and down (black filled squares). (a) 4 K, (b) 5 K, (c) 6 K, (d) 10 K, (e) 11 K and (f) 20 K.

B.2.3 $R_{yx}(B_x)$

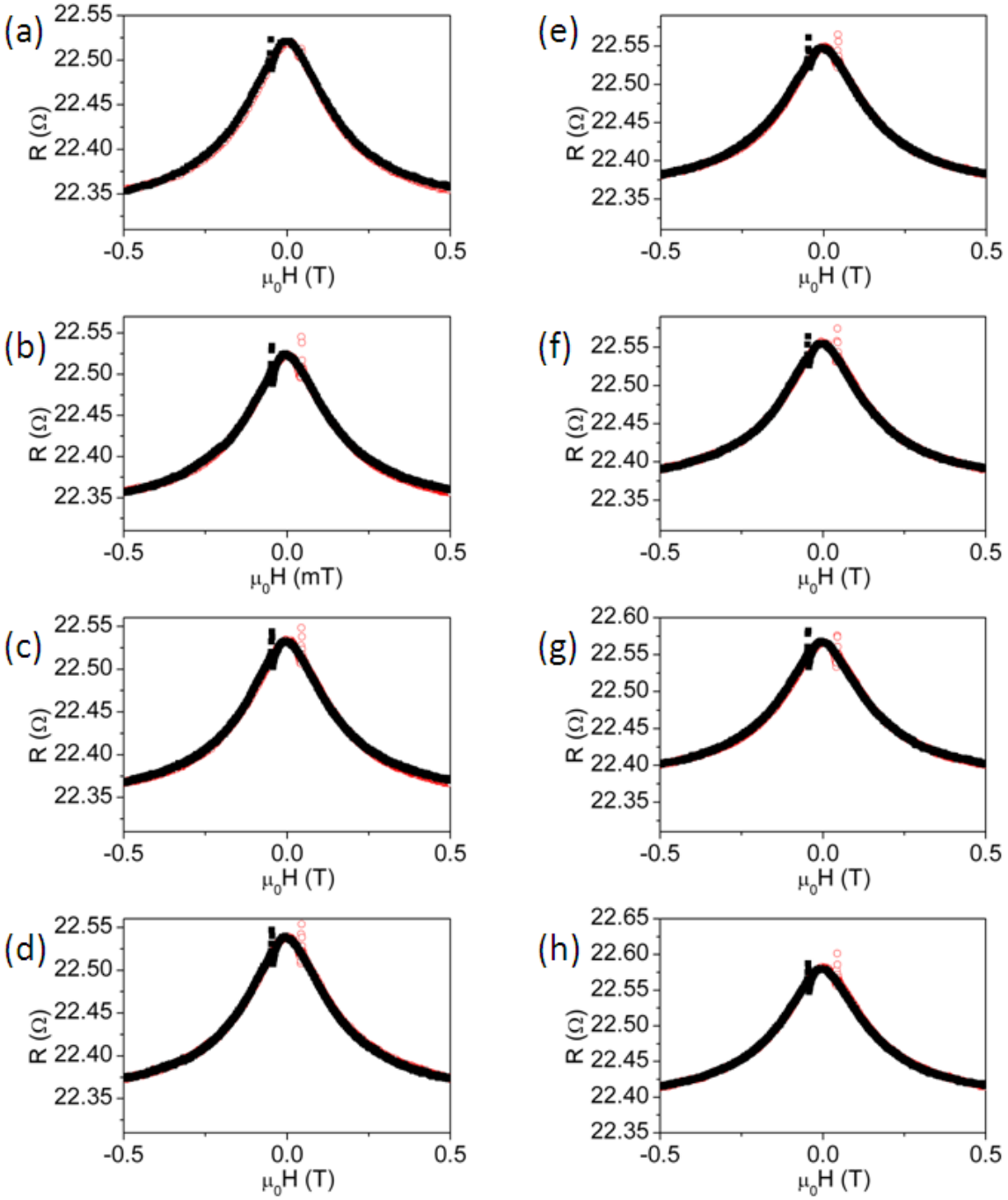

Figure B.26 $R_{yx}(B_x)$ configuration: the magnetic field was applied in the x-direction, the current was applied along the y-direction and the voltage was measured perpendicular to the current path. The magnetic field was swept up (red open circles) and down (black filled squares). (a) 2 K, (b) 3 K, (c) 4 K, (d) 5 K, (e) 6 K, (f) 7 K, (g) 8 K, (h) 10 K.

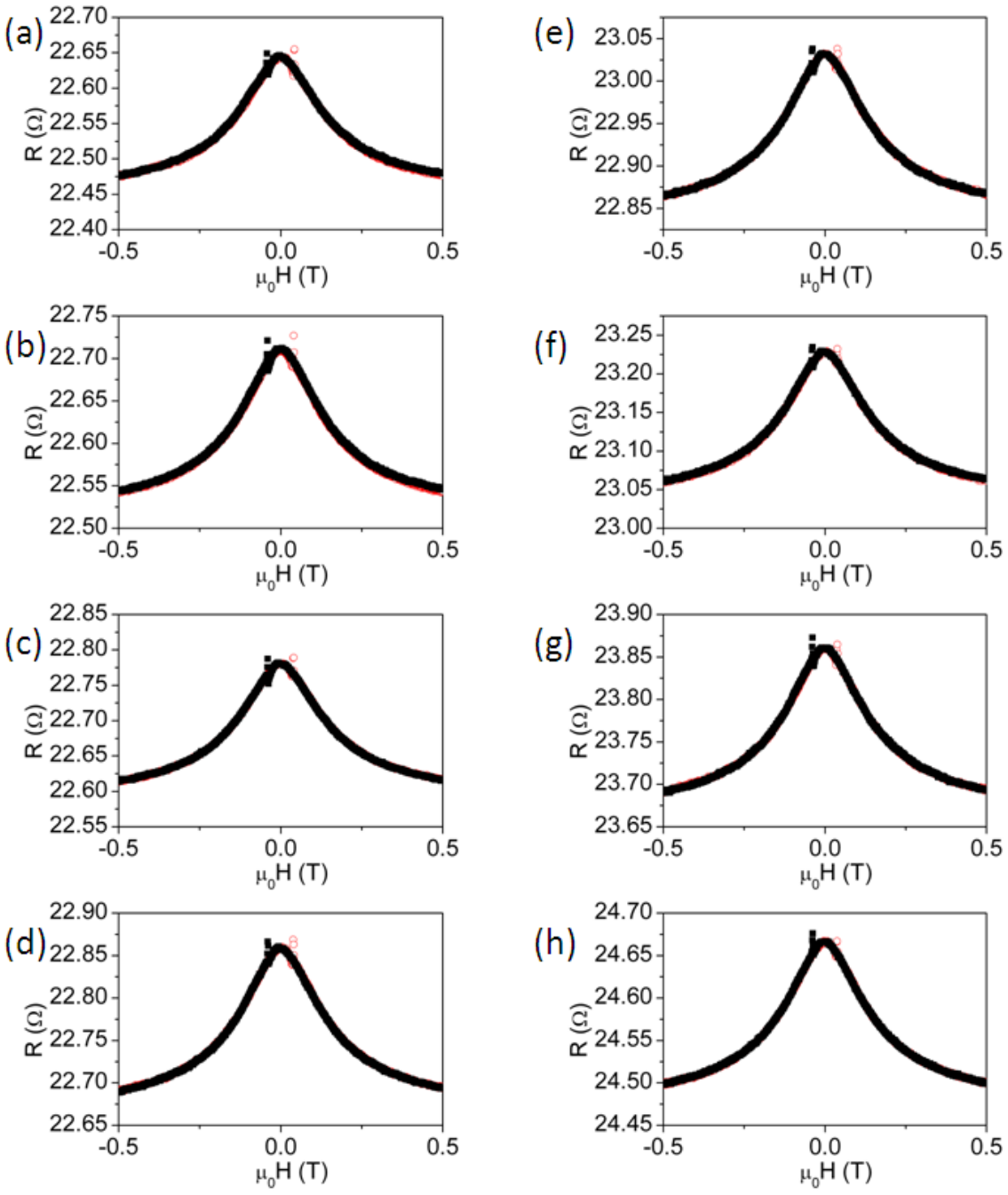

Figure B.27 $R_{yx}(B_x)$ configuration: the magnetic field was applied in the x-direction, the current was applied along the y-direction and the voltage was measured perpendicular to the current path. The magnetic field was swept up (red open circles) and down (black filled squares). (a) 15 K, (b) 20 K, (c) 25 K, (d) 30 K, (e) 40 K, (f) 50 K, (g) 75 K, (h) 100 K.

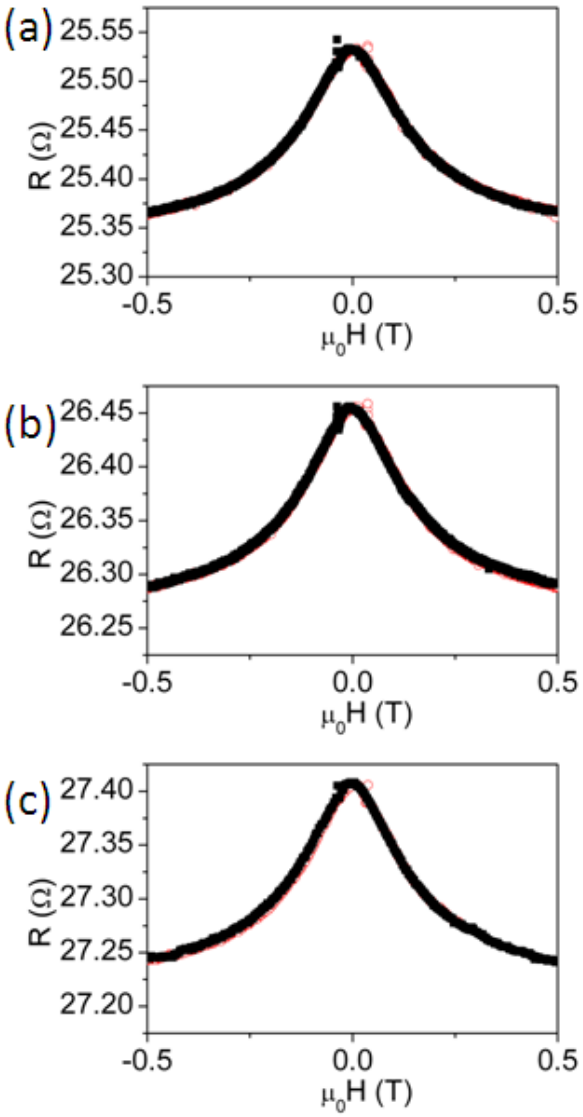

Figure B.28 $R_{yx}(B_x)$ configuration: the magnetic field was applied in the x-direction, the current was applied along the y-direction and the voltage was measured perpendicular to the current path. The magnetic field was swept up (red open circles) and down (black filled squares). (a) 125 K, (b) 150 K, (c) 175 K.

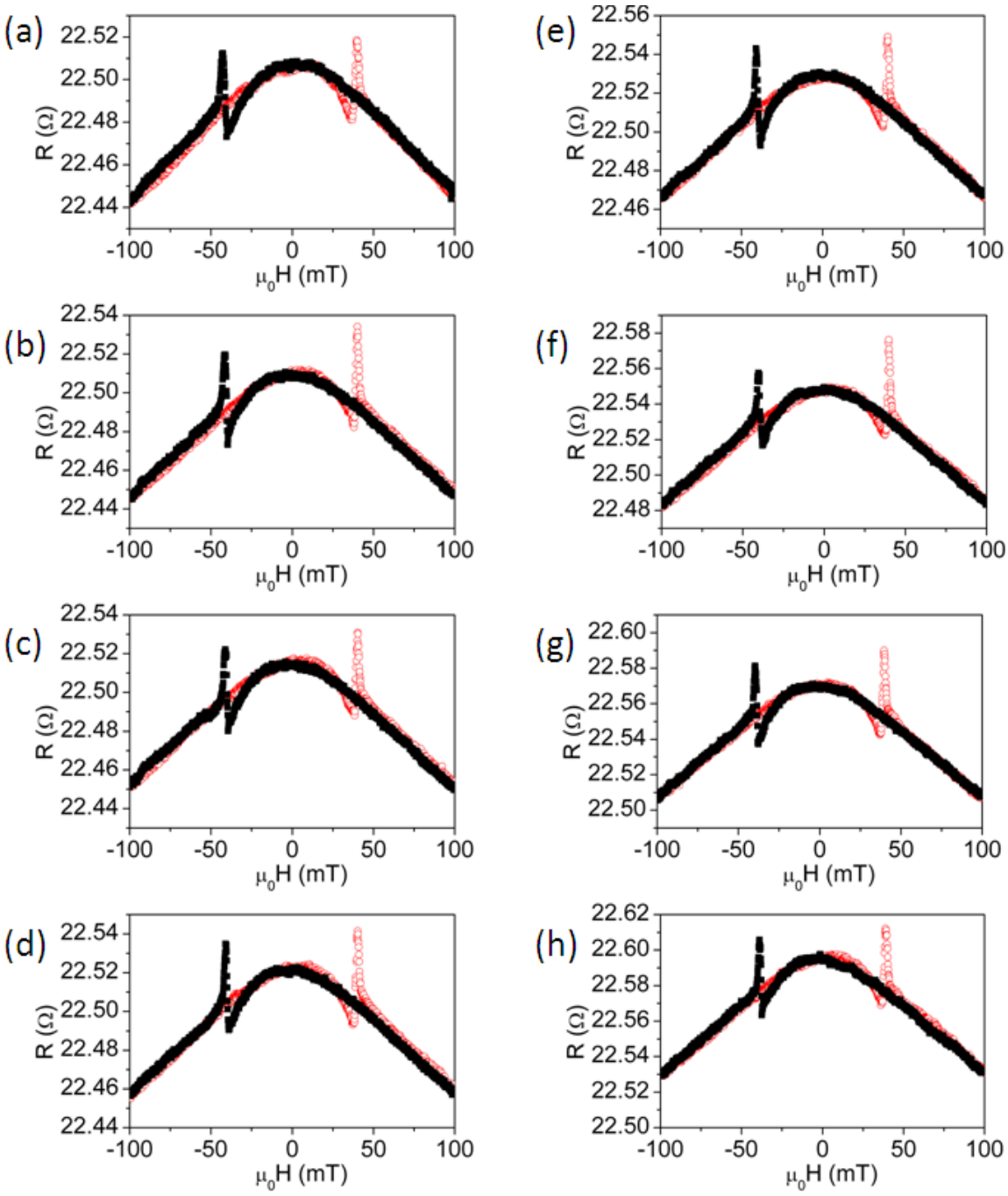

Figure B.29 $R_{yx}(B_x)$ configuration: the magnetic field was applied in the x-direction, the current was applied along the y-direction and the voltage was measured perpendicular to the current path. The magnetic field was swept up (red open circles) and down (black filled squares). (a) 2 K, (b) 3 K, (c) 4 K, (d) 5 K, (e) 6 K, (f) 8 K, (g) 10 K, (h) 12 K.

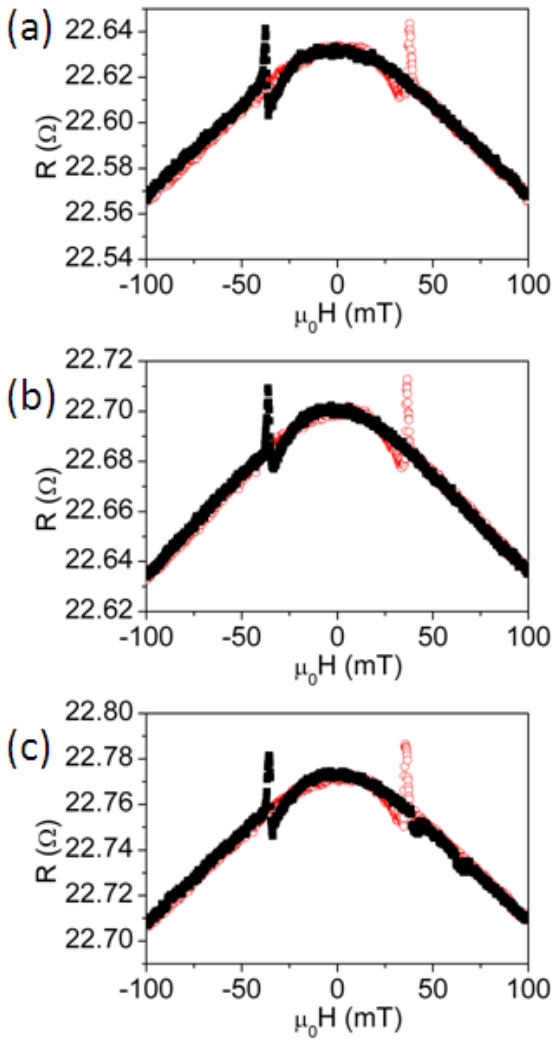

Figure B.30 $R_{yx}(B_x)$ configuration: the magnetic field was applied in the x-direction, the current was applied along the y-direction and the voltage was measured perpendicular to the current path. The magnetic field was swept up (red open circles) and down (black filled squares). (a) 15 K, (b) 20 K, (c) 25 K.

B.2.4 $R_{xy}(B_y)$

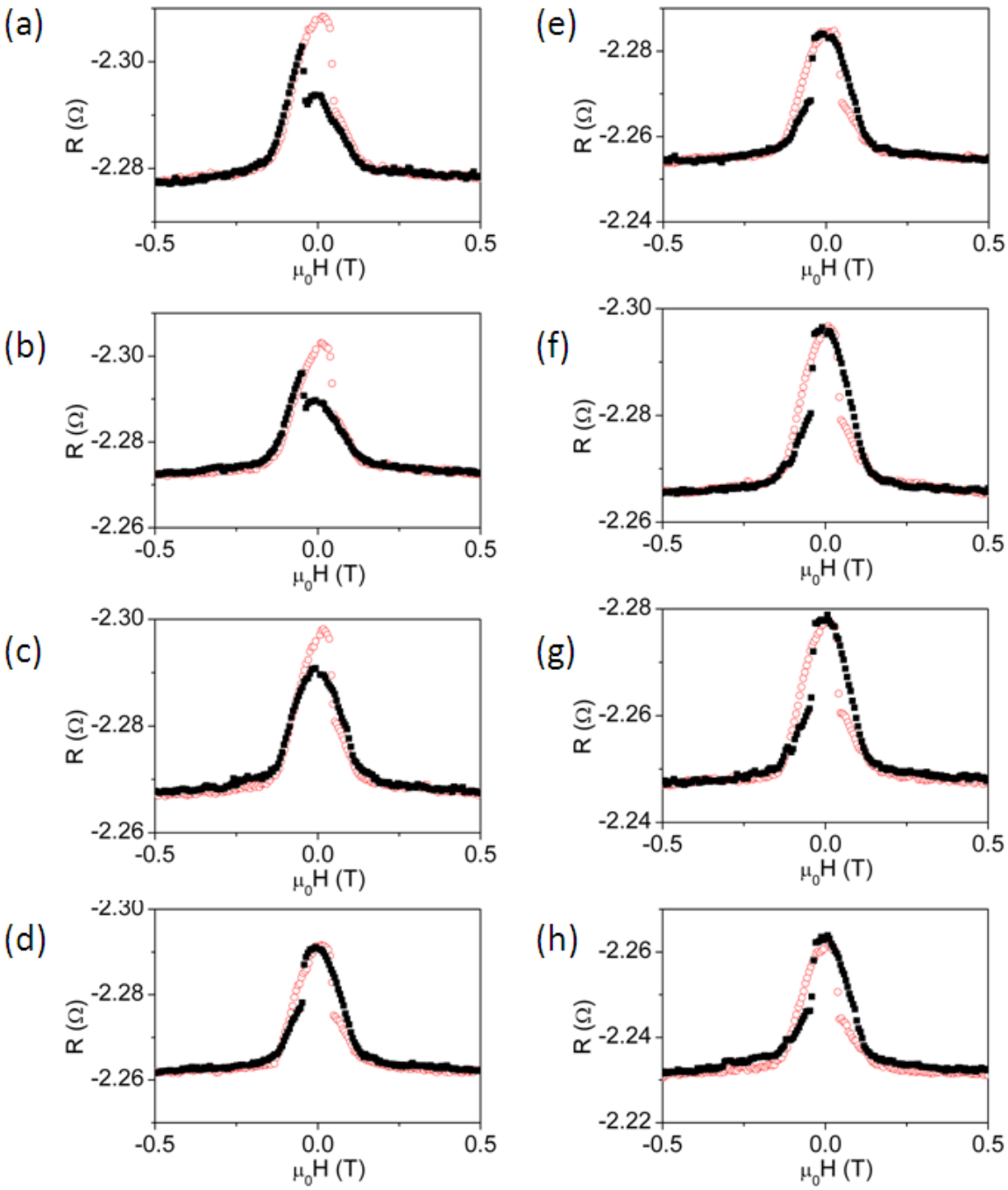

Figure B.31 $R_{xy}(B_y)$ configuration: the magnetic field was applied in the y-direction, the current was applied along the x-direction and the voltage was measured perpendicular to the current path. The magnetic field was swept up (red open circles) and down (black filled squares). (a) 5 K, (b) 8 K, (c) 10 K, (d) 12 K, (e) 15 K, (f) 20 K, (g) 25 K, (h) 30 K.

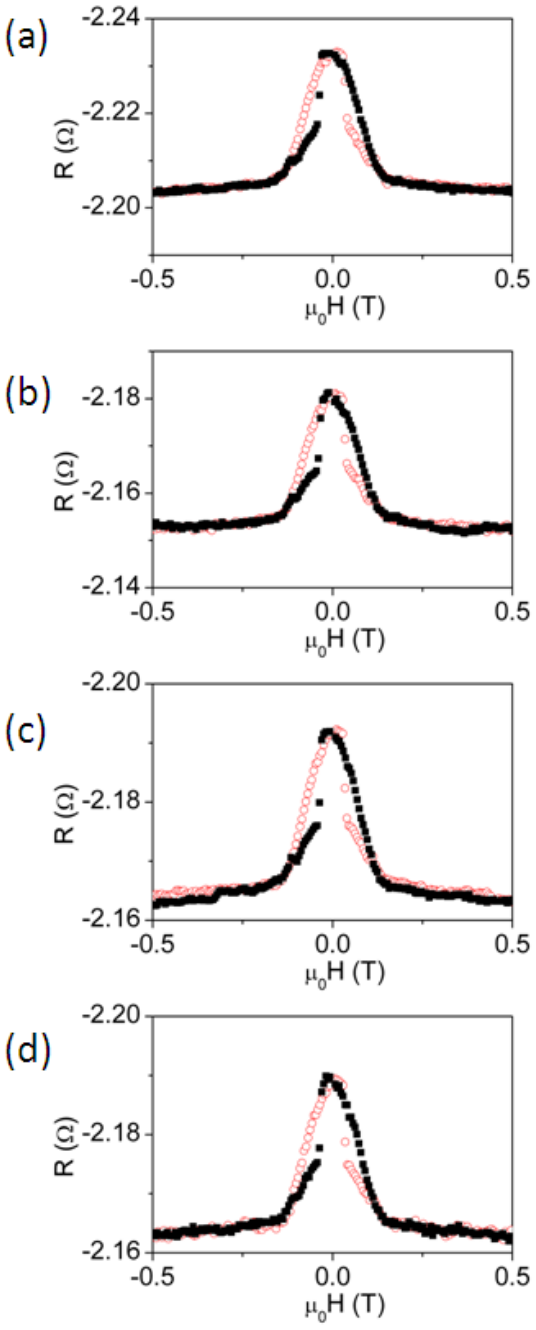

Figure B.32 $R_{xy}(B_y)$ configuration: the magnetic field was applied in the y-direction, the current was applied along the x-direction and the voltage was measured perpendicular to the current path. The magnetic field was swept up (red open circles) and down (black filled squares). (a) 50 K, (b) 75 K, (c) 100 K, (d) 125 K.

B.2.5 $R_{yx}(B_y)$

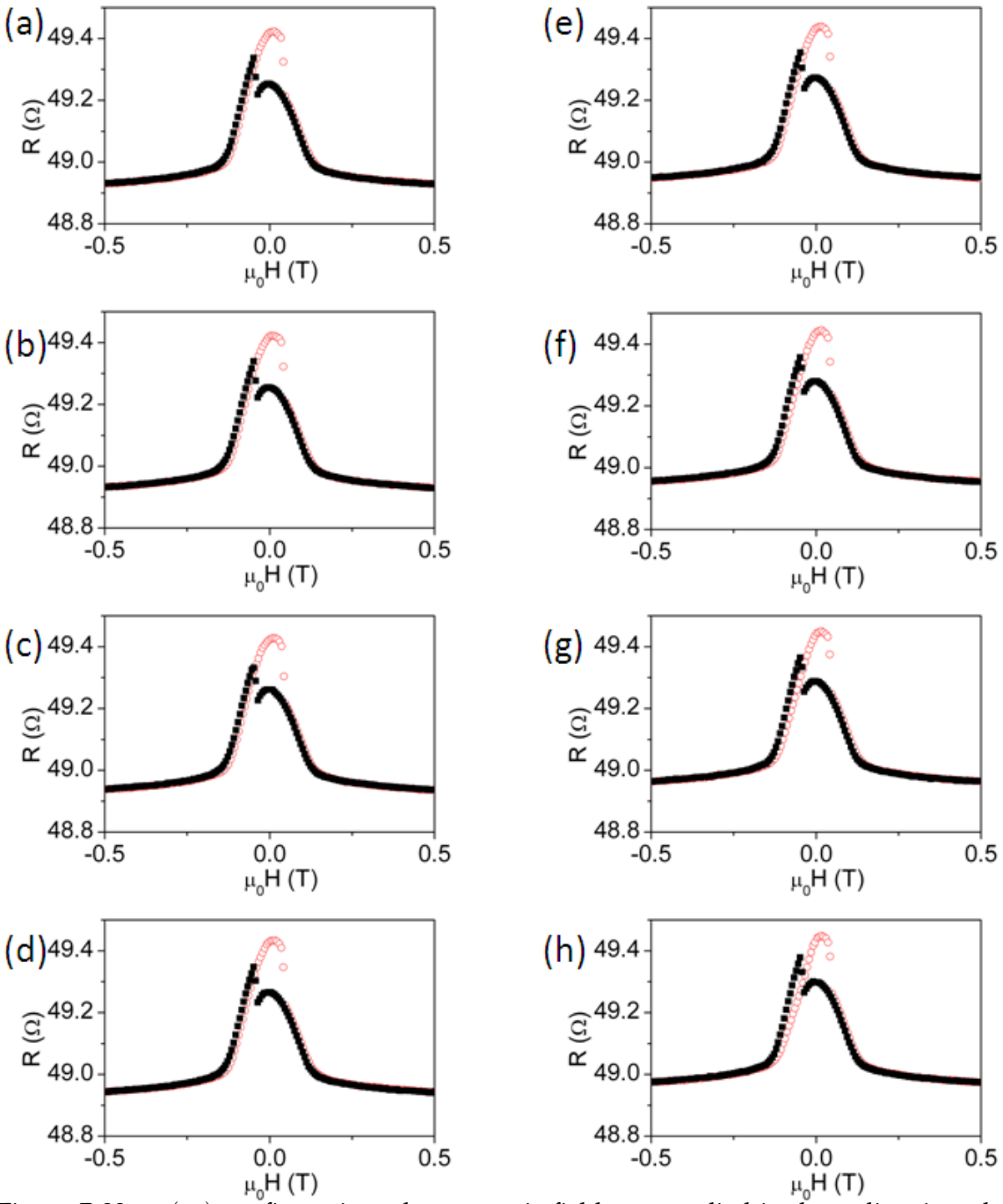

Figure B.33 $R_{yx}(B_y)$ configuration: the magnetic field was applied in the y-direction, the current was applied along the y-direction and the voltage was measured perpendicular to the current path. The magnetic field was swept up (red open circles) and down (black filled squares). (a) 2 K, (b) 3 K, (c) 4 K, (d) 5 K, (e) 6 K, (f) 7 K, (g) 8 K, (h) 9 K.

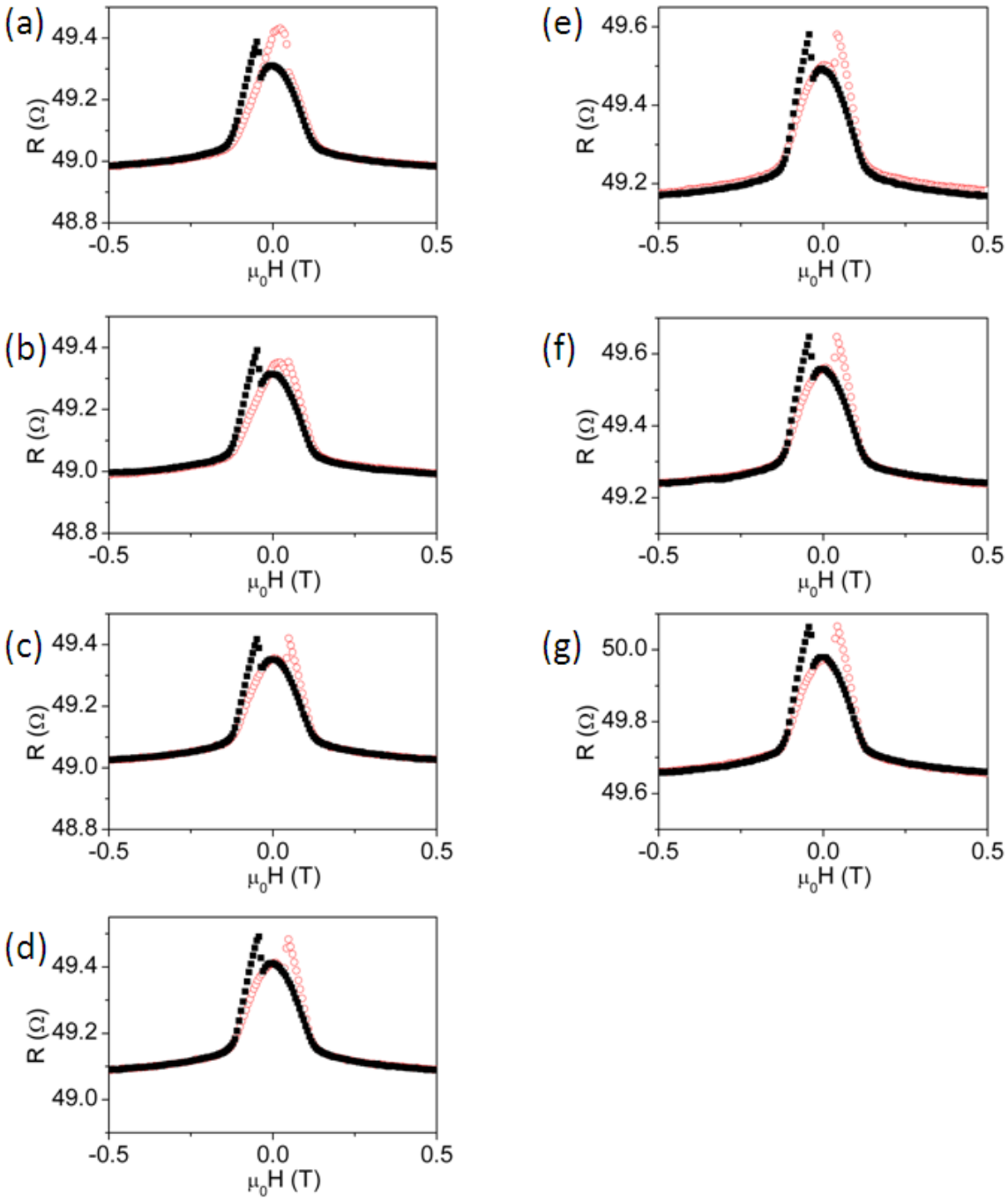

Figure B.34 $R_{yx}(B_y)$ configuration: the magnetic field was applied in the y-direction, the current was applied along the y-direction and the voltage was measured perpendicular to the current path. The magnetic field was swept up (red open circles) and down (black filled squares). (a) 10 K, (b) 12 K, (c) 15 K, (d) 20 K, (e) 25 K, (f) 30 K, (g) 50 K.

Appendix C

Copy Right Permissions

THE AMERICAN ASSOCIATION FOR THE ADVANCEMENT OF SCIENCE LICENSE TERMS AND CONDITIONS

Aug 08, 2013

This is a License Agreement between Katharina Zeissler ("You") and The American Association for the Advancement of Science ("The American Association for the Advancement of Science") provided by Copyright Clearance Center ("CCC"). The license consists of your order details, the terms and conditions provided by The American Association for the Advancement of Science, and the payment terms and conditions.

All payments must be made in full to CCC. For payment instructions, please see information listed at the bottom of this form.

License Number	3204171132202
License date	Aug 08, 2013
Licensed content publisher	The American Association for the Advancement of Science
Licensed content publication	Science
Licensed content title	Emerging Chirality in Artificial Spin Ice
Licensed content author	W. R. Branford, S. Ladak, D. E. Read, K. Zeissler, L. F. Cohen
Licensed content date	Mar 30, 2012
Volume number	335
Issue number	6076
Type of Use	Thesis / Dissertation
Requestor type	Scientist/individual at a research institution
Format	Print and electronic
Portion	Figure
Number of figures/tables	3
Order reference number	None
Title of your thesis / dissertation	Magnetic and electrical transport properties of artificial spin ice
Expected completion date	Aug 2013
Estimated size(pages)	300
Total	**0.00 GBP**

Terms and Conditions

American Association for the Advancement of Science TERMS AND CONDITIONS
Regarding your request, we are pleased to grant you non-exclusive, non-transferable permission, to republish the AAAS material identified above in your work identified above, subject to the terms and conditions herein. We must be contacted for permission for any uses other than those specifically identified in your request above.
The following credit line must be printed along with the AAAS material: "From [Full Reference Citation]. Reprinted with permission from AAAS."
All required credit lines and notices must be visible any time a user accesses any part of the AAAS material and must appear on any printed copies and authorized user might make.
This permission does not apply to figures / photos / artwork or any other content or materials included in your work that are credited to non-AAAS sources. If the requested material is sourced to or references non-AAAS sources, you must obtain authorization from that source as well before using that material. You agree to hold harmless and indemnify AAAS against any claims arising from your use of any content in your work that is credited to non-AAAS

NATURE PUBLISHING GROUP LICENSE
TERMS AND CONDITIONS

Aug 08, 2013

This is a License Agreement between Katharina Zeissler ("You") and Nature Publishing Group ("Nature Publishing Group") provided by Copyright Clearance Center ("CCC"). The license consists of your order details, the terms and conditions provided by Nature Publishing Group, and the payment terms and conditions.

All payments must be made in full to CCC. For payment instructions, please see information listed at the bottom of this form.

License Number	3204160547268
License date	Aug 08, 2013
Licensed content publisher	Nature Publishing Group
Licensed content publication	Nature
Licensed content title	Magnetic monopoles in spin ice
Licensed content author	C. Castelnovo,R. MoessnerandS. L. Sondhi
Licensed content date	Jan 3, 2008
Volume number	451
Issue number	7174
Type of Use	reuse in a thesis/dissertation
Requestor type	academic/educational
Format	print and electronic
Portion	figures/tables/illustrations
Number of figures/tables/illustrations	1
High-res required	no
Figures	Figure 2 (a)-(d)
Author of this NPG article	no
Your reference number	
Title of your thesis / dissertation	Magnetic and electrical transport properties of artificial spin ice
Expected completion date	Aug 2013
Estimated size (number of pages)	300
Total	0.00 GBP
Terms and Conditions	

Terms and Conditions for Permissions

Nature Publishing Group hereby grants you a non-exclusive license to reproduce this material for this purpose, and for no other use,subject to the conditions below:

NATURE PUBLISHING GROUP LICENSE TERMS AND CONDITIONS

Aug 08, 2013

This is a License Agreement between Katharina Zeissler ("You") and Nature Publishing Group ("Nature Publishing Group") provided by Copyright Clearance Center ("CCC"). The license consists of your order details, the terms and conditions provided by Nature Publishing Group, and the payment terms and conditions.

All payments must be made in full to CCC. For payment instructions, please see information listed at the bottom of this form.

License Number	3204160201240
License date	Aug 08, 2013
Licensed content publisher	Nature Publishing Group
Licensed content publication	Nature Physics
Licensed content title	Direct observation of the coherent precession of magnetic domain walls propagating along permalloy nanowires
Licensed content author	Masamitsu Hayashi,Luc Thomas,Charles Rettner,Rai MoriyaandStuart S. P. Parkin
Licensed content date	Jan 1, 2007
Volume number	3
Issue number	1
Type of Use	reuse in a thesis/dissertation
Requestor type	academic/educational
Format	print and electronic
Portion	figures/tables/illustrations
Number of figures/tables/illustrations	5
High-res required	no
Figures	Figure 5 (a) and (b)
Author of this NPG article	no
Your reference number	
Title of your thesis / dissertation	Magnetic and electrical transport properties of artificial spin ice
Expected completion date	Aug 2013
Estimated size (number of pages)	300
Total	0.00 USD
Terms and Conditions	

Terms and Conditions for Permissions

NATURE PUBLISHING GROUP LICENSE
TERMS AND CONDITIONS

Aug 08, 2013

This is a License Agreement between Katharina Zeissler ("You") and Nature Publishing Group ("Nature Publishing Group") provided by Copyright Clearance Center ("CCC"). The license consists of your order details, the terms and conditions provided by Nature Publishing Group, and the payment terms and conditions.

All payments must be made in full to CCC. For payment instructions, please see information listed at the bottom of this form.

License Number	3204151358758
License date	Aug 08, 2013
Licensed content publisher	Nature Publishing Group
Licensed content publication	Nature
Licensed content title	Zero-point entropy in 'spin ice'
Licensed content author	A. P. Ramirez, A. Hayashi, R. J. Cava, R. Siddharthan and B. S. Shastry
Licensed content date	May 27, 1999
Volume number	399
Issue number	6734
Type of Use	reuse in a thesis/dissertation
Requestor type	academic/educational
Format	print and electronic
Portion	figures/tables/illustrations
Number of figures/tables/illustrations	2
Figures	Figure 2 (a) and (b)
Author of this NPG article	no
Your reference number	
Title of your thesis / dissertation	Magnetic and electrical transport properties of artificial spin ice
Expected completion date	Aug 2013
Estimated size (number of pages)	300
Total	0.00 GBP
Terms and Conditions	

Terms and Conditions for Permissions

Nature Publishing Group hereby grants you a non-exclusive license to reproduce this material for this purpose, and for no other use,subject to the conditions below:

AMERICAN PHYSICAL SOCIETY
One Physics Ellipse, College Park, MD 20740 · http://www.aps.org

August 20, 2013

Dr. Katharina Zeissler
Imperial College London

Ref # 24253

Thank you for your permission request dated Aug. 8, 2013. We are pleased to grant you a non-exclusive, non-transferable permission, English rights, limited to **print and electronic format**, provided you meet the criteria outlined below. Permission is for a one-time use and does not include permission for future editions, updates, databases, translations, or any other matters. Permission must be sought for each additional use. This permission does not include the right to modify APS material.

Please print the required copyright credit line on the first page that the material appears: "Reprinted (abstract/excerpt/figure) with permission from [FULL REFERENCE CITATION] as follows: authors names, journal title, volume number, page number and year of publication. Copyright (YEAR) by the American Physical Society.

The following language must appear somewhere on the website: "Readers may view, browse, and/or download material for temporary copying purposes only, provided these uses are for noncommercial personal purposes. Except as provided by law, this material may not be further reproduced, distributed, transmitted, modified, adapted, performed, displayed, published, or sold in whole or part, without prior written permission from the American Physical Society."

Provide a hyperlink from the reprinted APS material (the hyperlink may be embedded in the copyright credit line). APS's link manager technology makes it convenient and easy to provide links to individual articles in APS journals. For information, see: http://link.aps.org/.

You must also obtain permission from at least one of the authors for each separate work, if you haven't done so already. The author's name and address can be found on the first page of the published Article.

Use of the APS material must not imply any endorsement by the American Physical Society.

Permission is granted for use of the following APS material only:

- Fig. 1, Phys. Rev. Lett. 94, 077202 (2005)
- Fig. 7, Phys. Rev. B 79, 214405 (2009)
- Fig. 1, Phys. Rev. Lett. 87, 047205 (2001)

Permission is limited to the single title specified of the publication as follows:
A thesis entitled "Magnetic and electrical transport properties of artificial spin ice" to be published by Imperial College London.

If you have any questions, please refer to the Copyright FAQ at: http://publish.aps.org/copyrightFAQ.html or send an email to assocpub@aps.org.

Sincerely,

Jamie L. Casey
Circulation and Fulfillment Assistant